

AN ABSTRACT OF THE DISSERTATION OF

Karoly Kozma for the degree of Doctor of Philosophy in Chemistry presented on November 4, 2019.

Title: Structural Elucidation of Metal-Oxo Systems by X-Ray Scattering Methods

Abstract approved: _____
May Nyman

Metal-oxo clusters are discrete molecular metal-oxides. Most metals form numerous cluster compounds that can be ligated, unligated, charged or neutral, controlling their solubility in water and/or organic solvents. They are important species to study reaction pathways from the monomeric building units to the bulk metal oxides, and have many application potentials in several industrial and technological areas. To reveal their structure-function relationship requires obtaining direct structural information about these clusters. However, structural information in amorphous solid materials or in solution is challenging to obtain. X-rays and neutrons are widely utilized for structural analyses on crystalline samples. Small-angle scattering (SAS) and total scattering (TS) techniques are performed to observe important structural features on disordered systems by observing particle size, shape and atom-pair correlations in real space. Studies within this dissertation utilize in-house small-angle X-ray scattering (SAXS) and pair distribution function (PDF) analysis of X-ray total scattering to extract structural information on various metal-oxo systems.

The thesis describes synthesis and characterization of metal-oxo systems both in solid and solution state, where a combination of these scattering methods along with other characterization techniques are utilized to obtain a complete structural description of metal-oxo cluster systems with metals from across the periodic table. The first study is a solid-state chemical reaction where crystalline $\text{NaBiO}_3 \cdot \text{XH}_2\text{O}$ loses its long-range order upon

contact with HNO_3 , and eventually it becomes a completely amorphous material. Sodium bismuthate is utilized for americium oxidation and separation in the nuclear fuel cycle, and also catalytic oxidation reactions. PDF analysis was performed to follow this reaction, considering the structural changes and describe the main features of the amorphous product. The following projects focus on solution characterizations. First, due to its novelty, the in-house total-scattering diffractometer was benchmarked for solution characterization of metal-oxo clusters. For these, we start with a simple system of water and standard solutions of $\{\text{SiW}_{12}\}$ Keggin ion and move forward to more complicated systems (uranyl-peroxide solutions) to benchmark the capability of the in-house instrumentation, as well as characterize an unknown cluster geometry. Following, PDF measurements were performed as a powerful complementary tool at different metal-oxo clusters in aqueous solutions. We proved that TiOSO_4 (an important intermediate in industrial TiO_2 production) dissolves and self-assembles as a $\{\text{Ti}_{18}\}$ -cluster in water, and eventually precipitates TiO_2 anatase. Scattering and spectroscopy techniques were utilized to characterize the changes during these reactions. Further, new zirconium-peroxo oxalate clusters with 9-coordinate zirconium and face-sharing connectivity were prepared, where stability order of those clusters was established based on SAXS and PDF data. The observed structural features are in good agreement with the acquired single-crystal data, where several new zirconium peroxo oxalate cluster compounds and conventional oxalate coordination compounds of Zr and Hf were synthesized depending on the counter cation. We differentiated the chemistry of these two metals that can be important for Zr/Hf separation for nuclear industry. These latter examples of Ti and Zr show that a laboratory diffractometer is still a very powerful complementary tool to perform PDF analysis, even with weak scattering elements or low concentrations, to acquire important structural information at conditions far from ideal.

©Copyright by Karoly Kozma

November 4, 2019

All Rights Reserved

Structural Elucidation of Metal-Oxo Systems by X-Ray Scattering Methods

by
Karoly Kozma

A DISSERTATION

submitted to

Oregon State University

in partial fulfillment of
the requirements for the
degree of

Doctor of Philosophy

Presented November 4, 2019
Commencement June 2020

Doctor of Philosophy dissertation of Karoly Kozma presented on November 4, 2019.

APPROVED:

Major Professor, representing Chemistry

Head of the Department of Chemistry

Dean of the Graduate School

I understand that my dissertation will become part of the permanent collection of Oregon State University libraries. My signature below authorizes release of my dissertation to any reader upon request.

Karoly Kozma, Author

ACKNOWLEDGEMENTS

I express sincere appreciation to Prof. May Nyman who accepted my application into her research group. She not just shaped me to a better scientist, but conversations with her inspired me throughout the past years. Thank you for your guidance, patience and full support during the past five years. I am proud to be one of your students.

Dr. Clement Falaise: for working together and great conversations about science – in general.

Dr. T. Wesley Surta: who introduced me to the magical world of PDF technique.

Dr. Pedro I. Molina: for his guidance during the first years.

Current and previous Nyman-group members who always created a supportive environment through the five years: Dr. Sara Goberna-Ferron, Dr. Harrison Neal, Dr. Lauren Fullmer, Dr. Dylan Sures, Dr. Omid Sadeghihosseinabadi, Dr. Nicolas Martin, Dr. Elliot Glass, Danielle Hutchison, Morgan Olsen, Mehran Amiri, Ana Arteaga, Rachelle Smith, Collin Muniz, Tasnim Rahman, Ian Colliard, Kieran Brunson, Lauren Palys, Cocoro Nagasaka, Andy Feng. These people supported and inspired me during the past five years.

The Department of Chemistry and Oregon State University: for supporting my research.

Adam Mate for his support and help in formatting the final dissertation.

My mother, father and my brother, Mihaly, who always supported me.

My friends who always encouraged me to succeed in what I do.

Without the support of all these people, this work would have not been accomplished.

CONTRIBUTION OF AUTHORS

Prof. May Nyman, my research advisor, always provided significant guidance on experimental design and manuscript writing, as well as thoughtful discussions on experimental results and their interpretations.

In Chapter 2, T. Wesley Surta and Prof. Michelle Dolgos provided valuable guidance and discussion to solid-state PDF data interpretation. Nicole M. Byrne also helped in PDF data collection and interpretation. Dr. Igor Lyubinetsky performed all XPS data collection. Wynn Stoxen provided important studies for Ce oxidation. Dr. Pedro I. Molina contributed to experimental design and insights into manuscript writing.

In Chapter 3, Dr. Clement Falaise and Harrison Neal synthesized / provided the starting materials for experiments with uranyl-peroxide nanoclusters.

In Chapter 4, Maoyu Wang and Prof. Zhenxing Feng performed Ti K-edge EXAFS measurements and data analyses, Dr. Nicolas P. Martin performed single-crystal data analysis. TEM images were collected by Peter Eschbach.

In Chapter 5, Dr. Lev N. Zakharov collected and analyzed single-crystal X-ray diffraction data. Morgan R. Olsen and Mehran Amiri collected ESI-MS data and Mehran Amiri provided the MS data analysis. Nicolas P. Martin provided valuable suggestions for single-crystal X-ray diffraction data collections.

TABLE OF CONTENTS (Continued)

	<u>Page</u>
3. Benchmarking solution PDF of metal-oxo clusters with laboratory diffractometer	31
3.1 Abstract	32
3.2 Introduction	32
3.2.1 Metal-oxo clusters	32
3.2.2 Pair distribution function (PDF) of solution samples	34
3.3 Experimental	36
3.4 Results and discussion	37
3.4.1 Water and silicotungstic acid solutions	37
3.4.2 Uranyl-peroxide nanoclusters in water	41
3.4.3 Further possibilities and limitations	48
3.5 Conclusion	53
3.6 Acknowledgement	54
4. The role of titanium-oxo clusters in sulfate process for TiO ₂ production	55
4.1 Abstract	56
4.2 Introduction	56
4.3 4.3. Experimental	58
4.3.1 Reagents and solution preparation	58
4.3.2 Crystallization	58
4.3.3 Characterization methods	59
4.4 Results and discussion	59
4.4.1 Solution behavior and solution characterization by X-ray scattering techniques	59
4.4.2 TiOSO ₄ solution structure by EXAFS	63

TABLE OF CONTENTS (Continued)

	<u>Page</u>
4.4.3. Single crystal structural description	64
4.4.4. Aging of TiOSO ₄ solutions.....	66
4.5 Conclusions.....	70
4.6 Acknowledgements.....	71
5. Counter cation controlled structural diversity of Zr/Hf oxalates and Zr-peroxo oxalates	72
5.1 Abstract.....	73
5.2 Introduction.....	73
5.3 Experimental.....	76
5.3.1. Syntheses	76
5.3.2. Characterization methods	78
5.4 Results and discussion	78
5.4.1. Structural description of Hf-oxalate compounds (compounds 1-6)	78
5.4.2. Structural description of Zr with 8-fold coordination (compound 7, 9, 12 and 13)	81
5.4.3. Zr rings with 9-fold coordination (compound 8, 10 and 11).....	83
5.4.4. Bulk solid-state and solution characterizations	88
5.4.5. Solution Characterization	90
5.5 Conclusion	97
5.6 Acknowledgements.....	98
6. Conclusions	99
7. Bibliography.....	102
8. Appendix A	120
9. Appendix B	132

TABLE OF CONTENTS (Continued)

Page

10. Appendix C 146

LIST OF FIGURES

<u>Figure</u>	<u>Page</u>
Figure 1.1 Schematic ball-stick representation of different metal-oxygen compounds. Metal-oxo cluster (B) are between the monomeric units of metal ions (A) and the infinite lattice of metal oxides (C). Color code: red sphere-oxygen, blue sphere-metal.....	2
Figure 1.2 The scattering vector or momentum transfer, defined by the incoming and scattered vectors. (Courtesy: ref ¹³)	4
Figure 1.3 Schematic representation of acquiring SAXS data from data collection (A). X-ray photons scatter when going through the solution sample containing metal-oxo cluster (top left). From the recorded image (top right) the scattering profile is obtained via data processing (bottom right). B represents our in-house Anton Paar instrumentation. (www.anton-paar.com)	5
Figure 1.4 Different regions of scattering profile provide different information about the studied compound in the system. The exact values of the regions are arbitrary, vary from system to system.	6
Figure 1.5 Rigaku Smartlab in-house laboratory diffractometer capable for X-ray total scattering measurements (A). B is the instrument chamber with a solution sample in the capillary attachment. (www.rigaku.com).....	7
Figure 1.6 Individual steps of data processing from the experimental scattering curve to the final PDF data. All steps are calculated simultaneously by PDFgetX3. ¹⁸ Blue curve represents the processed functions using the raw data, while red curves show data using tuned data processing parameters.	10
Figure 2.1 (A) Structural representation of NaBiO ₃ and (B) {Bi-O} sheet in the structure along the crystallographic <i>ab</i> plane (ICSD: 91776). (Bi- brown, Na-green octahedra)...	18
Figure 2.2 Comparison of PXRD patterns (A) and experimental PDF curves (B) of NaBiO ₃ ·3H ₂ O before and after dehydration. Corresponding Miller indices are assigned to the prominent peaks on the diffraction patterns.....	19
Figure 2.3 Experimental and calculated PDF curves of the anhydrous sample.....	20
Figure 2.4 Pair distribution function of NaBiO ₃ ·3H ₂ O, and simulations of model derived from the structure of NaBiO ₃	22
Figure 2.5 (A) X-ray scattering curves and (B) their Na:Bi ratio received by EDX of the acid-treated samples.....	23
Figure 2.6 Experimental PDF data of the acid-treated samples. Insets represent the atomic pair correlations in the pristine material. (Brown: Bi polyhedral, red: O, green: Na ⁺)	24
Figure 2.7 Monitoring the changes (A) at the neighboring Bi-Bi distance and (B) at the new arising Bi-Bi correlation in the acid-treated samples utilizing PDF analysis. Inset represents the atomic pair correlations in the pristine material. (Brown: Bi polyhedral, green: Na ⁺)	25
Figure 2.8 XPS of the Bi peak in the selected samples.	26

<u>Figure</u>	LIST OF FIGURES (Continued)	<u>Page</u>
Figure 2.9 TGA of NaBiO ₃ ·3H ₂ O and two selected acid-treated samples with the corresponding weight-loss.		28
Figure 2.10 Comparison of Ce ³⁺ oxidation in 1M HNO ₃ , using the different NaBiO ₃ ·3H ₂ O starting materials: pristine, pretreated with 0.37 M HNO ₃ (1:1), and pretreated with 5.7 M HNO ₃ (1:16).		29
Figure 3.1 Polyhedral representation of some uranyl-peroxide nanoclusters using the notations introduced by Burns <i>et al.</i>		34
Figure 3.2 Left: experimental X-ray total scattering curve of pure H ₂ O solvent. Right: experimental PDF analysis of the H ₂ O solvent.		38
Figure 3.3 Left: comparison of experimental PDFs of {SiW ₁₂ } solutions using different data collection time (fast scan: 0.5°/minute, slow scan: 0.2°/minute). Right: Concentration dependence of {SiW ₁₂ } solutions.		39
Figure 3.4 The experimental and simulated PDFs of {SiW ₁₂ } cluster in aqueous solution. The correlations assigned to the distinct peaks are present at the bottom: the polyhedral and ball-stick (oxygen atoms are eliminated for clarity) representation of the {SiW ₁₂ } Keggin ion.		41
Figure 3.5 Experimental PDF of U60-solution with the simulated curve of the cluster. .		43
Figure 3.6 The main three structural features in uranyl-peroxide nanoclusters we observe by solution PDF: neighboring U-U distance (A), the diagonal correlations in the building units (B), and the overall diameter (U to U, excluding yl-oxygens) of the cluster (C). ...		43
Figure 3.7 Experimental PDFs of saturated U24, U28 and U32R solutions with the simulated curve of the individual clusters.		45
Figure 3.8 SAXS curve of U-TMA cluster dissolved in methanol.		46
Figure 3.9 PDF of the U-TMA cluster in solid (top) and in solution (bottom) state.		47
Figure 3.10 PDF comparing the two step-wise reaction composition solutions, along with dissolved δ-{ZnCr ₁₂ } crystals plus simulated PDF for δ-{ZnCr ₁₂ }. The peak at 2 Å (Cr/Zn-O bond) is normalized for Cr ₂ Zn(O _x (OH) _y)(NO ₃) _{4.9} and Cr ₂ Zn(O _x (OH) _y)(NO ₃) _{3.7} , so intensity of the M-M peaks (A & B, M=Zn/Cr) can be compared. The strong negative dip around the 2 Å is due to background subtraction of the water peak at 2.7 Å.		49
Figure 3.11 PDF analysis of X-ray total scattering on solutions of 100 mM TMA{Ta ₆ } in 200mM TMAOH with added CsCl (0 to 12 molar equivalents) – ‘sim’ indicates a simulated function. (courtesy ⁹⁷)		52
Figure 3.12 PDF of TiOSO ₄ solution at different concentrations. The low scattering power of Ti cannot overcome the signal coming from H ₂ O solvent even at 1 M concentration level.		53

LIST OF FIGURES (Continued)

<u>Figure</u>	<u>Page</u>
Figure 4.1 Representations of the relevant structures in this study. A is $\text{TiOSO}_4 \cdot \text{H}_2\text{O}$, B shows two views of a $\{\text{Ti}_{18}\}$ cluster; and C shows the unit cell of anatase. Turquoise polyhedra are Ti-centered, red spheres are oxo or water ligands, yellow spheres are sulfur in sulfate anions, and white spheres are hydrogen, of water molecules (in $\text{TiOSO}_4 \cdot \text{H}_2\text{O}$ only).	60
Figure 4.2 SAXS curves of freshly dissolved TiOSO_4 solutions (the curves are scaled to compare the Guinier region). The simulated curve for $\{\text{Ti}_{18}\}$ -cluster is presented for comparison. Inset: pair distance distribution function (PDDF) analysis of TiOSO_4 solution (0.5 M, red) and simulated $\{\text{Ti}_{18}\}$ -cluster (black).	62
Figure 4.3 Ti EXAFS k-space (left) and Fourier-transformed R-space (right) of TiO_2 anatase, solid and dissolved $\{\text{Ti}_{18}\}$ and $\text{TiOSO}_4 \cdot \text{H}_2\text{O}$	63
Figure 4.4 Unit cell view of crystallized $\{\text{Ti}_{18}\}$, illustrating close association of Cl^- with the cluster. Ti-polyhedra are turquoise, sulfates are yellow and red ball-and-stick, Cl^- are pink spheres, TBA are black (C) and blue (N) spheres.	65
Figure 4.5 A: X-ray total scattering pattern of the precipitated solid from 0.25M TiOSO_4 solution after 21 days. The broad peaks (indicating low crystallinity) are in good agreement with the calculated peak positions of TiO_2 anatase phase (black). (Note: Mo $K\alpha$ radiation was used, where $\lambda=0.71 \text{ \AA}$.) Inset: TEM image of precipitate. Red lines correspond with particle size of 2.07, 2.21, 1.45, 1.88, 2.05 and 1.45 nm. B: Experimental PDF analysis of the X-ray total scattering curve. Atom-pair correlations are in good agreement with anatase phase with approximately 2.0 nm particle size.	66
Figure 4.6 PDFs of the wet slurry at different time. The red line is indicating the approximate size of the crystalline core of titanium-oxide nanoparticles. The red line indicates the estimated size of the crystalline core.	67
Figure 4.7 The linear correlation between the size of crystalline core and aging time. Amorphous materials are distinguished. Naturally aged samples (with no dilution) are also shown on the curve.	68
Figure 4.8 SAXS curves of aged samples of 0.25M TiOSO_4 solutions.	69
Figure 4.9 Ti K-edge K-space (left) and R-space (right) EXAFS data comparing dissolved $\{\text{Ti}_{18}\}$ to dissolved TiOSO_4 (fresh and aged; 1M). Differences observed in the R-space data primarily reflect the influences of poor statistics at higher k values.	70
Figure 5.1 Ball-stick representation of the obtained hafnium oxalate compounds (1) (infinite chains), (2) and (3) (dimer) and (4) - (6) monomer. Color code: Hf-blue, O-red, C-black and H-white.	79
Figure 5.2 Ball-stick representation of atoms in unit cells of (1), (2) and (6) with counter ions associated. Water molecules are omitted for clarity. Color code: Hf-blue, O-red, C-black, H-white, N-dark green, Li-grey, Na-light green and Cs-pink.	81
Figure 5.3 Planar view of (7). Color code: Zr-pale blue, O-red and C-black, respectively.	82

LIST OF FIGURES (Continued)

<u>Figure</u>	<u>Page</u>
Figure 5.4 Ball-stick representation of the building unit in {Zr ₈ }, {Zr ₁₂ } and {Zr ₁₆ }-cluster. A: the monomer unit, B: the connection mode between two monomer units via mixed hydroxo-peroxo groups and C: the connection mode between two monomer units via two peroxo group. Color code: Zr-pale blue, O-red and C-black.	84
Figure 5.5 Representation of {Zr ₈ }-cluster (8). The perspectives of {Zr ₈ }-cluster (left and center) and the unit cell (H ₂ O molecules are omitted) (right). Color code: Li-grey, O-red, C-black and Zr-O polyhedra: light blue.	85
Figure 5.6 Representation of {Zr ₁₂ }-cluster (10). The perspectives of {Zr ₁₂ }-cluster (left and center) and the unit cell (H ₂ O molecules are omitted) (right). Color code: K-purple, O-red, C-black and Zr-O polyhedra: light blue.	86
Figure 5.7 Polyhedral and ball-stick representation of {Zr ₁₆ }-cluster (11). The perspectives of {Zr ₁₆ }-cluster (left and center) and the unit cell (H ₂ O molecules are omitted) (right). Color code: Rb-tan, O-red, C-black and Zr-O polyhedra: light blue.	86
Figure 5.8 FT-IR spectra of the obtained solid products. Left: Hf products, right: Zr products. Numbers are indicating different IR bands assigned in Table 5.7.	89
Figure 5.9 Experimental (red) and calculated (black) SAXS curves of {Zr ₁₂ } (left) and {Zr ₈ }-cluster (right), intensity-normalized for comparison. The {Zr ₁₂ }-cluster is intact upon dissolution.	91
Figure 5.10 SAXS curves (offset for ease of viewing) of the dissolved Hf oxalate products. All solutions show scattering which are in good agreement (except for Li-Hf oxalate) with the [Hf ₄ (OH) ₄ (C ₂ O ₄) ₁₁] fragment model (inset).	93
Figure 5.11 PDF analysis of the observed X-ray total scattering measurements on reaction solutions and dissolved solids of Hf (left) and Zr (right). The different position of the arising peak between 3.0-3.6 Å indicates the different coordination mode for the two metals in aqueous conditions. (Hf-blue, Zr-pale blue and O-red).	95
Figure 5.12 ESI-MS graph of the dissolved crystal of {Zr ₁₂ }-cluster. The most intense signals originate from monomeric species with a presence of some oligomer species (see inlet).	97

LIST OF TABLES

<u>Table</u>	<u>Page</u>
Table 2.1 Experimental parameters for acid-treatment of NaBiO ₃ ·XH ₂ O	15
Table 2.2 Quantitative results from XPS on the selected samples, with Bi normalized to unity (see Table A6). (Peak positions: Bi ⁵⁺ : 157.59-158.81 eV, Bi ³⁺¹ : 157.59-157.93 eV and Bi ³⁺² : >159.50 eV)	27
Table 3.1 The observed peaks assigned to atom-pair correlations in {SiW ₁₂ } Keggin ion with the experimental and simulated distances.....	40
Table 3.2 Comparison of experimentally observed interatomic correlations in uranyl-peroxide nanocages with the values obtained by simulations.	44
Table 4.1 Summary of SAXS analysis of TiOSO ₄ solutions	61
Table 5.1 Selected synthetic parameters for preparation of described products. Acetone solvent diffusion was carried out at 4°C. (TMA ⁺ = tetramethylammonium ion, [N(CH ₃) ₄] ⁺)	77
Table 5.2 Selected interatomic distances from the crystallographically independent hafnium centers in multinuclear (1), (2) and (3) Hf oxalates. Parenthesis indicates errors.	80
Table 5.3 Selected interatomic distances around hafnium centers in (4), and (6) monomer Hf oxalates. Parenthesis indicates errors.	80
Table 5.4 Selected interatomic distances from the crystallographically independent Zr centers in (7), (9), (12) and (13) Zr(-peroxo)-oxalates.	83
Table 5.5 Selected interatomic distances from the crystallographically independent Zr centers in (8), (10) and (11) Zr-peroxo-oxalates.....	85
Table 5.6 Selected bond angles for compound (8), (10) and (11). (Note: “in” and “out” indicates the position of peroxide oxygens relative to the center of ring.	87
Table 5.7 FT-IR vibrational band positions (cm ⁻¹) of the obtained Hf-oxalate and Zr(-peroxo)-oxalate solid products.....	90
Table 5.8 List of assignment of the ESI-MS spectrum (negative mode) of {Zr ₁₂ } crystals dissolved in water.	96

LIST OF APPENDIX FIGURES

<u>Figure</u>	<u>Page</u>
Figure A 1 Images of the $\text{NaBiO}_3 \cdot 3\text{H}_2\text{O}$ and the acidified samples. $\text{NaBiO}_3:\text{HNO}_3$ ratio is increased from left to the right. Reaction conditions are collected in Table 2.1.	121
Figure A 2 Calibration curve to determine Ce^{4+} concentration in the Ce^{3+} oxidation tests. Absorbance values were recorded at 380 nm.	123
Figure A 3 TGA of hydrous sodium bismuthate starting material. Mass loss indicates the total water content of $\text{NaBiO}_3 \cdot 3\text{H}_2\text{O}$	123
Figure A 4 Powder X-ray diffraction pattern of the anhydrous NaBiO_3 (black) and following its suspension in neutral and basic conditions (A) or in acidic conditions (B).	124
Figure A 5 Models derived from NaBiO_3 structure: H_2O is in the voids of {Bi-O} sheet (A) and {Bi-O} and {Na-O} sheets are together with H_2O molecules (B). (Bi-O brown octahedra, Na-green, O-red spheres)	124
Figure A 6 Comparison of the simulated PDF curves of one {Bi-O} sheet (black) and this single sheet with the presence of H_2O (blue) and with Na^+ (red).	125
Figure A 7 (A) Scanning electron microscope (SEM) image of $\text{NaBiO}_3 \cdot 3\text{H}_2\text{O}$ and (B) EDX spectrum. EDX analysis shows 0.6:1 ratio to Na:Bi diverges greatly from the theoretical 1:1 ratio.	125
Figure A 8 Comparison of the PDF of selected acid-treated samples with the simulations of α - Bi_2O_3 (ICSD-15072) and {Bi ₆ }-cluster (ICSD-300008). The common Bi-Bi correlations in these known phases possess a Bi-Bi correlation are not observable in the acidified products.	126
Figure A 9 XPS data of $\text{NaBiO}_3 \cdot 3\text{H}_2\text{O}$ and two acid-treated samples (A)-Bi, (B)-O, (C)-Na and (D) surveys).	127
Figure A 10 XPS spectra of A) Bi and B) O for anhydrous NaBiO_3 , Bi_2O_3 and $\text{Bi}(\text{NO}_3)_3$	128
Figure A 11 Scanning electron microscope (SEM) images of acid-treated samples of (A)- $\text{NaBiO}_3:\text{HNO}_3=1:1$ ratio and B)- $\text{NaBiO}_3:\text{HNO}_3=1:16$ ratio.	128
Figure B 1 SAXS curves of dissolved TiOSO_4 in water (blue: 0.25M, green: 0.5M and red: 1.0M concentration). Inset shows the relation between the concentration at the observed intensity at $q=0.3 \text{ \AA}^{-1}$	136
Figure B 2 Ti K-edge EXAFS Fourier Transformation R-space modeling based fitting of (A) TiOSO_4 powder and (C) {Ti ₁₈ } powder; K-space of (B) TiOSO_4 powder and (D) {Ti ₁₈ } powder.	136
Figure B 3 The observed Ti-O distances in Ti-O polyhedra in the $\text{TiOSO}_4 \cdot \text{H}_2\text{O}$ unit cell (ICSD: 72973). Sulfate groups are eliminated for clarification. Letters represents the observed Ti K-edge EXAFS correlations assigned in Table B 1.	137

LIST OF APPENDIX FIGURES (Continued)

<u>Figure</u>	<u>Page</u>
Figure B 4 The observed Ti-Ti and Ti-S correlations in $\text{TiOSO}_4 \cdot \text{H}_2\text{O}$ crystal structure (ICSD: 72973) Oxygens and hydrogens are eliminated for clarification. Letters represents the observed Ti K-edge EXAFS correlations assigned in Table B 1.....	137
Figure B 5 The observed equatorial Ti-O correlations in a pentagonal $\text{Ti}(\text{Ti})_5$ unit (left) and the horizontal Ti-O correlations between two $\text{Ti}(\text{Ti})_5$ layers in $\{\text{Ti}_{18}\}$ -cluster (right). Sulfur, oxygen and hydrogen atoms are eliminated for clarification. Numbers represents the observed Ti K-edge EXAFS correlations assigned in Table B 1.....	138
Figure B 6 The observed Ti-Ti correlations in one pentagonal $\text{Ti}(\text{Ti})_5$ unit (left) and between two layers of $\text{Ti}(\text{Ti})_5$ unit in the $\{\text{Ti}_{18}\}$ -cluster (right). Sulfur, oxygen and hydrogen atoms are eliminated for clarification. Numbers represents the observed Ti K-edge EXAFS correlations assigned in Table B 1.....	138
Figure B 7 Representation of the average intensity according to the 2theta angle.....	139
Figure B 8 Illustration of disorder model between three sulfates and a Cl^- anion on one face of the $\{\text{Ti}_{18}\}$ cluster. The two Ti-centers of the cluster to which the disordered sulfates bind/associate are shown partially transparent (Ti is turquoise, O is red, S is yellow, Cl is pink). (1) half-occupied Cl^- , $\sim 3 \text{ \AA}$ from the Ti-bound water ligand, present only when sulfate 3 or 4 is present. (2) sulfate-1; $1/3^{\text{rd}}$ occupied; (3) sulfate-2; $1/3^{\text{rd}}$ occupied; (4) sulfate-3; $1/3^{\text{rd}}$ occupied. The sulfur atoms freely refined around $1/3^{\text{rd}}$ occupancy, so we fixed the occupancy to $1/3^{\text{rd}}$; and likewise fixed the associated oxos appropriately. When a sulfate is not bound to the Ti, there is a water molecule (H's not show, nor located in the electron density map). Therefore Ti is always octahedrally-coordinating to six oxygen atoms.....	139
Figure B 9 Illustration of sulfate-chloride disorder model on the opposite face of the cluster that is described in Figure B 8. There are two settings (each 50% occupied) in this model. The first is with sulfate terminally bound to a Ti in the capping layer of Ti_{18} . The second is with a water molecule bound to the Ti; the Cl-atom is 3 \AA from the oxygen of this water molecule. Color scheme is the same as described for Figure B 8.....	140
Figure B 10 Calculated yield of anatase formation from 0.25M TiOSO_4 solution at ambient conditions.....	140
Figure B 11 EDX spectrum of the obtained precipitated solid from 0.25 M TiOSO_4 solution. The observed S:Ti ratio is 1:4.....	141
Figure B 12 SAXS curves of aged samples of 1.0M TiOSO_4 solutions.....	142
Figure C 1 Experimental PXRD of the obtained Li-Hf oxalate product. It does not indicate crystallinity.	154
Figure C 2 Experimental PXRD of the obtained Li-Zr oxalate product along with calculated peak position of relevant reference structures. Product shows very poor crystallinity. .	154
Figure C 3 Experimental PXRD of the obtained Na-Hf oxalate product.	155

LIST OF APPENDIX FIGURES (Continued)

<u>Figure</u>	<u>Page</u>
Figure C 4 Experimental PXRD of the obtained Na-Zr oxalate product along with calculated peak position of relevant reference structure. Despite the crystallinity of the product it does not match known relevant phases. (Number in parenthesis indicate the ICSD code of the known phase.)	155
Figure C 5 Experimental PXRD of the obtained K-Hf oxalates along with calculated peak positions of relevant structures. Despite the crystallinity of the product it does not match known relevant phases. (Number in parenthesis indicates the ICSD code of the known phase.)	156
Figure C 6 Experimental PXRD of the obtained K-Zr oxalate product along with calculated peak positions of relevant reference structures. (Numbers in parenthesis indicate the ICSD code of the known phases.)	156
Figure C 7 Experimental PXRD of the obtained Rb-Hf oxalate product. Product shows poor crystallinity.	157
Figure C 8 Experimental PXRD of the obtained Rb-Zr oxalate product. Product shows poor crystallinity.	157
Figure C 9 Experimental PXRD of the obtained Cs-Hf oxalate product.....	158
Figure C 10 Experimental PXRD of the obtained Cs-Zr oxalate product.	158
Figure C 11 FT-IR spectra of the starting materials used.	159
Figure C 12 Top: Simulation of {Zr ₁₂ }-cluster shows radius of 6.6 Å. The simulated curve was obtained from the single-crystal structure. Bottom: we observed 6.3 Å radius modelling the experimental curve.....	160
Figure C 13 Pair distance distribution function (PDDF) analysis of the calculated and experimental SAXS profile of {Zr ₁₂ }-cluster. The larger extent and more intense correlation below 6 Å on the experimental curve indicating association with K ⁺ counter cations.	161
Figure C 14 Size distribution analysis on the dissolved Li-Zr-peroxo-oxalate product, from which {Zr ₃ } crystals are obtained. Analysis indicates two populations present in the solution.....	162
Figure C 15 SAXS curves (scaled) of the dissolved Zr oxalate products. All solutions show scattering indicating formation of a bigger specie, where the inset represents the [Zr ₄ (OH) ₄ (C ₂ O ₄) ₁₁] fragment used for simulation.	163
Figure C 16 Experimental and simulated mass spectrum between 420-460 m/z (in negative mode) of the solution obtained from dissolved crystals of {Zr ₁₂ }-cluster. A={Zr ₄ (O ₂) ₃ (C ₂ O ₄) ₄ (OH) ₂ } ²⁻ , B={Zr ₄ (O ₂) ₃ (C ₂ O ₄) ₄ (OH) ₂ (H ₂ O)} ²⁻ and C=, {Li ₃ Zr ₂ (O ₂) ₅ (C ₂ O ₄)} ¹⁻ respectively	163

LIST OF APPENDIX TABLES

<u>Table</u>	<u>Page</u>
Table A 1 Comparison of unit cell parameters of the two different NaBiO ₃ phases.....	129
Table A 2 Selected atomic distances in anhydrous NaBiO ₃ (ICSD: 91776)	129
Table A 3 Calculated parameters of the refinement for anhydrous NaBiO ₃	130
Table A 4 The refined anisotropic parameters extracted from the refinement of anhydrous NaBiO ₃	130
Table A 5 Atom percent ratios obtained by elemental analysis of the pristine NaBiO ₃ ·3H ₂ O and one selected acidified sample.....	130
Table A 6 Summary of XPS data on NaBiO ₃ ·3H ₂ O and the acid-treated samples.	131
Table A 7 Summary of XPS results for anhydrous NaBiO ₃ , Bi ₂ O ₃ and Bi(NO ₃) ₃ measurements.....	131
Table B 1 EXAFS fitting parameters for TiOSO ₄ and {Ti ₁₈ } in both solid phase and aqueous solution phase (CN: the coordination number; R: bonding distance; E ₀ : energy shift; σ ² : mean-square disorder).....	143
Table B 2 Crystal data and structure refinement for the obtained {Ti ₁₈ }-cluster.	144
Table B 3 Calculated parameters of the refinement for TiO ₂ anatase nanoparticle.....	144
Table B 4 Extracted quantitative data [†] from aged 0.25 M and 1.0 M TiOSO ₄ solutions. Size is represented in Å in terms of R _g , while the percentage represents the relative population.	145
Table C 1 Crystallographic data of multinuclear Hf compounds of (1), (2) and (3).	164
Table C 2 Crystallographic data of mononuclear Hf compounds of (4), (5) and (6).	165
Table C 3 Crystallographic data of 8-fold Zr compounds of (7), (9), (12) and (13).	166
Table C 4 Crystallographic data of 9-fold Zr compounds of (8), (10) and (11).	167
Table C 5 Atomic ratios in Hf oxalate samples by EDX-SEM.	168
Table C 6 Atomic ratios in of Zr-peroxo oxalate samples by EDX-SEM.	168

1. Introduction

1.1 Metal-oxo clusters

Metal-oxo clusters are molecular metal-oxide compounds that form by self-assembly of reactive oxometalate anion or polyoxocation precursors in aqueous or organic solution.¹ Many metals form numerous different geometries and dimensions, driven by energy minimization and controlled by reaction conditions. The importance of metal-oxo clusters are multifold. First, they are important intermediate species in the reaction path of building metal-oxide solids from monomeric unit (**Figure 1.1**).² The metal-oxo clusters are important in both nucleation and growth of metal-oxides or dissolution of metal oxides.^{3,4} Second, these clusters have distinct chemical composition, and their structural features along with their chemical properties can be characterized⁵ to provide spectroscopic models for transient species that cannot be isolated (i.e. reaction intermediates). Metals throughout the periodic table form metal-oxo cluster compounds, each one may have different structural topology and application potentials depending on the metal(s) and the exact composition.⁶ These clusters are good models to study catalysis and other chemical behavior of metals-oxides.

The primary way to obtain structural information is to perform scattering measurements on crystalline solid materials with X-rays or neutrons. However, these methods cannot be performed directly on solution samples or non-crystalline solid materials. Other characterization techniques are important (e.g. UV-Vis, Raman, NMR or mass spectroscopy) for characterization, but do not necessarily provide precise structural information that is important to understand solution speciation, and its relation to the solid-state structures. This dissertation provide characterization of several examples of various metal-oxo systems in solid and solution state using X-ray scattering methods with laboratory instruments (as opposed to synchrotron).

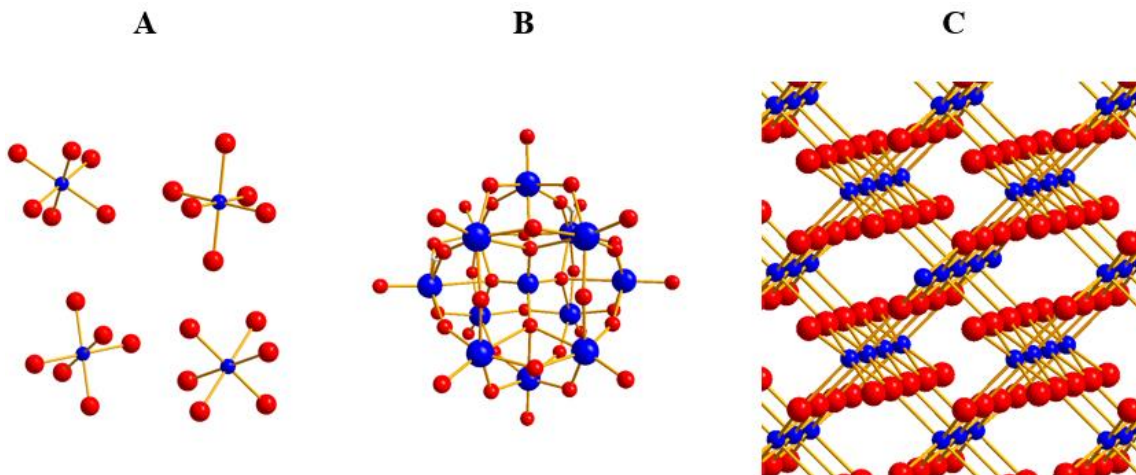


Figure 1.1 Schematic ball-stick representation of different metal-oxygen compounds. Metal-oxo cluster (B) are between the monomeric units of metal ions (A) and the infinite lattice of metal oxides (C). Color code: red sphere-oxygen, blue sphere-metal.

Metal-oxo clusters exist both in solid and solution state. They can form from solution prior to crystallization or during degradation of an ordered lattice, known as amorphization process. The small fragments determine the properties of bulk material which is difficult to predict and understand with no precise structural information. In solution, these species are also present when metal is dissolved in conditions conducive to self-assembly, or prior crystallization. Some also assemble from fragments in the solid state, but do not exist intact in solution^{7,8}. Formation of the cluster is determined by many factors including concentration, solvent, pH, counter ions, temperature and so on. Understanding the relationship between reaction conditions and the forming clusters is crucial to describe the solution speciation. X-ray (or neutron) scattering measurements (single-crystals or crystalline powder) on crystalline products provide information to describe the structure in the solid-state via single-crystal or powder diffraction. However, to acquire direct structural information from materials lacking order in a long-range scale is a complex task. These cases requires other characterization methods. However, scattering techniques can provide some valuable information about these systems. Thus, in the next sections we focus on how X-rays can be utilized to extract structural information from highly disordered and solution samples.

Herein, a very short introduction below presents the principles of two scattering methods: small-angle X-ray scattering (SAXS) and pair distribution function (PDF) analysis of X-ray total scattering measurements. We show what experimentation is used and how can we interpret these data. As we will see later, these laboratory instruments can be used routinely to acquire direct structural information about various metal-oxo systems. The second chapter is about the amorphization pathway of the crystalline hydrated $\text{NaBiO}_3 \cdot \text{XH}_2\text{O}$ upon acid-treatment in solid state, while the focus of later chapters is solution-state characterization of metal-oxo (or peroxy) clusters.

1.2 Small-Angle X-ray Scattering (SAXS)

Small-angle X-ray scattering (SAXS) is a powerful technique extensively used in biology, chemistry for both solid and solution samples. SAXS provides information about particle size, shape, and interaction between scattering particles. Just considering the solution state, it is extensively used in microbiology to study proteins and other biomolecules, in food sciences for colloidal studies, and in chemistry for macromolecules or metal-oxo clusters.⁹⁻¹² SAXS can be used routinely to extract structural information about size, shape and interactions of metal-oxo clusters in solution. These measurements consist of carefully collecting scattered X-ray photons at very low angle, where scattering from solute is dominant.

In the scattering methods there is no energy-exchange, the wavelength of incoming and scattered photons are identical, only their scattering momentum changes. The scattering vector or momentum transfer, q , is identified by the equation:

$$q = \frac{4\pi \sin(\theta)}{\lambda} \quad (\text{Eq. 1.1})$$

Where θ is the angle between scattered and incident beam, λ is the wavelength of X-ray photons, π is constant. The momentum transfer is also equivalent with the difference of the momentum vector of incoming and scattered vector, as shown in **Figure 1.2**. As we can see, q has linear relationship with $\sin(\theta)$, and an inverse relationship with λ . Therefore, using the scattering profile as a function of q is independent from the applied X-ray source, making comparable data using different X-ray sources.

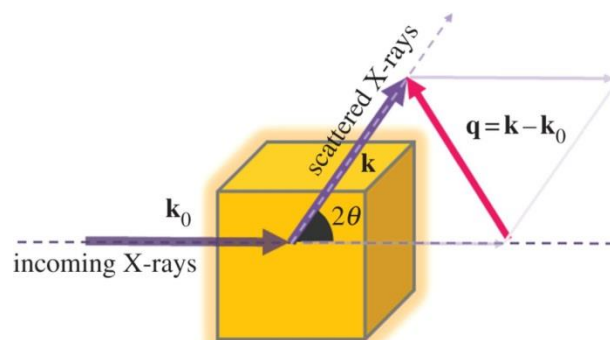


Figure 1.2 The scattering vector or momentum transfer, defined by the incoming and scattered vectors. (Courtesy: ref ¹³)

Our used in-house instrument and the schematic representation of obtaining scattering data is shown in **Figure 1.3**. SAXS data were collected on an Anton Paar SAXSess instrument using Cu-K α radiation ($\lambda=1.54056 \text{ \AA}$) and line collimation. The instrument is equipped with a 2-D image plate for data collection in the $q=0.018\text{--}2.5 \text{ \AA}^{-1}$ range. The lower q resolution is limited by the beam attenuator. All solutions, including background solutions, were contained in sealed borosilicate tubes with 1.5 mm diameter and 0.01 mm wall thickness (HR6-124, Hampton Research) placed at a distance of 26.1 cm from the image plates. Data collection times of 30 minutes were utilized. We used SAXSQUANT software for data collection and treatment including normalization, primary beam removal, background subtraction, desmearing and smoothing. Analysis, and data fitting were carried out utilizing IRENA macros with IgorPro 6.3 (Wavemetrics) software.¹⁴ To simulate scattering data from the crystal structure we used SolX software.^{15,16}

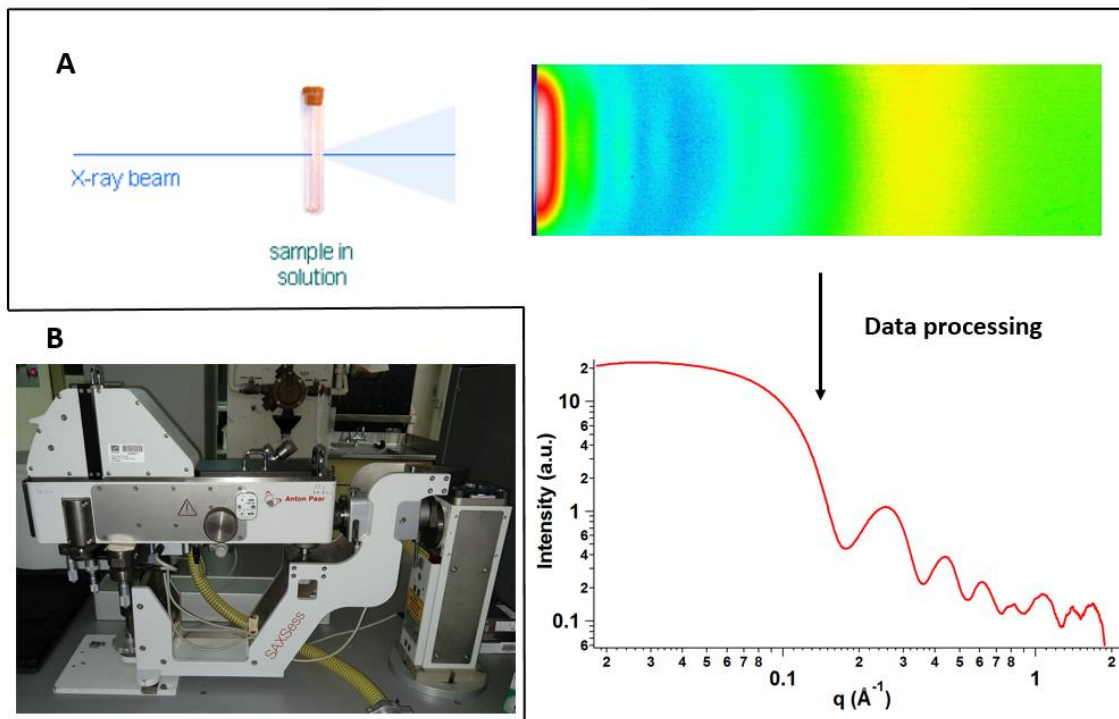


Figure 1.3 Schematic representation of acquiring SAXS data from data collection (**A**). X-ray photons scatter when going through the solution sample containing metal-oxo cluster (top left). From the recorded image (top right) the scattering profile is obtained via data processing (bottom right). **B** represents our in-house Anton Paar instrumentation. (www.anton-paar.com)

The momentum depends on the scatterer particles, including solvent and solute, resulting the scattering profile. This work focuses on metal-oxo clusters, so we shortly describe what information can be extracted regarding those molecules. Note; SAXS data is usually plotted as $\log I(q)$ vs. $\log q$. In metal-oxo chemistry the first information can be extracted is the size of scattering specie. After a flat plateau at low q , the scattering intensity descends, which is the Guinier-region. This indicates the size of the scatterer molecule. Bigger molecule correspond with a Guinier-region at smaller the q values. At higher q values, users may observe further oscillations providing information about the shape of the molecule. Molecules with different shape lead to different, defined features at higher q values, following the descent of the Guinier-region. This allow us to observe shape information (spherical, cylinder, core-shell structures, etc.). This region is called Fourier-region. Usually higher q values can be affected by solvent scattering, and we do not always include in data analysis. However, there is usually valuable visual information in this

region. After the Fourier-region, even higher q values are used to obtain information about the relative volume/surface ratio for large macro- and biomolecules. This is the Porod-region (**Figure 1.4**). The specific q values associated to the different regions are unique to each system.

Additionally, presence of multiple scattering particles in one solution is also observable. Careful data analysis can define scattering particles with different size and their relative concentrations, but must be considered carefully, and including supplementary analyses. Interactions between the scattering molecules are also observable in the scattering profile. These influence the curve at low q : 1) just before the sharp decline in the Guinier region there is a Coulombic peak (from the electrostatic interaction between charged molecules) or 2) a continuous negative slope at low q values (indicating aggregation). **Figure 1.4** represents a scattering profile of a monodisperse solution of metal-oxo cluster with well-defined oscillations up to 1.9 \AA^{-1} .

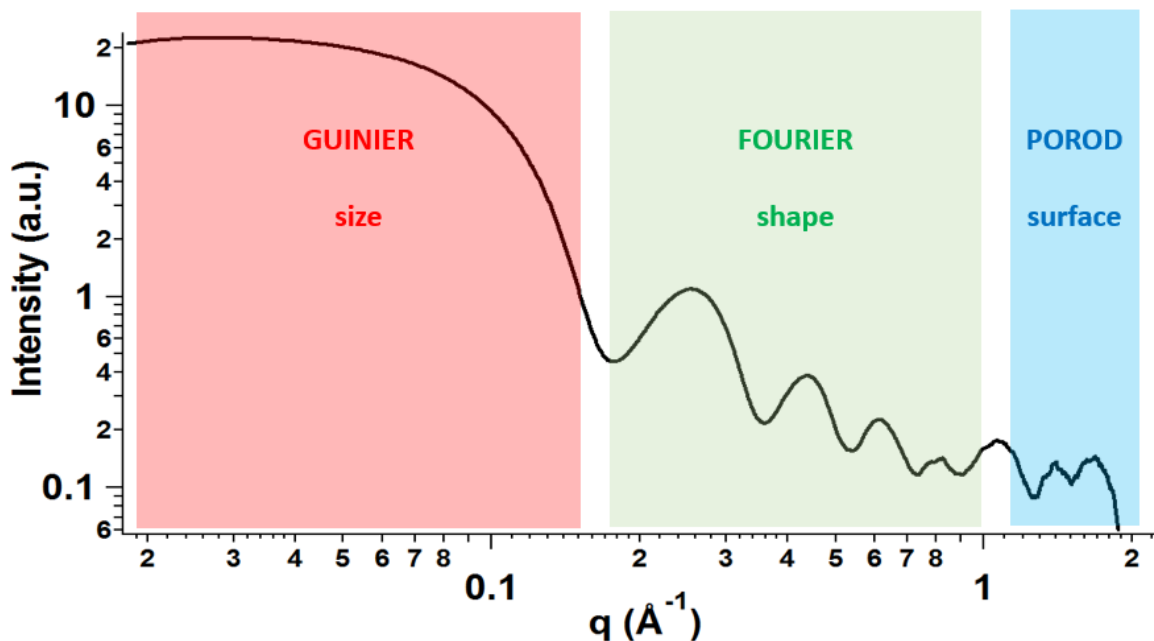


Figure 1.4 Different regions of scattering profile provide different information about the studied compound in the system. The exact values of the regions are arbitrary, vary from system to system.

Although SAXS is a powerful method, it requires other solution characterization methods for absolute identification of the studied cluster, e.g. UV-Vis, Raman, NMR, mass spectroscopy or single-crystal diffraction after crystallization.

1.3 Pair Distribution Function (PDF) analysis of X-ray total scattering

Crystallography focuses on the peaks appearing on the scattering profile (Bragg scattering). Total scattering measurements reveal both Bragg scattering features from crystalline materials and diffuse scattering where the signal is “hidden” in the baseline and background. While Bragg peaks provide information about crystallinity, unit cell parameters and average long-range order, information about short-range order and disorder is missing. Diffuse scattering arising in the background providing information about the short-range order (and disorder) of materials.¹⁷ Therefore, total scattering measurements are in high demand to probe materials with little long-range order. Total scattering measurements are the primary structural characterization methods to study transitions in the solid-state, amorphous materials, glasses or liquids. The general requirements for adequate data quality of the diffuse scattering are: high available q -space, high q resolution, good counting statistics at high q , and low instrument background. High q -space is obtained by using shorter wavelength (higher energy) of X-ray photons. That is why Cu X-ray sources cannot be used for total scattering measurements. The highest available q -space with Cu is $\sim 8 \text{ \AA}^{-1}$. Using Mo or Ag X-ray sources in laboratories or synchrotron sources reach appropriate q -range (above 15 \AA^{-1}).

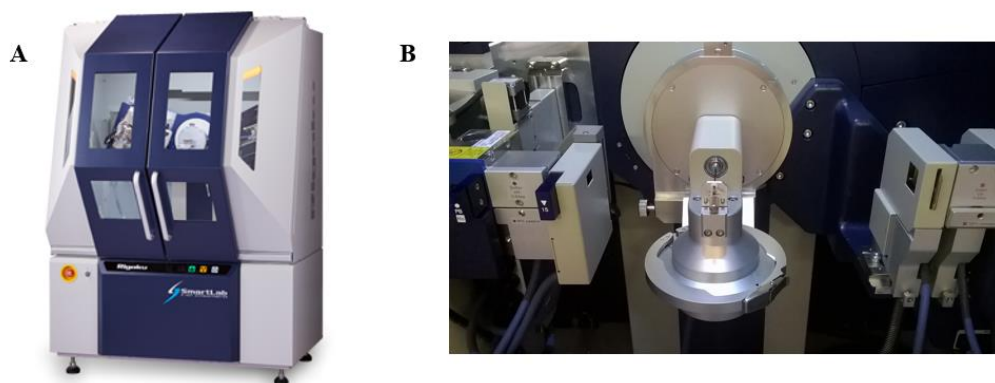


Figure 1.5 Rigaku Smartlab in-house laboratory diffractometer capable for X-ray total scattering measurements (A). B is the instrument chamber with a solution sample in the capillary attachment. (www.rigaku.com)

Our in-house X-ray total scattering measurements were performed with Rigaku Smartlab X-ray diffractometer with Mo-K α irradiation ($\lambda=0.71073$ Å) (**Figure 1.5**). Solution measurements were carried out in the 2θ range of 3.0-118.5° with transmission geometry. Solution samples were loaded in Kapton capillary with 1.46 mm inner diameter for irradiation. The theoretical q -range is up to a q_{max} of 15.5 Å⁻¹. A 0.2 °/minute data collection time with 0.01° step size, and D/teX Ultra-HE high-speed one-dimensional X-ray detector were utilized to ensure high quality scattering data. Solid-state measurements were carried out in the 2θ range of 3.0-158.6° with Bragg-Brentano geometry and 0.5 degree/minute data collection time.

PDFgetX3 was used to process scattering data into the corresponding PDFs.¹⁸ The corresponding simulations were created in PDFgui.¹⁹ During the data processing, the structure function ($S(q)$), then the reduced structure function ($F(q)$) has to be generated. In the last step, $F(q)$ is Fourier-transformed to obtain the reduced pair distribution function ($G(r)$)²⁰ (from now for simplicity, we use $G(r)$ as the pair distribution function) according to the following equations:

$$I(q) = I_{Bragg} + I_{diffuse} \quad (\text{Eq. 1.2})$$

where I_{Bragg} and $I_{diffuse}$ are intensities come from Bragg and diffuse scattering.

$$S(q) = \frac{I(q)}{\langle b \rangle^2} \quad (\text{Eq. 1.3})$$

where b represent the scattering amplitude (for X-rays b strongly depends on q and Z (atomic number)).

$$F(q) = q[S(q) - 1] \quad (\text{Eq. 1.4})$$

$$G(r) = \frac{2}{\pi} \int_0^\infty q[S(q) - 1] \sin(qr) dq \quad (\text{Eq. 1.5})$$

The data processing is represented in **Figure 1.6**, as well. All these steps are calculated simultaneously by PDFgetX3.¹⁸ However, during the data processing, users must define other parameters: the background scale, q_{min} , q_{max} (the window of the experimental q -space) and r_{poly} . (The r_{poly} . parameter controls the degree of data-correction polynomial, $r_{poly} = \pi n/q_{maxinst}$.) While the Fourier-transform would use infinite q -space in ideal case, we have limited q -space determined by experimental conditions. One can find optimal values

varying those parameters, where termination ripples and background oscillations are minimized, but resolution is still high enough for data analysis.

In general, atomic pair distribution function (PDF) yields a distribution of the interatomic distances. Distribution describes the “probability” of finding atomic pairs by a distance r . Interpretation of PDF contains three aspects: 1) peak positions are specific atom-pair correlations; 2) the peak shape is a probability distribution (normally it has Gaussian distribution, alteration indicates overlapping correlations or disorders) and 3) integrated peak intensity suggest information about the coordination number (multiplicity of the pair correlation). In the following projects we use the first two aspects for qualitative or some semi-quantitative analyses. Some current, quantitative analysis methods and software in the literature are peak fitting, small box modelling (PDFgui)¹⁹, large box modelling (RMCPProfile)²¹ or DISCUS for modelling disorders²².

PDF method is routinely used to study disordered and amorphous materials. Due to the lower accessibility for laboratory diffractometers, PDF measurements are mostly performed at synchrotron sources. However, some diffractometers are able to perform this type of measurements, which are set up with Mo ($\lambda=0.71073$ Å), Ag ($\lambda=0.561$ Å) or W ($\lambda=0.209$ Å) X-ray sources and high quality detectors.²³⁻²⁵ Applying this methodology on metal-oxo clusters, especially in solution, is a less utilized approach.

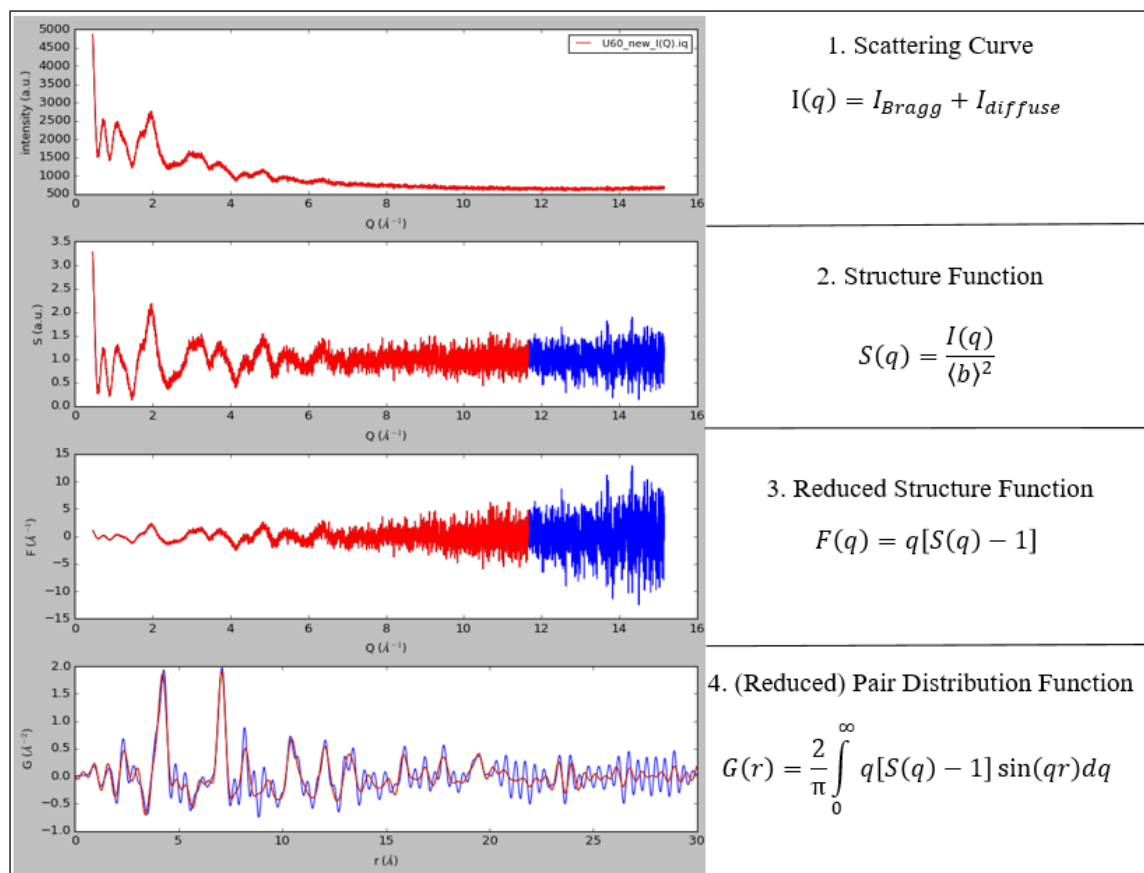


Figure 1.6 Individual steps of data processing from the experimental scattering curve to the final PDF data. All steps are calculated simultaneously by PDFgetX3.¹⁸ Blue curve represents the processed functions using the raw data, while red curves show data using tuned data processing parameters.

This dissertation starts with a solid-state chemistry project. Chapter 2 shows a study where a crystalline material of $\text{NaBiO}_3 \cdot \text{XH}_2\text{O}$ turns to amorphous during a chemical reaction in acidic solutions. PDF was utilized to extract important structural features of the forming metal-oxo fragments. After the solid-state measurements, aqueous solution samples were tested. Solution PDF measurements of metal-oxo clusters are less explored area, we started benchmarking the technique. Due to the complexity of both data collection and interpretation, qualitative or semi-quantitative analyses were performed. Chapter 3 includes more detailed discussion about total scattering measurements about metal-oxo clusters and their aqueous solutions in general. Chapter 4 provides a complete study to characterize aqueous solutions of TiOSO_4 . In Chapter 5 Zr-peroxo oxalate clusters and Zr/Hf oxalate complexes were synthesized and characterized. These last two chapters are

focusing on different, specific chemical systems where both SAXS and PDF were utilized as powerful complementary techniques to acquire structural information from solution states.

2. Probing the local structure of crystalline $\text{NaBiO}_3 \cdot \text{XH}_2\text{O}$ and its acidified derivatives

Karoly Kozma, T. Wesley Surta, Pedro I. Molina Igor Lyubinetzky, Wynn Stoxen, Nicole
M. Byrne, Michelle Dolgos and May Nyman

Journal of Solid State Chemistry 263 (2018) 216-223

2.1 Abstract

Sodium bismuthate is a commercially available, inexpensive, non-toxic and very potent inorganic oxidant and photocatalyst. It is one of the important reagents for oxidative separation of Am^{3+} from the chemically similar lanthanide ions, for its recovery or safe disposal from reprocessed nuclear fuel. While the structure of NaBiO_3 has been described from powder and neutron diffraction; the structure of $\text{NaBiO}_3 \cdot \text{XH}_2\text{O}$, the manufactured form of sodium bismuthate, is currently unknown. Herein, we describe the structure of $\text{NaBiO}_3 \cdot \text{XH}_2\text{O}$ ($X=3$) using pair distribution function (PDF) analysis of X-ray total scattering data. In our proposed structure model, $\text{NaBiO}_3 \cdot 3\text{H}_2\text{O}$ is similar to NaBiO_3 , but with turbostratic disorder in the stacking direction of the alternating Bi-O and Na-O layers. We propose locations for the lattice water, and its role in creating turbostratic disorder. We also used PDF to describe the structural evolution of sodium bismuthate upon exposure to nitric acid, the conditions employed in for nuclear fuel reprocessing. We supported the proposed model for pristine $\text{NaBiO}_3 \cdot 3\text{H}_2\text{O}$ and its acidified derivatives by a variety of techniques including thermogravimetry, infrared spectrometry, powder X-ray diffraction (PXRD), energy dispersive X-ray spectroscopy (EDX) and X-ray photoelectron spectroscopy (XPS). By employing both surface and bulk techniques, we hypothesize that the bismuth reduced to Bi^{3+} upon aqueous acid exposure remains in the lattice, rather than completely dissolving and/or depositing on the surface, as prior suggested. Using pretreated acidified sodium bismuthate samples, we delineated the effects of acid strength vs. bismuthate structure/composition on Ce^{3+} to Ce^{4+} oxidation efficacy.

2.2 Introduction

Bismuth is an inert, inexpensive, non-toxic metal, and the heaviest of all the stable chemical elements. Bismuth has two accessible oxidation states, +3 and +5, respectively. Subsalicylate and subcitrate coordination complexes of Bi^{3+} are routinely used to treat gastrointestinal disorders and peptic ulcers.²⁶ The structure directing effects of Bi^{3+} 's lone pair is exploited in Pb-free piezoelectrics.²⁷ On the other hand, the +5 oxidation state bismuthate $[\text{X}^{\text{n}+}(\text{BiO}_3)_n]$ ($X=\text{Li}^+, \text{Na}^+, \text{K}^+, \text{Ag}^+, \text{Mg}^{2+}, \text{Sr}^{2+}, \text{Ba}^{2+}, \text{Zn}^{2+}$ and Pb^{2+}) is photocatalytically-active, and is as a promising alternative to TiO_2 for degradation of organic pollutants.²⁸⁻³² Bismuthate, $[\text{BiO}_3]^-$ is a strong oxidizer (NaBiO_3 : +2.03 V vs

SHE),³³ exploited to oxidize and separate valuable elements in the nuclear fuel cycle.³⁴ Specifically, NaBiO₃ oxidizes Am³⁺ to [AmO₂]²⁺ which can then be isolated from other chemically-similar fission products (Ln³⁺) by solvent extraction with several phosphate and phosphonate ligands.^{35–37} The extracted [AmO₂]²⁺ can then be either disposed safely or repurposed in fast reactor fuel.

The reduction of Bi⁵⁺ to Bi³⁺ paired with americium oxidation in the acidic conditions employed in nuclear fuel reprocessing is not well understood, and there is conflicting data in the literature. Bismuth was proposed to be dissolved in the pentavalent state (Bi⁵⁺), as determined by iodometry.³⁴ However, standard Pourbaix diagrams suggest Bi⁵⁺ cannot exist in aqueous solution at any pH, and Bi³⁺ persists well above the Eh stability window for water. Mincher *et al.* described a decrease in the concentration of [AmO₂]²⁺ in solution if the solid NaBiO₃ is removed.³⁸ These observations and studies point towards a heterogeneous oxidation process, in which Bi⁵⁺ is reduced to Bi³⁺ at the surface of the particles, and it may or may not become a part of the evolving solid lattice. Ding and coworkers³² suggest Bi³⁺ self-dopes the lattice along with co-doped ‘holes’, responsible for the increasingly dark color with acid treatment. Their X-ray diffraction (PXRD) and X-ray photoelectron spectroscopy (XPS) analyses of sodium bismuthate respectively show that the material becomes X-ray amorphous with mild acid treatment, and up to 35% of surface bismuth is trivalent. They additionally noted that Bi³⁺ could be deposited as a hexameric phase, (Bi₆O₄(NO₃)₅(OH)₅·0.5H₂O) on the surface of the sodium bismuthate particles.

Because NaBiO₃·XH₂O is the commercially available form employed by the nuclear energy and photocatalysis communities, an evaluation of its structure is important to understand structure-function relationships. Additionally, since bismuthate rapidly becomes amorphous in its photocatalytic form and in extremely acidic environments of nuclear fuel reprocessing solutions, the structural evolution with acidification is likewise important. Herein, we examine the short range order of both NaBiO₃·XH₂O (X=3) and its evolution upon acid-treatment. Pair distribution function (PDF) analysis of X-ray total scattering yields structural information, while XPS, wet chemical analysis, and energy-dispersive X-ray spectroscopy (EDX) provide information about the elemental composition and the oxidation states, on both the surface and in the bulk. We document the oxidation efficacy as a function of structural and Bi⁵⁺/Bi³⁺ evolution, employing the

$\text{Ce}^{3+}/\text{Ce}^{4+}$ redox couple as a surrogate for Am^{3+} oxidation.³⁹ From these data, we produce a structural model for the hydrated form of sodium bismuthate, and indicates how the local environment evolves as the material becomes X-ray amorphous. Additionally, by pre-acidifying sodium bismuthate prior to performing the $\text{Ce}^{3+}/\text{Ce}^{4+}$ oxidation studies, we delineate the effects of solution conditions and materials state on oxidation efficacy.

2.3 Experimental

2.3.1. Materials and reagents

$\text{NaBiO}_3 \cdot \text{XH}_2\text{O}$ (Fischer), $\text{Ce}(\text{NO}_3)_3 \cdot 6\text{H}_2\text{O}$ (Sigma Aldrich, 99%), $(\text{NH}_4)_2\text{Ce}(\text{NO}_3)_6$ (Alfa Aesar, 98+%) and concentrated HNO_3 (Macron Fine Chemicals) solution were used as received. Deionized water (18.2 M Ω , Millipore) was used to prepare all solutions.

2.3.2. Acid treatment of $\text{NaBiO}_3 \cdot 2\text{H}_2\text{O}$

Table 2.1 Experimental parameters for acid-treatment of $\text{NaBiO}_3 \cdot \text{XH}_2\text{O}$

Sample	$\text{NaBiO}_3:\text{HNO}_3$ molar ratio	$[\text{HNO}_3]$ (M)	pH of starting HNO_3 solution	pH of suspension
0	1:0	0	-	> 9
1	1:0.1	0.04	1.85	6
2	1:0.5	0.18	1.22	2.7
3	1:1	0.37	0.85	1.31
4	1:2	0.72	0.55	0.75
5	1:4	1.43	0.11	0.31
6	1:8	2.86	< 0	< 0
7	1:16	5.72	< 0	< 0
8	1:31	11.42	< 0	< 0

NaBiO_3 was prepared from $\text{NaBiO}_3 \cdot \text{XH}_2\text{O}$ by heating at 210°C for three hours in the air, as described elsewhere.⁴⁰ Acidified $\text{NaBiO}_3 \cdot \text{XH}_2\text{O}$ samples were prepared by suspending 1.00 g $\text{NaBiO}_3 \cdot \text{XH}_2\text{O}$ in eight, 10 mL volumes of HNO_3 dilutions in water at different concentrations. The $\text{NaBiO}_3:\text{HNO}_3$ molar ratio and the pH of these suspensions,

along with the concentration and the pH of the initial HNO₃ solutions, are shown **Table 2.1**. The suspensions were stirred for two hours at room temperature and a solid phase was isolated from these mixtures by centrifugation, washed three times with water and finally dried under vacuum. The color of these dry samples varied from light orange to dark brown as a function of the NaBiO₃:HNO₃ ratio (**Figure A 1**).

2.3.3. Cerium oxidation studies

NaBiO₃·XH₂O (100 mg) and acidified NaBiO₃·2H₂O were suspended in 1M HNO₃, 8mM Ce(NO₃)₃ solutions. The molar ratio NaBiO₃:Ce(NO₃)₃ in these mixtures was 2:1. The oxidation reactions were halted at different time intervals by passing aliquots through 0.45 μm nylon mesh filters, using plastic disposable syringes, into quartz cuvettes of 1 cm path length. UV-Vis spectra of these filtrates were recorded and the intensity of the absorption band at 380 nm was used to quantify the concentration of Ce⁴⁺ via a calibration previously obtained with (NH₄)₂Ce(NO₃)₆ (**Figure A 2**).

2.3.4. Characterization methods

Powder X-ray diffraction (PXRD) was performed on a Rigaku Miniflex diffractometer (Cu-Kα radiation, λ = 1.54 Å) from 5° to 60° 2θ in Bragg-Brentano geometry. To perform pair distribution function (PDF) analysis we used a Rigaku Smartlab X-ray diffractometer with Mo-Kα radiation (λ=0.71 Å) in the 2θ range of 3-158.6° with Bragg-Brentano geometry. A 0.5 degree/minute data collection time was used to ensure high resolution scattering data. The theoretical Q-range is up to a Q_{max} of 17.49 Å⁻¹. Thermogravimetric analysis (TGA) was performed on TA Instruments SDT Q600. Energy dispersive X-ray spectroscopy (EDX) measurements were performed on Quanta 600 scanning electron microscopy (SEM). Elemental analysis was performed by Galbraith Laboratories (Knoxville, TN). X-ray photoelectron spectroscopy (XPS) was performed utilizing PHI 5600 system with Al Kα X-ray source. UV-visible (UV-Vis) spectra were recorded with Thermoscientific Evolution 220 UV-Visible Spectrophotometer. The Ce⁴⁺ peak was monitored at 380 nm for quantification and to avoid overlap with other species. Initially, the calibration curve was generated with Ce⁴⁺ concentration ranging from 1 mM to 9 mM, in relevant solution conditions (**Figure A 2**).

2.4 Theory

PDF analysis of the X-ray total scattering data is a powerful characterization method to investigate the structural changes at the atomic-level in the solid-state. These measurements require a high Q -range. The Mo X-ray source ($\lambda=0.71 \text{ \AA}$) employed provides a Q_{max} of 17.49 \AA^{-1} . PDFgetX3 was utilized to process scattering data into the corresponding PDF.¹⁸ The raw scattering curve ($I(Q)$) is normalized to obtain the structure function, $S(Q)$. Next we define the reduced structure function by applying the operation:

$$F(Q) = Q[S(Q) - 1] \quad (\text{Eq. 1.4})$$

Q is the momentum vector, $S(Q)$ is the structure function and $F(Q)$ is the reduced structure function. The reduced structure function is used for Fourier transform, which yields the pair distribution function, $G(r)$ (PDF). The pair distribution function is defined by

$$G(r) = \frac{2}{\pi} \int_0^{\infty} Q[S(Q) - 1] \sin(Qr) dQ \quad (\text{Eq.1.5})$$

The resulting PDF is the real space representation of the atomic pair separations. The distribution describes the probability of finding an atomic pair separated by a distance r . A PDF of a crystalline material has a long-range order and will continue to high r , whereas only a few peaks are observed at low r in amorphous materials or solutions, due to lack of long-range order. In this study, we describe the transition from crystalline to amorphous material in detail. All simulations shown were created in PDFgui.¹⁹

2.5 Results and discussion

2.5.1. NaBiO₃ and NaBiO₃·XH₂O (X=3) structures

Only two phases of NaBiO₃, the anhydrous and a hydrated (described as NaBiO₃·2H₂O), have been reported, and their unit cell parameters are shown in **Table A 1**. Of these two phases, detailed structural characterization (i.e. atomic positions and interatomic distances) of only anhydrous NaBiO₃ has been determined (ICSD code: 91776) by powder diffraction and neutron diffraction.^{40,41} Anhydrous NaBiO₃ crystallizes in the R-3 space group (ilmenite). Edge-sharing {BiO₆} octahedral (Bi-O = 2.09-2.14(3) Å) form hexagonal motifs within extended layers in the structure (**Figure 2.1**) and these alternate with layers of {NaO₆} (Na-O = 2.40-2.47(4) Å) arranged in an equivalent fashion within the layer. The vacancies arising from the hexagonal arrangement of octahedra in these

layers are not aligned. Therefore, the layer packing follows an A-B-A pattern, and no tunnels exist in the structure. The closest Bi-Bi distance between $\{\text{BiO}_6\}$ layers is 5.03 Å.

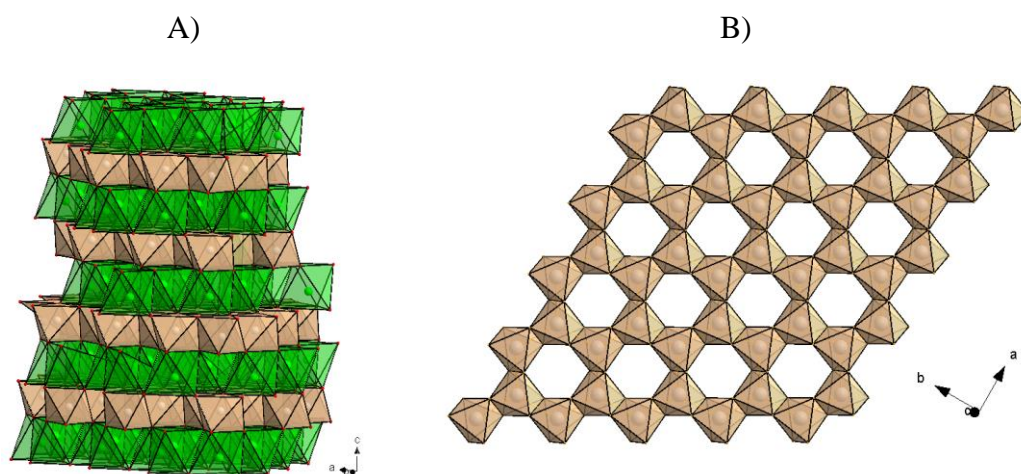


Figure 2.1 (A) Structural representation of NaBiO₃ and (B) {Bi-O} sheet in the structure along the crystallographic *ab* plane (ICSD: 91776). (Bi- brown, Na-green octahedra)

PXRD (**Figure 2.2A**) confirmed that Fisher Scientific sodium bismuthate is the reported NaBiO₃·2H₂O rather than anhydrous NaBiO₃, as described by the vendor. There are few syntheses reported for bismuthate compounds, and they generally involve electrochemical oxidation of Bi³⁺ in a hydrous alkali hydroxide flux.^{42,43} The hydrous flux is likely the source of lattice water in NaBiO₃·XH₂O. PXRD analysis of NaBiO₃·XH₂O indicates crystallographic anisotropy. The full width at half maximum (FWHM) of the (001) peak in the PXRD data is greater than the FWHM of the (110) peak (**Figure 2.2A**). The (001) plane is located on the crystallographic *ab* plane, and this suggests substantial crystallographic disorder along the *c* axis. However, TGA analysis suggests there are three lattice waters per formula unit (16.41% weight loss; **Figure A 3**). Since our diffraction pattern matches that of reported NaBiO₃·2H₂O, it is likely variable amounts of lattice water is possible, and will be discussed later.

In order to investigate the local structure of anhydrous NaBiO₃ to compare to that of NaBiO₃·3H₂O (we will refer to this as a trihydrate from here forth, as identified by TGA), we prepared it by the earlier described heat-treatment. PXRD (**Figure 2.2A**) confirmed that the NaBiO₃·3H₂O had lost the lattice H₂O molecules, and transformed into the prior-

reported anhydrous NaBiO_3 structure.⁴⁰ Anhydrous NaBiO_3 does not rehydrate readily, even after six months in ambient conditions. Soaking the dehydrated phase in neutral water or NaOH solution did not lead to its rehydration (**Figure A 4**). Soaking anhydrous NaBiO_3 in aqueous acid does reintroduce some water to the bulk material, but not without structure degradation and alteration (**Figure A 4**). In fact, even neutral water treatment leads to some degradation of long-range order.

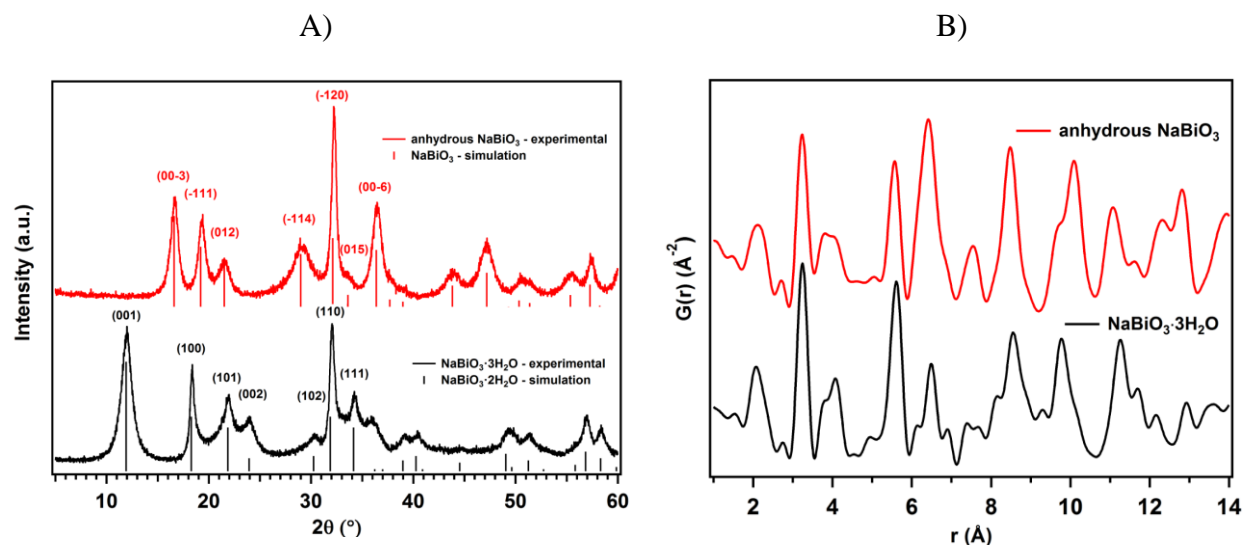


Figure 2.2 Comparison of PXRD patterns (A) and experimental PDF curves (B) of $\text{NaBiO}_3 \cdot 3\text{H}_2\text{O}$ before and after dehydration. Corresponding Miller indices are assigned to the prominent peaks on the diffraction patterns.

The PDF of anhydrous NaBiO_3 shows the expected correlation peaks corresponding to the interatomic distances described previously (**Table A 2**). The experimental and calculated PDFs, based on the reported structure of NaBiO_3 ⁴⁰, are shown in **Figure 2.3** Experimental and calculated PDF curves of the anhydrous sample.. Refinement parameters are compiled in **Table A 3** and **Table A 4**. The closest intralayer Bi-Bi correlation arises at 3.2 Å, while the most intense peak at 6.2 Å can be assigned to Bi-Bi interlayer correlation. Interestingly, the most prominent differences between the calculated and experimental PDFs of NaBiO_3 are at the r values of 3.9 -4.2 Å. Correlations in this range originate from non-neighboring, intralayer Bi-O and interlayer Bi-Na correlations. This will be discussed later.

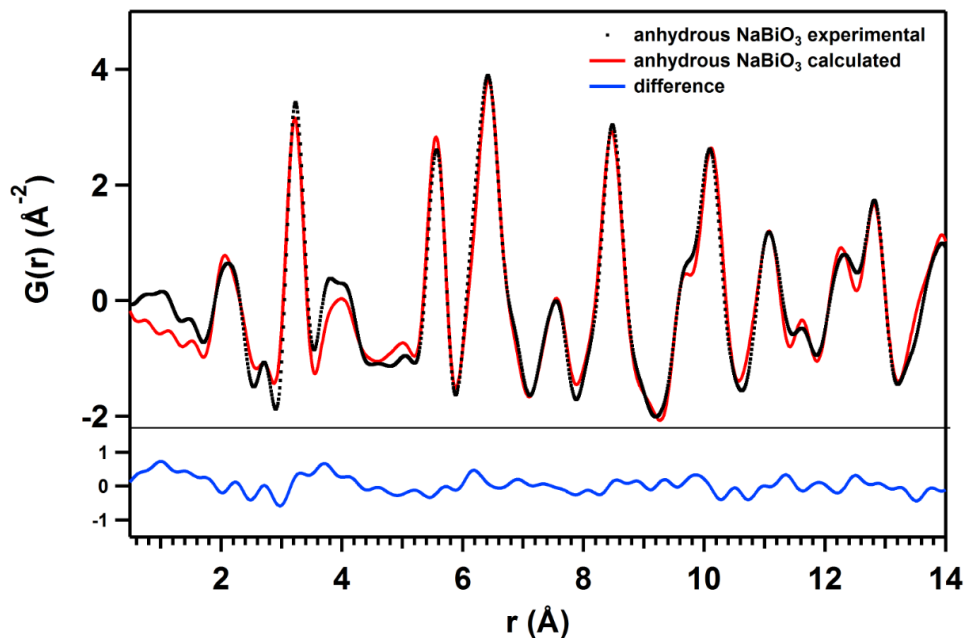


Figure 2.3 Experimental and calculated PDF curves of the anhydrous sample.

In **Figure 2.2B**, we compare the experimental PDF of the $\text{NaBiO}_3 \cdot 3\text{H}_2\text{O}$ to that of anhydrous NaBiO_3 . The biggest difference is the diminution of the Bi-Bi correlations in the $\text{NaBiO}_3 \cdot 3\text{H}_2\text{O}$ phase, most notably the correlations at 6.2, 8.5 and 10 Å. The 6.2 Å peak is has strongest contributions from interlayer Bi-Bi distances, while both intralayer and interlayer Bi-Bi distances are present at 8.5 and 10 Å. In order to explain the difference between $\text{NaBiO}_3 \cdot 3\text{H}_2\text{O}$ and anhydrous NaBiO_3 , we considered alternative structural models, discussed below. First, we simulated a single {Bi-O} layer derived from NaBiO_3 (**Figure 2.4** and **Figure 2.1B** for one {Bi-O}-sheet model), in which we observe only the intralayer Bi-Bi, Bi-O and O-O correlations. The most intense peaks in the single-sheet simulation correspond with first and second coordination sphere Bi-Bi distances (3.5 and 5.5 Å, respectively). At greater distances the peak intensities diminish, with loss of contribution from the interlayer correlations. In order to delineate the contribution of Na^+ ions and possible locations of H_2O molecules, we built two additional models. First, oxygens were placed in the center of each hexagonal void of the isolated {Bi-O} sheet. Second, oxygens were placed in both the {Bi-O} and {Na-O} voids in a double-layer model (one Bi-O layer and one Na-O layer, **Figure A 5**). There are four voids per formula unit, and $3/4^{\text{th}}$ of these must contain H_2O molecules in $\text{NaBiO}_3 \cdot 3\text{H}_2\text{O}$. Water hydrogens

were excluded from the model due to their negligible contribution to X-ray data, and their likelihood to disorder within the structure.

The double-layer model is the closest to the chemical formula of $\text{NaBiO}_3 \cdot 3\text{H}_2\text{O}$ and yields greater changes in the PDF than a single {Bi-O}-sheet with H_2O in the hexagonal voids (**Figure A 6**). The most intense interlayer Bi-O correlation appears around 3.2-3.3 Å, which exactly overlaps with the intralayer edge-sharing Bi-Bi correlation. Additionally, there is increase in intensity of the peak between 3.9-4.2 Å (overlapping with several inter- and intra- layer atom pair correlations), and at distances greater than 8 Å corresponding with the additional non-neighboring Bi-O and Bi-Na correlations (**Figure A 6**). On the other hand, Na-O and O-O correlations do not contribute substantially. The Bi-Bi and Bi-O correlations dominate the PDFs, due to Bi's strong scattering power.

As shown in **Figure 2.4**, the $\text{NaBiO}_3 \cdot 3\text{H}_2\text{O}$ experimental PDF data agrees well with the simulation of one {Bi-O} sheet. These structural investigations of $\text{NaBiO}_3 \cdot 3\text{H}_2\text{O}$ show a lack of interlayer contributions in the PDF. Only the intralayer Bi-Bi correlations can be identified from the experimental PDF data, meaning there is little or no order in the orientation of the sheets relative to each other. This is consistent with the crystallographic anisotropy observed in the Bragg diffraction peaks, and is referred to as turbostratic disorder. Intercalated graphite materials, $\text{V}_2\text{O}_5 \cdot n\text{H}_2\text{O}$ xerogel and LiCoO_2 likewise possess turbostratic disorder.⁴⁴⁻⁴⁶ Since dehydration of $\text{NaBiO}_3 \cdot 3\text{H}_2\text{O}$ results in ordering of the layers, we can assume the lattice water gives rise to this disorder, perhaps optimizing H-bonding of the water molecules to the lattice O^{2-} .

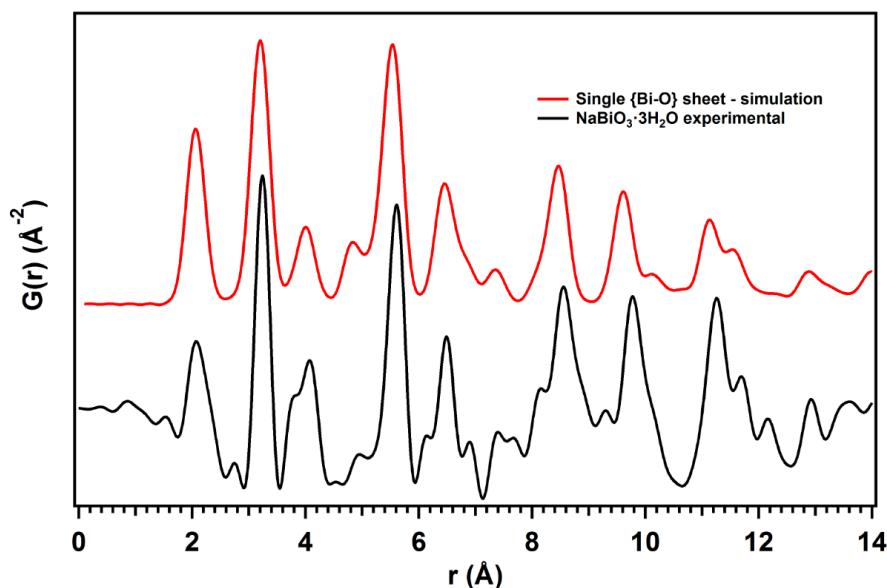


Figure 2.4 Pair distribution function of $\text{NaBiO}_3 \cdot 3\text{H}_2\text{O}$, and simulations of model derived from the structure of NaBiO_3 .

2.5.2. Short range structural evolution from HNO_3 treatment of $\text{NaBiO}_3 \cdot 3\text{H}_2\text{O}$

Acidification of sodium bismuthate yields a dark colored, amorphous material that is photocatalytically active.³² Additionally, americium oxidation is implemented in nitric acid solution in nuclear fuel reprocessing. Therefore evolution of the bismuthate's short-range order with acidification is of interest. PXRD using $\text{Mo-K}\alpha$ irradiation (**Figure 2.5A**) reveals decreasing long-range order of the NaBiO_3 with increasing HNO_3 concentration of the acid treatment. Only one peak at $2\theta = 14.7^\circ$ remains (corresponding to [110] plane, $d = 2.8 \text{ \AA}$) with descending intensity. Additionally, one broad peak arises at $2\theta = 11.7^\circ$ ($d = 3.5 \text{ \AA}$). This had been observed in prior studies by Ding et al. (using $\text{Cu K}\alpha$ source this peak is observed at $2\theta = 25.6^\circ$).⁴⁷ Simultaneously, as the material loses its crystallinity, the Na^+ content decreases. Above 1:4 $\text{NaBiO}_3:\text{HNO}_3$ ratio, the Na^+ content becomes negligible, as indicated by EDX data (**Figure 2.5B**).

We can only rely on EDX data for comparison amongst a series of related samples because 1) EDX is not quantitative for lighter elements such as Na, and 2) EDX is predominantly a surface technique. We use XPS (discussed below) to both quantify sodium and bismuth and investigate change in bismuth oxidation with acidification. However, XPS is also a surface technique, so we have complemented compositional analyses with wet

chemistry techniques (Galbraith Laboratories, Inc.; see **Figure 2.5B** and **Table A 5**). All analyses are reported as Na:Bi ratio for comparison. For $\text{NaBiO}_3 \cdot 3\text{H}_2\text{O}$, both EDX and XPS report a Na:Bi ratio of less than 1. The XPS values are quantitatively reliable ($\sim 0.7:1$, Na:Bi), suggesting the particle surfaces are sodium-poor. On the other hand, the bulk chemical analysis gives a Na:Bi ratio of close to 1. We also compared the 1:1 $\text{NaBiO}_3:\text{HNO}_3$ treated sample by the three analyses. These values, on the other hand, agree; $\sim 0.2:1$; Na:Bi. Therefore we can assume that 1) the EDX and XPS determined values are valid for the discussions that follow concerning evolution of sodium bismuthate with acidification, and 2) the acidified sodium bismuthate materials are compositionally similar on the surface and bulk.

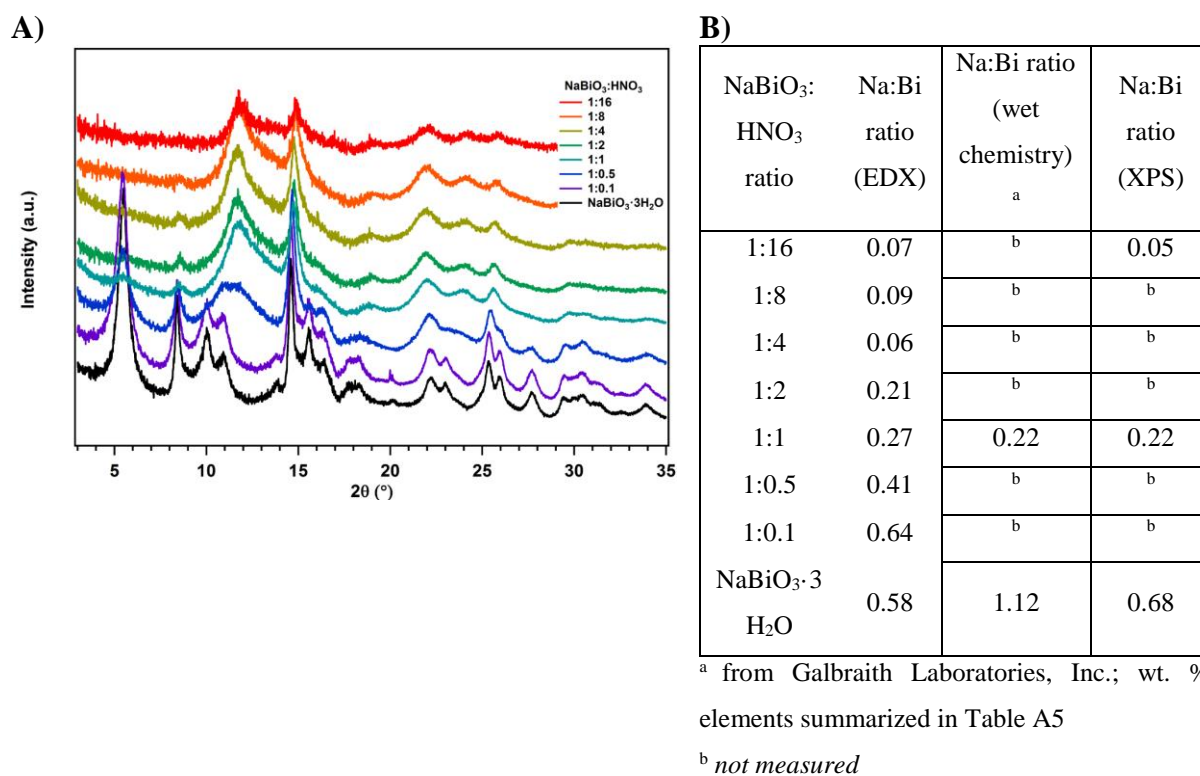


Figure 2.5 (A) X-ray scattering curves and (B) their Na:Bi ratio received by EDX of the acid-treated samples.

PDF analysis of the X-ray scattering curves were utilized to extract atomic level structural information (**Figure 2.6**). We observe that the non-neighboring Bi-Bi correlations at 5.6 Å and at 6.5 Å diminish with increased acid strength. The peak at 6.5 Å

is no longer present by 1:1 NaBiO₃:HNO₃ ratio, while the peak at 5.6 Å disappears above the ratio of 1:4. The loss of these peaks and the order of diminution (longer correlation followed by the shorter correlation) is exactly consistent with decreased long-range order within the hexagonal Bi-O sheets. Lack of Na⁺ is corroborated by EDX data.

The peak at 2.05 Å represents the direct Bi-O bonds in NaBiO₃·3H₂O pristine material. As higher HNO₃ concentration is applied, the peak maximum shifts to greater distances, representing increase in average Bi-O bond lengths (**Figure 2.6**). This is consistent with the change in oxidation state from Bi⁵⁺ to Bi³⁺. Increased concentration of Bi³⁺ initiates further changes in the lattice. Accommodation of the lone pair electrons on bismuth forces Bi³⁺ to distort its coordination environment, and along with it, the hexagonal ring arrangement. The highest intensity correlation at 3.2 Å assigned to the neighboring Bi-Bi distance decreases upon addition of more HNO₃ (**Figure 2.7A**), also indicating destruction of the hexagonal rings.

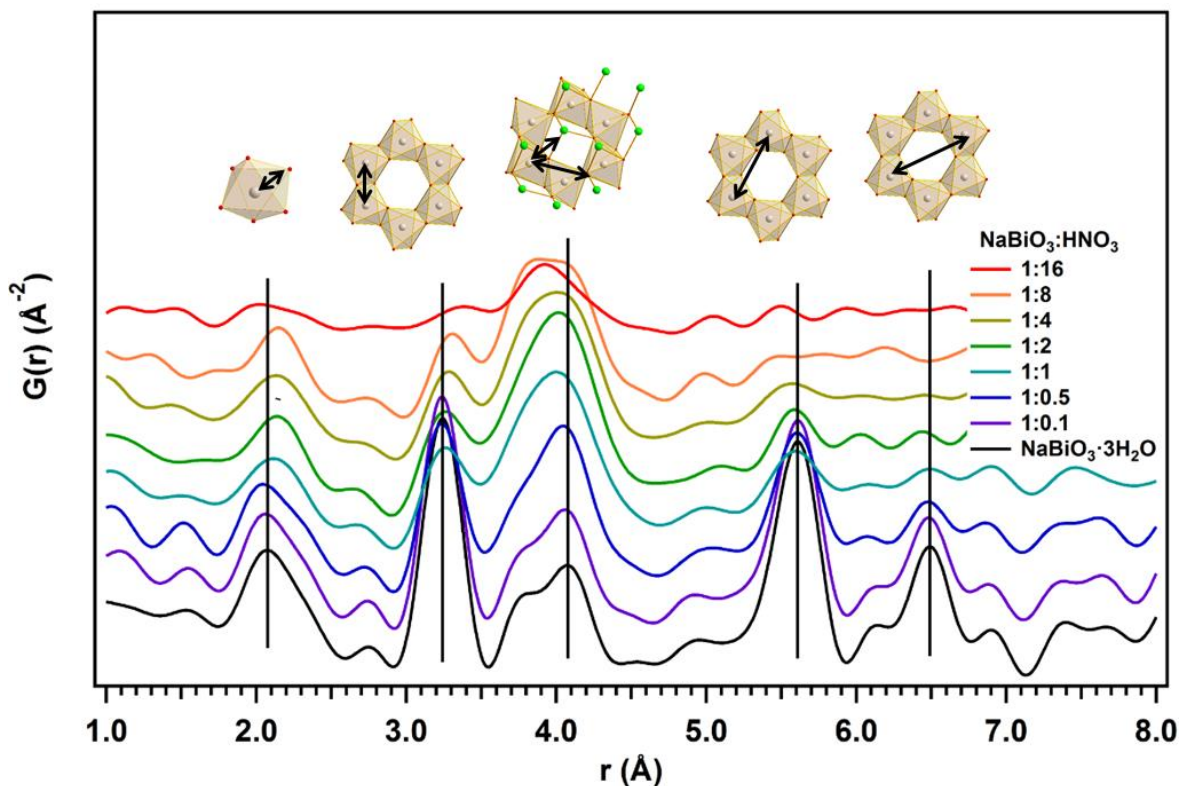


Figure 2.6 Experimental PDF data of the acid-treated samples. Insets represent the atomic pair correlations in the pristine material. (Brown: Bi polyhedral, red: O, green: Na⁺)

Very prominent changes occur in the r region of 3.6 Å–4.4 Å (**Figure 2.7B**). Several correlations are present in this region, complicating interpretation. Three Bi-Na correlations are found at 3.85 Å, 3.95 Å and 4.39 Å, and we observe two Bi-O correlations at 3.95 Å and 4.06 Å. The structure changes as described below. First, Bi^{5+} changes oxidation state and, therefore, its correlations with oxygens are altered. Second, Na^+ exits the lattice (as shown by the compositional analyses). Third, Bi^{3+} distorts the {Bi-O} sheet, altering the Bi-Bi distances. These effects together result in significant growth and broadening of the 3.6 Å–4.4 Å region, due to the distribution of environments that are possible in this now-amorphous material. We can speculate that the average distance between Bi^{5+} - Bi^{3+} and Bi^{3+} - Bi^{3+} will be in this r range of 3.6 Å–4.4 Å. There is one crystal structure available in the literature that contains mixed valence state bismuth, the pyrochlore-type $\text{Na}_{0.39}\text{Bi}_{3.47}\text{O}_7$ (ICSD code: 73964).³⁹ In this structure, Bi^{5+} and Bi^{3+} polyhedra are edge-sharing, and the neighboring Bi-Bi distance is 3.86 Å (**Figure A 8**), in good agreement with our observations. We speculate that edge-shared Bi^{5+} - Bi^{3+} contributes significantly to the emerging and evolution of the broad correlation peak. The peak broadness indicates possible corner *and* edge-shared Bi^{5+} - Bi^{3+} and Bi^{3+} - Bi^{3+} polyhedra, whose correlations would appear at distances greater than 3.87 Å. We can rule out the formation of both Bi_2O_3 and the { Bi_6 } cluster due to their different Bi-Bi atom pair correlations in their calculated PDF (**Figure A 8**).

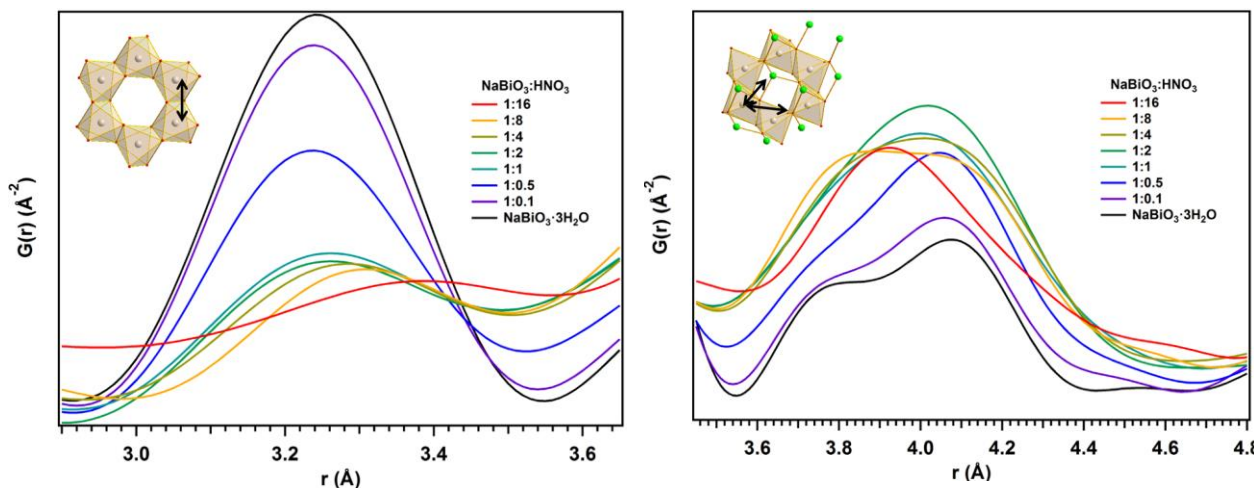


Figure 2.7 Monitoring the changes (**left**) at the neighboring Bi-Bi distance and (**right**) at the new arising Bi-Bi correlation in the acid-treated samples utilizing PDF analysis. Inset represents the atomic pair correlations in the pristine material. (Brown: Bi polyhedral, green: Na^+)

XPS analyses of selected acid-treated samples provide further information about oxidation states of Bi on the surface. (Detailed XPS data are collected in **Figure A 9**, **Figure A 10**, and in **Table A 6** and **Table A 7**, respectively). The results are summarized in **Figure 2.8**. Pristine $\text{NaBiO}_3 \cdot 3\text{H}_2\text{O}$ shows Bi^{5+} only, but the Na:Bi ratio deviates from the 1:1 formula (0.7 Na per Bi). Consistent with this, the oxygen is also deficient, if we assume the deficiency is the framework oxos, and not the lattice water. The $\text{Bi}^{5+}:\text{Bi}^{3+}$ ratio is ~50:50 in the 1:1 $\text{NaBiO}_3:\text{HNO}_3$ acid-treated sample, while this value reaches 29:71 $\text{Bi}^{5+}:\text{Bi}^{3+}$ for the 1:16 $\text{NaBiO}_3:\text{HNO}_3$ sample (**Table 2.2**). The oxygen content likewise decreases. Bi^{3+} in acid-treated samples has two very distinct chemical environments. The first peak arises at 157.59-157.93 eV, and its ratio is relatively stable in samples from different acid concentrations. The second peak (>159.50 eV) arises with higher HNO_3 concentration treatments ($\text{NaBiO}_3:\text{HNO}_3$ ratio of 1:16). None of these new peaks can be identified with known standard materials (i.e. Bi_2O_3 and $\text{Bi}(\text{NO}_3)_3$ reference materials).

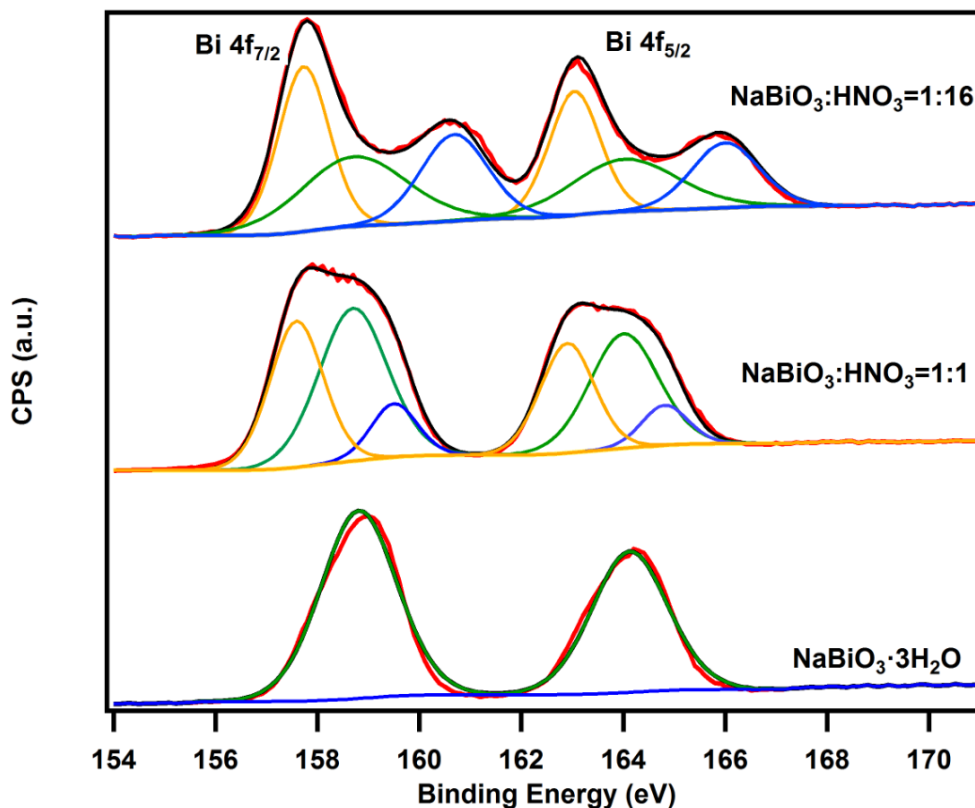


Figure 2.8 XPS of the Bi peak in the selected samples.

Table 2.2 Quantitative results from XPS on the selected samples, with Bi normalized to unity (see Table A6). (Peak positions: Bi⁵⁺: 157.59-158.81 eV, Bi³⁺₁: 157.59-157.93 eV and Bi³⁺₂: >159.50 eV)

NaBiO ₃ :HNO ₃ ratio	Composition	Bi ⁵⁺ :Bi ³⁺ ₁ :Bi ³⁺ ₂ percent
NaBiO ₃ ·3H ₂ O	Na _{0.68} BiO _{4.23}	100% : 0% : 0%
1:1	Na _{0.22} BiO _{2.23}	50.33% : 37.75% : 11.92%
1:16	Na _{0.05} BiO _{1.97}	29.07% : 38.76% : 34.34%

2.5.3. Sodium and hydrous content of acid-treated NaBiO₃·3H₂O

The loss of Na⁺ from the lattice is not expected, if we just consider charge-balance requirements for the Bi⁵⁺ to Bi³⁺ reduction. The pH change of the acidification solutions with addition of NaBiO₃·3H₂O (pH increases, see **Table 2.1**) suggests the Na-loss occurs by ion exchange (Na⁺ for H⁺). Alternatively, the H⁺ drives release of O²⁻ ligands from the lattice, by formation of H₂O; this would also increase the pH. Thermogravimetry supports the latter mechanism, because with increasing acidification and removal of sodium, the volatile content of the acidified bismuthate goes down rather than up (**Figure 2.9**). This suggests loss of hydrous species including H₂O, H₃O⁺ and OH⁻, along with loss of sodium, diminution of long range order, and conversion of Bi⁵⁺ to Bi³⁺. Reasons for loss of both sodium and hydrous species could be related to the structure directing effect of the Bi³⁺ lone pair. The lone pair does not require coordination or H-bonding for stabilization. Also, the loss of oxo ligands (acid-promoted dehydration) further condenses the lattice, leaving no room for sodium or such hydrous species. This suggests that Bi⁵⁺ becomes less accessible to perform oxidation reactions (i.e. in its employment in the nuclear fuel cycle) as time of acid exposure or acid strength increases.

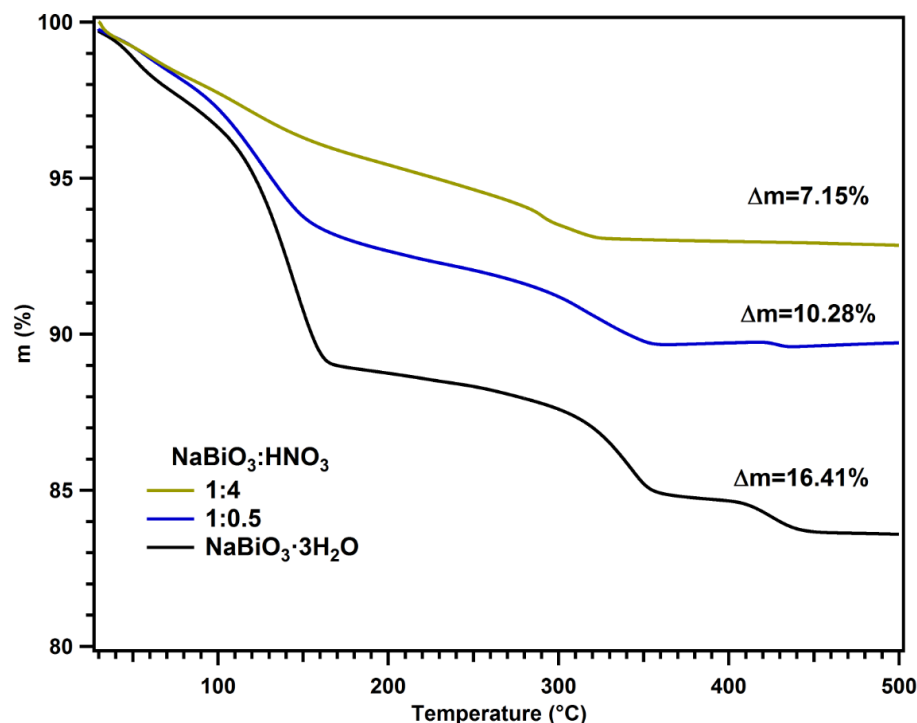


Figure 2.9 TGA of $\text{NaBiO}_3 \cdot 3\text{H}_2\text{O}$ and two selected acid-treated samples with the corresponding weight-loss.

2.5.4. Ce^{3+} oxidation studies

Ce^{3+} oxidation by sodium bismuthate in acidic media is an acceptable surrogate reaction to evaluate americium oxidation.³² We compared three samples in the cerium oxidation studies: $\text{NaBiO}_3 \cdot 3\text{H}_2\text{O}$ starting material and two selected samples that have been pre-treated by acidification. Cerium oxidation with $\text{NaBiO}_3 \cdot 3\text{H}_2\text{O}$ and with the two acid-treated samples (1:1 and 1:16 $\text{NaBiO}_3:\text{HNO}_3$; **Figure 2.10**) reveals a negative effect of acidification on oxidation efficacy. Oxidation of Ce^{3+} is complete within one hour with pristine $\text{NaBiO}_3 \cdot 3\text{H}_2\text{O}$, approximately two hours with the $\text{NaBiO}_3:\text{HNO}_3=1:1$ sample, and more than 3 hours with the $\text{NaBiO}_3:\text{HNO}_3=1:16$ sample.

By applying a pre-treatment step, we can delineate the effects of degradation of the NaBiO_3 material upon acid exposure with the effect of pH on redox potentials. Based on our XPS and PDF results, acidification in HNO_3 reduces the original Bi^{5+} content, and compositional analysis shows the Bi^{3+} is contained in the bulk, as well as the surface. The morphology of the acidified samples does not show any significant microscopic changes by SEM (**Figure A 11**). A previous study noted that acidification increases the specific

surface area by approximately 10% shown by N_2 sorption measurements,^{44,45} not a significant change. Moreover, based on TGA results, we have surmised that the material becomes denser.

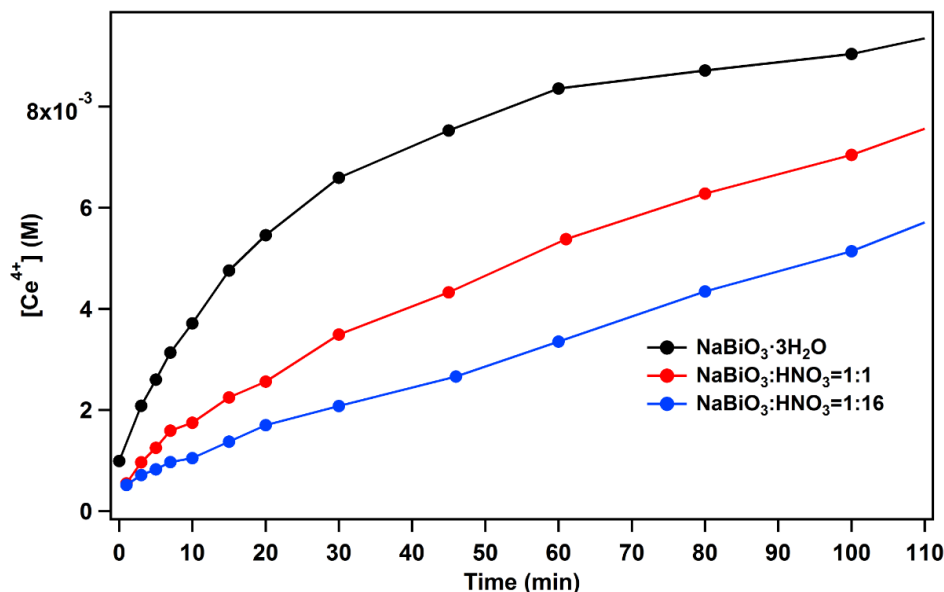


Figure 2.10 Comparison of Ce^{3+} oxidation in 1M HNO_3 , using the different $NaBiO_3 \cdot 3H_2O$ starting materials: pristine, pretreated with 0.37 M HNO_3 (1:1), and pretreated with 5.7 M HNO_3 (1:16).

2.6 Conclusions

Pentavalent bismuth oxides and mixed pentavalent/trivalent bismuth oxides are potentially important materials for oxidation reactions and photocatalysis. The only commercial source of Bi^{5+} is sodium bismuthate, and its form is a hydrated lattice whose structure has not been reported. Here we have used PDF analysis from total X-ray scattering to compare to the known structure of anhydrous $NaBiO_3$. We have shown that reported $NaBiO_3 \cdot 2H_2O$ can exhibit higher degrees of hydration; we measured 3 lattice waters per formula unit, $NaBiO_3 \cdot 3H_2O$. This hydrous phase possesses a structure similar to anhydrous $NaBiO_3$, with turbostratic disorder in the stacking of the hexagonal $\{Bi-O\}$ sheets. The most logical position for the water is in the vacancies within the hexagonal Na-O layers, and H-bonding of the water molecules to framework oxos and/or binding of the water to Na^+ likely distorts these layers, leading to the turbostratic disorder.

Acidification of hydrous (or anhydrous) NaBiO_3 and further analyses via powder X-ray diffraction, PDF, XPS, and EDX suggested the reduced bismuth (Bi^{3+}) remains in the lattice, promoting the amorphization of the material. Bismuth likely remains in the structure due to its low mobility. On the other hand, more highly mobile and soluble sodium and water migrate out of the lattice, leaving a denser structure. PDF results suggest the formation of a complex oxide containing edge-sharing Bi^{5+} - Bi^{3+} , edge-sharing Bi^{3+} - Bi^{3+} and corner-sharing Bi^{5+} - Bi^{3+} polyhedra. The origin of the intense color of mixed $\text{Bi}^{3+}/\text{Bi}^{5+}$ phases that appears upon acidification is not well-understood. Neither scattering data nor XPS data indicate formation of known Bi^{3+} phases. The intense color suggests an unusual phase with unique electronic properties, whose structure-property relationship will be revealed and exploited in the future.

Currently, nuclear energy scientists are seeking to improve sodium bismuthate performance for oxidation, separation and recovery of americium in the nuclear fuel cycle. In this study, we correlated the loss of oxidation efficacy with decreased Bi^{5+} in the lattice, induced by pretreatment with acid. Different from prior studies that identified increasing acidity of the oxidation conditions as the only means to increase oxidation efficacy, we delineated the opposing effects of degradation of the sodium bismuthate from the effect of shifted Eh potential in acidic media. While it was noted prior that Bi^{3+} dissolves from the degrading bismuthate, our study clearly shows plenty remains. Therefore modifying the material or conditions so that Bi^{3+} dissolves more cleanly and rapidly from this sacrificial oxidant would yield a more effective process. Alternatively, one may consider deposition of a sodium bismuthate film on an electrode, and employing it as an oxidant with an applied voltage, in order to retain the pentavalent bismuth.

2.7 Acknowledgements

The experiments for this study were done as part of the Under graduate Summer School in Radiochemistry funded by the U.S. Department of Energy's Office of Nuclear Energy under grant DE-NE0008478. NMB and WS were student participants in this program. The XPS was performed at the Northwest Nanotechnology Infrastructure, a member of the National Nanotechnology Coordinated Infrastructure, which is supported by the National Science Foundation (Grant ECCS-1542101).

3. Benchmarking solution PDF of metal-oxo clusters with laboratory diffractometer

Karoly Kozma, May Nyman

In preparation (2019)

3.1 Abstract

Pair distribution function (PDF) analyses are highly in demand by material chemistry community to obtain direct structural information of amorphous or poorly crystalline materials and even solutions. PDF requires high-quality data collection, and thus far synchrotron sources are the main facilities to acquire this data. More recently, laboratory diffractometers have improved and provided publishable data. This study shows how a laboratory diffractometer can be used as a routine technique for solution PDF measurement of metal-oxo clusters in water. We benchmarked our in-house facility with standard metal-oxo clusters, for example silicotungstic acid (SiW_{12}) and different uranyl-peroxide nanoclusters. We observed metal-metal correlations in solutions with good agreement with structures observed in their solid state. We also proved that combination of small-angle X-ray scattering (SAXS) and PDF together can extract information about investigated species without crystallographic data. At the end of this chapter, additional examples are provided to prove that this method is a powerful complementary technique, and, despite the limitations of the in-house setup, still capable to provide important information from solutions.

3.2 Introduction

3.2.1. Metal-oxo clusters

Metal-oxo clusters are molecular metal-oxide compounds that form by self-assembly of reactive oxometalate precursors in aqueous or organic solution.¹ They are key intermediates in the reaction pathway from water soluble metal ions to insoluble metal oxides, and isolation of these enable elucidation and control over reaction pathways. POMs are structurally and chemically diverse with reactivities leading to use in catalysis⁴⁸ and sustainable energy,⁴⁹ electronics,⁵⁰ sensors,⁵¹ radionuclide capture^{5,52} and biomedical applications.⁵³ The traditional metal-oxo clusters are polyoxometalates (POMs) composed of high-valent (typically d^0 or d^1) group V and VI transition metals (V, Mo, W, Nb and Ta) possessing negative charge on the compound. The first report of a POM was by Keggin in 1933 with the pioneering structural studies of 12-phosphotungstic acid ($\text{H}_3\text{PW}_{12}\text{O}_{40}$).⁵⁴ The central tetrahedral $[\text{PO}_4]$ anion is connected to four trimer $[\text{W}_3\text{O}_{15}]$ units. Those trimers are connected by corner-shared oxygens, while in the trimer unit edge-shared polyhedra are

observed. Since then, this unit and its isomers have been observed for numerous other metals, like other group V and VI metals, Al^{55,56}, Sn⁵⁷ or even Fe^{58,59} and the open-shell Cr⁶⁰ metal ions. Reports of these novel structures and emerging application potentials attract considerable interest from researchers. There are many other structures metal-oxo clusters can form. An additional example is the relatively new class of hollow-cage uranyl-peroxide polyoxometalates built up by uranyl ions.⁶¹

Burns' discovery of uranyl-peroxide cages in 2005 opened a new area of polyoxometalate chemistry.⁶²⁻⁶⁴ Since then nearly 70 new structures have been isolated based with 16-124 uranyl-peroxide polyhedra. The size of these nanoclusters varies from 1.5 to nearly 4 nm.⁶⁵ Their structures have very intriguing features: the [UO₂]²⁺ cation has yl-oxygens in *trans* positions, and the assembly of metal polyhedra occurs through the bridging equatorial ligands. The bridging ligands are peroxide and hydroxide ions, but other inorganic (phosphate, pyrophosphate) and organic (oxalate) agents have also been successfully incorporated into these cages. The U-(O₂)-U bond angles are less than 180° (vary between 134° and 159°) creating a bent connection.⁶⁶ Due to this structural feature, uranyl-peroxide clusters create hollow cages, or nanocapsules, where the inside has no uranyl ions, but counter cations, solvents⁶⁷ or other smaller clusters⁶⁸ in some extreme cases.

Depending on the reaction conditions, the size (and morphology) of the uranyl-peroxide clusters varies. In each structures the observed building blocks are uranyl-peroxide polyhedra. These monomers self-assembly to secondary building units: tetramer, pentamer or hexamer faces including four, five or six of those monomer units. Some of these building units have isolated from solutions,⁶⁹ demonstrating they form first in the self-assembly of the capsules. In this chapter, we use the nomenclature introduced by Burns et al. to describe nuclearity of the uranyl-peroxide nanoclusters.⁶⁶

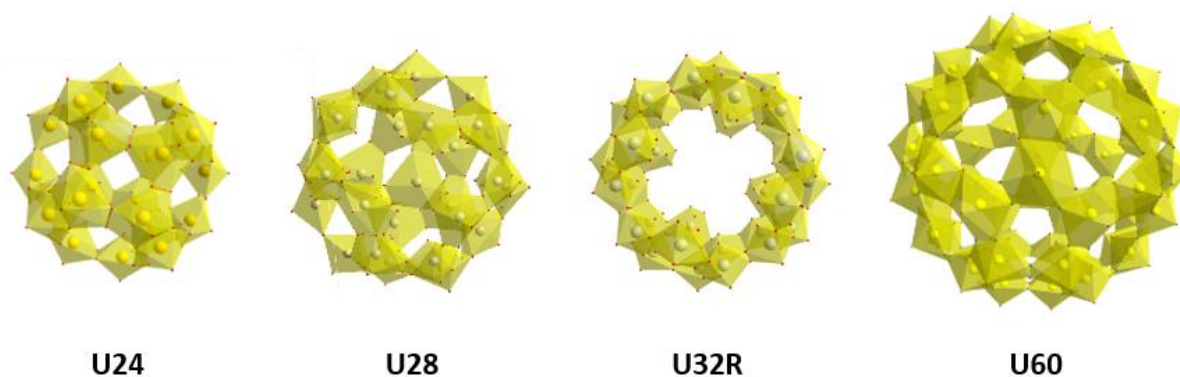


Figure 3.1 Polyhedral representation of some uranyl-peroxide nanoclusters using the notations introduced by Burns *et al.*

3.2.2. Pair distribution function (PDF) of solution samples

Single-crystal diffraction methods provide the absolute identification of these polyoxometalate or metal-oxo cluster compounds. However, sometimes single-crystal diffraction data is not possible. Additionally, investigation of their structures in solution requires alternative methods. Beyond the traditional solution characterization methods (UV-Vis, Raman, NMR spectroscopy, etc.), scattering methods can still provide direct structural information of the investigated system. For this purpose the scattering profile is analyzed instead of distinct diffraction peaks.¹⁷ The two main scattering methods are small-angle scattering or total scattering (both X-ray and neutrons) techniques. Small-angle X-ray scattering (SAXS) is utilized to extract information about the size and shape of the dissolved species in solution. This method is highly effective to explore metal-oxo clusters in solutions.¹⁰ The total (X-ray) scattering measurements provide different structural information. After Fourier-transformation, the obtained function is the pair distribution function (PDF) which is a probability histogram of atomic distances. This method requires high available q -space (higher than 15 \AA^{-1}), high q resolution, good counting statistics at high q , and low instrument background.⁷⁰ This methodology can be carried out mostly at synchrotron sources due to availability of these conditions, but a few examples of laboratory diffractometers are also suitable, as the detector quality improves, combined with high energy X-ray sources (Mo, Ag or W sources – 17.5 \AA^{-1} , 22.0 \AA^{-1} or 59.0 \AA^{-1} q_{max} values).

The PDF method has been widely utilized to explore structure of materials with no or little order: atom-pair correlations are still observable in disordered, amorphous materials, glasses or liquid samples. In addition, transition between different solid phases, amorphization, and crystallization pathways can be explored via this method. Liquid samples have similar features to amorphous materials, considering the lack of long-range order in the structure. Total scattering still provides significant information about these systems. Most studies of the liquid state explore the structure of water^{71,72}, solvent mixtures⁷³, proteins⁷⁴ or simple salt solutions.^{75,76} Even these simple systems exhibit complexity in their interpretation. For instance, the structure of pure H₂O solvents has been extensively studied by scattering methods to extract information about coordination conditions and hydrogen-bond network in liquid H₂O. Similarly, information about the hydration sphere of different metal salt solutions (alkali,^{75,76} alkali earth,⁷⁷ transition metal⁷⁸ or rare earth metal⁷⁹) has been studied thoroughly. Study of metal-oxo clusters in solutions by PDF is yet a less explored area with few examples in the literature. The stable Keggin structures are good candidates to investigate and create a model by this technique.⁸⁰ The real potential of solution PDF is to monitor the formation of these metal-oxo clusters or to extract structural information where no crystallographic information available.⁸¹ For example, formation of Zr and Hf sulfate clusters were monitored to understand their self-assembly pathways.^{82,83}

Because of limited accessibility of PDF techniques (synchrotron facilities and appropriate expertise), there are few examples in the literature studying metal-oxo clusters in solution.^{23,24} Our goal is to utilize in-house PDF facility to extract structural information about metal-oxo species. This method along with SAXS could provide direct structural information when growing single-crystals is challenged by disorder, instability, poor crystal quality, etc. First, we collected data on pure water and the standard H₃SiW₁₂O₄₀ (SiW₁₂) Keggin ion to benchmark the method. Later, uranyl-peroxide nanoclusters are in focus of our study. We test saturated solution of four of these clusters: U60, U32R, U28 and U24 (using Burns' notation, see figure 1). Solution PDF measurements of metal-oxo clusters are unique systems, where the short-range order of the solvent is present with the (sometime) long-range order of the cluster compound. In addition, the solution state allows us to observe the individual clusters without intermolecular correlations which would be

present in solid-state measurements. We will also discuss the main drawbacks of these lab instrument solution measurements: the scattering power of the metal and its concentration, as well as the long time-period of data collection. Lighter elements or lower concentration (or both) cannot overcome the signal of water, making interpretation not unequivocal or sometimes, impossible. It is not possible to study dynamic systems.

3.3 Experimental

To perform PDF analysis of X-ray total scattering measurements, we used Rigaku Smartlab X-ray diffractometer with Mo-K α irradiation ($\lambda=0.71 \text{ \AA}$) in the 2θ range of 3-118.0° with transmission geometry. The theoretical q -range is up to a q_{max} of 15.4 \AA^{-1} . A 0.2°/minute data collection time was used (when not noted otherwise) to ensure high quality scattering data. Samples were loaded in Kapton capillary with 1.46 mm inner diameter for irradiation. Measurements on the empty Kapton capillary were carried out with the same experimental conditions for background subtraction.

Fundamentally, data analysis is similar to that used for solid measurements. PDFgetX3 was to process scattering data into the corresponding PDFs. Use of this software is described in detail in the literature by Juhas and co-workers.¹⁸ All simulations shown were created in PDFgui.¹⁹ We used the XYZ structure files to create simulations of the metal-oxo clusters. This format lacks the information about the unit cell, but provides adequate information of the individual cluster, without correlation between the clusters. Consequently, the simulated data is sufficient for qualitative comparisons, but not appropriate for further calculations and refinement to extract quantitative information.

First, we collected data on empty Kapton capillary for background corrections and collected the pure H₂O solvent for future reference. Next, we used silicotungstic acid (H₃SiW₁₂O₄₀) solutions (or {SiW₁₂}) at 100 mM, 50 mM and 20 mM concentrations. This compound is stable, commercially available, and easy to prepare standard solutions at the required concentrations. Silicotungstic acid was purchased from Sigma-Aldrich.

Later, we measured solutions of different uranyl-peroxide nanoclusters. For these, we created saturated solutions of U60 (Li_{48+m}K₁₂(OH)_m[(UO₂)₆₀(O₂)₆₀(OH)₆₀], $m \sim 20$)⁶⁴, U32R ((NH₄)₄₀[(UO₂)₃₂(O₂)₄₄(OH)₁₆])⁸⁴, U28 (K₂₈[(UO₂)₂₈(O₂)₄₂])⁶² and U24 (Li₂₄[(UO₂)₂₄(O₂)₂₄(OH)₂₄])⁶², respectively (**Figure 3.1**). Since, we used excess of these clusters to make solutions, and the supernatant was filtered, we do not know the exact

concentration values of these solutions, but based on the solubility behavior we observed this solubility order: U32R < U28 ~ U24 < U60. The U28 and U24 clusters were prepared by Dr. Clement Falaise (Oregon State University), the other clusters (U32R and U60) were provided by Burns research group (University of Notre Dame).

3.4 Results and discussion

3.4.1. Water and silicotungstic acid solutions

Before we investigate any metal-oxo systems we need to corroborate the features of pure H₂O solvent. The experimental total scattering curve with its Fourier-transformed function are present in **Figure 3.2**. The X-ray total scattering curve shows one intense, very broad peak at 7-23°. This broad feature is indicating the lack of long-range order in the structure. Performing Fourier-transformation we acquire the pair distribution function of pure H₂O solvent. We can distinguish two different parts on the PDF of water: while there are some correlations at short-range distances below ~5 Å, there are only oscillations, ripples with similar magnitude and frequency above 6 Å. We observe the first peak at 0.89 Å. Although this peak could correlate to the O-H bond in water, due to data processing we do not interpret any features below 1-1.2 Å. It is related to the polynomial correction of structure function that mostly influences the very beginning of PDF (below 1.2-1.5 Å).⁸⁵ The most intense peak is located at 2.85 Å, which can be assigned to the O_w-O_w distance. This is the distance between neighboring oxygens of water molecules connected by hydrogen bonding, in good agreement with previous scattering studies.⁷¹ This peak position varies if the H-bond network is disturbed, for example in ionic salt solutions.⁷⁶

We can also observe a very broad, low intensity features in the 3.7-5.3 Å region, which appears as distinct peaks. This region correlates to the second hydration sphere of water, where several H₂O molecules are present. Solutions are dynamic with all molecules in motion, which is why this region has low intensity very broad features. Some subtle oscillations may also appear on this broad feature, but they do not have exact *r* location changing data processing parameters, indicating their origin from termination ripples. Also, no other peaks are observable at higher distances, confirming the lack of long-range ordered structure.

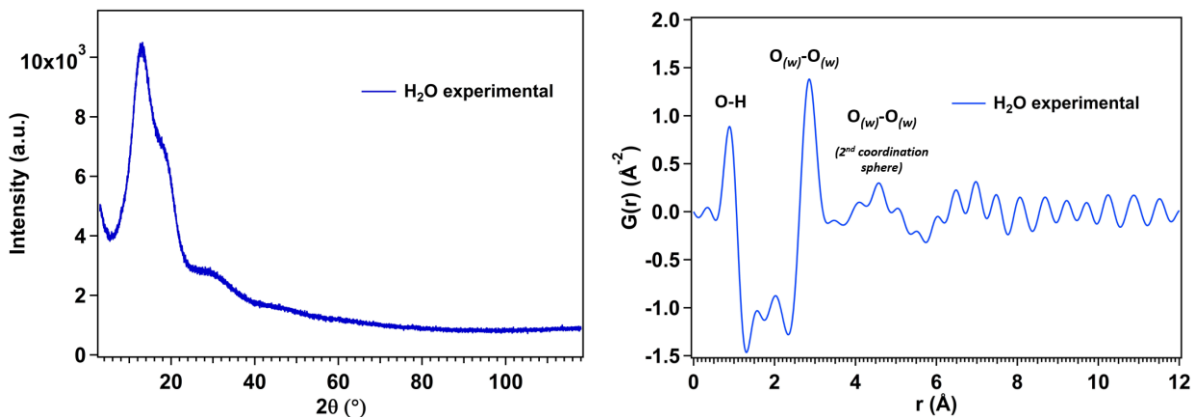


Figure 3.2 Left: experimental X-ray total scattering curve of pure H₂O solvent. Right: experimental PDF analysis of the H₂O solvent.

Another notable feature of H₂O PDF is the “dip” at short distances around 2 Å. This area in the solid-state measurements provides information about the average number density of the material: as $r \rightarrow 0$, $G_{(r)}$ function asymptotes $G_{(r)} \rightarrow -4\pi\rho_0r$, where ρ_0 is the average number density of the material. This latter quantity is difficult to interpret in highly disordered materials and in dynamic systems due to the molecular motions. As we will see later, the depth of this valley depends on the concentration, the scattering elements, and counter ions. In addition, this region is greatly affected by background subtraction. Overall, the experimental PDF of H₂O is in good agreement with measurements carried out at synchrotron sources, allowing us to use this method to study other solution samples.^{71,72}

Following the H₂O measurement, we tested solutions of H₃SiW₁₂O₄₀ with 20 mM, 50 mM and 100 mM standard concentration. In order to find the best experimental conditions, we varied several parameters. Here, we show two of the most important ones and how they influence the final PDF data. These variables are the scanning speed (or data collection time) and the concentration of the studied species. We studied the same {SiW₁₂} solution using 0.5°/minute and 0.2°/minute with 0.01° step size. Notably, the 0.5°/minute scan speed is a 4-hour data collection, and the 0.2°/minute scan speed translates to a nearly 10-hour data collection time in the 3-118° range. These results are presented in **Figure 3.3A**. As we can see, longer data collection time results better data as expected. Nevertheless, the intensity of the ripples at higher distances is dampened with longer data collection. It can have significant effect when the intensity of atomic-pair correlation is comparable to that ripple, especially for longer distance correlations. It shows that our in-house instrument

requires a $0.2^\circ/\text{minute}$ data collection speed for solution samples to ensure high quality data. Additional experiments, described below, were carried out with this optimized parameter.

Next we probed the effect of concentration. The experiment series includes three samples with 20 mM, 50 mM and 100 mM concentrations of $\{\text{SiW}_{12}\}$, presented in **Figure 3.3B**. Changing the concentration we observe significant changes in the short-range distances. Firstly, while the peaks we observed for H_2O (below 1 \AA and at $\sim 2.8 \text{ \AA}$) have significant contributions at 20 mM concentration, but increasing the concentration diminishes these contributions. Although they are still present at 100 mM concentration, the intensity of the first peak is comparable to those ripples at higher distances. The peaks of metal-metal correlations in $\{\text{SiW}_{12}\}$ arise simultaneously. While water-peak and the neighboring M-M distance is comparable in the 20 mM solution, the M-M correlations dominates the PDF of the 100 mM sample. The other interesting effect is related to the “dip” $\sim 2 \text{ \AA}$ discussed prior for H_2O . This valley has lower absolute intensity with increased concentration, approaching the zero line. This indicates that higher concentration, and higher average number density can minimize the valley (see the $-4\pi\rho_0r$ value above).

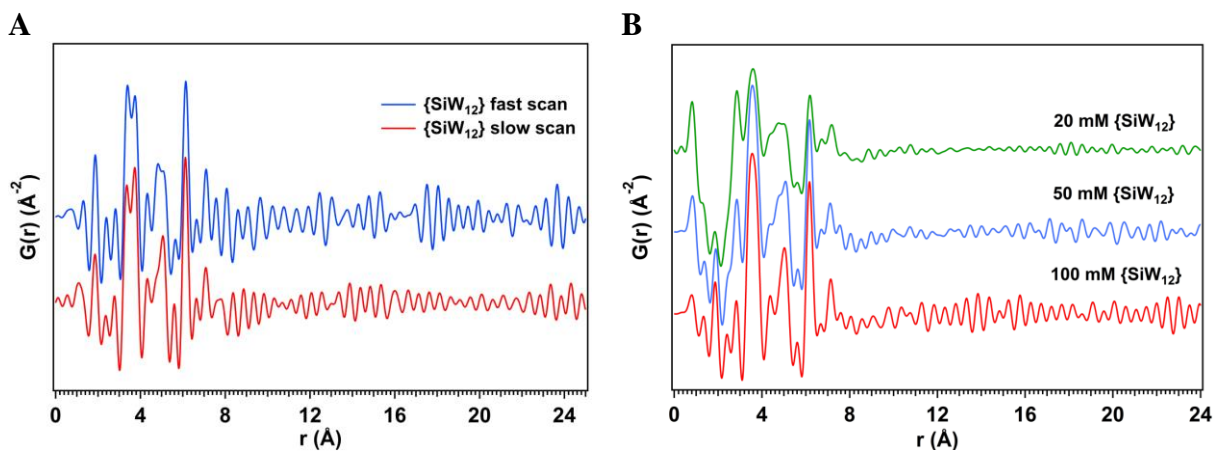


Figure 3.3 Left: comparison of experimental PDFs of $\{\text{SiW}_{12}\}$ solutions using different data collection time (fast scan: $0.5^\circ/\text{minute}$, slow scan: $0.2^\circ/\text{minute}$). Right: Concentration dependence of $\{\text{SiW}_{12}\}$ solutions.

After optimization of experimental conditions (instrumental parameters), we measured 100 mM $\{\text{SiW}_{12}\}$ solution to study the observed atom-pair correlations. The experimental and simulated PDF curves along with the represented atom-pair correlations in $\{\text{SiW}_{12}\}$ is shown in **Figure 3.4** and **Table 3.1**. As discussed above, the water peak at 2.84 \AA has low

intensity. Peak **A** represents the metal-oxygen (W-O or Si-O) distances in the structure at 1.87 Å (simulation: 1.87 Å). This is the only M-O correlation clearly observable in the PDF. As it is represented on the simulated curve, the individual metal-oxygen correlations at 1.6 Å (Si-O), 1.7 Å (W=O), 1.9 Å (W-O) and 2.3 Å (W-O) are not observed separately, only their broad average. Since the scattering power of oxygen is very low compared to the metals, contributions of M-O correlations at higher distances, as well as O-O correlations become negligible. The second and most intense peak (**B**) at 3.56 Å (simulation: 3.63 Å) correlates with two metal-metal correlations Si-W and edge-sharing W-W (**Table 3.1** and **Figure 3.4**), but those peaks overlapping with each other. Peak **C** (experimental: 5.03 Å, simulated: 4.95 Å) and **D** (experimental: 6.17 Å, simulated: 6.12 Å) represent W-W correlations between {W₃} trimer units, as illustrated in **Figure 3.4**. Finally, peak **E** represent the longest W-W distances in the {SiW₁₂} cluster, which is the overall diameter or the compound, if the terminal yl-oxos are not considered. The experimental value is 7.14 Å, in good agreement with the simulated 7.11 Å value. We can see all peaks in the simulation are accounted for in the experimental data. Results are in good agreement with data from a synchrotron source, reported prior by Levy and his co-workers.⁸⁶ Intensity of the PDF peaks are correlated to the multiplicity of the correlations, in general. In our case we cannot compare those intensities with the simulated curve directly because 1) the simulated model does not have unit cell information; 2) influence of water (as well as the hydration sphere) is not included in the starting model that just contains the cluster. Consequently, single-crystal structures provide a good starting model to predict structures in solution and simulate PDFs of a metal-oxo cluster. As we will see in the later examples and studies, our PDF interpretations provide qualitative or semi-quantitative information, quantitative data were not extracted.

Table 3.1 The observed peaks assigned to atom-pair correlations in {SiW₁₂} Keggin ion with the experimental and simulated distances.

Peak	Atom-pair correlation	Distance (Å) (experimental/simulated)
A	Si-O, W=O and W-O	1.87 / 1.87
B	Si-W, W-W (edge-shared)	3.56 / 3.63
C	W-W (corner-shared)	5.03 / 4.95
D	W-W	6.17 / 6.12
E	W-W (diameter)	7.14 / 7.11

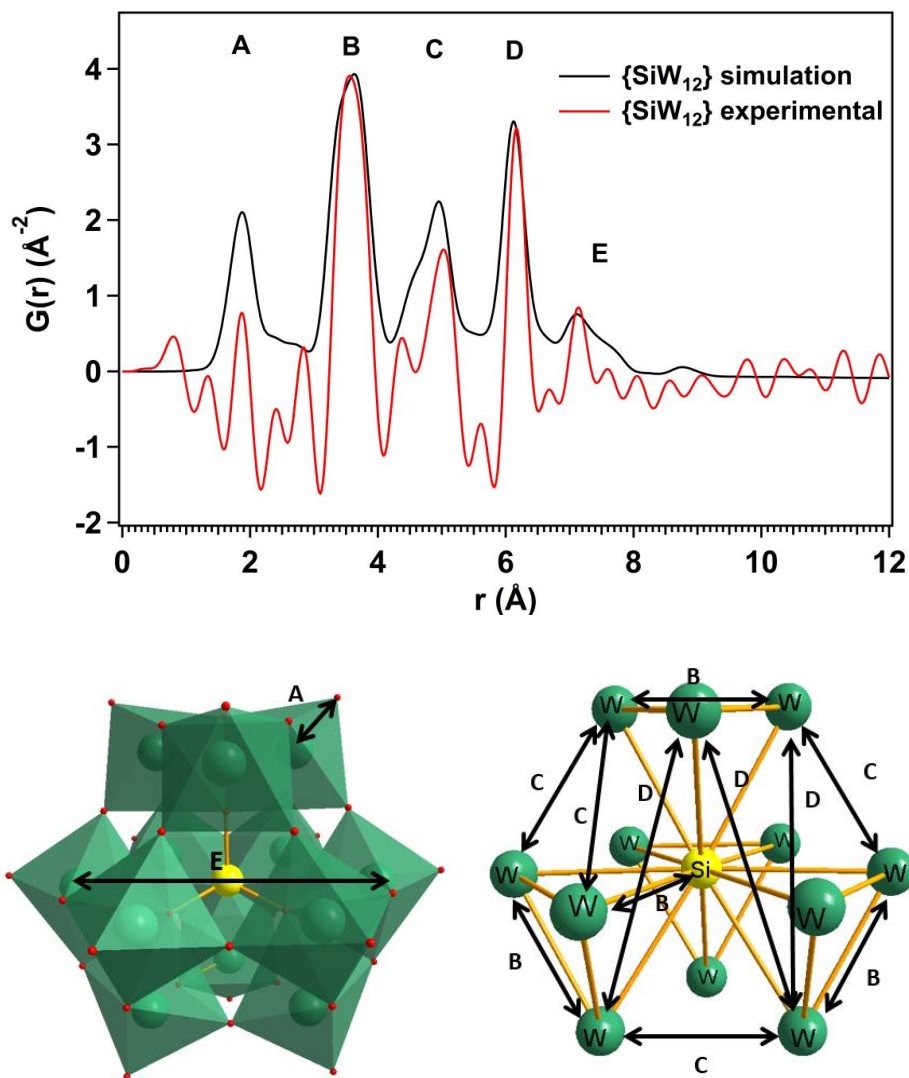


Figure 3.4 The experimental and simulated PDFs of $\{\text{SiW}_{12}\}$ cluster in aqueous solution. The correlations assigned to the distinct peaks are present at the bottom: the polyhedral and ball-stick (oxygens are eliminated for clarity) representation of the $\{\text{SiW}_{12}\}$ Keggin ion.

3.4.2. Uranyl-peroxide nanoclusters in water

We also studied metal-oxo clusters, where the intramolecular correlations can reach higher distances, in some cases a few nanometer distances. For this, stable large clusters with good scattering elements were chosen. Uranyl peroxo clusters are ideal candidates, because they contain the heaviest naturally occurring element (uranium), they form stable, rigid hollow nanoclusters. Additionally, they can be prepared easily to make monodisperse

solutions, as well as to study by other characterization techniques. We probed the saturated solutions of U60, U32R, U28 and U24 to extract structural information by PDF analysis. PDF analyses of solutions containing uranyl-peroxo cages revealed important features about the measurements. Uranyl peroxo nanoclusters can reach high aqueous solubility due to the large anionic charge, the mobility of counter cations to enter the hollow and the forming big hydration sphere (nearly 1 molar U concentration has been reached with U60 by Peruski *et al*)⁸⁷. The first example is the U60 solution where we experienced the highest solubility among the cluster compounds. Solution PDF reveals individual nanoclusters as shown in **Figure 3.5**. Experimental and simulated PDF curves are in very good agreement. Due to the high concentration, signal arising from water (water peak and dip) is minimal. Here, we focus on three main feature on this curve: the correlations arising from neighboring U-U distance (**A**), the diagonal U-U distance in the building blocks (**B**) and the overall diameter of the cluster (**C**). These three main features are visually represented in **Figure 3.6**.

The experimental neighboring U-U distance (**A**) (4.23 Å) of edge-sharing uranyl polyhedra matches perfectly with the simulated value. The diagonal U-U correlation (**B**) is also very close (7.08 Å) to the simulated value (7.06 Å). As it is represented on the simulation, diagonal U-U correlations of different faces (hexagonal vs. pentagonal faces) are not separated from each other. Furthermore, the overall size around 21-22 Å (by single-crystal X-ray and SAXS measurements) is also observed by PDF.⁸⁸ Although, in these big molecules, sometimes it is difficult to define the certain atom-pair correlations at higher distances, the good scattering power of U dominates the overall function. As we can see on both the experimental and simulated data, several intense peaks appear between peak **B** and **C**, indicating further pair correlations can be assigned to different U-U distances in the rigid structure, but assigning those correlations with different multiplicity in that distance range is complicated and not practical. The PDF as a fingerprint proves the stability of this cluster and shows it is intact in its aqueous solution. We do not observe any other correlations, meaning no distinct correlation from counter cations (K⁺), and hydration sphere is negligible, as well as there is no interaction between the clusters at this concentration (which effects are not included in simulations).

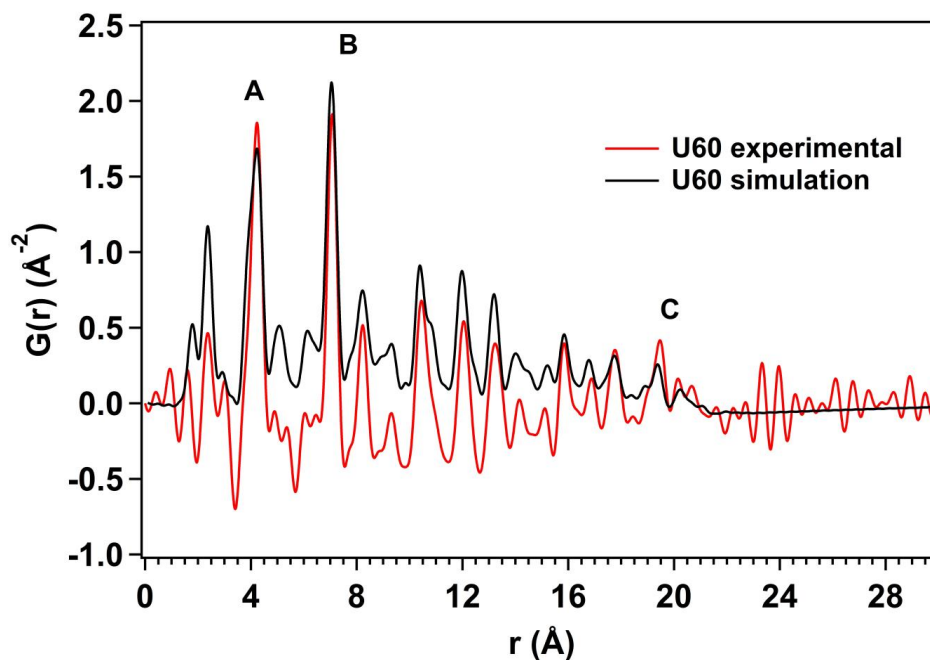


Figure 3.5 Experimental PDF of U60-solution with the simulated curve of the cluster.

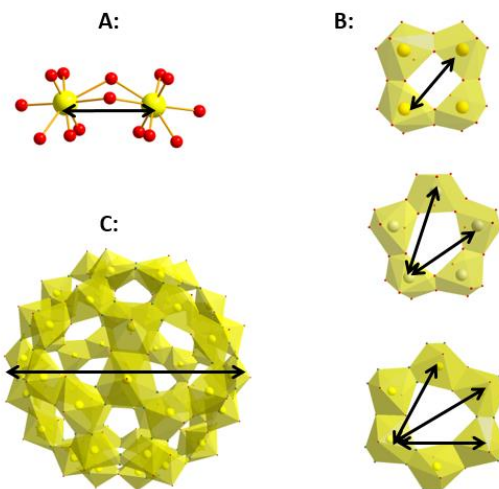


Figure 3.6 The main three structural features in uranyl-peroxide nanoclusters we observe by solution PDF: neighboring U-U distance (A), the diagonal correlations in the building units (B), and the overall diameter (U to U, excluding yl-oxygens) of the cluster (C).

Following U60-solution measurements, we probed the saturated U32R, U28 and U24 solutions. The results are presented in **Figure 3.7**. The extracted distances with the simulated values for **A** and **B** are summarized in

Table 3.2. As we can see, peak **A** and **B** are still the most intense atom-pair correlations in these systems, and they are in good agreement with the simulated curves. However, the overall diameter (**C**) is not necessarily observable on each function. In the case of U28 and U24, the cluster diameter is in the range of 13-16 Å.⁸⁹ Comparing the experimental PDFs with the simulated ones, the correlation at the highest distance is still distinguishable from the oscillations in the experimental PDFs. The PDF of both U24 and U28 follow the simulated pattern. However, the PDF data of U32R shows worse quality. Comparing experimental and simulated curves, correlation **A** and **B** are observable, but simulated peaks at higher distances are not observed in the experimental data. In addition, ripples dominate the curves above 12-13 Å, and it is not possible to define the cluster size in solution without prior knowledge or additional characterization data, like small-angle X-ray scattering (SAXS). We hypothesize these effects are related to the lower solubility. This is supported by the more dominant water signal in these PDFs (as well as prior experience with these ammonia salts of U32). As we can see the water peak ~ 2.8 Å is still negligible for U24 and U28, but its intensity is comparable to the first U-U correlation in U32R solution. On the other hand, the dip is more pronounced, as well. As we compare the locations of the correlations, we can also observe higher uncertainty to the solution with lower concentration. While peak **A** and **B** are in good agreement with the simulations in U60, these locations are shifted to higher distances in U32R. This example shows how important to choose the right experimental conditions and models to study metal-oxo cluster solutions by PDF.

Table 3.2 Comparison of experimentally observed interatomic correlations in uranyl-peroxide nanocages with the values obtained by simulations.

	A (experimental/simulated) (Å)	B (experimental/simulated) (Å)
U24	4.13 / 4.04	7.06 / 6.98
U28	4.23 / 4.20	6.84 / 6.83
U32R	4.34 / 4.19	7.08 / 7.01
U60	4.23 / 4.23	7.08 / 7.06
U-TMA*	4.37 _(aq) / 4.31 _(s)	7.62 _(aq) / 7.60 _(s)

* The values are corresponding to solution (*aq*) and solid (*s*) state.

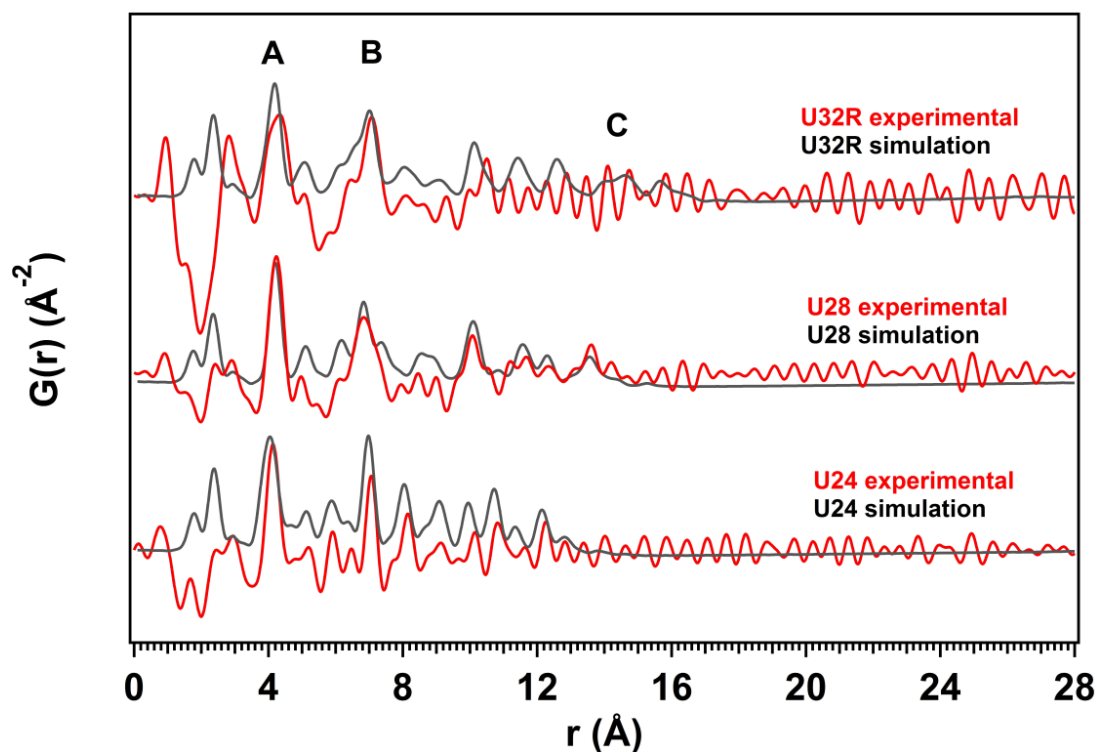


Figure 3.7 Experimental PDFs of saturated U24, U28 and U32R solutions with the simulated curve of the individual clusters.

Based on the results, utilizing PDF along with SAXS can provide important structural insights about the studied metal-oxo clusters in solution state. This can be crucial when single-crystal structure is not available due to inability to crystallize the cluster or grow crystals of suitable quality. SAXS can provide information about the size (as well as dispersity/purity of the solution), and PDF provides information about atom-pair correlations (metal-metal distances) in short-range order. These two, independent measurements can be a starting point to investigate relevant structural features with no crystal structure, or to build a structural model to determine the structure simply from the solution-phase data. The next example illustrates a method, where structural information about a novel uranyl-peroxide nanocluster is extracted with no crystallographic information.

A simple solution of uranyl nitrate plus peroxide and tetramethylammonium hydroxide (TMAOH) yields a monodisperse solution containing a very large, novel hollow capsule.

Here, we do not discuss the experimental details of its synthesis and solution speciation, we just focus on its characterization by X-ray scattering methods. This new compound can be synthesized in its pure form and both solution and solid-state characterization is feasible. However, crystallization attempts do not result single-crystals or the quality of grown crystals is not adequate to extract any structural information. SAXS measurements suggests size of 3.7 nm of this cluster. The precipitated cluster that is dissolved in methanol is presented in **Figure 3.8**. Analysis of SAXS data suggests the hollow (core-shell) structure observed for many other uranyl-peroxide clusters. The size is remarkably bigger than the other clusters. The previously shown U60 cluster has an overall diameter of 21-22 Å. The 37 Å diameter indicates a nuclearity that is much higher than the previously reported uranyl-peroxide nanoclusters.

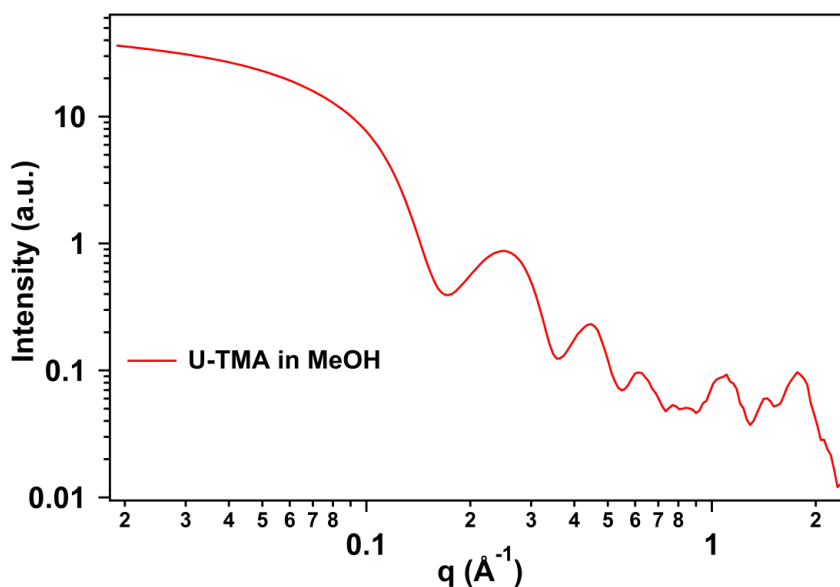


Figure 3.8 SAXS curve of U-TMA cluster dissolved in methanol.

We also investigated the atom-pair correlations of this currently-unknown cluster. We collected data both in solution and solid state, the locations of those correlations are present in

Table 3.2. Both solution and solid-state PDF is present in **Figure 3.9**. We can observe two main peaks at 4.31 Å (**A**) and at 7.60 Å (**B**) in solid state. These values are 4.37 Å (**A**) and 7.62 Å (**B**) in aqueous solution. Similarly to standard uranyl-peroxo cluster solutions

of known capsule structures, **A** represents the neighboring U-U, **B** represents the diagonal U-U correlation in the building unit. Longer distances are observed for both correlations compared to the correlations for the known nanocluster solutions (~ 0.1 Å larger for **A** and >0.5 Å larger for **B**). We explain this as the effect of bigger cluster size. Reasonable assumption is that the cluster has the same building units: uranyl peroxy polyhedra connected by both peroxy and hydroxo bridges assembled to those four-, five- or six-membered face building units. Without changing drastically the connectivity between polyhedra, changing the bond angles and dihedral angles can change the U-U distances. The U-(O₂)-U bond angle getting closer to 180° can increase the bond distances. Although this less effect on the neighboring U-U distances (**A**), the diagonal U-U distances in the building unit (**B**) can exhibit significant changes. It is reasonable, because the bigger size of the cluster suggests less curvature of the shell compared to e.g. U60.

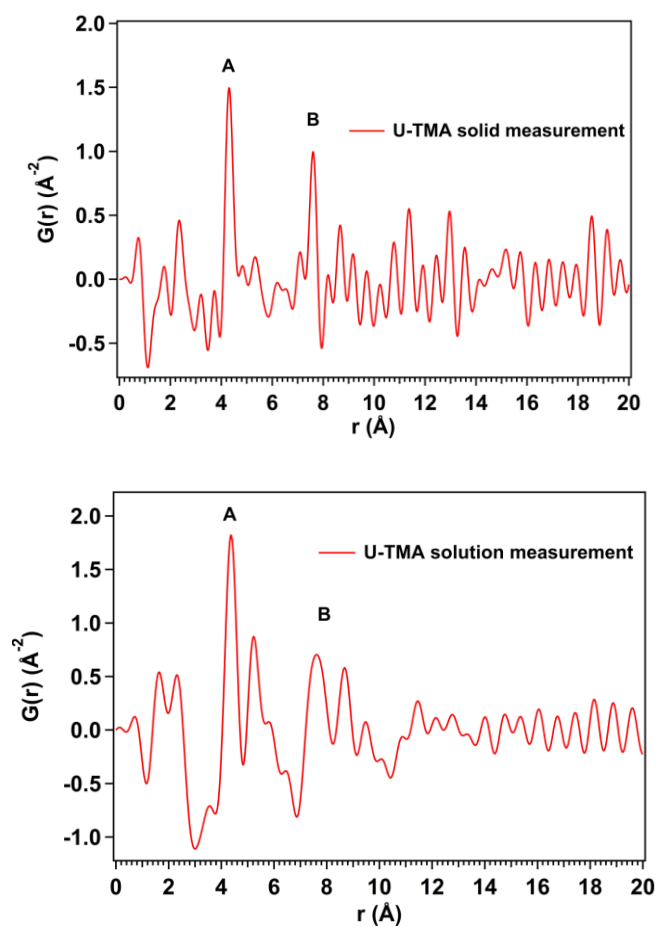


Figure 3.9 PDF of the U-TMA cluster in solid (top) and in solution (bottom) state.

Unlike the U60 solution, we cannot observe well-defined structures at higher distances. We hypothesize the concentration is lower than in saturated U60 solution. Additionally, in solid-state we expect to observe both intermolecular and intramolecular correlations⁹⁰, but single-crystal structural information is necessary for the absolute identification of the origin of peaks. In summary, PDF data supports our observation of bigger size of the cluster. The investigated bond distances along with SAXS scattering profile is a good starting point to build a theoretical model which may describe both SAXS and PDF data.

3.4.3. Further possibilities and limitations

We studied several additional metal-oxo systems in solution state. Three examples are summarized here, and the full studies are described in the corresponding publications.

3.4.3.1. Formation of the δ -{ZnCr₁₂} Keggin ion

The in-house instrumentation is limited to study systems without significant change over time. However, choosing the adequate reaction conditions we can monitor reaction pathways. The following example shows how PDF can be performed to monitor the formation of the novel δ -{ZnCr₁₂} ([Zn(H₂O)₃]ZnO₄Cr₁₂(OH)₂₄(H₂O)₁₂](NO₃)₈·xH₂O) Keggin ion acidic solution. This is the first reported Keggin ion structure built up by transition metals with valence electrons (Cr³⁺) with no organic stabilizing ligands.

While SAXS of the reaction solutions shows progression of size and size-distribution of the scattering species,⁶⁰ PDF analysis shows pair correlations of atoms within the scattering species (**Figure 3.10**). We use the simulated PDF for δ -{ZnCr₁₂}, as well the experimental PDF of redissolved δ -{ZnCr₁₂} crystals to identify metal-metal and metal-oxygen pair correlations in the reaction solutions containing {ZnCr₂}-trimer units with different nitrate concentration. All the PDFs exhibit a peak at ~2.0 Å, which is the Zn-O or Cr-O bond. This is present regardless of speciation. In the reaction solutions containing the {ZnCr₂}-trimer units, there is also a strong peak at ~3.0 Å (peak **A**), consistent with the M-M (Cr-Cr, Zn-Cr) distance of edge-sharing polyhedra. The relative intensity of this peak in the two spectra is similar; meaning the number of edge-sharing polyhedra does not change considerably, with the removal of nitrate, forcing condensation. The third major peak at ~3.5 Å (labeled **B**), is the M-M correlation of corner-sharing polyhedra. Interestingly, this peak grows with the removal of nitrate, progressing cluster formation. The biggest

correlated change noted in the ESI-MS with nitrate removal is increase in population of Zn- Cr dimers. The combined PDF and ESI MS results suggest that the crucial step of $\delta\text{-}\{\text{ZnCr}_{12}\}$ formation is the assembly of the Cr- octahedra around the Zn-center via corner linking, promoted by removing nitrate from the solution.

This is an excellent example to monitor formation of a metal-oxo species choosing the right experimental conditions by changing concentration of nitrate ion. The solution study was supported by SAXS and ESI-MS measurements, as well. Additionally, both Cr and Zn metals are light elements ($3d$ metals) compared to the previous studies. To overcome the problem of weak scattering of studied elements, PDF measurements were performed at high, 1 M concentration of Cr. Even at that high concentration, it is more challenging to define distinct features correlating to the Keggin structure at higher distances on the experimental curves. The full study is described in the recent publication of Wang and co-workers.⁶⁰

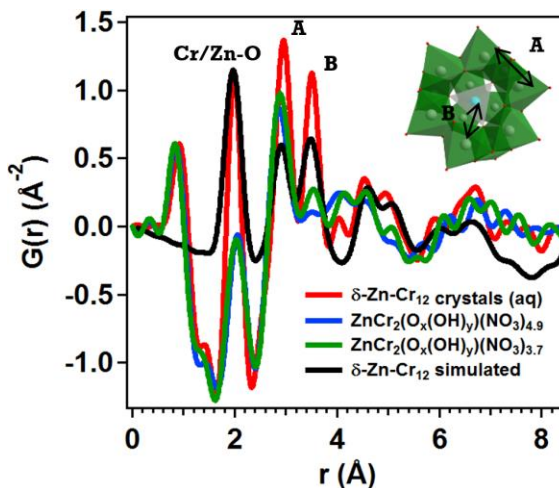


Figure 3.10 PDF comparing the two step-wise reaction composition solutions, along with dissolved $\delta\text{-}\{\text{ZnCr}_{12}\}$ crystals plus simulated PDF for $\delta\text{-}\{\text{ZnCr}_{12}\}$. The peak at 2 Å (Cr/Zn-O bond) is normalized for $\text{Cr}_2\text{Zn}(\text{O}_x(\text{OH})_y)(\text{NO}_3)_{4.9}$ and $\text{Cr}_2\text{Zn}(\text{O}_x(\text{OH})_y)(\text{NO}_3)_{3.7}$, so intensity of the M-M peaks (A & B, M=Zn/Cr) can be compared. The strong negative dip around the 2 Å is due to background subtraction of the water peak at 2.7 Å.

3.4.3.2. Contact ion-pairing in solutions

Under ideal conditions, interactions between particles can be observed in solution. Electrostatic interaction between anions and cations can form different type of ion-pairs in solution, where contact ion-pairing may form as strong or long-lived interactions between

ions, similar to those observed in a solid-state lattice. With an ideal model (high scattering power elements, high solubility, variable that can be probed and compared to a standard state), PDF can probe this behavior in solution. The next example describes contact ion-pairing between hexatantalate {Ta₆} or hexaniobate {Nb₆} Lindquist polyoxometalate anions ([M₆O₁₉]⁸⁻, M=Ta, Nb) and Cs⁺ counter cations.

In order to define an atomistic model that accurately represents the binding of Cs⁺ to the POMs, we need to know the solution ‘structure’. Past small-angle X-ray scattering (SAXS) studies of the Cs-hexametalates have been executed in highly alkaline solutions with excess Cs⁺,^{91,92} and more recently in water alcohol mixtures.⁹³ Neither of these conditions are representative of the current experiments and, moreover, atomic-level ion pairs are not absolutely defined by SAXS. The prior studies also forced ion association by respectively a huge excess of Cs⁺ and by decreasing the solvent polarity. In the current system, we utilize conditions that simply ensure deprotonation of the clusters based on pH,⁹⁴ and variable stoichiometric amounts of Cs. Clearly evident in both the simulated PDF of {Ta₆} and the 100 mM TMA{Ta₆} without any added Cs is two strong peaks of *cis* Ta–Ta (3.4 Å) and *trans* Ta–Ta (4.8 Å) in the cluster (**Figure 3.11**). There is also a weak peak around 2.0 Å that arises from the Ta–O bonds. Since the peak intensity is mostly determined by the scattering power of the elements, the peaks for M–M (M = metal) pairs are much more intense than those for M–O pairs. Although one can expect several peaks for the different metal–oxygen distances, only the first coordination sphere at ~2.0 Å is unambiguous and its intensity is significantly smaller than those at metal–metal distances. The peaks at greater distances have lower intensity in the experimental curves due to the inverse relationship between distance and peak intensity. Increasing the concentration of CsCl in the solutions results in a diminution of the water peak (~2.8 Å), which is exacerbated by the superposition with the shortest metal–metal distance (~3.4 Å). This phenomenon is common, since the hydration sphere of the free ions (Cs⁺ and Cl⁻) have contributions for this region and we can see the superposition of these different peaks in the short distance range.⁹⁵ A distinct peak appears at 4.1 Å and becomes more intense with added CsCl. This distance is very close to the Ta–Cs distances seen in the solid state crystal structure of Cs₈Ta₆O₁₉·14H₂O, confirming the similarity between the aqueous and solid state Cs⁺ environments. Additionally, upon normalizing the peak heights at the *trans* Ta–

Ta distance (4.8 Å), the Ta–Cs peak grows monotonically, reaching a maximum. This agrees with the determined ‘carrying capacity’ of Cs⁺ from the published NMR experiments. The *cis* Ta–Ta distance at 3.4 Å, on the other hand, grows with added Cs⁺. This pair distance overlaps with those of Cs–O and Cl–O pairs, according to prior X-ray scattering studies of CsCl and KCl solutions.^{75,96} We can discount significant contribution from Cl–O due to both the disorder of water that is hydrogen-bonded to Cl⁻,⁹⁵ as well as the relatively low electron density of this atom pair. On the other hand, the Cs–O pair produces significant scattering from Cs, and the number of Cs–O bonds formed is directly correlated with the number of Cs⁺ in solution, regardless of whether they are bonded to water only or bonded directly to the cluster, with the rest of its coordination sphere completed with water molecules. Another peak arises at 6.6 Å with added Cs⁺, attributable to either a *trans* Ta–Cs or Cs–Cs distance. The peak intensity monotonically increases with increasing Cs⁺ concentration and does not exist in the absence of Cs⁺. The analogous {Nb₆} solutions were also tested and exhibited very similar behavior to the {Ta₆} solutions, with distinct Nb–Cs and Cs–Cs peaks growing monotonically with added Cs⁺ at 4.1 Å and 6.7 Å.⁹⁷ These data provide a rare example of atomic-level evidence for ion-pairing in simple solutions that do not contain an excess of either the cation or anion.

This example presents an excellent example to monitor contact ion-pairing in solution with a polyoxometalate and its Cs⁺ counter cation. The solution study was supported by ¹³³Cs-NMR and computational methods, as well. The complete study was published by Sures and co-workers.⁹⁷

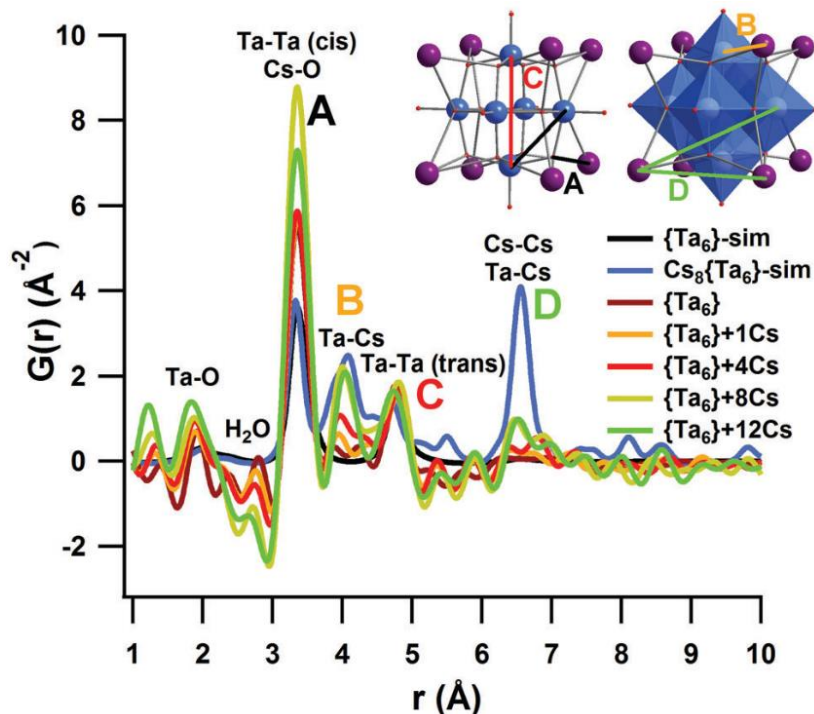


Figure 3.11 PDF analysis of X-ray total scattering on solutions of 100 mM TMA $\{Ta_6\}$ in 200mM TMAOH with added CsCl (0 to 12 molar equivalents) – ‘sim’ indicates a simulated function. (courtesy ⁹⁷)

3.4.3.3. TiOSO₄ solutions

Finally, to illustrate the effect of the scattering power of the metal, we investigated several other metal-oxo cluster solutions. Shortly, we show PDF analysis of some TiOSO₄ solutions. There is exponential relationship between scattering power and increasing Z (atomic number). Thus, we investigated several metal-oxo systems of $3d$ transition metals, see the example of δ - $\{ZnCr_{12}\}$ above. The following example is the second lightest transition metal ($Z=22$). As we will discuss in the following chapter, TiOSO₄ solution speciation is dominated by the large and rigid $\{Ti_{18}\}$ -cluster, as suggested by SAXS, Ti K-edge EXAFS and single-crystal diffraction of clusters crystallized from these solutions. Solution PDF analyses were also conducted with less success. **Figure 3.12** shows measurements of TiOSO₄ solutions from 250 mM to 1000 mM along with 1 M KHSO₄ solution as a reference. (The 1 M KHSO₄ solution has the elements with very similar/same scattering power at the required concentration, where we do not expect any long-range order in solution.) Despite the high concentration of Ti in these solutions, the overall

function is still dominated by H₂O. Although we can observe some correlations in 3-5 Å distance range, the intensity is too low to assign them to any specific metal-metal correlations. Although there is no doubt about the presence of larger species (confirmed by the above-mentioned techniques), we are unable to extract any further structural information. This example shows that solution PDF is very powerful complementary method, but it still has some significant limitations. Although the better resolution and higher accuracy provides higher quality data and faster data collection at synchrotron sources, the problems of weak scattering elements and low concentration are still concerns for solution samples regardless the facility. The full study of TiOSO₄ solutions is described the following chapter.⁹⁸

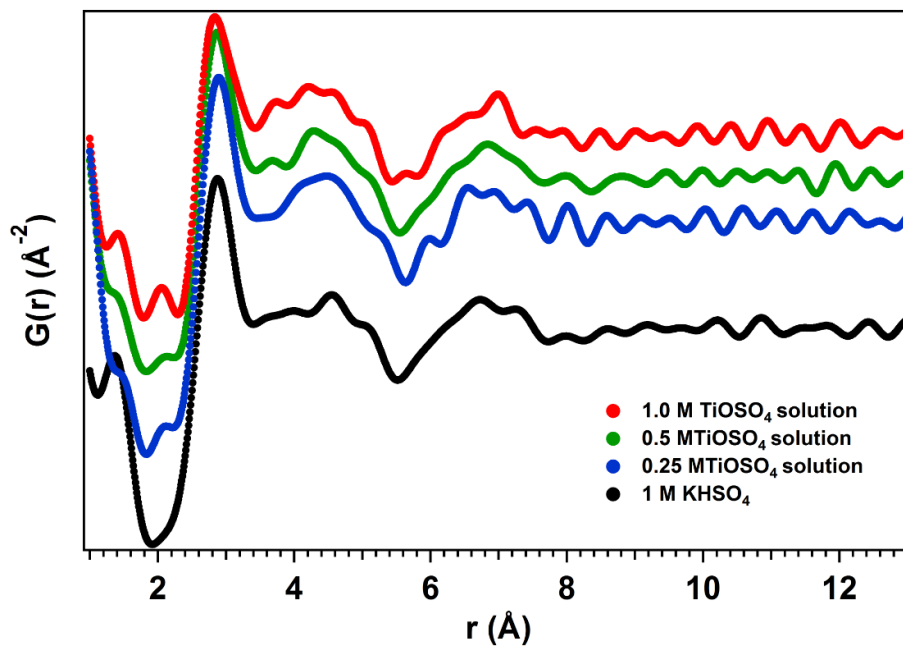


Figure 3.12 PDF of TiOSO₄ solution at different concentrations. The low scattering power of Ti cannot overcome the signal coming from H₂O solvent even at 1 M concentration level.

3.5 Conclusion

Here we benchmarked the use of in-house PDF facility to probe metal-oxo clusters in aqueous solutions. The instrument uses Mo K α X-ray source that reached the maximum scattering vector of $q_{max} \sim 15.5 \text{ \AA}^{-1}$. First, we showed that pure H₂O and standard solutions

of $\{\text{SiW}_{12}\}$ gives the expected scattering profile and PDF functions. Then we studied several uranyl-peroxide nanoclusters. With these measurements we could observe the main features of the nanoclusters: 1) the neighboring metal-oxygen and metal-metal correlations, 2) non-neighboring correlations at higher distances and 3) the overall size of these molecules (nanoclusters) in several cases. In the solution state, concentration has a considerable effect on the observed PDFs: with lower metal concentrations water has increased contribution, challenging observance of pair correlations. Individual metal-oxo clusters were observed (unlike in solid-state measurements) eliminating the correlations between the molecules. However, observing both the highly disordered structure of the solvent (H_2O in our cases) and the distinct structure of these metal-oxo clusters create a special system where qualitative and semi-quantitative analysis can be carried out.

In summary, PDF analysis of X-ray total scattering measurements is very powerful complementary method to extract structural information on the investigated systems. It provides direct structural information, especially when coupled with SAXS. We have also provided an example in which it may be possible to determine a structure with no crystallographic information or to study the stability and interactions of the investigated species in solution state. We probed atom-pair correlations that are intra-cluster, as well as correlations assigned to contact ion-pairing between clusters and counterions. Synchrotron sources remain the only facilities to study dynamic systems and follow reaction pathways in much shorter time-periods. In addition, better resolution (distinguishing closely spaced correlations) and longer pair correlations still likely requires data from a synchrotron facility. However, we have been able to publish qualitative data of solution speciation that is supported by other characterization techniques. Moreover, by collecting and processing data year-round, we have the opportunity to identify and benchmark systems that must be studied at synchrotron facilities, ensuring optimal efficiency during beamtime.

3.6 Acknowledgement

We thank Dr. Harrison Neal, Dr. Clement Falaise and the research group of Peter C. Burns to provide uranyl-peroxide nanoclusters for my experiments. We also thank Dr. Dylan Sures, Prof. Wei Wand and Mehran Amiri for the opportunity to participate in their research using our in-house PDF analysis method.

4. The role of titanium-oxo clusters in sulfate process for TiO₂ production

Karoly Kozma, Maoyu Wang, Pedro I. Molina, Nicolas P. Martin, Zhenxing Feng and
May Nyman

Dalton Transactions 48 (2019) 11086-11093

4.1 Abstract

TiO₂ is manufactured for white pigments, solar cells, self-cleaning surfaces and devices, and other photocatalytic applications. One industrial synthesis of TiO₂ entails: 1) dissolution of ilmenite ore (FeTiO₃) in aqueous sulfuric acid which precipitates the Fe while retaining the Ti in solution, followed by 2) dilution or heating the Ti sulfate solution to precipitate the pure form of TiO₂. The underlying chemistry of these processing steps remain poorly understood. Here we show dissolution of a simple Ti^{IV}-sulfate salt, representative of the industrial sulfate production of TiO₂, immediately self-assembles into a soluble Ti-octadecameric cluster, denoted {Ti₁₈}. We observed {Ti₁₈} in solution by small-angle X-ray scattering and Ti extended X-ray absorption fine structure (Ti-EXAFS), and ultimately crystallized it for absolute identification. The {Ti₁₈} metal-oxo cluster was prior-reported as a polycation; but shown here, it can also be a polyanion, dependent on the number of sulfate ligands it carries. After immediate self-assembly, the {Ti₁₈}-cluster persists until TiO₂ precipitates, with no easily identified structural intermediates in solution or solid-state; despite the fact that the atomic arrangement of {Ti₁₈} differs vastly from that of titania. The evolution from solution phase {Ti₁₈} to precipitated TiO₂ nanoparticles was detailed by X-ray scattering, and Ti-EXAFS. We offer a hypothesis for the key mechanism of complete separation of Fe from Ti in the industrial sulfate process. These findings also highlight the emerging importance of the unusual Ti(Ti)₅ pentagonal building unit, featured in {Ti₁₈} as well as other early d⁰ transition metal chemistries including Nb, Mo and W. Finally, this study presents an example of crystal growth mechanisms in which the observed ‘pre-nucleation cluster’ does not necessarily predicate the structure of the precipitated solid.

4.2 Introduction

Titanium dioxide and titanates have been studied since Fujishima and Honda demonstrated the photooxidation behavior of simple and earth abundant TiO₂⁹⁹. Since this initial discovery, titanium-dioxide forms have been synthesized, doped, and engineered to understand form-function relationships, and to improve the catalytic efficacy^{100–103}. Titania is an ideal white pigment, in addition to photocatalyst^{104,105}. It is utilized in self-cleaning surfaces (nanomaterial forms) or scaffolding on buildings for degradation of air

pollutants^{104–107}. Titanium is the second most abundant transition metal in the geosphere; its oxide materials are very stable and considered as low toxicity materials¹⁰⁸. These industrially important oxides are produced in water, but the Ti-speciation and the influence of solution conditions on the formed material has not been well-elucidated¹⁰⁹.

One process to obtain titanium dioxide is from sulfuric acid solutions at elevated temperature¹¹⁰. This sulfate process uses ilmenite (FeTiO_3), the most earth-abundant source of titanium. After removing iron by precipitation, TiO_2 is obtained from the remaining titanium sulfate solution. The ore source and the applied methodology determines product purity. Also, physical parameters (e.g. color) of the produced TiO_2 depend on the conditions that promote Fe/Ti separation. Hence, investigations of relevant titanium sulfate solutions are important to optimize this industrial process. In prior studies, Raman-spectroscopy was utilized to characterize speciation, and all reports hypothesized aqua or sulfato coordination complexes of titanyl monomers (TiO^{2+})^{109,111,112}. Formation of larger species like titanium-oxo clusters (TOC) was speculated in the process of nucleating TiO_2 , but mechanisms and reaction pathways are not understood^{2,112–114}.

Metal-oxo clusters, which can be considered molecular metal oxides, are useful models to understand solution processes; in particular, incipient precipitation and crystallization of the related oxide phases.¹¹⁵ These clusters are sometimes isolated as stable entities without organic ligands; in particular the aluminum polycations^{55,56} and the transition metal (Group V/VI) polyoxometalates.^{5,60,116} However, most metal-oxo cluster intermediates must be stabilized by organic ligands for isolation. Nonetheless, even ligated clusters are useful structural models to understand self-assembly processes, and to perform experiments to determine their relevancy on the reaction pathway from monomer to metal oxide^{117,118}. Group IV metal-oxo clusters, including Ti^{IV} ¹¹⁹, are an emerging class of inorganic (meaning without organic ligation) aqueous polycations^{120–124}, and even polyanions^{125–127}. Only recently, Wang *et al.* has pioneered the expansion of aqueous TOCs¹²⁸. Several TOCs have been reported with different nuclearity^{119,129–132} including $\{\text{Ti}_4\}$, $\{\text{Ti}_6\}$, $\{\text{Ti}_8\}$, $\{\text{Ti}_{18}\}$ and heterometallic $\{\text{Ti}_{22}\text{Bi}_6\}$ ¹³³ with respectively 4, 6, 8, 18 or 22 titanium polyhedra ligated with only O^{2-} , OH^- and H_2O (and sulfate in some cases). One of the most fascinating compounds exhibits pentagonal bipyramid coordination ($\{\text{Ti}_{18}\}$ -cluster), in addition to the common octahedral geometry. This cluster is a stack of three $\text{Ti}(\text{Ti})_5$ pentagonal units

(**Figure 4.1B**) in which the pentagonal bipyramid shares five edges with Ti-octahedra in a planar arrangement. Similar units have been also observed in polyoxometalate clusters of Nb¹³⁴, Mo¹³⁵ and W¹³⁶. The recent discovery of purely inorganic, water-soluble TOCs brings forth opportunity to synthesize and design new titanates with controlled chemical and structural composition through the reaction.

Here we show that in TiOSO₄ solutions representative of those employed in TiO₂ production, {Ti₁₈} is the dominant specie. This hypothesis was formulated from corroborative solution-characterization techniques including small-angle X-ray scattering (SAXS), pair distribution function (PDF) analysis of X-ray total scattering, and titanium extended X-ray absorption fine structure (Ti-EXAFS). Ultimately crystallization of {Ti₁₈} supported this hypothesis. We also tracked to evolution from solution-phase {Ti₁₈} to precipitated TiO₂. Intriguingly, we cannot identify the structural intermediate between {Ti₁₈} and TiO₂, suggesting rapid conversion. Nonetheless, observed rapid self-assembly of a Ti-cluster that cannot accommodate heteroatoms provides one underpinning mechanism for Fe/Ti separations, and other important metal-metal separations in industry.

4.3 4.3. Experimental

4.3.1. Reagents and solution preparation

Titanium(IV) oxysulfate, TiOSO₄·nH₂O (Ti≥99%) and tetrabutylammonium chloride, N(C₄H₉)₄Cl (TBA-Cl) (≥97%) were purchased from Sigma-Aldrich. Concentrated H₂SO₄ was purchased from Macron Fine Chemicals. We also used TiCl₄ (99%) for control experiments purchased from Beantown Chemicals. The materials were used as received. Deionized (DI) water (18.2 MΩ, Millipore) was used to prepare all solutions. Solutions for EXAFS, SAXS and PDF measurements were prepared by adding a predetermined amount of TiOSO₄ to deionized water and stirring vigorously for 3-4 hours at room temperature to ensure complete dissolution. Note: these solutions cannot be heated, because they yield anatase, per the industrial process.

4.3.2. Crystallization

{Ti₁₈}-cluster: In order to validate that TiOSO₄ solution is dominated by {Ti₁₈} and provide control samples for the EXAFS studies, we crystallized {Ti₁₈} by employing tetrabutylammonium ion (TBA⁺). We dissolved 800 mg TiOSO₄ in 5 mL DI water and

added 1.39 g TBA-Cl. After complete dissolution, the solution was filtered through a 0.45 μm nylon mesh syringe filter. Colorless crystals appeared after twelve days.

4.3.3. Characterization methods

Detailed description of techniques, experimental parameters and data processing and interpretation is provided in the Appendix B and summarized here. SAXS data were collected on SAXSess instrument (Anton Paar) to obtain information about the dispersity and the size of the species present in solution. The local coordination environments were probed by Ti K-edge extended X-ray absorption fine structure (EXAFS) analysis at 5BM and 20 BM of the Advanced Photon Source (APS) at Argonne National Laboratory (ANL). Single-crystal X-ray diffraction proved identification of clusters observed in solution, and these details of data collection and structure solution and refinement are summarized in the Appendix B. We performed X-ray total scattering measurements to perform pair distribution function (PDF) analysis with a Rigaku Smartlab X-ray diffractometer (Mo-K α radiation). Transmission electron microscopy (TEM) images were acquired using a high angle annular dark field detector on an FEI Titan TEM operated at 200 keV in STEM mode. Energy dispersive X-ray spectroscopy (EDX) measurements were performed on Quanta 600 scanning electron microscopy (SEM).

4.4 Results and discussion

4.4.1. Solution behavior and solution characterization by X-ray scattering techniques

Representative structures of the key phases of this study, $\text{TiOSO}_4 \cdot \text{H}_2\text{O}$, $\{\text{Ti}_{18}\}$ and anatase TiO_2 are shown in Figure 4.1. Briefly, $\text{TiOSO}_4 \cdot \text{H}_2\text{O}$ is a framework structure containing zigzag chains of TiO_6 -octahedra along the b -axis. The octahedra are corner-linked by oxo-ligands in a cis-configuration. Three bonds to Ti are from the sulfates, and remaining bond of hexacoordinate Ti is to a terminal water molecule. Each SO_4 -tetrahedron bridges four TiO_6 -octahedra. The $\{\text{Ti}_{18}\}$ cluster is a stack of three pentagonal $\text{Ti}(\text{Ti})_5$ units. Within the cluster core, there are 27 oxo ligands; five within each layer around the equatorial belt of the pentagonal bipyramid (edge-sharing) and six that link each set of two layers together (corner-sharing). Terminal ligands are water molecules, and BVS suggests there are no hydroxyl ligands present in the various formulations of $\{\text{Ti}_{18}\}$. The five Ti -octahedra of the middle layer have two terminal water molecules each, while the octahedra

of the cap layers have varying degrees of replacement of two water ligands by a bridging sulfate ligand around the perimeter of the pentagonal units, or one water ligand replaced by a terminally-bound sulfate on the pentagon face. The degree of replacement varies in different crystalline lattices¹²⁸. Like most Ti-oxo phases, anatase contains only Ti-octahedra. In Figure 4.1, the Ti-octahedra in the center of the unit cell is highlighted as semi-transparent; all Ti are crystallographically equivalent in anatase. Each octahedron links to four others by edge-sharing (solid polyhedra, Figure 4.1) and four by corner-sharing (not shown). Each oxo ligand bridges three Ti-octahedra.

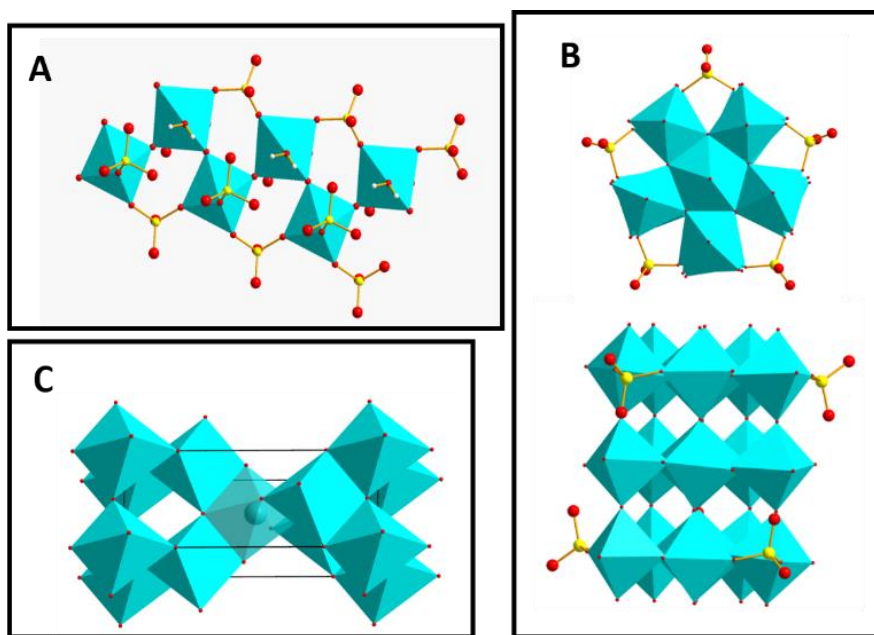


Figure 4.1 Representations of the relevant structures in this study. **A** is $\text{TiOSO}_4 \cdot \text{H}_2\text{O}$, **B** shows two views of a $\{\text{Ti}_{18}\}$ cluster; and **C** shows the unit cell of anatase. Turquoise polyhedra are Ti-centered, red spheres are oxo or water ligands, yellow spheres are sulfur in sulfate anions, and white spheres are hydrogen, of water molecules (in $\text{TiOSO}_4 \cdot \text{H}_2\text{O}$ only).

TiOSO_4 (for brevity, will name without hydration henceforth) dissolves in water after several hours of vigorous stirring. Somewhat non-intuitive, solubility increases with concentration. Solutions must have a concentration of 0.2 M or greater, otherwise hydrolysis reactions overcome the dissolution process. This is because the self-buffering behavior of the Ti^{IV} -centers (bound water deprotonates) yields acidic solutions, which retains solubility, and acidity scales with concentration. The pH for solutions of 0.25 - 1.0 M TiOSO_4 is summarized in **Table 4.1**. SAXS curves of these solutions (**Figure 4.2**) scaled

to match in the flat plateau region ($q < 0.1 \text{ \AA}^{-1}$) emphasizes the difference in the Guinier region ($q = 0.1 - 0.5 \text{ \AA}^{-1}$), demonstrating that cluster size becomes slightly smaller with increasing concentration, evidenced by the shift in the Guinier region to higher q -value. The flat plateau at lower q -values indicates that solutions contain approximately spherical, monodisperse particles with no evidence of aggregation (would exhibit a negative slope) or ordering (would exhibit a positive slope) in solution. The simulated scattering curve for $\{\text{Ti}_{18}\}$ matches remarkably well with the experimental scattering curves, up to $q = 0.6 \text{ \AA}^{-1}$. The deviation from this match, above $q > 0.6 \text{ \AA}^{-1}$ increases with higher concentration and could be due to the presence of small species such as monomers, or some beam attenuation with increasing dissolved species. Additionally, Ti with 22 electrons scatters only moderately better than the S of the sulfate (16 electrons); wherein the sulfate, if not bonded to the cluster, contributes to the background scattering in the high- q region of the curve. Nonetheless, the SAXS data suggests dissolved TiOSO_4 could be predominantly $\{\text{Ti}_{18}\}$.

Table 4.1 Summary of SAXS analysis of TiOSO_4 solutions

Sample	pH	R_g (\AA) (Guinier-fit)
[Ti]=0.25M	1.40	5.8
[Ti]=0.50M	1.05	5.4
[Ti]=1.0M	0.77	4.9
[Ti]=0.50M, 1M HNO_3	< 0.5	4.1 (ref ¹³³)
$\{\text{Ti}_{18}\}$ (simulated)	N/A	5.3
Ti(Ti) ₅ -pentagon (simulated)	N/A	4.1
$\{\text{Ti}_4\}$ with sulfate / without sulfate (simulated)	N/A	4.3 / 3.5 (ref ¹²⁹)
$\{\text{Ti}_6\}$ (simulated)	N/A	4.2 (ref ¹³⁷)
$\{\text{Ti}_8\}$ (simulated)	N/A	4.8 (ref ¹³²)

Mathematical analysis of the scattering curves provides more quantitative evidence that dissolved TiOSO_4 spontaneously self-assembles into $\{\text{Ti}_{18}\}$. The radius of gyration (R_g ; the shape independent, root mean weighted average of scattering vectors through the scattering particle) for the three solutions are summarized in **Table 4.1**, along with the R_g from simulated $\{\text{Ti}_{18}\}$ ^{15,16}. The R_g for simulated $\{\text{Ti}_{18}\}$ matches precisely that of 0.5 M TiOSO_4 , while the 0.25 M solution has slightly larger average cluster size, and the 1.0 M solution has smaller average cluster size. We also compare the pair distance distribution function (PDDF; probability histogram of scattering vectors through the cluster) of the 0.5

M TiOSO₄ solution to that from simulated {Ti₁₈}, and these also exhibit a good match (Figure 4.2). The maximum linear extent of the simulated and experimental PDDF, where the probability of scattering intensity goes to zero, is 13.8 Å. This is consistent with various measured distances across the cluster which range from ~12-16 Å; depending on the direction through the cylindrical cluster.

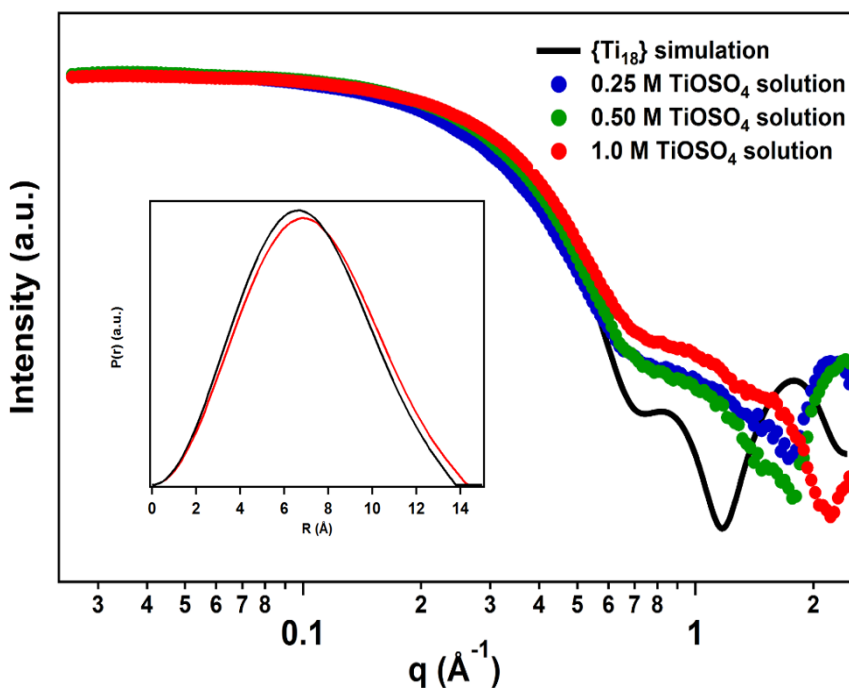


Figure 4.2 SAXS curves of freshly dissolved TiOSO₄ solutions (the curves are scaled to compare the Guinier region). The simulated curve for {Ti₁₈}-cluster is presented for comparison. Inset: pair distance distribution function (PDDF) analysis of TiOSO₄ solution (0.5 M, red) and simulated {Ti₁₈}-cluster (black).

We suggest the slightly larger R_g for the 0.25 molar solution indicates some hydrolysis reactions linking clusters are initiated. In contrast, {Ti₁₈} in the 1.0 M solution may be ‘losing’ layers. An organically ligated cluster featuring a {Ti₁₂} unit (minus one layer) has very recently been isolated¹³⁸. Dissolving TiOSO₄ in acid instead of neat water leads to a significant decrease in the size of scattering species. Prior we observed a 4.1 Å R_g in 0.5M TiOSO₄ in 1M HNO₃ solution¹³³, corresponding precisely with that of the simulated single pentamer unit. We assume increasing acid concentration may hinder stacking of the Ti(Ti)₅-pentamers or even formation of the pentamer. On the other hand, we cannot rule out formation of other, water-soluble small sulfate-decorated TOCs with similar size in

that acidic media, for instance, the sulfate-decorated $\{\text{Ti}_4\}$ -cluster¹²⁹ (**Table 4.1**). The I₀-intensity of the non-scaled scattering curves is not linearly-correlated with concentrations, indicating the cluster size is decreasing with increasing concentration (**Figure B 1**).

4.4.2. TiOSO_4 solution structure by EXAFS

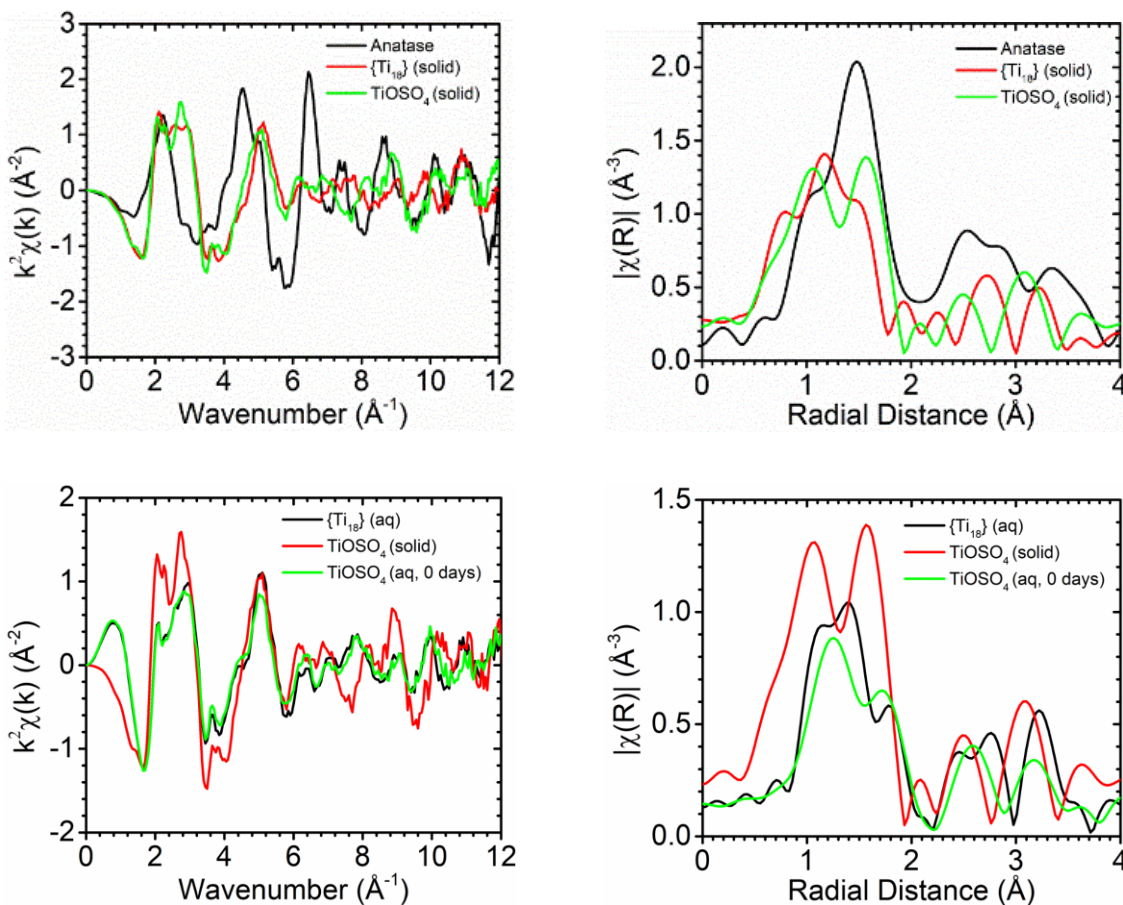


Figure 4.3 Ti EXAFS k-space (left) and Fourier-transformed R-space (right) of TiO_2 anatase, solid and dissolved $\{\text{Ti}_{18}\}$ and $\text{TiOSO}_4 \cdot \text{H}_2\text{O}$.

Ti K-edge EXAFS^{139–145} provided atomic-level information about both solutions and solids for this study. The k-space and R-space data of Ti solids (TiO_2 anatase, crystallized and dissolved $\{\text{Ti}_{18}\}$, and $\text{TiOSO}_4 \cdot \text{H}_2\text{O}$, **Figure 4.3**), benchmarks atomic-level structural differences between the three materials. Model-based fitting of the Ti K-edge data out to 4 Å in TiOSO_4 and $\{\text{Ti}_{18}\}$ were well-reproduced (**Table B 1**) by using scattering paths from TiOSO_4 and $\{\text{Ti}_{18}\}$ crystal structure models (see also **Figure B 3-6** for relevant bond distances).

In contrast, the k and R-space EXAFS spectra of aqueous TiOSO_4 differs from the solid TiOSO_4 , but looks similar to crystallized and redissolved $\{\text{Ti}_{18}\}$ (**Figure 4.3**). Quantitative analysis shows that the first shell ($R < 2 \text{ \AA}$) Ti-O coordination numbers (CNs) for TiOSO_4 solution (3.8), and $\{\text{Ti}_{18}\}$ solution (3.6) are both considerably less than that of the solids (both defined as 6.00, see **Table B 1**), and less than what we expect for octahedral and pentagonal bipyramidal Ti. The decrease of total coordination number from the EXAFS model in the dissolved Ti-species is likely due to ligand lability of the dissolved species. On the other hand, the k-space EXAFS spectrum of redissolved, crystallized $\{\text{Ti}_{18}\}$ (discussed below) is nearly identical to that of dissolved TiOSO_4 , strongly suggesting dissolved TiOSO_4 assembles into $\{\text{Ti}_{18}\}$ clusters, in agreement with the SAXS data.

There are some differences between the R-space of dissolved TiOSO_4 and redissolved $\{\text{Ti}_{18}\}$. As discussed below, the only way $\{\text{Ti}_{18}\}$ can be crystallized is with tetrabutylammonium (TBA) and chloride counterions and co-ions. The peak(s) in the R-space between 3-4 \AA correspond to Ti-Ti and Ti-S pairs within the sulfate-capped $\{\text{Ti}_{18}\}$ (see **Figure B 4-6**). This peak is more pronounced in the crystallized and dissolved $\{\text{Ti}_{18}\}$, likely due to stabilization of decorating sulfate ligands by the TBA and Cl^- ions in solution. The number of sulfates with which $\{\text{Ti}_{18}\}$ has been crystallized is variable (discussed below), suggesting this ligand is labile in solution. Similarly, there are more pronounced peaks for $\{\text{Ti}_{18}\}$, corresponding with Ti-O pairs (1-2 \AA) and around $R=2.8 \text{ \AA}$, corresponding with distal Ti-O distances in the cluster and/or substitution of Cl^- for H_2O or sulfate.

4.4.3. Single crystal structural description

We attempted to isolate the dominant cluster form from TiOSO_4 solutions for absolute identification. Adding different counter ions and crystallization agents (e.g. alkali ions, tetraalkylammonium ions or γ -cyclodextrin) and employing different crystallization methods (solvent evaporation, solvent diffusion) were not successful. The prior-reported and crystallized $\{\text{Ti}_{18}\}$ was obtained from a mixture of TiCl_4 and sulfuric acid (crystallized with tetrabutylammonium, TBA^+)¹²⁸. To include all the same ions, we added TBA-Cl to a solution of TiOSO_4 (1.0 M; see experimental) and obtained crystals by slow solvent evaporation. The average formulation in the final refined structure is $[\text{Ti}_{18}\text{O}_{27}(\text{H}_2\text{O})_{25}(\text{SO}_4)_{9.5}](\text{Cl})_5(\text{TBA})_6 \cdot 13.5\text{H}_2\text{O}$ (**Figure 4.4**). Due to twinning and

significant disorder in every crystal we analysed, the refined X-ray data is of sub-optimal quality. However, it served two important functions: 1) the $\{\text{Ti}_{18}\}$ core is clearly observed, despite the disorder of solvent, counterions and sulfate; and 2) *because* of the disordered and presumably labile sulfate observed in the structure, we can explain the very high solubility of this cluster in water, despite its relatively low ionic charge. These points are discussed below.

The X-ray structure provides strong evidence that TiOSO_4 self-assembles into $\{\text{Ti}_{18}\}$ immediately upon dissolution as observed by SAXS. Moreover, isolation of $\{\text{Ti}_{18}\}$ from solution also enabled the comparative EXAFS studies described above. The average formulation of the cluster core including the sulfates is very close to neutral, $[\text{Ti}_{18}\text{O}_{27}(\text{SO}_4)_{9.5}]^{-1}$. In solution and the crystallized solid, there is likely a labile mixture of neutral clusters plus clusters with a small negative charge and clusters with a small positive charge. This both enables the high solubility and the lack of observed structure factor (ordering in solution) in SAXS data, since there should be minimal repulsion between clusters with a charge range of -1 to +1. Details of the sulfate-chloride disorders are described and illustrated in the Appendix B. Five different compositional variations of $\{\text{Ti}_{18}\}$ were reported prior, based on number and location of decorating sulfate or selenate anions. These included six, eight and nine sulfate/selenate anions, with respective charge of 4+, 2+, and 0. This prior and currently observed variation of sulfate ligation strengthens the argument that a mixture of polyanions and polycations coexist in dissolved TiOSO_4 .

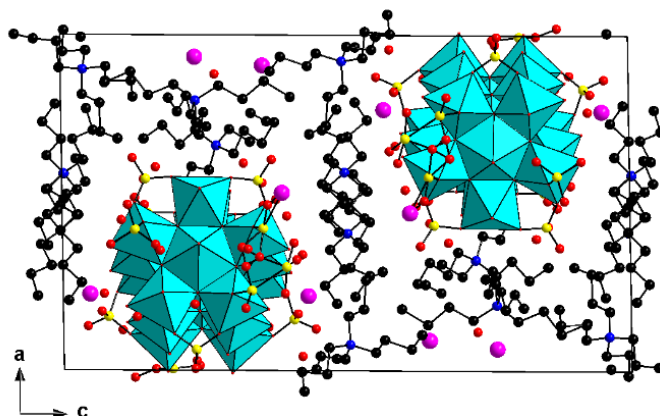


Figure 4.4 Unit cell view of crystallized $\{\text{Ti}_{18}\}$, illustrating close association of Cl^- with the cluster. Ti-polyhedra are turquoise, sulfates are yellow and red ball-and-stick, Cl^- are pink spheres, TBA are black (C) and blue (N) spheres.

4.4.4. Aging of TiOSO₄ solutions

Per the industrial sulfate process, titanium sulfate solutions precipitate anatase TiO₂ upon dilution or heating¹⁴⁶. In this study, aging TiOSO₄ solutions at ambient conditions also produced anatase-TiO₂, but the process is significantly slower. For 0.25M TiOSO₄, precipitation appears after 6 days, while the solid product is apparent at around 45 days of aging the 1.0 M solution. Higher concentration of [Ti⁴⁺] implies higher [H⁺] concentration (**Table 4.1**), suppressing hydrolysis and condensation reactions. Contrarily, decreased Ti-concentration accelerates TiO₂ formation. We prepared several 0.25 M TiOSO₄ solutions and collected the solid product in the 6-80 day time-period to determine a yield approaching 50% in approximately 3 months (**Figure B 10**). We could collect enough solid product for further characterization after 21 days. Despite the poor crystallinity of the obtained precipitate shown by the X-ray total scattering curve, PDF analysis of that curve confirmed formation of TiO₂ anatase phase (**Figure 4.5**). Additionally, the observed particle size is 1.96 nm using a spherical nanoparticle model for refinement by PDFGui¹⁹ (**Table B 3**), in good agreement with TEM analysis (**Figure 4.5A**). EDX indicated the formation of sulfate-decorated anatase nanoparticles with 1:4 S:Ti ratio (**Figure B 11**).

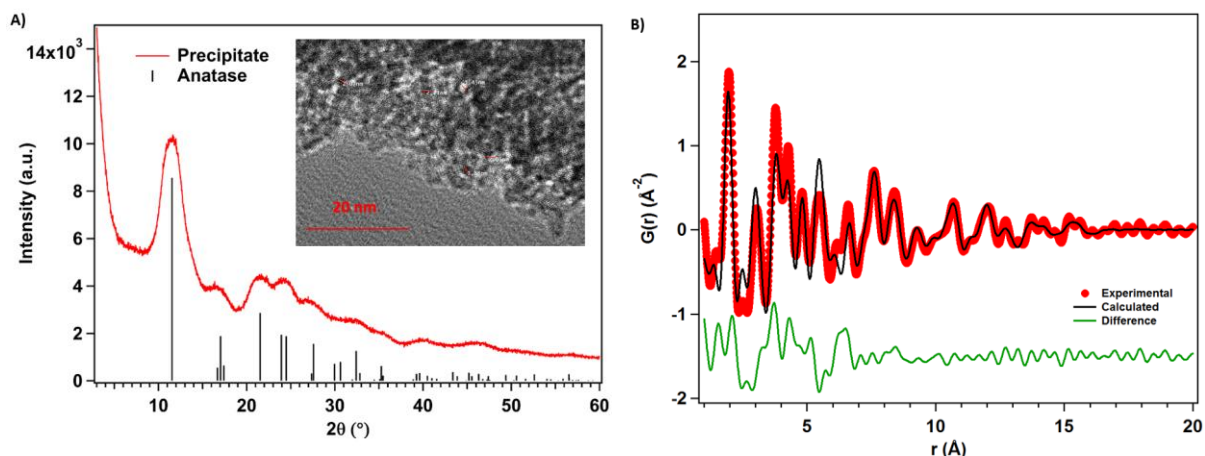


Figure 4.5 A: X-ray total scattering pattern of the precipitated solid from 0.25M TiOSO₄ solution after 21 days. The broad peaks (indicating low crystallinity) are in good agreement with the calculated peak positions of TiO₂ anatase phase (black). (Note: Mo K α radiation was used, where $\lambda=0.71$ Å.) Inset: TEM image of precipitate. Red lines correspond with particle size of 2.07, 2.21, 1.45, 1.88, 2.05 and 1.45 nm. **B:** Experimental PDF analysis of the X-ray total scattering curve. Atom-pair correlations are in good agreement with anatase phase with approximately 2.0 nm particle size.

In order to monitor structural changes in the solid phase of the formed Ti-oxide, we triggered precipitate formation of TiOSO_4 solution. 20 mL, 1 M TiOSO_4 solution was added to 1 L DI water. Precipitate forms, settles and then was collected to perform X-ray total scattering measurements during 3.5 months' time-period. Samples were not treated (no drying nor heating) prior measurements to eliminate any structural changes in that process. The PDF analysis of the collected patterns are in **Figure 4.6**. We observe formation of amorphous phase at the beginning, but new arising peaks at higher distances indicate the formation and growth of crystalline core during aging. Those peaks are distinct after 15 days aging and are in good agreement with anatase phase of TiO_2 (similarly to the previously shown naturally aged sample). We also determined the size of the crystalline core and we found linear correlation with the aging time as shown in **Figure 4.7**. The atom-pair correlations at short-range order do not change significantly, and we cannot observe sharp changes for those peak positions which may indicate geometry or coordination change during the transformation. Therefore, we performed characterization on the solution during aging.

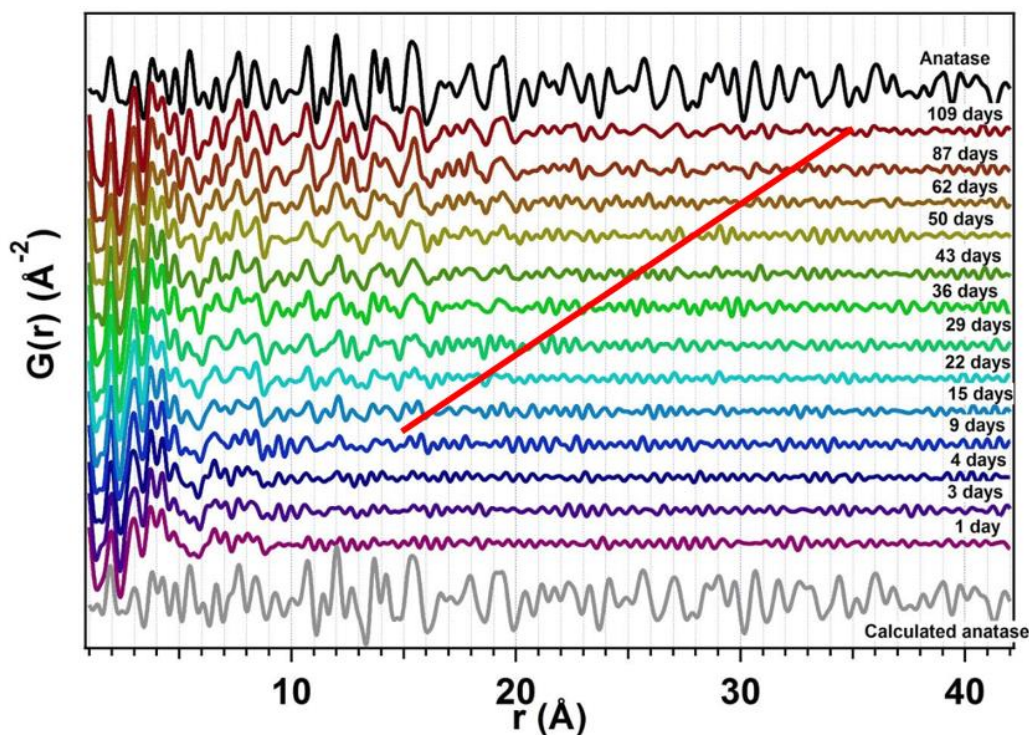


Figure 4.6 PDFs of the wet slurry at different time. The red line is indicating the approximate size of the crystalline core of titanium-oxide nanoparticles. The red line indicates the estimated size of the crystalline core.

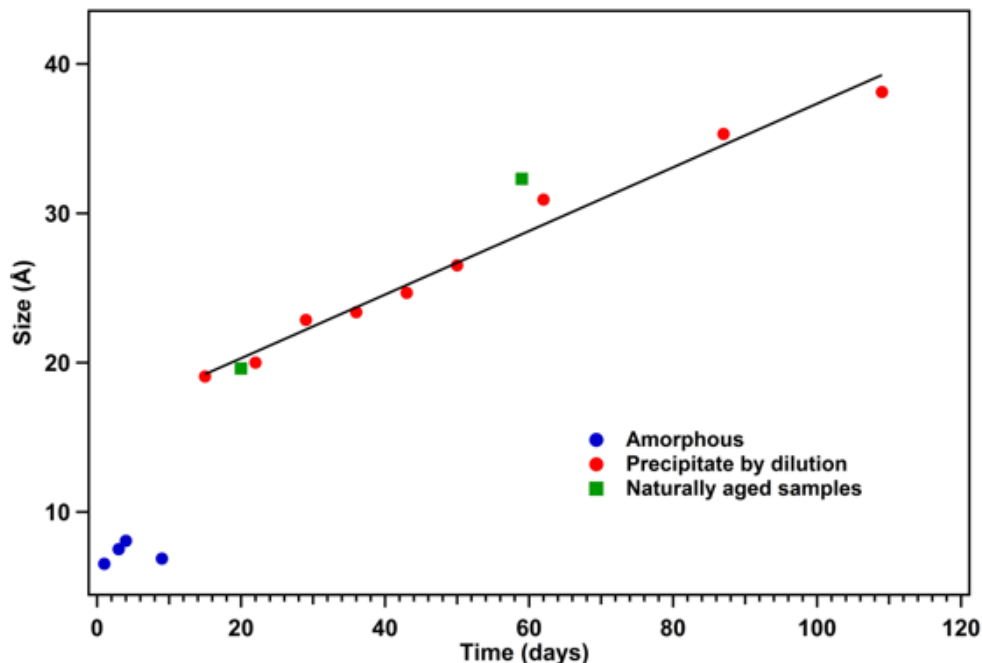


Figure 4.7 The linear correlation between the size of crystalline core and aging time. Amorphous materials are distinguished. Naturally aged samples (with no dilution) are also shown on the curve.

SAXS shows that $\{Ti_{18}\}$ evolves into larger soluble species with $TiOSO_4$ solution aging (**Figure 4.8 & Figure B 12**). Consistent with the time delay preceding TiO_2 precipitation, formation of this species is slower in higher concentration $TiOSO_4$ solutions. Intriguingly, the new species also has a distinct size, suggesting it could also be a TOC molecular cluster. We used a two-phase model to fit the data, and the four parameters (radius and % population) are summarized in **Table B 4**. The second population is roughly twice the size of $\{Ti_{18}\}$ and similar to the TiO_2 nanoparticles that eventually precipitate (~ 2 nm). This larger species appears prior to precipitation and its size does not change over time, suggesting it is likewise a molecular titanium-oxo cluster rather than TiO_2 nanoparticles. Additionally, we filtered the solutions immediately before measuring the SAXS data to ensure no colloidal particles are present in the solution. The maximum population of this larger species is less than 10%, according to the SAXS analysis.

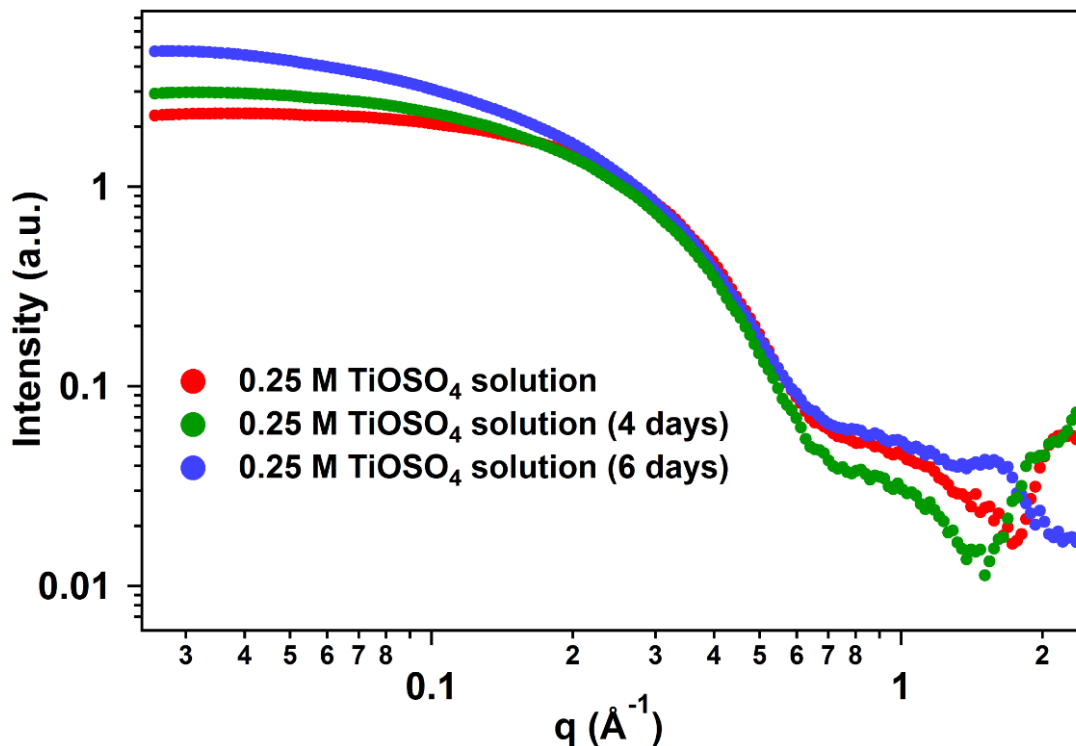


Figure 4.8 SAXS curves of aged samples of 0.25M TiOSO₄ solutions.

While SAXS shows increasing size of TOCs with solution aging, EXAFS reveals this occurs without significant atomic-level structural change within the TOCs (**Figure 4.9**). These results suggest the second hypothetical TOC has similar short-range order as {Ti₁₈}. Zhang et al. recently published two intriguing TOC clusters (organically ligated) that provides a model for joining {Ti₁₈} clusters without significantly altering the short-range order¹³⁸. These clusters feature double stacks of the Ti(Ti)₅ unit that are linked side-by-side; with or without a 90° rotation. Zhang and coworkers also compared the orientation of Ti in these side-by-side stacks to the arrangement of Ti in brookite and in anatase TiO₂. This recent study taken together with our current results may present a consistent model for the conversion of Ti(Ti)₅, {Ti₁₈}, and related clusters to TiO₂.

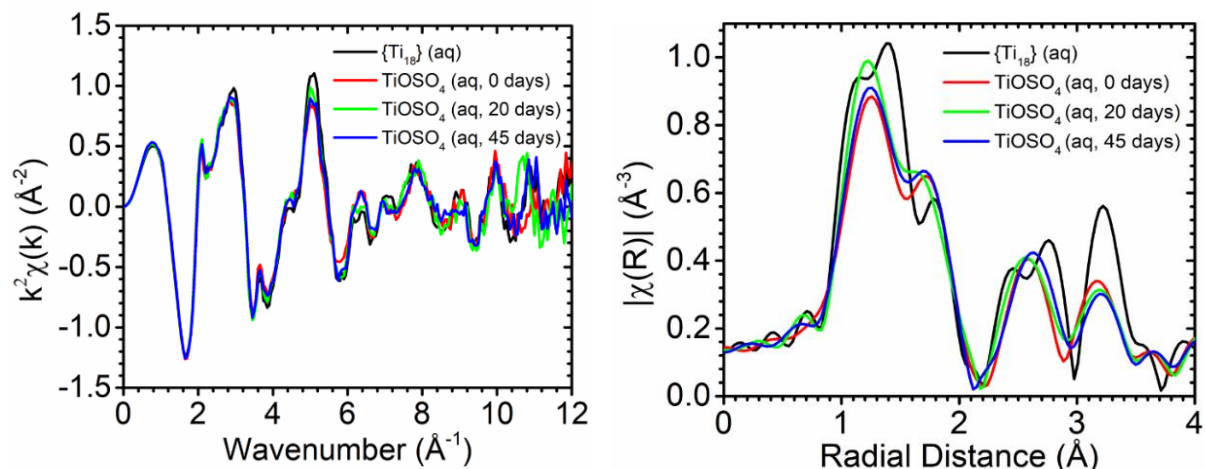


Figure 4.9 Ti K-edge K-space (left) and R-space (right) EXAFS data comparing dissolved $\{Ti_{18}\}$ to dissolved $TiOSO_4$ (fresh and aged; 1M). Differences observed in the R-space data primarily reflect the influences of poor statistics at higher k values.

4.5 Conclusions

Here we demonstrate that high solubility of Ti in the sulfate process may be controlled by its speciation as discrete $\{Ti_{18}\}$ polycations that by definition, eliminate heteroatoms such as Fe. Moreover, the $\{Ti_{18}\}$ clusters persist in solution state without structural change, even in equilibrium with precipitating TiO_2 . This latter point is particularly remarkable because the atomic and polyhedral arrangements of $\{Ti_{18}\}$ and TiO_2 are profoundly different. This leads to questions about the relevance and role of prenucleation clusters in other simple metal oxide systems such as iron oxides. The unusual pentagonal bipyramidal Ti and pentagonal $Ti(Ti)_5$ unit that is the key foundation and scaffold of $\{Ti_{18}\}$ is becoming more commonly observed since its discovery in 2016¹²⁸, even in sulfate-free and non-aqueous conditions¹³⁸. The pentagonal unit, now recognized and even common in multiple early d^0 transition metals (also Mo, W and Nb) inspires understanding of its stability, formation mechanism, and design of new functional metal oxides built of the pentagonal unit. Other ongoing studies include investigating formation of $\{Ti_{18}\}$ in the presence of Fe; relevant to the industrial sulfate process. Finally, we endeavour to understand the atomic level process of conversion of dissolved $\{Ti_{18}\}$ to precipitated TiO_2 from both a computational and experimental perspective.

4.6 Acknowledgements

This study was supported by the U.S. Department of Energy, Office of Basic Energy Sciences, Division of Material Sciences and Engineering, under award DE SC0010802.

5. Counter cation controlled structural diversity of Zr/Hf oxalates and Zr-peroxo oxalates

Karoly Kozma, Lev N. Zakharov, Mehran Amiri, Morgan R. Olsen and May Nyman

In preparation (2019)

5.1 Abstract

Zirconium and hafnium are the two most similar elements on the periodic table, challenging necessary separations to access high purity forms for nuclear and microelectronics applications. In this study, we differentiate their chemistry based on their reactivity with the combination of the competitive H₂O₂ and oxalate ligands, and different counterions to the anionic complexes. With Hf, we prepared a polymeric chain $\{(N(CH_3)_4)[Hf_2(OH)_2(C_2O_4)_5]\}_n \cdot 12H_2O$ (**1**), dimeric $(Na_6[Hf_2(OH)_2(C_2O_4)_6] \cdot 17H_2O)$ (**2**) and $(Li_2K_4[Hf_2(OH)_2(C_2O_4)_6] \cdot 8H_2O)$ (**3**), and mononuclear $(K_4Hf(C_2O_4)_4 \cdot 5.1H_2O)$ (**4**), $(Rb_4Hf(C_2O_4)_4 \cdot 5H_2O)$ (**5**) and $(Cs_4Hf(C_2O_4)_4 \cdot 5H_2O)$ (**6**). In analogous reaction conditions, Zr yielded $(N(CH_3)_4)_6[Zr_6(O_2)_6(OH)_6(C_2O_4)_6] \cdot 7.58H_2O$ (**7**) ($\{Zr_6\}$), $Li_{12}[Zr_8(O_2)_{12}(OH)_4(C_2O_4)_8] \cdot 30H_2O$ (**8**) ($\{Zr_8\}$), $Na_4Zr(C_2O_4)_4 \cdot 1.5H_2O$ (**9**), $K_{18}[Zr_{12}(O_2)_{18}(OH)_6(C_2O_4)_{12}] \cdot 30H_2O$ (**10**) ($\{Zr_{12}\}$), $Rb_{24}[Zr_{16}(O_2)_{24}(OH)_8(C_2O_4)_{16}] \cdot nH_2O$ (**11**) ($\{Zr_{16}\}$), $(Rb_4Zr(C_2O_4)_4 \cdot 5.25H_2O)$ (**12**) and $Cs_4Zr(C_2O_4)_4 \cdot 5H_2O$ (**13**). While we observe complexation of Zr with peroxide, Hf only complexes oxalate. Different alkali counter cations also yielded different nuclearity species; particularly the Zr-ring complexes: $\{Zr_6\}$ with TMA, $\{Zr_8\}$ with Li, $\{Zr_{12}\}$ with K, and $\{Zr_{16}\}$ with Rb. Additionally, while most Zr coordination complexes have eight-fold geometries, the multinuclear alkali-Zr compounds are 9-coordinate and face-sharing, a unique Zr coordination environment. We performed solid-state (powder X-ray diffraction, infrared-spectroscopy) and solution state (small-angle X-ray scattering, X-ray total scattering, electron-spray ionization mass spectroscopy) characterizations in addition to single-crystal X-ray diffraction to understand fundamental differences between aqueous Zr and Hf chemistry and to explore the effect of the counter cations.

5.2 Introduction

Separating zirconium and hafnium is notoriously difficult, but absolutely necessary for multiple high precision applications. Zr is used in ceramics¹⁴⁷, precision castings, nuclear technologies^{148,149} and biomedical applications.^{150,151} Applications of Hf that demand purity include superalloys, microprocessors^{121,152} and the nuclear industry¹⁵³. Despite their similar chemical behavior, they possess considerably different nuclear properties, exploited in the nuclear industry. Zr is almost neutron transparent (0.18 barns), which makes it an ideal

cladding material in nuclear reactors. In contrast, Hf has huge thermal neutron capture cross-section (105 barns), which makes it a good material in control rods.¹⁵³ Thus one becomes a poison for the other in these opposed applications. The difficulty of the separation originates from their very similar chemical properties:^{153–155} a nearly identical ionic radius (0.84 Å for Zr⁴⁺ and 0.83 Å for Hf⁴⁺)¹⁵⁶ and invariable charge (+4 oxidation state). Most of their aqueous solution chemistry is limited to very acidic conditions, otherwise they readily hydrolyze and precipitate in water.

Zr and Hf are also used to probe chemical behavior of fission products in the reprocessing of spent nuclear fuel (SNF). Their similarities to tetravalent actinides make them good surrogates to test and develop separation chemistries for reprocessing SNF.¹⁵⁷ In addition, Zr is one of the fission products in SNF, with concentrations as high as 80 mM.^{158,159} Most separation methods include extraction and/or complexation. One of the most studied complexing agent is oxalic acid ((COOH)₂) due to its easy accessibility and propensity to make chelate compounds, used for Pu separation in nuclear fuel reprocessing plants.^{160,161} Complexation studies of Zr oxalate has yielded several crystal structures including the mononuclear tetraoxalate^{162–165}, a dimer¹⁶⁶ and a polymeric compound¹⁶⁷ from aqueous acid. Hf oxalate solutions and solids are less studied. One mononuclear tetracomplex has been reported,^{164,168} in addition to solution studies.¹⁶⁹ In all Zr and Hf oxalate compounds the metals form five-member chelate rings with the bidentate oxalate ligand, and eightfold coordination of the metals. Without oxalate, acidic aqueous Zr and Hf form a tetrameric species [M₄(OH)₈(H₂O)₁₂]⁸⁺ both in solid and solution state.^{123,124} These oligomeric metal-oxo species are important to understanding bulk solid phase formation from solution. With sulfate, a cationic 11-mer, 18-mer and 19-mer Zr and Hf metal-oxo clusters have been obtained.^{120–122} Additionally with sulfate, negatively charged polyanions (hexamers¹⁷⁰ and one Hf-nonamer¹²⁵) have also been reported.

It is also well-known that the radioactive environment of SNF in aqueous cooling ponds generates H₂O₂,¹⁷¹ which is also a good complexing agent for non-redox-active metals such as Zr/Hf; as observed in peroxide-bridged Hf₆ and Zr₂₅ ring clusters, and Zr-tetrahedron.^{8,172,173} Although the stability of Zr with peroxide ligands has been shown very recently by isolation of these structures¹⁷⁴, few zirconium peroxo salts and complexes have been reported,^{175–177} and even fewer for Hf.¹⁷⁸ Combining peroxide and oxalate ligands with

aqueous acidic Zr and Hf may provide tunability of solubility and precipitation, important for high precision and cost-effective separations. Dengel *et al.* investigated peroxy oxalate compounds of zirconium and hafnium.¹⁷⁹ However, this sole study was limited to vibrational spectroscopy with no crystallographic information. Here we have targeted mixed peroxy-oxalate compounds of zirconium and hafnium. This study can help to reveal the solution speciation with competing ligands, benefiting reprocessing SNF or Zr-Hf separations for numerous applications.

In this study, we describe synthesis and structural descriptions of Zr peroxy oxalate complexes (six structures) and Hf oxalate species (six structures) from mildly acidic aqueous solutions, and the distinct influence of the counter cation. Single-crystal X-ray diffraction reveals that while Hf forms monomers, dimers and polymers with oxalate; Zr form metal-peroxy-oxalate ring clusters, in addition to the prior-described monomeric tetraoxalato complexes. Interestingly, Hf-peroxy complexes are not obtained from mild acid. In addition to single-crystal X-ray diffraction characterization, we characterized solid-state compounds and solutions with energy-dispersive X-ray spectroscopy from scanning electron microscopy (EDX-SEM), small-angle X-ray scattering (SAXS), Fourier-transform infrared spectroscopy (FT-IR), electrospray ionization mass spectroscopy (ESI-MS) and pair distribution function (PDF) analysis of X-ray total scattering. We observed several roles of the alkali counter cations. The nuclearity of the isolated molecules changes with the counterion. In the order of TMA^+ - Li^+ - Na^+ - K^+ - Rb^+ - Cs^+ , the Hf oxalate nuclearity decreases from polymeric (TMA^+), dimeric (Li^+ and Na^+), to monomeric (K^+ / Rb^+ / Cs^+). Zr-peroxy-oxalate clusters display the opposite trend: TMA, Li, K and Rb respectively isolate $\{\text{Zr}_6\}$, $\{\text{Zr}_8\}$, $\{\text{Zr}_{12}\}$, and $\{\text{Zr}_{16}\}$ -peroxy-oxalate ring clusters with increasing nuclearity. The face-sharing feature of these clusters is also retained in solution. The wealth of structures and solution-phase data presented here provides new foundational knowledge for developing Zr/Hf separation processes and understanding of the differences between Zr and Hf chemistry, and the underlying relativistic effect that renders these elements so similar.

5.3 Experimental

5.3.1. Syntheses

All products were obtained from aqueous solutions. Solutions were prepared mixing $\text{ZrOCl}_2/\text{HfOCl}_2$, oxalic acid and hydrogen peroxide in water. Metal concentration in the reaction solutions was ~55 mM for both Zr and Hf. Metal-to-oxalic acid ratio was 1 - 1.5. We used less than the stoichiometric ratio of oxalic acid (1:4) to suppress its strong chelating effect that leads to precipitation. Hydrogen peroxide (30% H_2O_2 solution) was added with a metal-to-peroxide ratio of 1 - 3. Next, we increased the pH to ~4.8-4.9 by adding hydroxide solutions (tetramethylammonium hydroxide (TMAOH), LiOH, NaOH, KOH, RbOH or CsOH), to investigate the effect of the applied counter ions. At pH=4.8-4.9, solutions became clear (or a very thin suspension). We filtered the solutions prior the crystallization experiments.

We utilized two crystallization methods: slow solvent evaporation (over several days to weeks duration), and solvent diffusion with acetone at 4°C in refrigerator (hours to a few days time span). While acetone diffusion was efficient for most of the alkali counter ion solutions, TMA^+ counter ions yielded very few single-crystals in addition to gels. Therefore, characterization of TMA compounds is limited only to single-crystal data analysis. It is also worth noting that crystallization of **(3)** and **(4)** occurred from the same reaction conditions, but from different batches. To clarify the effect of K^+ and Li^+ , we prepared solid product using only KOH and only LiOH for further characterization. However, single-crystal formation in these solutions was not successful.

Some of the selected reaction conditions during sample preparations and the obtained products are summarized in **Table 5.1**. The detailed experimental procedure of each compound is described in Appendix C.

Table 5.1 Selected synthetic parameters for preparation of described products. Acetone solvent diffusion was carried out at 4°C. (TMA⁺ = tetramethylammonium ion, [N(CH₃)₄]⁺)

Metal and counter ions	Crystallization method, duration	Formula obtained by SC-XRD	Notation
Hf ⁴⁺ , TMA ⁺	Evaporation, 2 weeks	{(TMA) ₄ [Hf ₂ (OH) ₂ (C ₂ O ₄) ₅]} _n · 12H ₂ O	(1)
Hf ⁴⁺ , Li ⁺	Acetone diffusion, 1 day	No single-crystals	Li-Hf oxalate
Hf ⁴⁺ , Na ⁺	Acetone diffusion, 5 days	Na ₆ [Hf ₂ (OH) ₂ (C ₂ O ₄) ₆] · 17H ₂ O	Na-Hf oxalate (2)
Hf ⁴⁺ , Li ⁺ and K ⁺	Acetone diffusion, 1 day	Li ₂ K ₄ [Hf ₂ (OH) ₂ (C ₂ O ₄) ₆] · 8H ₂ O and K ₄ Hf(C ₂ O ₄) ₄ · 5.1H ₂ O	(3) and (4)
Hf ⁴⁺ , K ⁺	Acetone diffusion, 1 day	No single-crystals	K-Hf oxalate
Hf ⁴⁺ , Rb ⁺	Acetone diffusion, 2-3 days	Rb ₄ Hf(C ₂ O ₄) ₄ · 5H ₂ O	Rb-Hf oxalate: (5)
Hf ⁴⁺ , Cs ⁺	Acetone diffusion, 1-2 days	Cs ₄ Hf(C ₂ O ₄) ₄ · 5H ₂ O	Cs-Hf oxalate: (6)
Zr ⁴⁺ , TMA ⁺	Evaporation, 2 weeks	(TMA) ₆ [Zr ₆ (O ₂) ₆ (OH) ₆ (C ₂ O ₄) ₆] · 7.58H ₂ O	(7) or {Zr ₆ }
Zr ⁴⁺ , Li ⁺	Acetone diffusion, 6 days	Li ₁₂ [Zr ₈ (O ₂) ₁₂ (OH) ₄ (C ₂ O ₄) ₈] · 30H ₂ O	Li-Zr oxalate (8) or {Zr ₈ }
Zr ⁴⁺ , Na ⁺	Acetone diffusion, 4 days	Na ₄ Zr(C ₂ O ₄) ₄ · 1.5H ₂ O	Na-Zr oxalate (9)
Zr ⁴⁺ , K ⁺	Acetone diffusion, 1 day	K ₁₈ [Zr ₁₂ (O ₂) ₁₈ (OH) ₆ (C ₂ O ₄) ₁₂] · 30H ₂ O	K-Zr oxalate (10) and {Zr ₁₂ }
Zr ⁴⁺ , Rb ⁺	Evaporation or acetone diffusion, 5 days	Rb ₂₄ [Zr ₁₆ (O ₂) ₂₄ (OH) ₈ (C ₂ O ₄) ₁₆] · 65H ₂ O and Rb ₄ Zr(C ₂ O ₄) ₄ · 5.25H ₂ O	Rb-Zr oxalate (11) or {Zr ₁₆ } and (12)
Zr ⁴⁺ , Cs ⁺	Acetone diffusion, 1 day	Cs ₄ Zr(C ₂ O ₄) ₄ · 5H ₂ O	Cs-Zr oxalate (13)

5.3.2.Characterization methods

We collected single-crystal X-ray diffraction data (SC-XRD) from the samples summarized in **Table 5.1**. Due to the very low yield of TMA compounds, we were not able to carry out solid-state and solution characterization of the obtained product. In the cases of alkali salts, we collected the solid obtained from acetone diffusion for further characterization. We utilized solid-state characterization methods including powder X-ray diffraction (PXRD), energy dispersive X-ray spectroscopy from scanning electron microscopy (EDX-SEM) and Fourier-transform infrared (FT-IR) spectroscopy. Solution characterization of some selected samples included small-angle X-ray scattering (SAXS), pair distribution function analysis (PDF) of X-ray total scattering curves and electrospray ionization mass spectroscopy (ESI-MS). Detailed description of instrumentation and techniques are described in Appendix C.

5.4 Results and discussion

5.4.1.Structural description of Hf-oxalate compounds (compounds 1-6)

For all syntheses, addition of alkali or TMA hydroxide was necessary to enable solubility of the reaction solutions. Crystals of mono and multinuclear Hf-oxalato complexes were crystallized from peroxide-oxalate, ~pH-4.8 solutions. The anionic mono and dinuclear complexes grew with charge-balancing alkali cations via acetone solvent diffusion, while anionic Hf-oxalate chains form with TMA⁺ counter ions via solvent evaporation. In all compounds, Hf has an eight-fold coordination (**Figure 5.1**) with distorted antiprismatic geometry.

$\{(TMA)_4[Hf_2(OH)_2(C_2O_4)_5]\}_n \cdot nH_2O$ (**1**) contains polymeric chains of hafnium oxalate crystallized in a monoclinic cell. The chains consist of dihydroxide-bridged dimers that are bridged by oxalates. The Hf-(μ -OH) distances are 2.087(1) and 2.113(1) Å, and the Hf- $O_{oxalate}$ distances are 2.295(1) Å and 2.210(1) Å. Each Hf also binds two terminal oxalate ligands to complete the coordination sphere, these Hf- $O_{oxalate}$ distances are 2.154(1)-2.206(1) Å (**Table 5.2**). The Hf-Hf distance is 3.48 Å through (OH) bridges and 5.87 Å through the oxalate bridges. There is one prior-reported polymeric Zr; oxalate-bridged zig-zag chain¹⁶⁷.

Crystals of the isolated dihydroxide-bridged, dinuclear $A_6[\text{Hf}_2(\text{OH})_2(\text{C}_2\text{O}_4)_6]$ molecule was obtained with Na^+ ions (**2**) or the combination of Li^+ and K^+ ions (**3**) (**Table 5.2**). This dimer is the repeat unit of the infinite chains obtained with TMA (compound **1**). The Hf - (μ -OH) bond distances are between 2.095(8)-2.145(4) Å, the Hf-oxalate oxygen bond distances are 2.168(10)-2.245(6) Å, and the Hf-Hf distances are 3.51-3.54 Å. In prior-reported multinuclear Zr oxalate compounds, the bridging ligand is always an oxalate ion^{166,167}. We explain the presence of hydroxo bridges by the higher pH in the reaction solution (pH~4.8 instead of pH<2.0). Crystallization with only Li^+ counter ions was not successful, we obtained only amorphous precipitate. EDX analyses indicated the difference in the Hf:K ratio when using only K^+ or combination of Li^+ and K^+ ions (**Table C 5**). Those numbers suggest the monomer (**4**) is dominant in K^+ solution, while the dimer (**3**) is dominant from a solution containing Li/K^+ .

The monomeric $A_4[\text{Hf}(\text{C}_2\text{O}_4)_4] \cdot n\text{H}_2\text{O}$ hafnium tetraoxalato complexes ($A=\text{K}^+, \text{Rb}^+$ and Cs^+), (**4**), (**5**) and (**6**), were obtained using heavier alkali counter ions (**Table 5.1**). Hf-*Oxalate* bond distances are 2.153(1) - 2.219(16) Å, in a good agreement with a prior-reported Hf tetraoxalato complex (2.17-2.22 Å)¹⁶⁸, although shorter than in the mixed metal Cd-Hf oxalate compound (2.23-2.49 Å)¹⁶⁴. Some selected interatomic distances are listed in **Table 5.2** and **Table 5.3**. Crystallographic data is collected for mononuclear and multinuclear Hf oxalates in in **Table C 1** and **Table C 2**, respectively.

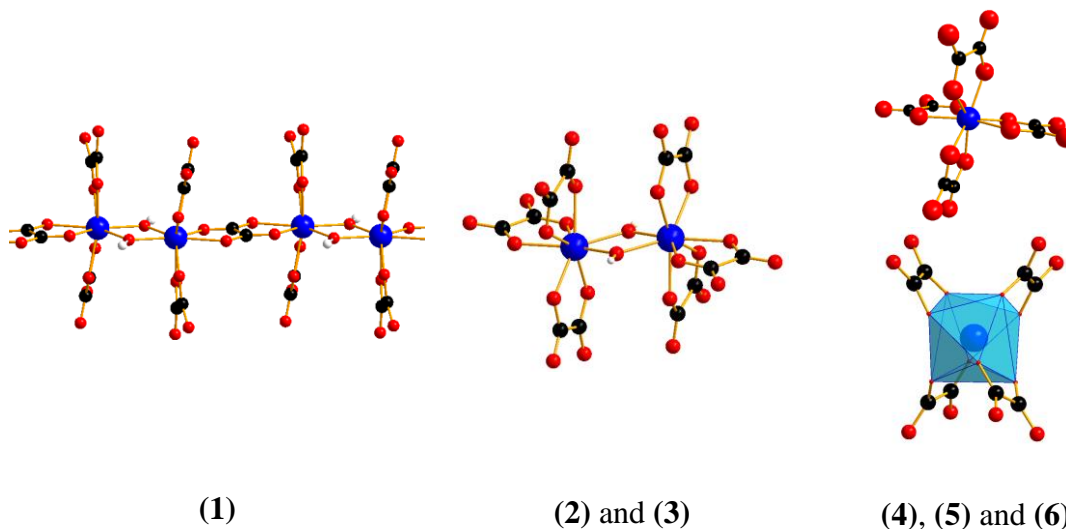


Figure 5.1 Ball-stick representation of the obtained hafnium oxalate compounds (**1**) (**infinite chains**), (**2**) and (**3**) (**dimer**) and (**4**) - (**6**) **monomer**. Color code: Hf-blue, O-red, C-black and H-white.

Table 5.2 Selected interatomic distances from the crystallographically independent hafnium centers in multinuclear (1), (2) and (3) Hf oxalates. Parenthesis indicates errors.

	(1) (TMA-Hf)	(2) (Hf1) (Na-Hf)	(2) (Hf2) (Na-Hf)	(3) (Li-K-Hf)
Hf-O (μ -OH) (Å)	2.0866(1)	2.0951(76),	2.1012(75)	2.1071(52)
Hf-O (μ -OH) (Å)	2.1132(1)	2.1139(75),	2.1281(72)	2.1449(44)
Hf-O (Å)	2.1535(1)	2.1676(102),	2.1889(80)	2.1726(52)
Hf-O (Å)	2.1642(1)	2.1738(80),	2.1927(83)	2.1851(47)
Hf-O (Å)	2.1982(1)	2.2043(95),	2.199(9)	2.1935(47)
Hf-O (Å)	2.2059(1)	2.2052(97),	2.2146(65)	2.2085(48)
Hf-O (Å)	2.2103(1) (μ -ox)	2.2229(58),	2.2232(79)	2.2141(59)
Hf-O (Å)	2.2951(1) (μ -ox)	2.2240(66),	2.2238(53)	2.2450(57)
Hf-O_(average) (Å)	2.178	2.176	2.184	2.184
Hf-Hf (Å)	3.4840(1)	3.5139(7)	3.5139(7)	3.5410(5)

Table 5.3 Selected interatomic distances around hafnium centers in (4), and (6) monomer Hf oxalates. Parenthesis indicates errors.

	(4) (Hf1) (K-Hf)	(4) (Hf2) (K-Hf)	(5) (Hf1) (Rb-Hf)	(5) (Hf2) (Rb-Hf)	(6) (Cs-Hf)
Hf-O (Å)	2.1553(84)	2.1554(84)	2.1758(93)	2.1534(84)	2.1795(184)
Hf-O (Å)	2.1571(92)	2.1603(84)	2.1767(90)	2.1619(83)	2.1795(184)
Hf-O (Å)	2.1606(82)	2.1618(81)	2.1770(101)	2.1672(90)	2.1799(184)
Hf-O (Å)	2.1614(73)	2.1759(81)	2.1806(93)	2.1759(81)	2.1799(184)
Hf-O (Å)	2.1753(56)	2.1800(84)	2.1882(87)	2.1834(104)	2.2185(156)
Hf-O (Å)	2.1825(84)	2.1865(83)	2.1891(99)	2.2063(103)	2.2185(156)
Hf-O (Å)	2.1931(83)	2.1957(83)	2.2009(84)	2.2088(84)	2.2194(156)
Hf-O (Å)	2.2104(83)	2.2079(84)	2.2085(86)	2.2268(95)	2.2194(156)
Hf-O_(average) (Å)	2.174	2.178	2.187	2.185	2.199

The lack of obtained Hf-peroxide ligands in these structures suggests that the bonding between Hf and peroxide is unlikely or unstable under the applied reaction conditions. Utilizing lower than stoichiometric ratio of oxalic acid still creates with 8-fold oxalate coordination-complexes, suggesting that is very stable and favorable for Hf oxalates. The

only difference in the reaction solutions were the applied counter cations, suggesting they influence the connectivity of the Hf-oxalate complexes. While K^+ , Rb^+ or Cs^+ counter ions yield mononuclear species, Na^+ or Li^+ ions promote dimers, while TMA^+ counter cation dictates the formation of polymeric chains. **Figure 5.2** shows the coordination environment of the alkalis with the different Hf-oxalate species. There is direct bonding between the oxalate oxygens and the alkali cations. The clear trend in decreasing linking between Hf-oxalates with increasing alkali size is related to the competing oxalate-alkali coordination. Larger alkalis that can accommodate more bonds and have readily removable hydration spheres form outer sphere complexes with Hf-oxalate, halting the polymerization. If TMA^+ (with no coordinating ability) is used instead of alkalis, only polymers are crystallized. The observed solid-state structures likely affect solution association as well, which will be discussed later.

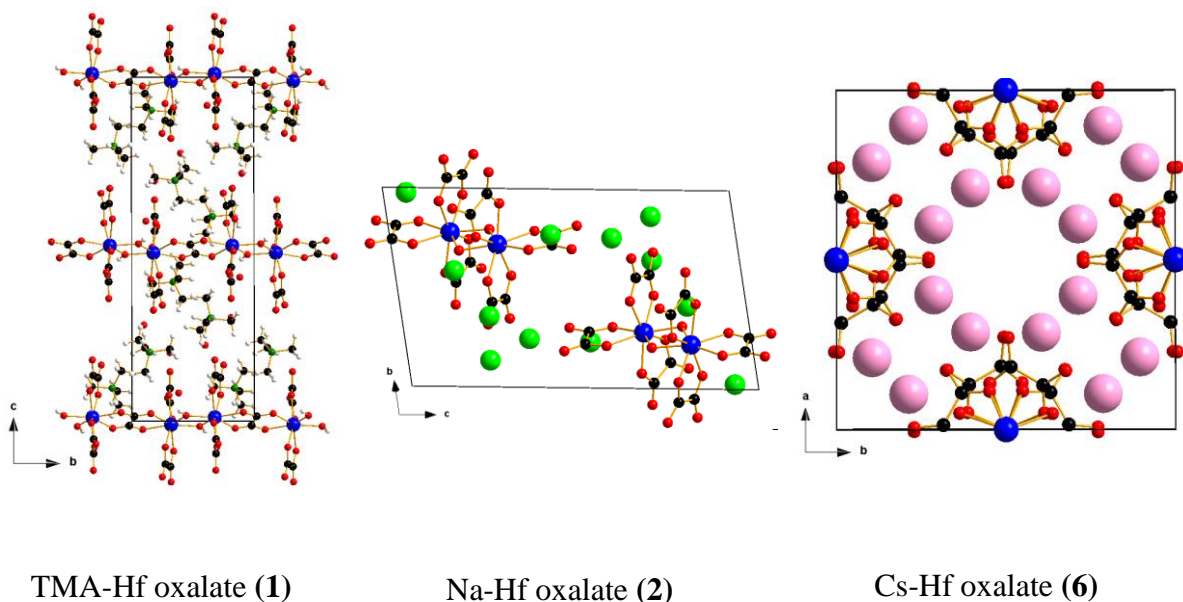


Figure 5.2 Ball-stick representation of atoms in unit cells of (1), (2) and (6) with counter ions associated. Water molecules are omitted for clarity. Color code: Hf-blue, O-red, C-black, H-white, N-dark green, Li-grey, Na-light green and Cs-pink.

5.4.2. Structural description of Zr with 8-fold coordination (compound 7, 9, 12 and 13)

Intriguingly, Zr compounds differ significantly from the obtained Hf compounds. Some of the products are similar to the above-described hafnium structures, but Zr-peroxide

binding tends to trigger the formation of different metal-hydroxide/peroxide bridged ring clusters. We isolated a range of Zr^{4+} compounds. Na^+ (compound **9**) and Cs^+ (compound **12**) ions isolated monomeric tetraoxalates similar to the above-described Hf-compounds, and prior reported with Na.¹⁸⁰ The Zr- $O_{oxalate}$ bond distances are summarized in **Table 5.4**.

Utilizing the TMA^+ counter ion isolated a $\{Zr_6\}$ -cluster, (**7**), with the 6 metal centers linked in a ring by one hydroxo and one peroxo group. Both μ -(OH) and μ -(O_2) bridges are disordered throughout the framework over two positions (see details in Appendix C). Zr is 8-coordinate; one bidentate oxalate completes the coordination sphere of each Zr (**Figure 5.3**). The same hexagonal Zr-ring motif was observed prior, stabilized between two lacunary silicotungstate anions, instead of the oxalate ligands.¹⁷³ Also, the analogous Hf hexamer with hydroxide capping ligands has been isolated.¹⁷² The connections of metal-oxo polyhedra create a 6-member ring, where the Zr-Zr distance average is 3.267 Å. **Table 5.4** contains important interatomic distances observed in (**9**), (**12**) and (**13**). Crystallographic data of 8-fold Zr compounds is in **Table C 3**.

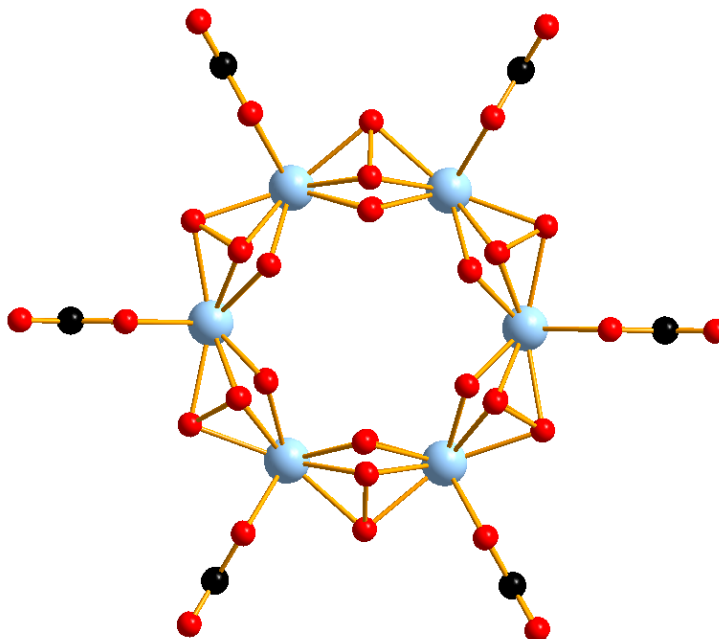


Figure 5.3 Planar view of (**7**). For clarity only one possible position is shown for μ -(OH) and μ -(O_2) bridges over the disorders. Color code: Zr-pale blue, O-red and C-black, respectively.

Table 5.4 Selected interatomic distances from the crystallographically independent Zr centers in **(7)**, **(9)**, **(12)** and **(13)** Zr(-peroxo)-oxalates.

	(9) (Na-Zr)	(12) (Zr1) (Rb-Zr)	(12) (Zr2) (Rb-Zr)	(13) (Cs-Zr)
Zr-O (Å)	2.1577(54)	2.1676(108)	2.1546(108)	2.1605(253)
Zr-O (Å)	2.1577(54)	2.1767(108)	2.1636(114)	2.1606(253)
Zr-O (Å)	2.1769(48)	2.1842(114)	2.1693(114)	2.1992(239)
Zr-O (Å)	2.1771(48)	2.1867(102)	2.1943(108)	2.1992(239)
Zr-O (Å)	2.2145(59)	2.1960(114)	2.1977(88)	2.2102(228)
Zr-O (Å)	2.2145(59)	2.1973(112)	2.2077(125)	2.2105(228)
Zr-O (Å)	2.2336(57)	2.2000(115)	2.2292(109)	2.2422(214)
Zr-O (Å)	2.2337(57)	2.2269(112)	2.2351(114)	2.2425(214)
Zr-O_(average) (Å)	2.196	2.192	2.194	2.203
Zr-Zr (Å)	N/A	N/A	N/A	N/A

5.4.3. Zr rings with 9-fold coordination (compound **8**, **10** and **11**)

Li⁺, K⁺ or Rb⁺ counter cations led to isolation of ring-shape peroxo-oxalate cluster with unusual 9-coordinate Zr-O polyhedral building units with distorted monocapped square antiprism geometry.

In each of these compounds, Zr is bound to three peroxo groups (two coordinating oxygens of each), one hydroxo group and one oxalate group (bidentate coordination; **Figure 5.4A**). The Zr-O_{oxalate} bonds range from 2.17-2.21 Å, the Zr-O_{hydroxyl} distance is ~2.13 Å, and the Zr-O_{peroxo} bonds are 2.12-2.27 Å. All peroxo and hydroxyl ligands are bridging. To our knowledge, there is only one 9-coordinate Zr compound reported in the literature thus far¹⁸¹. Rude *et al.* has synthesized the 12-fold cuboctahedron coordination of Zr with four [BH₄]⁻ ligands¹⁸², but these currently reported structures have the highest coordination number with oxygen donor atoms. This type of coordination environment is more common for larger lanthanide and actinide ions; but thus far, not for Zr. The coordination environment also represents a link between chemistry of transition metals and *f*-elements.

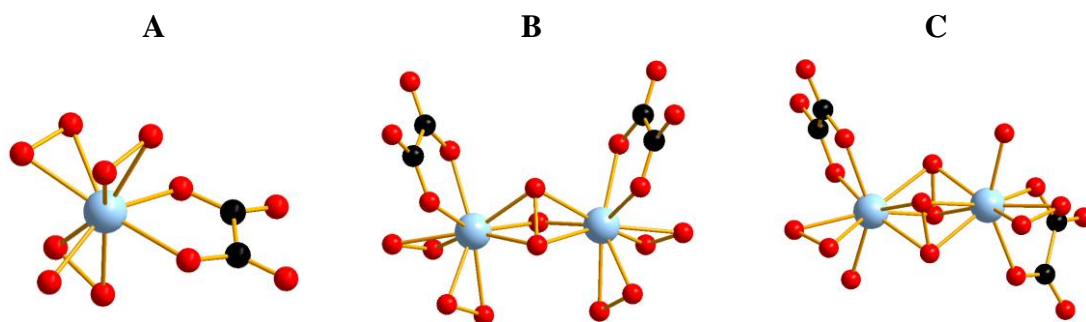


Figure 5.4 Ball-stick representation of the building unit in $\{\text{Zr}_8\}$, $\{\text{Zr}_{12}\}$ and $\{\text{Zr}_{16}\}$ -cluster. **A**: the monomer unit, **B**: the connection mode between two monomer units via mixed hydroxo-peroxo groups and **C**: the connection mode between two monomer units via two peroxo group. Color code: Zr-pale blue, O-red and C-black.

The connectivity between polyhedra is also unusual in these clusters. We observe two alternating linkages between the polyhedra, both face-sharing. Each Zr shares a face on one side via two peroxide bridges, and on the other side with one peroxide and one hydroxide, the latter is also featured in the $\{\text{Zr}_6\}$ -cluster (**Figure 5.4B-C**). The respective Zr-Zr distances are 3.17-3.20 Å and 3.31-3.34 Å. The rings can be described as linked dimer units that are bridged by two peroxides: 4 dimers in $\{\text{Zr}_8\}$, 6 in $\{\text{Zr}_{12}\}$, and 8 in $\{\text{Zr}_{16}\}$ (**Figure 5.5-5.7**). For comparison, there are a few multinuclear peroxo compound of Zr reported. There is a Zr-peroxo-fluoro trimer, where one bridging peroxo group between the metal centers results 3.903 Å Zr-Zr distance.¹⁷⁵ On the other hand, the μ -4 connection has been prior observed in $[\text{M}_2(\text{O}_2)_2]$ dimer units (M=Zr or Hf) for both Zr^{183,184} and Hf¹⁸⁵. These dimer units were stabilized by bulky organic ligands or lacunary polyoxometalate ligands. In the absence of these rigid ligands, zig-zag rings are formed (**Figure 5.5-5.7**). Interestingly, the observed Zr-Zr distance is similar to that in some Zr³⁺ compounds with a Zr-Zr bond^{186,187}, but the reaction conditions and white color rules out oxidation state change on the metal centers.

Although metal-oxo clusters of Zr with high nuclearity have been reported, most of them are cationic and they do not have bridging peroxo ligands. In addition, cluster formation with bridging peroxo groups is well-known for uranyl nanocages, but less common for transition metals.⁶¹ There is one unique example of high-nuclearity wheel-shaped peroxotitanate with bridging peroxo ligands.¹⁸⁸ Crystallographic data of 9-fold Zr compounds is in **Table C 4**.

Table 5.5 Selected interatomic distances from the crystallographically independent Zr centers in **(8)**, **(10)** and **(11)** Zr-peroxo-oxalates.

	(8) (Zr1) (Li-Zr)	(8) (Zr2) (Li-Zr)	(10) (Zr1) (K-Zr)	(10) (Zr2) (K-Zr)	(11) (Zr1) (Rb-Zr)	(11) (Zr2) (Rb-Zr)
Zr-O (Å)	2.1342(90)	2.1216(74)	2.1562(108)	2.1522(116)	2.1390(126)	2.1466(119)
Zr-O (Å)	2.1479(104)	2.1541(103)	2.1572(107)	2.1564(97)	2.1540(136)	2.1489(149)
Zr-O (Å)	2.1702(104)	2.1588(77)	2.1574(104)	2.1672(86)	2.1600(135)	2.1636(119)
Zr-O (Å)	2.1782(109)	2.1640(126)	2.1718(113)	2.1736(130)	2.1698(139)	2.1796(132)
Zr-O (Å)	2.1862(82)	2.1877(105)	2.1986(122)	2.1924(107)	2.1762(142)	2.1864(130)
Zr-O (Å)	2.1926(81)	2.1981(87)	2.2141(97)	2.2165(108)	2.1890(123)	2.2015(110)
Zr-O (Å)	2.1930(87)	2.2046(98)	2.2159(92)	2.2249(114)	2.2146(138)	2.2124(138)
Zr-O (Å)	2.1993(77)	2.2298(83)	2.2235(123)	2.2264(99)	2.2328(142)	2.2192(129)
Zr-O (Å)	2.2662(102)	2.2703(107)	2.2563(131)	2.2312(105)	2.2524(130)	2.2313(116)
Zr-O_(average) (Å)	2.185	2.188	2.195	2.193	2.186	2.188
Zr-Zr (<i>via</i> μ -4) (Å)	3.1964(15)	3.1962(15)	3.1876(18)	3.1889(18)	3.1655(20)	3.1657(20)
Zr-Zr (<i>via</i> μ -3) (Å)	3.3050(19)	3.3442(20)	3.3411(19)	3.3397(16)	3.3417(20)	3.3265(20)

High nuclearity of the formed metal-peroxo oxalate cluster was promoted by the alkali counter cations. The cation size appears to determine the ring-size, a larger cation yield a larger ring ($\text{Li}^+\text{-}\{\text{Zr}_8\}$ (**Figure 5.5**), $\text{K}^+\text{-}\{\text{Zr}_{12}\}$ (**Figure 5.6**), and $\text{Rb}^+\text{-}\{\text{Zr}_{16}\}$ (**Figure 5.7**)).

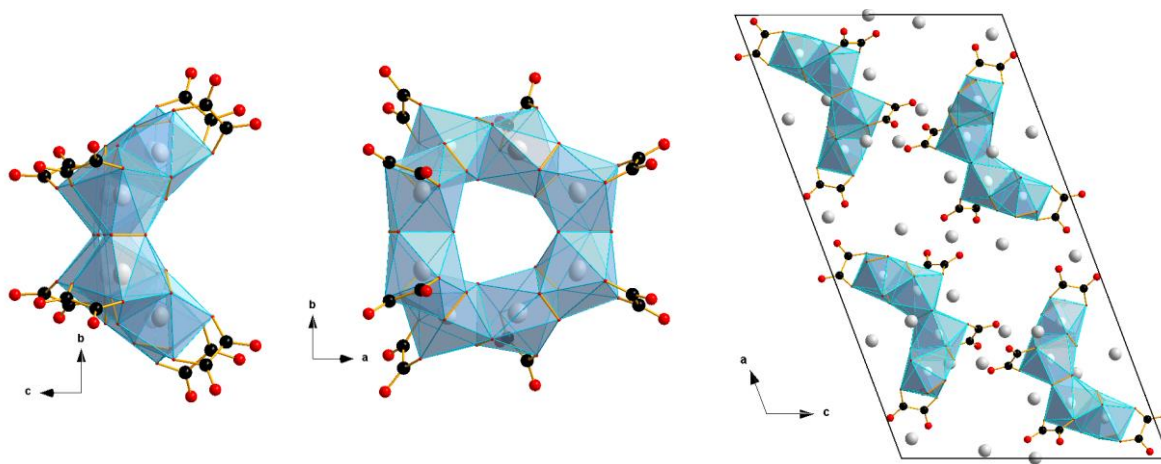


Figure 5.5 Representation of $\{\text{Zr}_8\}$ -cluster **(8)**. The perspectives of $\{\text{Zr}_8\}$ -cluster (left and center) and the unit cell (H_2O molecules are omitted) (right). Color code: Li-grey, O-red, C-black and Zr-O polyhedra: light blue.

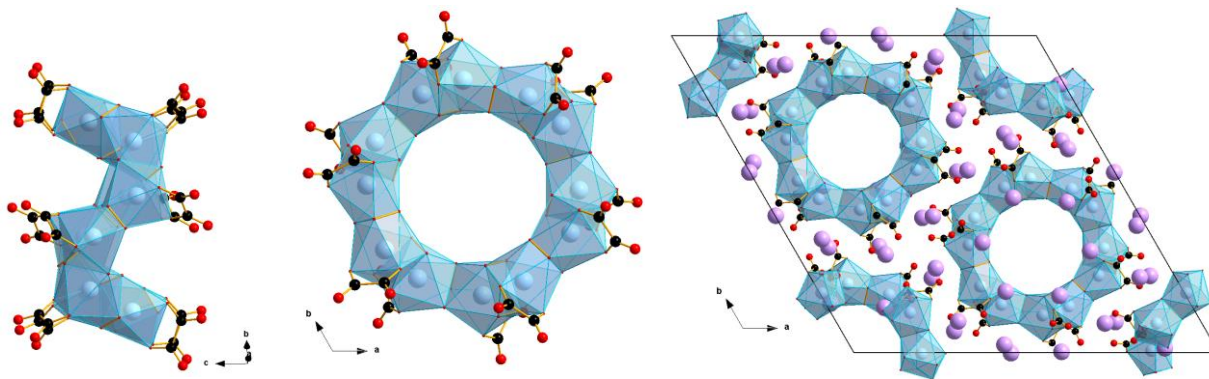


Figure 5.6 Representation of $\{\text{Zr}_{12}\}$ -cluster (**10**). The perspectives of $\{\text{Zr}_{12}\}$ -cluster (left and center) and the unit cell (H_2O molecules are omitted) (right). Color code: K-purple, O-red, C-black and Zr-O polyhedra: light blue.

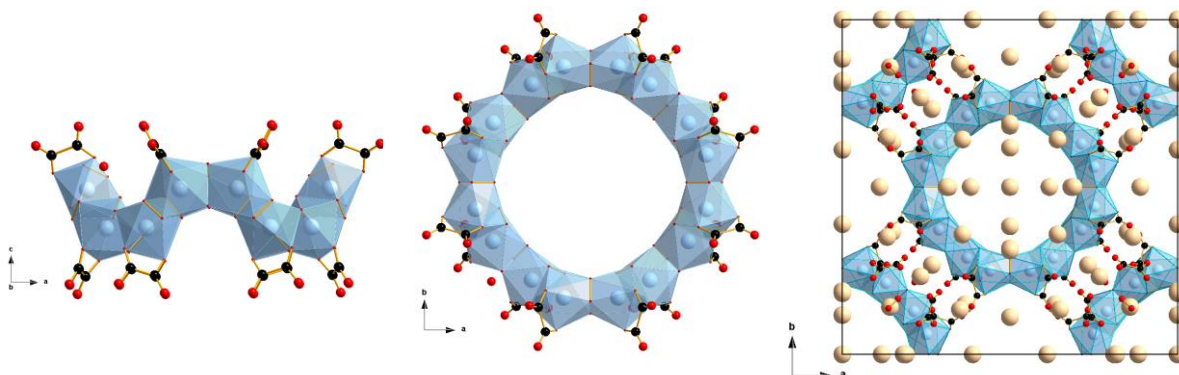


Figure 5.7 Polyhedral and ball-stick representation of $\{\text{Zr}_{16}\}$ -cluster (**11**). The perspectives of $\{\text{Zr}_{16}\}$ -cluster (left and center) and the unit cell (H_2O molecules are omitted) (right). Color code: Rb-tan, O-red, C-black and Zr-O polyhedra: light blue.

It is interesting that identical reaction conditions for Zr and Hf lead to Zr-peroxo-oxalate species vs. Hf-oxalate species. The reaction solutions are slightly acidic ($\text{pH}\sim 4.8$), and peroxide must deprotonate in order to coordinate. Metal cations, particularly highly charged metal cations, are described as acidic and can also promote deprotonation. Since the pK_a-1 of peroxide is >11 , then it is likely the tetravalent metals play a role in peroxide deprotonation. Our recent report showed that Zr promote peroxide decomposition in acidic solutions⁸; and current (unpublished) studies showed that under the same conditions that Hf is less active in promoting peroxide decomposition. Additionally, at $\text{pH}>12$ with no

other metals or alkali counterions present, the peroxide-linked Hf₆ cluster has been isolated,¹⁷² and peroxide has also shown to bind Hf in solution prior studies.¹⁸⁹ Another point to consider is peroxide is very sensitive to impurities: if there is a redox active impurity in the Hf—even in trace amounts—it can accelerate peroxide decomposition. At this point, we do not have a conclusive answer to this noteworthy difference between Hf and Zr behavior under the applied solution conditions. However, we do note that the Zr-peroxide-Zr dihedral angle is bent in every case, similar to the computationally and experimentally observed uranyl peroxide species.^{61,190} Perhaps this phenomenon of the ‘inherently bent’ metal-peroxide-metal dihedral angle is more common and universal, beyond uranyl peroxide chemistry.

Similar to the Hf compounds, the only difference in sample preparation was the applied counter ion, which indicates their significant role in metal-oxo cluster assembly. In contrast to the readily explained role in controlling connectivity between Hf-oxalate polyhedra, we cannot easily rationalize why larger alkalis seem to stabilize larger Zr-oxalate-peroxide rings. However it again is likely related to bonding of the alkalis to oxalate ligands during the self-assembly process, which is reflected in bonding in the crystalline lattices. Since the ring structures are built of the quadruply-bridged dimer units and they are present in solution (discussed below), perhaps the alkalis play a role in linking the dimers together. The major difference between the rings of different sizes is the curvature. Smaller rings require greater curvature. Perhaps the curvature of the smaller rings provides better coordination environments for smaller alkalis, and vice versa.

Table 5.6 Selected bond angles for **compound (8)**, **(10)** and **(11)**. (Note: “in” and “out” indicates the position of peroxide oxygens relative to the center of ring.)

	{Zr ₈ }-cluster	{Zr ₁₂ }-cluster	{Zr ₁₆ }-cluster
Zr-(OH)-Zr (μ-3)	101.5° - 103.1°	101.1°	100.0° - 102.4°
Zr-(O ₂)-Zr (μ-3)	98.2° - 100.6°	99.0° - 101.2°	97.7° - 102.2°
Zr-(O ₂) _{in} -Zr (μ-4)	92.5° - 94.1°	93.2°	91.6° - 92.4°
Zr-(O ₂) _{out} -Zr (μ-4)	91.4° - 94.5°	92.5° - 93.6°	91.8° - 92.7°
Zr-Zr-Zr	124.1° - 128.7°	126.0° - 126.3°	128.0° - 132.8°

5.4.4. Bulk solid-state and solution characterizations

Note: solid-state characterization was only carried out for samples that were obtained in pure forms. For example, no compounds with TMA counterions could be characterized since crystalline materials are mixed with gel. Since single-crystals of **(3)** and **(4)** grew from the same reaction conditions, we applied only KOH and only LiOH to produce solid materials of Li-Hf and K-Hf oxalate for further characterization. We reckoned that using these conditions we can distinguish **(1)** and **(2)**, even they crystallized out from the reaction solution of Li⁺-K⁺ ion mixture (**Table 5.1**).

Crystallinity was confirmed by PXRD when Na⁺, K⁺, Rb⁺ or Cs⁺ counter ions were used (Li⁺ products showed poor crystallinity). However, peak positions in the diffraction patterns are not in good agreement with that calculated patterns in some cases (**Figure C 1-C10**). We attempted to match the experimental with calculated diffraction patterns of our isolated structures, as well as other known zirconium or hafnium oxalates with partial success. These analyses indicate either that the product can crystallize in different phases resulting a mixture of different species, or there is dehydration of the bulk samples (this is a common problem for cluster salts with lattice water). Phase impurity is suggested by semi-quantitative EDX analyses, where in most cases the observed metal:alkali ratio is different from the ones observed in single-crystal data. The hafnium oxalates are alkali deficit, compared to the values we expect from the crystal structures. (**Table C 5**). Similar effects trends are observed for Zr products (**Table C 6**).

FT-IR provided more information about the product mixtures (**Figure 5.8**). The products do not contain any starting materials (**Figure C 11**), and they are similar to each other. In general, we observe 5 IR bands in the Hf products and 6 IR bands in the obtained Zr products. **Table 5.7** contains the prominent IR-transmittance positions. The one additional IR band observed at 844-851 cm⁻¹ wavenumber for each Zr products (peak **2** in **Figure 5.8** and in **Table 5.7**) is the stretch of the peroxy group. There is yet one more peak at 1334.9 cm⁻¹ (peak **5**) in Li-Zr product which was not observed in the other products. This also suggests that despite the lack of crystallographic information about Zr-peroxy oxalate species with Na⁺ and Cs⁺ ions, the Zr-peroxy interaction still exists in those products. IR measurements indicate Zr-peroxy bonding regardless of the alkali counter cation, even though the products cannot always be crystallized. In addition, the missing

peroxo vibrational band in the Hf products correlates with its absence in crystallized products.

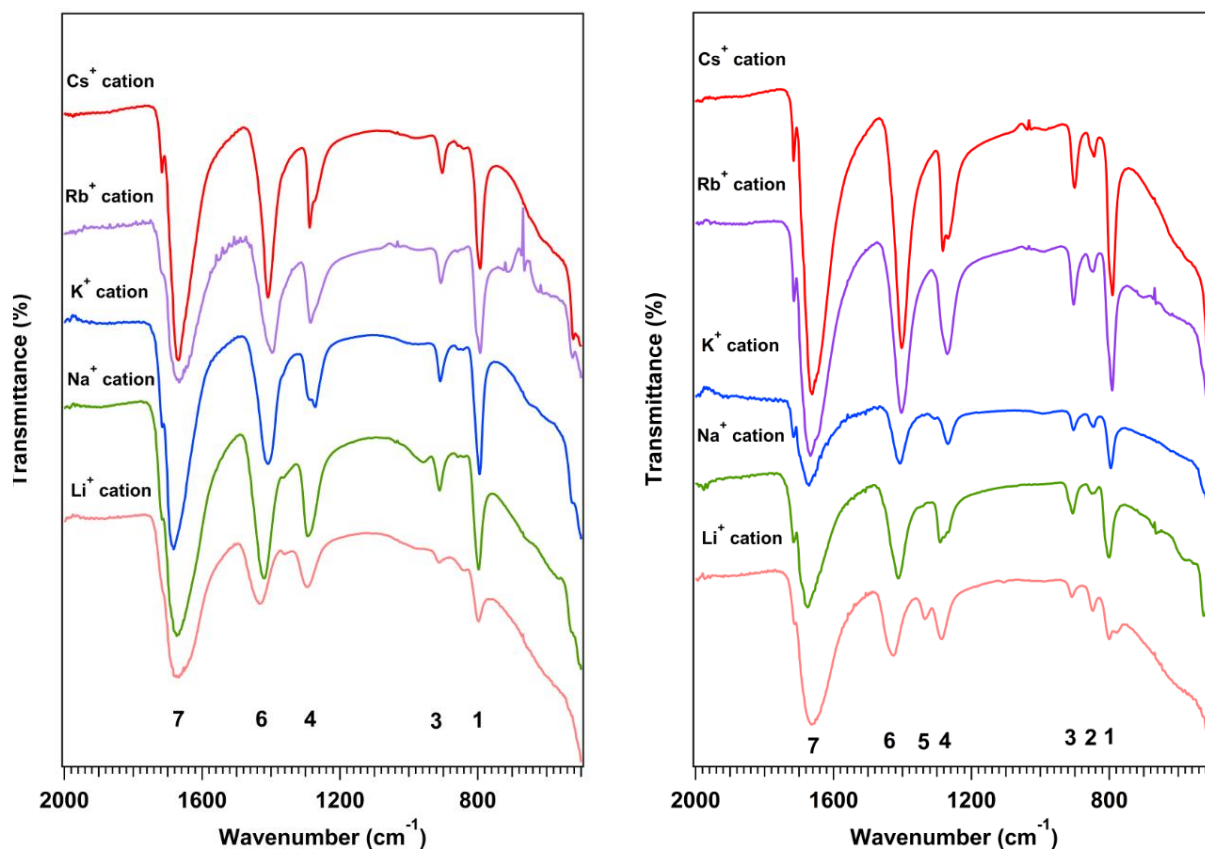


Figure 5.8 FT-IR spectra of the obtained solid products. Left: Hf products, right: Zr products. Numbers are indicating different IR bands assigned in **Table 5.7**.

Table 5.7 FT-IR vibrational band positions (cm^{-1}) of the obtained Hf-oxalate and Zr(-peroxo)-oxalate solid products.

System	Peak 1	Peak 2 (O-O)	Peak 3	Peak 4	Peak 5	Peak 6	Peak 7
Cs-Hf oxalate	793.2	-	902.8	1287.8	-	1408.9	1668.1 & 1716.7
Rb-Hf oxalate	793.1	-	907.1	1285.3	-	1396.9	1666.5
K-Hf oxalate	794.5	-	908.9	1271.7	-	1408.9	1682.6
Na-Hf oxalate	797.4	-	910.9	1293.3	-	1418.2	1673.8
Li-Hf oxalate	798.1	-	911.8	1295.3	-	1433.7	1667.4
Cs-Zr-oxalate	790.9	844.4	900.7	1282.8	-	1402.4	1662.1 & 1715.7
Rb-Zr oxalate (Zr ₁₆)	791.9	847.3	903.4	1270.0	-	1403.0	1667.1 & 1714.8
K-Zr oxalate(Zr ₁₂)	795.5	846.0	903.7	1268.0	-	1406.8	1670.9
Na-Zr oxalate	800.9	850.1	906.2	1290.7	-	1412.0	1674.78 & 1715.9
Li-Zr oxalate(Zr ₈)	800.2	847.8	908.7	1286.9	1334.9	1425.7	1663.4

5.4.5.Solution Characterization

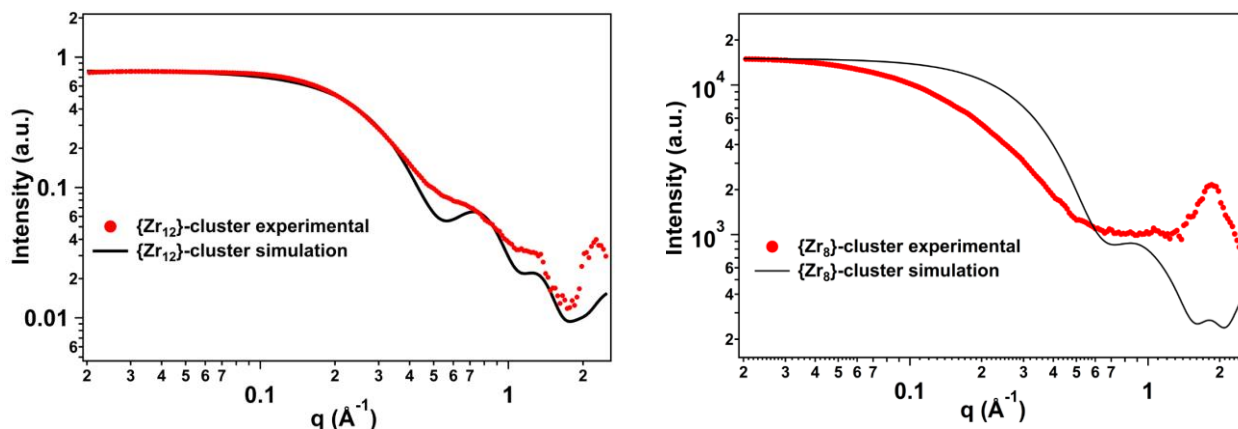


Figure 5.9 Experimental (red) and calculated (black) SAXS curves of {Zr₁₂} (left) and {Zr₈} (right), intensity-normalized for comparison. The {Zr₁₂} cluster is intact upon dissolution.

SAXS. SAXS is a powerful method to investigate solution speciation, especially to identify larger metal-oxo clusters. Scattering at low q (proportional to scattering angle) provides information about dispersity, particle size and shape¹⁰. We performed SAXS measurements on the dissolved solid products. Although the cluster materials are poorly soluble (<10mg/1mL water), compared to simple oxalates, they scatter well due to the larger size and good electron density contrast. SAXS clearly shows the presence of the {Zr₁₂}-compound in water **Figure 5.9**. The Guinier-region ($q \sim 0.1\text{-}0.4 \text{ \AA}^{-1}$) of the experimental-curve matches very well with the simulated scattering curve calculated from single crystal structure. The radius of particle from the observed curve is 6.3 \AA , which is in good agreement with the calculated value from the simulated curve (6.6 \AA) (**Figure C 12**). The flat, plateau region at low q -range suggests the solution is monodisperse with no aggregation. The similar scattering profile at higher q -values ($0.3 \text{ \AA}^{-1} < q < 1.0 \text{ \AA}^{-1}$) indicates similar shape that of {Zr₁₂}-cluster. The simulated curve above $q > 1.0 \text{ \AA}^{-1}$ shows two distinct oscillations characteristic of the ring shape, that are not present in the experimental data. This is often the case for solutions in which solvent scattering dominates at high- q , or contain smaller species in addition to the large clusters. Alternatively, there may be K⁺ counterions bonded inside and outside the ring, adding some polydispersity and ‘smearing’ out the oscillations. This hypothesis is supported by pair distance distribution function (PDDF) analysis. The overall extent for the experimental data is larger than of calculated curve (14.6 \AA vs. 16.4 \AA diameter) and the correlations in $3\text{-}7 \text{ \AA}$ are more intense

suggesting association with K^+ cations (**Figure C 13**). In summary, the data indicates stability of the $\{Zr_{12}\}$ -cluster in aqueous conditions; it is intact upon dissolution in neat water.

Contrarily, the simulated and experimental curves of the $\{Zr_8\}$ -cluster are not in good agreement. The experimental curve declines at lower q value, suggesting presence of bigger species (**Figure 5.9**). Performing size distribution approximation, we observed formation of two species with 12.1 Å and 32.5 Å mean diameter (**Figure C 14**). The smaller species (which is more dominant, 96.2% relative concentration) can correlate to intact $\{Zr_8\}$ -cluster ($R_g=5.36$ Å by simulation), and the bigger specie (3.8% relative concentration) could be an aggregate of several clusters. The terminal oxalate ligands can easily bridge to other clusters, especially if not mediated by the alkali counterions. Perhaps the K^+ of $\{Zr_{12}\}$ bonds and associated to the terminal oxalate ligands, while the Li^+ of $\{Zr_8\}$ do not. All the other solutions (including Zr and Hf products) indicate scattering by aggregates that cannot be assigned to our observed compounds. The Guinier-region ($q=0.09-0.5$ Å⁻¹) of these solutions has the same feature. Although the size of the present particles is around 1 nm diameter, the scattering profile is different from the above-described clusters. This may indicate the formation of other species: the scattering profile has a good match with the chain of two dimers of $[M_4(OH)_4(C_2O_4)_{11}]$ unit obtained from the polymeric chain of compound (**1**) for dissolved Na-Zr oxalate and Na-, K-, Rb- and Cs-Hf oxalates (**Figure 5.10** and **Figure C 15**). The similarity of all SAXS curves suggest that formation of this specie is common. We also attempted to simulate the SAXS profile of Li-Hf oxalate with long polymeric chain, but the slope obtained from experimental curve is steeper than that of simulations indicating a different type of aggregation. To observe the different coordination environments for the two metals in aqueous media, PDF analysis of X-ray total scattering measurements was performed.

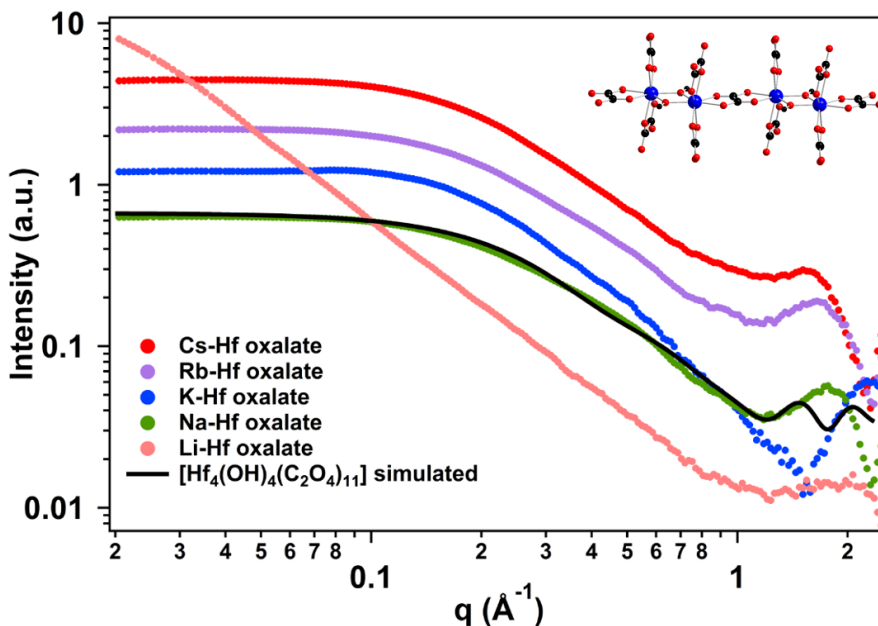


Figure 5.10 SAXS curves (offset for ease of viewing) of the dissolved Hf oxalate products. All solutions show scattering which are in good agreement (except for Li-Hf oxalate) with the $[\text{Hf}_4(\text{OH})_4(\text{C}_2\text{O}_4)_{11}]$ fragment model (inset).

PDF: PDF analyses of reaction solutions and dissolved solids were utilized to observe different coordination environment for the two metals (face-sharing for Zr, edge-sharing for Hf), and determine the role of pre-assembly processes. In **Figure 5.11** we compare PDF of the reaction solution and the dissolved products of Zr and Hf. PDF of both Zr and Hf reaction solutions are similar to that of a simple salt solution, in which the neighboring O-O correlations of the H_2O solvent is dominant at $\sim 2.8 \text{ \AA}$. After dissolution of solid products in neat water, small differences are observable by PDF. Owing to the low concentrations, correlations from water still dominates the overall function, but a new shoulder appears at the O-O peak at $\sim 3.1\text{-}3.3 \text{ \AA}$. In order to confirm these are real peaks, and not ripples (attributes due to the limited q -range) we varied parameters during data processing. The peaks were still observed and do not change their position which confirms they arise from atom pair-correlations. The low concentration in these samples bolsters our argument that this peak is assignable to the metal-metal correlation. The scattering power is much greater for Zr-Zr than for Zr-O.

Hf oxalate solutions with different alkali counter cations do not show significant changes. The edge-shared Hf-O polyhedra (observed in solid-state structures with Li^+ and

Na⁺ counter cations) has a characteristic Hf-Hf distance at 3.4-3.6 Å, where a low intensity peak is apparent in the Na, K, Rb and Cs-Hf oxalate solutions. Although this feature may appear in a PDF of pure H₂O (comes from the structure of H₂O or due to limited q /instrumentation effects; which is still questioned in the literature^{72,191}), this can indicate the formation Hf-Hf edge-sharing coordination upon dissolution. This is in good agreement with our SAXS results, where we could model scattering with the [Hf₄(OH)₄(C₂O₄)₁₁] fragment. This fragment has Hf-Hf correlations at the observed distance. Li-Hf oxalate did not stay long enough in solution during X-ray total scattering data collection supposedly due to the polymerization we have observed in SAXS. Other alkali Hf oxalate PDF results are in **Figure 5.11**.

PDF of Zr solutions are more informative. The face-sharing mode for Zr-O polyhedra is in the range of 3.1-3.3 Å, which is easily observable in several samples. The correlation is dominant for the {Zr₁₂}-cluster, but is also present in other redissolved solids, with the exception of the product obtained with Na⁺ and Cs⁺ counter cations. Based on the intensity of this arising peak in the solutions, we can establish a stability order for the μ -4 face-sharing mode with different counter cations: Na⁺ < Cs⁺ < Rb⁺ < Li⁺ << K⁺. This is in good agreement with the observed single-crystal structures: we see simple tetraoxalate monomers with Na⁺, Rb⁺ and Cs⁺, and ring clusters with Rb⁺, Li⁺ and K⁺ (both structure types are isolated for Rb⁺, indicating the turning point in the stability order). On the other hand, FT-IR also suggests interaction between Zr and peroxide ion for all alkali counter cations in the solid-state. Considering these two observations, we assume the μ -4 connection mode may form in the presence of all alkali cations, but only Rb⁺, Li⁺ and K⁺ stabilize these face-sharing dimers in solution, particularly K⁺. We can also conclude that the alkalis play an important role in assembling this unique diperoxide bridged face-sharing dimer with Zr (**Figure 5.11**).

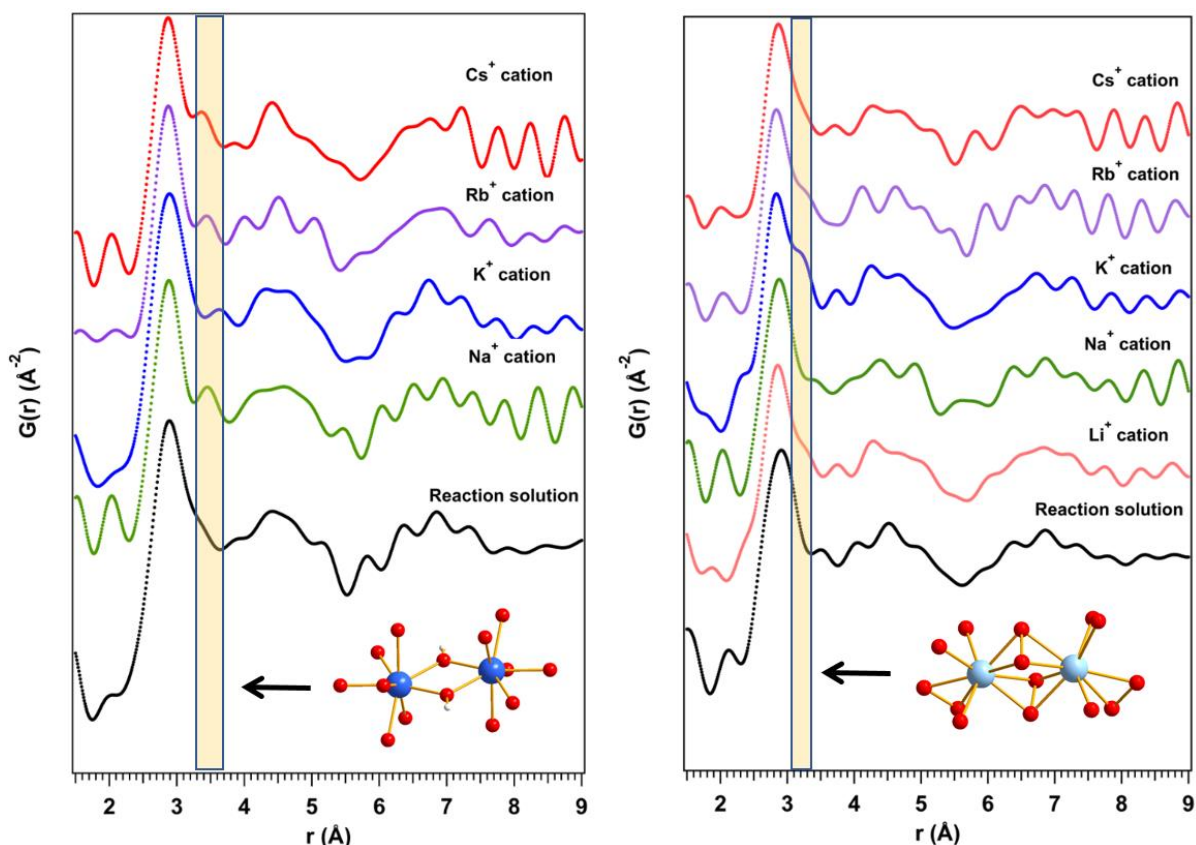


Figure 5.11 PDF analysis of the observed X-ray total scattering measurements on reaction solutions and dissolved solids of Hf (left) and Zr (right). The different position of the arising peak between 3.0-3.6 Å indicates the different coordination mode for the two metals in aqueous conditions. (Hf-blue, Zr-pale blue and O-red)

ESI-MS: Finally, ESI-MS was performed to extract compositional information about solution species. Mass spectroscopy investigations can determine the exact composition for the detected species. Both Zr and Hf have their unique isotopic pattern which aids absolute identification of the signals in MS, especially for multi-nuclear complexes. We were able to detect signals only from the solution of dissolved $\{Zr_{12}\}$ -cluster (K-Zr-peroxo-oxalate) due to the limited solubility of our products. **Figure 5.12** and **Table 5.8** summarizes the observed species. The complete cluster of $\{Zr_{12}\}$ is not observed, likely due to fragmentation in this semi-destructive technique, but several monomers and oligomer fragments are observed. Most of the observed compounds (eleven of them) comprise one metal center (monomers), one species has two metal centers (dimer) and three species contain four metal centers (tetramers). The mononuclear species dominate

the spectrum, the abundance of the dimer and tetramer species are low. All species contain oxalate ligands, but we observe oxo (O^{2-}), peroxy (O_2^{2-}), hydroxo (OH^-) and water (H_2O) ligands as well. We simulated the peak envelopes for some of the relevant, multinuclear species. Comparison of observed and simulated peaks is in **Figure C 16**. The oxo ligands are derived from deprotonation of hydroxide or decomposition of peroxide from the ionization process.

Table 5.8 List of assignment of the ESI-MS spectrum (negative mode) of $\{Zr_{12}\}$ crystals dissolved in water.

Species	m/z – observed	m/z – calculated
$\{ZrO(C_2O_4)_2\}^{2-}$	140.92	140.93
$\{Zr(O_2)(C_2O_4)_2\}^{2-}$	148.92	148.93
$\{KZr(O_2)(C_2O_4)_2(OH)\}^{2-}$	176.91	176.91
$\{Zr(C_2O_4)_3\}^{2-}$	176.91	176.92
$\{KZr(C_2O_4)_3(OH)\}^{2-}$	204.90	204.90
$\{K_5ZrO(O_2)_3(OH)_3(H_2O)_4\}^{2-}$	259.87	259.86
$\{KZr_4(O_2)_5(C_2O_4)_3(OH)_2\}^{3-}$	286.82	286.82
$\{K_2ZrO(O_2)(C_2O_4)(OH)\}^{1-}$	320.81	320.80
$\{K_2ZrO(O_2)(C_2O_4)(OH)(H_2O)\}^{1-}$	338.82	338.81
$\{KZr(C_2O_4)_3\}^{1-}$	392.80	392.80
$\{Zr_4(O_2)_3(C_2O_4)_4(OH)_2\}^{2-}$	422.75	422.75
$\{Zr_4(O_2)_3(C_2O_4)_4(OH)_2(H_2O)\}^{2-}$	431.75	431.76
$\{Li_3Zr_2(O_2)_5(C_2O_4)\}^{1-}$	448.76	448.78
$\{K_3ZrO(O_2)(C_2O_4)_2(H_2O)\}^{1-}$	448.76	448.75
$\{K_3Zr(C_2O_4)_4\}^{1-}$	558.70	558.71

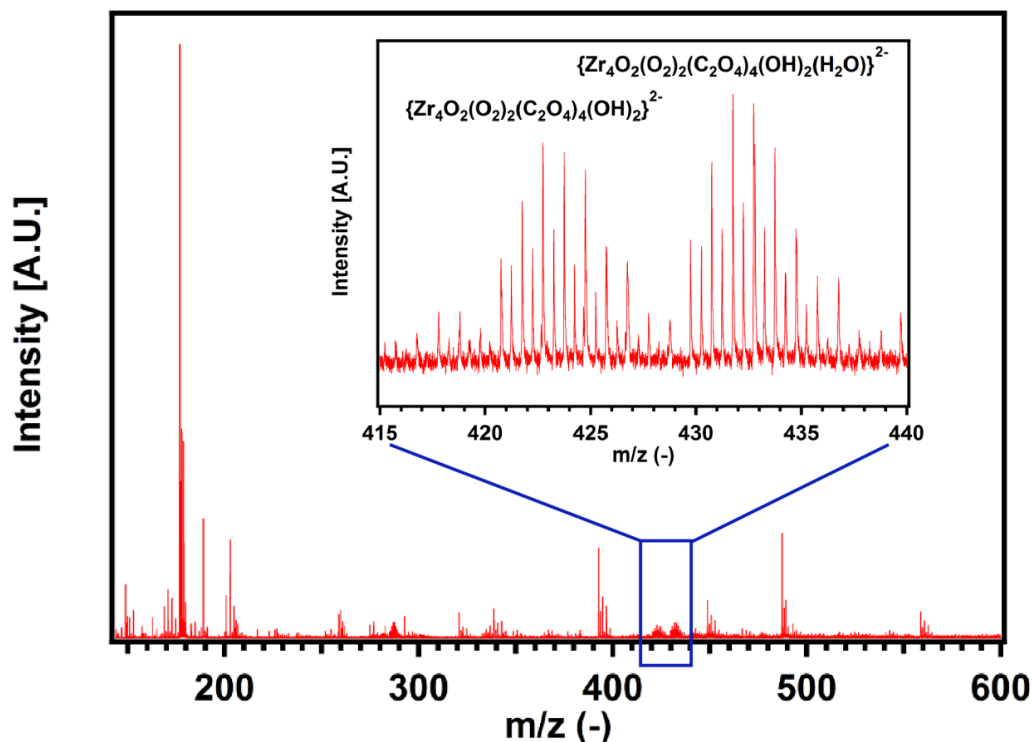


Figure 5.12 ESI-MS graph of the dissolved crystal of $\{Zr_{12}\}$ -cluster. The most intense signals originate from monomeric species with a presence of some oligomer species (see inlet).

5.5 Conclusion

Differentiating chemical behavior of Zr and Hf is important to separate them in their pure form for different industrial applications, particularly nuclear applications in which Zr is exploited for its neutron transparency and Hf is exploited for neutron absorption. We investigated Zr and Hf speciation using oxalate and peroxide ligands simultaneously along with the effect of counter ions for the formed anionic species in mildly acidic conditions (TMA⁺, Li⁺, Na⁺, K⁺, Rb⁺ and Cs⁺ cations). From thirteen structures of isolated compounds, we are able to state distinct differences between Zr and Hf speciation, as well as delineate the effect of the counterions. From Hf solutions, only polymeric chains (TMA⁺), dimer oxalates (Li⁺ and Na⁺), and monomer tetraoxalate complexes (K⁺, Rb⁺ and Cs⁺) were isolated. Here there is a clear correlation between species and counterion association; where minimal association leads to formation of polymers (TMA). On the other hand, more extensive association of the heavy alkalis only stabilize monomer species,

due to stronger interaction in solution, preventing polymerization. On the other hand, Zr assembles into rings with bridging peroxides and terminal oxalates with nuclearities including TMA- $\{Zr_6\}$, Li- $\{Zr_8\}$, K- $\{Zr_{12}\}$, and Rb- $\{Zr_{16}\}$. Meanwhile Na and Cs only isolated monomer forms, and we observed monomer with Rb, as well. These clusters feature rare and unusual structural features including 9-coordinate Zr, and face-sharing polyhedra leading to very short Zr-Zr distances. While the effect of the counterions is clear and partially rationalized based on ion-association behavior, the differences between Zr and Hf are not understood at this point. In particular, why does Zr stably bind peroxide in these conditions, while Hf does not? The Zr-peroxide-Zr bond appears inherently bent, leading to formation of ring-shaped clusters. It is therefore reasonable that different conditions could be found that lead to formation of capsules. The fundamental difference between Zr and Hf behavior in these experiments can for now, only be attributed to the relativistic effect. This phenomenon influences group IV Zr and Hf more than any other groups on the periodic table.

5.6 Acknowledgements

This study was supported by the U.S. Department of Energy, Office of Basic Energy Sciences, Division of Material Sciences and Engineering, under award DE SC0010802. K.K. also thanks Dr. Nicolas P. Martin for his useful suggestions for single-crystal X-ray diffraction data collections.

6. Conclusions

The work presented in this dissertation is focused on extracting structural information of metal-oxo clusters using in-house laboratory X-ray scattering methods to derive fundamental and applied information about aqueous-metal oxide systems. SAXS is routinely used in laboratories to determine speciation of metal-oxo clusters in solution regarding size and shape information. The novelty of this work is utilizing X-ray total scattering measurements with a laboratory diffractometer. These methods are mostly used at synchrotron sources where the accessibility is very competitive, thus, possessing a laboratory facility is a huge benefit. This dissertation includes four separated projects showing various chemical problems where scattering techniques were successfully applied to access structure, and sometimes property, information. In general, PDF analysis can work as a very powerful complimentary method, depending on the studied chemical system.

The first study is an amorphization pathway in solid-state. We developed a model to describe the crystal structure of the commercially available hydrated $\text{NaBiO}_3 \cdot \text{XH}_2\text{O}$. PDF analysis supported the hypothesis of a turbostatic disorder in the structure. Upon acid-treatment, the crystalline sheets degrade leaving small metal-oxo fragments with no long-range order in solid-state. PDF analysis followed this reaction pathway by losing long-range order in the reaction and observation of the new metal-metal correlations. XPS analysis indicates one chemical environment for Bi^{5+} and two, new distinct chemical environments for Bi^{3+} in the solid state. We hypothesized a mixed edge-sharing and corner-sharing environments between Bi-O polyhedra supported by the broad metal-metal correlation peak observed in the PDF. This study showed that degradation of crystalline material to amorphous product can be followed successfully by PDF. The study provide better understanding of structural features in acidified sodium-bismuthate, which has potential in photocatalysis, as well as it forms during the process of americium oxidation in reprocessing and recovery of spent nuclear fuel.

Following the bismuthate project, we performed solution X-ray total scattering measurements. Even with synchrotron sources, study of metal-oxo cluster solutions does

not have a very extensive literature, thus benchmarking of this technique is required. Our findings proved that solution measurements can be performed successfully, and even yield publishable data (several examples described). Reaction conditions are critical for these measurements, where the two main factors are the scattering power of the present elements and their concentrations. Generally, heavier elements provide stronger scattering, and higher concentration can overcome signal of H₂O. During the benchmarking procedure, we tested the pure H₂O solvent and standard solutions of [SiW₁₂O₄₀]⁵⁻ Keggin ion. Then, we probed different uranyl-peroxo nanocluster solutions (U60, U32R, U28 and U24 saturated solutions). Depending on the concentrations either we see all the features of the individual clusters determined in simulations, or only the most intense correlations appear besides the intense water signal. Thus, interpretation of PDF of metal-oxo cluster solutions mostly are qualitative or semi-quantitative, requires the precise knowledge of the solution conditions.

The last two projects of this dissertation demonstrates two specific systems where reaction conditions are far from ideal scattering features (Ti: low scattering power; Zr: low concentrations), but solution PDF data still provides valuable information. Solution studies of aqueous TiOSO₄ showed unprecedented results of quick self-assembly of purely inorganic titanium-oxo cluster. SAXS, Ti K-edge EXAFS and single-crystal data supported the hypothesis of the presence of titanium-oxo cluster in aqueous solutions of TiOSO₄, proved to be the {Ti₁₈}-cluster. In addition, following the changes in both solid-state (PDF) and solution state (SAXS and Ti-EXAFS) we probed the transition to the TiO₂ anatase phase. The study provide significant knowledge about titanium-based metal-oxo clusters and the formation of titanium-oxide from aqueous conditions that is important industrial product.

The last study presented new zirconium-peroxo oxalate clusters, where we identified four new cluster structures, where counter cation differentiated the different cluster geometries. The clusters feature unique face-shared polyhedra connectivity, and in three cases 9-coordinated Zr coordination, shown by single-crystal X-ray diffraction data. Interestingly, this connectivity can stay intact when they dissolve in water, proved by PDF measurements. The study also show interesting aspect where counter cations determine the structure of products: while zirconium-peroxo cluster formation is observed for TMA⁺, Li⁺,

K^+ and Rb^+ cations (nuclearity varies with counter cation), Na^+ or Cs^+ ions result conventional tetraoxalate complexes. Interestingly, applying identical reaction conditions using Hf precursor material instead of Zr, multi- (with TMA^+ , Li^+ or Na^+ ions) or mononuclear (K^+ , Rb^+ , Cs^+) conventional oxalate coordination compounds form which difference can be beneficial for distinguishing Zr and Hf chemistry for both understanding of the periodic table, and in applications where separation of Zr and Hf is crucial.

In summary, in-house total X-ray scattering measurements provide a very powerful tool to acquire structural information from various systems. The thesis emphasizes the importance of PDF analysis of total scattering measurements. Both solid-state and solution samples can be tested to extract information about atom-pair correlations. Studying solution samples of metal-oxo clusters by this technique is relatively underdeveloped, where the type of elements, concentrations, solvent, counter ions all influence the resulted pair distribution function. This dissertation provided numerous examples where individual clusters are observed by this method, and also where only subtle changes in PDF indicate the existence of bigger species in the solution compared to reference samples. Thus, for absolute identification, additional characterization methods (and crystallizations) are required. This thesis has shown a broad conspectus about the possibilities of using this instrumentation in future studies.

7. Bibliography

- (1) Cronin, L.; Müller, A. Special Issue. *Chem. Soc. Rev.* **2012**, *41* (22), 7325–7648.
- (2) Bøjesen, E. D.; Iversen, B. B. The Chemistry of Nucleation. *CrystEngComm* **2016**, *18* (43), 8332–8353.
- (3) Gebauer, D.; Cölfen, H. Prenucleation Clusters and Non-Classical Nucleation. *Nano Today* **2011**, *6* (6), 564–584.
- (4) Lee, J.; Yang, J.; Kwon, S. G.; Hyeon, T. Nonclassical Nucleation and Growth of Inorganic Nanoparticles. *Nat. Rev. Mater.* **2016**, 16034.
- (5) Nyman, M.; Burns, P. C. A Comprehensive Comparison of Transition-Metal and Actinyl Polyoxometalates. *Chem. Soc. Rev. Chem. Soc. Rev* **2012**, *41* (41), 7354–7367.
- (6) Hutin, M.; Rosnes, M. H.; Long, D. L.; Cronin, L. *Polyoxometalates: Synthesis and Structure - From Building Blocks to Emergent Materials*; Elsevier Ltd., 2013; Vol. 2.
- (7) Wang, W.; Fullmer, L. B.; Bandeira, N. A. G.; Goberna-Ferrón, S.; Zakharov, L. N.; Bo, C.; Keszler, D. A.; Nyman, M. Crystallizing Elusive Chromium Polycations. *Chem* **2016**, *1* (6), 887–901.
- (8) Sommers, J. A.; Hutchison, D. C.; Martin, N. P.; Kozma, K.; Keszler, D. A.; Nyman, M. Peroxide-Promoted Disassembly-Reassembly of Zr-Polyoxocations. *J. Am. Chem. Soc.* **2019**, *141*, 16894–16902.
- (9) Kikhney, A. G.; Svergun, D. I. A Practical Guide to Small Angle X-Ray Scattering (SAXS) of Flexible and Intrinsically Disordered Proteins. *FEBS Lett.* **2015**, *589* (19), 2570–2577.
- (10) Nyman, M. Small-Angle X-Ray Scattering to Determine Solution Speciation of Metal-Oxo Clusters. *Coord. Chem. Rev.* **2017**, *352*, 461–472.
- (11) Li, M.; Zhang, M.; Wang, W.; Cheng, S. Z. D.; Yin, P. The Applications of Small-Angle X-Ray Scattering in Studying Nano-Scaled Polyoxometalate Clusters in Solutions. *J. Nanoparticle Res.* **2018**, *20* (5), 124.

- (12) Li, T.; Senesi, A. J.; Lee, B. Small Angle X-Ray Scattering for Nanoparticle Research. *Chem. Rev.* **2016**, *116* (18), 11128–11180.
- (13) Borfecchia, E.; Garino, C.; Salassa, L.; Lamberti, C.; A, P. T. R. S. Synchrotron Ultrafast Techniques for Photoactive Transition Metal Complexes. **2013**, No. June.
- (14) Ilavsky, J.; Jemian, P. R. Irena: Tool Suite for Modeling and Analysis of Small-Angle Scattering. *J. Appl. Crystallogr.* **2009**, *42* (2), 347–353.
- (15) Zhang, R.; Thiyagarajan, P.; Tiede, D. M. Probing Protein Fine Structures by Wide Angle Solution X-Ray Scattering. *J. Appl. Crystallogr.* **2000**, *33* (3 I), 565–568.
- (16) Tiede, D. M.; Zhang, R.; Chen, L. X.; Yu, L.; Lindsey, J. S. Structural Characterization of Modular Supramolecular Architectures in Solution. *J. Am. Chem. Soc.* **2004**, *126* (43), 14054–14062.
- (17) Egami, T.; Billinge, S. J. L. *Underneath the Bragg Peaks: Structural Analysis of Complex Materials*; Pergamon, 2012; Vol. 7.
- (18) Juhas, P.; Davis, T.; Farrow, C. L.; Billinge, S. J. L. PDFgetX3: A Rapid and Highly Automatable Program for Processing Powder Diffraction Data into Total Scattering Pair Distribution Functions. *J. Appl. Crystallogr.* **2013**, *46* (2), 560–566.
- (19) Farrow, C. L.; Juhas, P.; Liu, J. W.; Bryndin, D.; Božin, E. S.; Bloch, J.; Proffen, T.; Billinge, S. J. L. PDFfit2 and PDFgui: Computer Programs for Studying Nanostructure in Crystals. *J. physics. Condens. matter* **2007**, *19* (33), 335219.
- (20) Keen, D. A. A Comparison of Various Commonly Used Correlation Functions for Describing Total Scattering. *J. Appl. Cryst.* **2001**, *34*, 172–177.
- (21) Tucker, M. G.; Keen, D. A.; Dove, M. T.; Goodwin, A. L.; Hui, Q. RMCProfile: Reverse Monte Carlo for Polycrystalline Materials. *J. Phys. Condens. Matter* **2007**, *19*, 335218.
- (22) Proffen, H.; Act, C.; Miinchen, L. M. U. Discus a Program for Diffuse Scattering and Defect Structure Simulation. *J. Appl. Cryst* **1997**, *30*, 171–175.
- (23) Sommariva, M.; Gateshki, M.; Gertenbach, J.-A.; Bolze, J.; König, U.; Vasile, B. S.; Surdu, V.-A. Characterizing Nanoparticles with a Laboratory Diffractometer: From Small-Angle to Total X-Ray Scattering. *Powder Diffr.* **2014**, *29* (2013), S47–S53.
- (24) Thomae, S. L. J.; Prinz, N.; Hartmann, T.; Teck, M.; Correll, S.; Zobel, M. Pushing

- Data Quality for Laboratory Pair Distribution Function Experiments. *Rev. Sci. Instrum.* **2019**, *90* (4), 043905.
- (25) Sommariva, M. Multi-Technique Approach for Nanoparticles Characterization on a Laboratory X-Ray Diffractometer. *Solid State Phenom.* **2013**, *203–204*, 17–20.
- (26) Sadler, P. J.; Li, H.; Sun, H. Coordination Chemistry of Metals in Medicine: Target Sites for Bismuth. *Coord. Chem. Rev.* **1999**, *185–186*, 689–709.
- (27) Esquivel-Gaon, M.; Anguissola, S.; Garry, D.; Gallegos-Melgar, A. del C.; Saldaña, J. M.; Dawson, K. A.; De Vizcaya-Ruiz, A.; Del Razo, L. M. Bismuth-Based Nanoparticles as the Environmentally Friendly Replacement for Lead-Based Piezoelectrics. *RSC Adv.* **2015**, *5* (35), 27295–27304.
- (28) Ding, Y.; Xia, X.; Ruan, Y.; Tang, H. In Situ H⁺-Mediated Formation of Singlet Oxygen from NaBiO₃ for Oxidative Degradation of Bisphenol A without Light Irradiation: Efficiency, Kinetics, and Mechanism. *Chemosphere* **2015**, *141*, 80–86.
- (29) Ding, Y.; Zhou, P.; Tang, H. Visible-Light Photocatalytic Degradation of Bisphenol A on NaBiO₃ Nanosheets in a Wide PH Range: A Synergistic Effect between Photocatalytic Oxidation and Chemical Oxidation. *Chem. Eng. J.* **2016**, *291*, 149–160.
- (30) Takei, T.; Haramoto, R.; Dong, Q.; Kumada, N.; Yonesaki, Y.; Kinomura, N.; Mano, T.; Nishimoto, S.; Kameshima, Y.; Miyake, M. Photocatalytic Activities of Various Pentavalent Bismuthates under Visible Light Irradiation. *J. Solid State Chem.* **2011**, *184* (8), 2017–2022.
- (31) Kako, T.; Zou, Z.; Katagiri, M.; Ye, J. Decomposition of Organic Compounds over NaBiO₃ under Visible Light Irradiation. *Chem. Mater.* **2007**, No. 7, 198–202.
- (32) Ding, Y.; Yang, F.; Zhu, L.; Wang, N.; Tang, H. Bi³⁺ Self Doped NaBiO₃ Nanosheets: Facile Controlled Synthesis and Enhanced Visible Light Photocatalytic Activity. *Appl. Catal. B Environ.* **2015**, *164*, 151–158.
- (33) Ford-Smith, M. H.; Habeeb, J. J. Kinetics of Oxidation-Reduction Reactions between Elements of Groups V and VII. Part I. Bismuth(V) with Halide Ions and Other Reductants. *J. Chem. Soc. Dalton Trans.* **1973**, 0 (4), 461.
- (34) Hara, M.; Suzuki, S. Oxidation of Americium (III) with Sodium Bismuthate. *J. Radioanal. Chem.* **1977**, *36*, 95–104.

- (35) Martin, L. R.; Mincher, B. J.; Schmitt, N. C. Extraction of Americium(VI) by a Neutral Phosphonate Ligand. *J. Radioanal. Nucl. Chem.* **2009**, 282 (2), 523–526.
- (36) Mincher, B. J.; Martin, L. R.; Schmitt, N. C. Diamylamylphosphonate Solvent Extraction of Am(VI) from Nuclear Fuel Raffinate Simulant Solution. *Solvent Extr. Ion Exch.* **2012**, 30 (5), 445–456.
- (37) Mincher, B. J.; Martin, L. R.; Schmitt, N. C. Tributylphosphate Extraction Behavior of Bismuthate-Oxidized Americium. *Inorg. Chem.* **2008**, 47 (15), 6984–6989.
- (38) Grimes, T. S.; Horne, G. P.; Dares, C. J.; Pimblott, S. M.; Mezyk, S. P.; Mincher, B. J. Kinetics of the Autoreduction of Hexavalent Americium in Aqueous Nitric Acid. *Inorg. Chem.* **2017**, acs.inorgchem.7b00990.
- (39) Mills, A.; Li, X. Kinetics of Reductive Dissolution of Sodium Bismuthate by CeIII and MnII Ions. *J. Chem. Soc. Faraday Trans.* **1994**, 90 (19), 2939–2944.
- (40) Kumada, N.; Kinomura, N.; Sleight, A. W. Neutron Powder Diffraction Refinement of Ilmenite-Type Bismuth Oxides: ABiO₃ (A = Na, Ag). *Mater. Res. Bull.* **2000**, 35 (14–15), 2397–2402.
- (41) Aurivillius, B. X-Ray Studies on “Sodium Metabismuthate.” 1955, pp 1219–1221.
- (42) Nguyen, T. N.; Giaquinta, D. M.; Davis, W. M.; zur Loye, H. C. Electrosynthesis of KBiO₃ (Potassium Bismuth Oxide): A Potassium Ion Conductor with the KSbO₃ (Potassium Antimony Oxide) Tunnel Structure. *Chem. Mater.* **1993**, 5 (9), 1273–1276.
- (43) Sinkov, S. I.; Lumetta, G. J. Americium(III) Oxidation by Copper(III) Periodate in Nitric Acid Solution as Compared with the Action of Bi(V) Compounds of Sodium, Lithium, and Potassium. *Submitted* **2015**, 103 (8), 541–552.
- (44) Zheng, T.; Dahn, J. R. The Effect of Turbostratic Disorder on the Staging Transitions in Lithium Intercalated Graphite. *Synth. Met.* **1995**, 73 (1), 1–7.
- (45) Petkov, V.; Trikalitis, P. N.; Bozin, E. S.; Billinge, S. J. L.; Vogt, T.; Kanatzidis, M. G. Structure of V₂O₅·nH₂O Xerogel Solved by the Atomic Pair Distribution Function Technique. *Phys. B* **2002**, No. 8, 10157–10162.
- (46) Billinge, S. J. L.; Kanatzidis, M. G. Beyond Crystallography: The Study of Disorder, Nanocrystallinity and Crystallographically Challenged Materials with Pair Distribution Functions. *Chem. Commun.* **2004**, No. 7, 749.

- (47) Kinomura, N.; Hosoda, M.; Kumada, N.; Kojima, H. Preparation of Pyrochlore Type $\text{Na}_{0.39}\text{Bi}_{3.47}\text{O}_7$ Containing Bi^{5+} by Low Temperature Hydrothermal Reaction. *J. Ceram. Soc. Jpn.* **1993**, *963*, 966.
- (48) Hill, C. L. Progress and Challenges in Polyoxometalate-Based Catalysis and Catalytic Materials Chemistry. *J. Mol. Catal. A Chem.* **2007**, *262* (1–2), 2–6.
- (49) Ji, Y.; Huang, L.; Hu, J.; Streb, C.; Song, Y. Polyoxometalate-Functionalized Nanocarbon Materials for Energy Conversion, Energy Storage and Sensor Systems. *Energy Environ. Sci.* **2015**, *8* (3), 776–789.
- (50) Shiddiq, M.; Komijani, D.; Duan, Y.; Gaita-Ariño, A.; Coronado, E.; Hill, S. Enhancing Coherence in Molecular Spin Qubits via Atomic Clock Transitions. *Nature* **2016**, *531* (7594), 348–351.
- (51) Herrmann, S.; Ritchie, C.; Streb, C. Polyoxometalate - Conductive Polymer Composites for Energy Conversion, Energy Storage and Nanostructured Sensors. *Dalt. Trans.* **2015**, *44* (16), 7092–7104.
- (52) Qiu, J.; Burns, P. C. Clusters of Actinides with Oxide, Peroxide, or Hydroxide Bridges. *Chem. Rev.* **2013**, *113* (2), 1097–1120.
- (53) Hasenknopf, B. Polyoxometalates: Introduction to a Class of Inorganic Compounds and Their Biomedical Applications. *Front. Biosci.* **2005**, *10*, 275–287.
- (54) Keggin, J. F. Structure of the Molecule of 12-Phosphotungstic Acid. *Nature* **1933**, *131* (3321), 908–909.
- (55) Johansson, G. On the Crystal Structures of Some Basic Aluminium Salts. *Acta Chem. Scand.* **1960**, *14*, 771–773.
- (56) Casey, W. H. Large Aqueous Aluminum Hydroxide Molecules. *Chem. Rev.* **2006**, *106* (1), 1–16.
- (57) Saha, S.; Park, D. H.; Hutchison, D. C.; Olsen, M. R.; Zakharov, L. N.; Marsh, D.; Goberna-Ferrón, S.; Frederick, R. T.; Diulus, J. T.; Kenane, N.; et al. Alkyltin Keggin Clusters Templated by Sodium. *Angew. Chemie - Int. Ed.* **2017**, *56* (34), 10140–10144.
- (58) Michel, F. M.; Ehm, L.; Antao, S. M.; Lee, P. L.; Chupas, P. J.; Liu, G.; Strongin, D. R.; Schoonen, M. A. A.; Phillips, B. L.; Parise, J. B. The Structure of Ferrihydrite, a Nanocrystalline Material. *Science* (80-.). **2007**, *316* (June), 1726–1729.

- (59) Sadeghi, O.; Zakharov, L. N.; Nyman, M. Aqueous Formation and Manipulation of the Iron-Oxo Keggin Ion. *Science* (80-.). **2015**, *347* (6228), 1359–1362.
- (60) Wang, W.; Amiri, M.; Kozma, K.; Lu, J.; Zakharov, L. N.; Nyman, M. Reaction Pathway to the Only Open-Shell Transition-Metal Keggin Ion without Organic Ligation. *Eur. J. Inorg. Chem.* **2018**, *2018* (42), 4638–4642.
- (61) Nyman, M.; Burns, P. C. A Comprehensive Comparison of Transition-Metal and Actinyl Polyoxometalates. *Chem. Soc. Rev.* **2012**, *41* (22), 7354–7367.
- (62) Burns, P. C.; Kubatko, K. A.; Sigmon, G.; Fryer, B. J.; Gagnon, J. E.; Antonio, M. R.; Soderholm, L. Actinyl Peroxide Nanospheres. *Angew. Chemie - Int. Ed.* **2005**, *44* (14), 2135–2139.
- (63) Forbes, T. Z.; McAlpin, J. G.; Murphy, R.; Burns, P. C. Metal-Oxygen Isopolyhedra Assembled into Fullerene Topologies. *Angew. Chemie - Int. Ed.* **2008**, *47* (15), 2824–2827.
- (64) Sigmon, G. E.; Unruh, D. K.; Ling, J.; Weaver, B.; Ward, M.; Pressprich, L.; Simonetti, A.; Burns, P. C. Symmetry versus Minimal Pentagonal Adjacencies in Uranium-Based Polyoxometalate Fullerene Topologies. *Angew. Chemie - Int. Ed.* **2009**, *48* (15), 2737–2740.
- (65) Burns, P. C.; Nyman, M. Captivation with Encapsulation: A Dozen Years of Exploring Uranyl Peroxide Capsules. *Dalt. Trans.* **2018**, *47* (17), 5916–5927.
- (66) Sigmon, G. E.; Ling, J.; Unruh, D. K.; Moore-Shay, L.; Ward, M.; Weaver, B.; Burns, P. C. Uranyl-Peroxide Interactions Favor Nanocluster Self-Assembly. *J. Am. Chem. Soc.* **2009**, *131* (46), 16648–16649.
- (67) Xie, J.; Neal, H.; Szymanowski, J.; Burns, P. C.; Alam, T. M.; Nyman, M.; Gagliardi, L. Resolving Confined ⁷Li Dynamics of Uranyl Peroxide Capsule U24. *Inorg. Chem.* **2018**, *57*, 5514–5525.
- (68) Renier, O.; Falaise, C.; Neal, H.; Kozma, K.; Nyman, M. Closing Uranyl Polyoxometalate Capsules with Bismuth and Lead Polyoxocations. *Angew. Chemie - Int. Ed.* **2016**, *55* (43), 13480–13484.
- (69) Arteaga, A.; Zhang, L.; Hickam, S.; Dembowski, M.; Burns, P. C.; Nyman, M. Uranyl–Peroxide Capsule Self-Assembly in Slow Motion. *Chem. - A Eur. J.* **2019**, *25* (24), 6087–6091.

- (70) Billinge, S. J. L. The Rise of the X-Ray Atomic Pair Distribution Function Method: A Series of Fortunate Events. *Philosophical Transactions of the Royal Society A: Mathematical, Physical and Engineering Sciences*. 2019.
- (71) Head-Gordon, T.; Hura, G. Water Structure from Scattering Experiments and Simulation. *Chem. Rev.* **2002**, *102* (8), 2651–2669.
- (72) Amann-Winkel, K.; Bellissent-Funel, M.-C.; Bove, L. E.; Loerting, T.; Nilsson, A.; Paciaroni, A.; Schlesinger, D.; Skinner, L. X-Ray and Neutron Scattering of Water. *Chem. Rev.* **2016**, *116* (13), 7570–7589.
- (73) Neilson, G. W.; Adya, A. K.; Ansell, S. 8 Neutron and X-Ray Diffraction Studies on Complex Liquids. *Annu. Reports Prog. Chem. - Sect. C* **2002**, *98* (1), 271–320.
- (74) Meisburger, S. P.; Thomas, W. C.; Watkins, M. B.; Ando, N. X-Ray Scattering Studies of Protein Structural Dynamics. *Chem. Rev.* **2017**, *117* (12), 7615–7672.
- (75) Ohtaki, H.; Fukushima, N. A Structural Study of Saturated Aqueous Solutions of Some Alkali Halides by X-Ray Diffraction. *J. Solution Chem.* **1992**, *21* (1), 23–38.
- (76) Lawrence, R. M. X-Ray Diffraction Studies of Aqueous Alkali-Metal Halide Solutions. *J. Chem. Phys.* **1967**, *47* (11), 4758–4765.
- (77) Jalilehvand, F.; Spångberg, D.; Lindqvist-Reis, P.; Hermansson, K.; Persson, I.; Sandström, M. Hydration of the Calcium Ion. An EXAFS, Large-Angle x-Ray Scattering, and Molecular Dynamics Simulation Study. *J. Am. Chem. Soc.* **2001**, *123* (3), 431–441.
- (78) Broadbent, R. D.; Neilson, G. W.; Sandstrom, M. The Hydration Structure of Cr³⁺ in a Concentrated Aqueous- Solution. *J. Physics-Condensed Matter* **1992**, *4* (3), 639–648.
- (79) Smcl, I. I. I.; Habenschuss, A.; Spedding, F. H. The Coordination (Hydration) of Rare Earth Ions in Aqueous Chloride Solutions from X-ray Diffraction. III. SmCl₃, EuCl₃, and Series Behavior. **2003**, *442* (1980).
- (80) Leroy, F.; Miró, P.; Poblet, J. M.; Bo, C.; Bonet Ávalos, J. Keggin Polyoxoanions in Aqueous Solution: Ion Pairing and Its Effect on Dynamic Properties by Molecular Dynamics Simulations. *J. Phys. Chem. B* **2008**, *112* (29), 8591–8599.
- (81) Becker, J.; Bremholm, M.; Tyrsted, C.; Pauw, B.; Jensen, K. M. O.; Eltzholt, J.; Christensen, M.; Iversen, B. B. Experimental Setup for in Situ X-Ray

- SAXS/WAXS/PDF Studies of the Formation and Growth of Nanoparticles in near- and Supercritical Fluids. *J. Appl. Crystallogr.* **2010**, *43* (4), 729–736.
- (82) Hu, Y.-J.; Knope, K. E.; Skanthakumar, S.; Kanatzidis, M. G.; Mitchell, J. F.; Soderholm, L. Understanding the Role of Aqueous Solution Speciation and Its Application to the Directed Syntheses of Complex Oxidic Zr Chlorides and Sulfates. **2013**.
- (83) Kalaji, A.; Skanthakumar, S.; Kanatzidis, M. G.; Mitchell, J. F.; Soderholm, L. Changing Hafnium Speciation in Aqueous Sulfate Solutions: A High-Energy X-Ray Scattering Study. *Inorg. Chem.* **2014**, *53* (12), 6321–6328.
- (84) Sigmon, G. E.; Burns, P. C. Rapid Self-Assembly of Uranyl Polyhedra into Crown Clusters. *J. Am. Chem. Soc.* **2011**, *133* (24), 9137–9139.
- (85) Juhás, P.; Davis, T.; Farrow, C. L.; Billinge, S. J. L. PDFgetX3 Documentation. 2015.
- (86) Levy, H. A.; Agron, P. A.; Danford, M. D. Structure of Silico-Tungstic Acid in Aqueous Solution. *J. Chem. Phys.* **1959**, *30* (6), 1486–1488.
- (87) Peruski, K. M.; Bernales, V.; Dembowski, M.; Lobeck, H. L.; Pellegrini, K. L.; Sigmon, G. E.; Hickam, S.; Wallace, C. M.; Szymanowski, J. E. S.; Balboni, E.; et al. Uranyl Peroxide Cage Cluster Solubility in Water and the Role of the Electrical Double Layer. *Inorg. Chem.* **2017**, acs.inorgchem.6b02435.
- (88) Wylie, E. M.; Peruski, K. M.; Weidman, J. L.; Phillip, W. A.; Burns, P. C. Ultrafiltration of Uranyl Peroxide Nanoclusters for the Separation of Uranium from Aqueous Solution. *ACS Appl. Mater. Interfaces* **2014**, *6* (1), 473–479.
- (89) Falaise, C.; Nyman, M. The Key Role of U28 in the Aqueous Self-Assembly of Uranyl Peroxide Nanocages. *Chem. - A Eur. J.* **2016**, *22* (41), 14678–14687.
- (90) S. J. L. Billinge; V. Petkov; Th. Proffen. Structure on Different Length-Scales from Powder Diffraction: The Real-Space Pair Distribution Function (PDF) Technique.
- (91) Antonio, M. R.; Nyman, M.; Anderson, T. M. Direct Observation of Contact Ion-Pair Formation in Aqueous Solution. *Angew. Chemie - Int. Ed.* **2009**, *48* (33), 6136–6140.
- (92) Fullmer, L. B.; Molina, P. I.; Antonio, M. R.; Nyman, M. Contrasting Ion-Association Behaviour of Ta and Nb Polyoxometalates. *Dalt. Trans.* **2014**, *43* (41),

15295–15299.

- (93) Fullmer, L. B.; Nyman, M. Probing Crystallization Pathways in Group V Polyoxometalate Solutions. *J. Clust. Sci.* **2017**, *28* (2), 813–823.
- (94) Balogh, E.; Anderson, T. M.; Rustad, J. R.; Nyman, M.; Casey, W. H. Rates of Oxygen-Isotope Exchange between Sites in the [H_xTa 6O₁₉](8-x)-(Aq) Lindqvist Ion and Aqueous Solutions: Comparisons to [H_xNb6O₁₉] (8-x)-(Aq). *Inorg. Chem.* **2007**, *46* (17), 7032–7039.
- (95) Mile, V.; Pusztai, L.; Dominguez, H.; Pizio, O. Understanding the Structure of Aqueous Cesium Chloride Solutions by Combining Diffraction Experiments, Molecular Dynamics Simulations, and Reverse Monte Carlo Modeling. *J. Phys. Chem. B* **2009**, *113* (31), 10760–10769.
- (96) Li, F.; Yuan, J.; Li, D.; Li, S.; Han, Z. Study on the Structure of Aqueous Potassium Chloride Solutions Using the X-Ray Diffraction and Raman Spectroscopy Methods. *J. Mol. Struct.* **2015**, *1081*, 38–43.
- (97) Sures, D. J.; Serapian, S. A.; Kozma, K.; Molina, P. I.; Bo, C.; Nyman, M. Electronic and Relativistic Contributions to Ion-Pairing in Polyoxometalate Model Systems. *Phys. Chem. Chem. Phys.* **2017**, *19* (13), 8715–8725.
- (98) Kozma, K.; Wang, M.; Molina, P. I.; Martin, N. P.; Feng, Z.; Nyman, M. The Role of Titanium-Oxo Clusters in the Sulfate Process for TiO₂ Production. *Dalt. Trans.* **2019**, *48*, 11086–11093.
- (99) Fujishima, A.; Honda, K. Electrochemical Photolysis of Water at a Semiconductor Electrode. *Nature* **1972**, *238* (5358), 37–38.
- (100) Ma, Y.; Wang, X. L.; Jia, Y. S.; Chen, X. B.; Han, H. X.; Li, C. Titanium Dioxide-Based Nanomaterials for Photocatalytic Fuel Generations. *Chem. Rev.* **2014**, *114* (19), 9987–10043.
- (101) Schneider, J.; Matsuoka, M.; Takeuchi, M.; Zhang, J.; Horiuchi, Y.; Anpo, M.; Bahnemann, D. W. Understanding TiO₂ Photocatalysis: Mechanisms and Materials. *Chem. Rev.* **2014**, *114* (19), 9919–9986.
- (102) Hashimoto, K.; Irie, H.; Fujishima, A. TiO₂ Photocatalysis: A Historical Overview and Future Prospects. *Jpn. J. Appl. Phys.* **2005**, *44* (12), 8269–8285.
- (103) De Angelis, F.; Di Valentin, C.; Fantacci, S.; Vittadini, A.; Selloni, A. Theoretical

- Studies on Anatase and Less Common TiO₂ Phases: Bulk, Surfaces, and Nanomaterials. *Chem. Rev.* **2014**, *114* (19), 9708–9753.
- (104) Zhang, Y.; Jiang, Z.; Huang, J.; Lim, L. Y.; Li, W.; Deng, J.; Gong, D.; Tang, Y.; Lai, Y.; Chen, Z. Titanate and Titania Nanostructured Materials for Environmental and Energy Applications: A Review. *RSC Adv.* **2015**, *5* (101), 79479–79510.
- (105) Li, Y. F.; Liu, Z. P. Particle Size, Shape and Activity for Photocatalysis on Titania Anatase Nanoparticles in Aqueous Surroundings. *J. Am. Chem. Soc.* **2011**, *133* (39), 15743–15752.
- (106) Lan, Y.; Lu, Y.; Ren, Z. Mini Review on Photocatalysis of Titanium Dioxide Nanoparticles and Their Solar Applications. *Nano Energy* **2013**, *2* (5), 1031–1045.
- (107) Rahimi, N.; Pax, R. A.; Gray, E. M. A Review of Functional Titanium Oxides. I: TiO₂ and Its Modifications. *Prog. Solid State Chem.* **2016**, *44* (3), 86–105.
- (108) Shi, H.; Magaye, R.; Castranova, V.; Zhao, J. Titanium Dioxide Nanoparticles: A Review of Current Toxicological Data. *Part. Fibre Toxicol.* **2013**, *10* (15).
- (109) Szilágyi, I.; Königsberger, E.; May, P. M. Characterization of Chemical Speciation of Titanyl Sulfate Solutions for Production of Titanium Dioxide Precipitates. *Inorg. Chem.* **2009**, *48* (5), 2200–2204.
- (110) Zhang, W.; Zhu, Z.; Cheng, C. Y. A Literature Review of Titanium Metallurgical Processes. *Hydrometallurgy* **2011**, *108* (3–4), 177–188.
- (111) Hixson, A. W.; Plechner, W. W. Hydrated Titanium Oxide: Thermal Precipitation from Titanium Sulfate Solutions. *Ind. Eng. Chem.* **1933**, *25* (3), 262–274.
- (112) Wang, W.; Liu, Y.; Xue, T.; Li, J.; Chen, D.; Qi, T. Mechanism and Kinetics of Titanium Hydrolysis in Concentrated Titanyl Sulfate Solution Based on Infrared and Raman Spectra. *Chem. Eng. Sci.* **2015**, *134*, 196–204.
- (113) Simonsen, M.; Sjøgaard, E. Identification of Ti Clusters during Nucleation and Growth of Sol-Gel Derived TiO₂ Nanoparticles. *Eur. J. Mass Spectrom.* **2013**, *19* (4), 265–273.
- (114) Simonsen, M. E.; Sjøgaard, E. G. Sol-Gel Reactions of Titanium Alkoxides and Water: Influence of PH and Alkoxy Group on Cluster Formation and Properties of the Resulting Products. *J. Sol-Gel Sci. Technol.* **2010**, *53* (3), 485–497.
- (115) Sadeghi, O.; Zakharov, L. N.; Nyman, M. Aqueous Formation and Manipulation of

- the Iron-Oxo Keggin Ion. *Science* (80-.). **2015**, *347* (6228), 1359–1362.
- (116) Pope, M. T. *Heteropoly and Isopoly Oxometalates*; 1983; Vol. 8.
- (117) Falaise, C.; Neal, H. A.; Nyman, M. U(IV) Aqueous Speciation from the Monomer to UO₂ Nanoparticles: Two Levels of Control from Zwitterionic Glycine Ligands. *Inorg. Chem.* **2017**, *56* (11), 6591–6598.
- (118) Sadeghi, O.; Amiri, M.; Reinheimer, E. W.; Nyman, M. The Role of Bi³⁺ in Promoting and Stabilizing Iron Oxo Clusters in Strong Acid. *Angew. Chemie - Int. Ed.* **2018**, *57*, 6247–6250.
- (119) Fang, W.-H.; Zhang, L.; Zhang, J. Synthetic Strategies, Diverse Structures and Tuneable Properties of Polyoxo-Titanium Clusters. *Chem. Soc. Rev.* **2018**, *47* (2), 404–421.
- (120) Squattrito, P. J.; Rudolf, P. R.; Clearfield, A. Crystal Structure of a Complex Basic Zirconium Sulfate. *Inorg. Chem.* **1987**, *26* (25), 4240–4244.
- (121) Ruther, R. E.; Baker, B. M.; Son, J. H.; Casey, W. H.; Nyman, M. Hafnium Sulfate Prenucleation Clusters and the Hf₁₈ Polyoxometalate Red Herring. *Inorg. Chem.* **2014**, *53* (8), 4234–4242.
- (122) Kalaji, A.; Soderholm, L. Aqueous Hafnium Sulfate Chemistry: Structures of Crystalline Precipitates. *Inorg. Chem.* **2014**, *53* (20), 11252–11260.
- (123) Clearfield, A.; Vaughan, P. A. The Crystal Structure of Zirconyl Chloride Octahydrate and Zirconyl Bromide Octahydrate. *Acta Crystallogr.* **1956**, *9* (7), 555–558.
- (124) Muha, G. M.; Vaughan, P. A. Structure of the Complex Ion in Aqueous Solutions of Zirconyl and Hafnyl Oxyhalides. *J. Chem. Phys.* **1960**, *33* (1), 194–199.
- (125) Kalaji, A.; Soderholm, L. A Novel Nonanuclear Hafnium Oxide-Hydroxide-Sulphate Cluster Crystallised from Aqueous Solution. *Chem. Commun.* **2014**, *50* (8), 997–999.
- (126) Goberna-Ferron, S.; Park, D. H.; Amador, J. M.; Keszler, D. A.; Nyman, M. Amphoteric Aqueous Hafnium Cluster Chemistry. *Angew. Chemie - Int. Ed.* **2016**, *55* (21), 6221–6224.
- (127) Chakraborty, B.; Weinstock, I. A. Water-Soluble Titanium-Oxides: Complexes, Clusters and Nanocrystals. *Coord. Chem. Rev.* **2019**, *382*, 85–102.

- (128) Zhang, G.; Liu, C.; Long, D. L.; Cronin, L.; Tung, C. H.; Wang, Y. Water-Soluble Pentagonal-Prismatic Titanium-Oxo Clusters. *J. Am. Chem. Soc.* **2016**, *138* (35), 11097–11100.
- (129) Zhang, G.; Hou, J.; Tung, C. H.; Wang, Y. Small Titanium Oxo Clusters: Primary Structures of Titanium(IV) in Water. *Inorg. Chem.* **2016**, *55* (7), 3212–3214.
- (130) Gao, M. Y.; Wang, F.; Gu, Z. G.; Zhang, D. X.; Zhang, L.; Zhang, J. Fullerene-like Polyoxotitanium Cage with High Solution Stability. *J. Am. Chem. Soc.* **2016**, *138* (8), 2556–2559.
- (131) Zhang, G.; Li, W.; Liu, C.; Jia, J.; Tung, C. H.; Wang, Y. Titanium-Oxide Host Clusters with Exchangeable Guests. *J. Am. Chem. Soc.* **2018**, *140* (1), 66–69.
- (132) Reichmann, M. G.; Hollandert, F. J.; Bell, A. T. Structure of [Ti₈O₁₂(H₂O)₂₄]C₁₈.HCl.7H₂O. *Acta Crystallogr.* **1987**, *17* (1), 1681–1683.
- (133) Molina, P. I.; Kozma, K.; Santala, M.; Falaise, C.; Nyman, M. Aqueous Bismuth Titanium–Oxo Sulfate Cluster Speciation and Crystallization. *Angew. Chemie - Int. Ed.* **2017**, *56* (51), 16277–16281.
- (134) Tsunashima, R.; Long, D. L.; Miras, H. N.; Gabb, D.; Pradeep, C. P.; Cronin, L. The Construction of High-Nuclearity Isopolyoxoniobates with Pentagonal Building Blocks: [HNb₂₇O₇₆]₁₆-and [H₁₀Nb₃₁O₉₃(CO₃)]₂₃-. *Angew. Chemie - Int. Ed.* **2010**, *49* (1), 113–116.
- (135) Müller, A.; Kögerler, P.; Dress, A. W. M. Giant Metal-Oxide-Based Spheres and Their Topology: From Pentagonal Building Blocks to Keplerales and Unusual Spin Systems. *Coord. Chem. Rev.* **2001**, *222* (1), 193–218.
- (136) Schäffer, C.; Merca, A.; Bögge, H.; Todea, A. M.; Kistler, M. L.; Liu, T.; Thouvenot, R.; Gouzerh, P.; Müller, A. Unprecedented and Differently Applicable Pentagonal Units in a Dynamic Library: A Keplerales of the Type {(W)W₅}₁₂{Mo₂}₃₀. *Angew. Chemie - Int. Ed.* **2009**, *48* (1), 149–153.
- (137) Zhang, G.; Hou, J.; Li, M.; Tung, C.-H.; Wang, Y. Counteranion-Stabilized Titanium(IV) Isopolyoxocationic Clusters Isolated from Water. *Inorg. Chem.* **2016**, *55*, 4704–4709.
- (138) Fan, X.; Wang, J.; Wu, K.; Zhang, L.; Zhang, J. Isomerism in Titanium-Oxo Clusters: Molecular Anatase Model with Atomic Structure and Improved

- Photocatalytic Activity. *Angew. Chemie Int. Ed.* **2019**, *58*, 1320–1323.
- (139) Miyanaga, T.; Watanabe, I.; Ikeda, S. Structures of Hydrated Titanium and Vanadium Ions in Aqueous Solutions Studied by X-Ray Absorption Spectroscopy. *Bull. Chem. Soc. Jpn.* **1990**, *63* (11), 3282–3287.
- (140) Lundberg, D.; Persson, I. Structure of a Hydrated Sulfonatotitanyl(IV) Complex in Aqueous Solution and the Dimethylsulfoxide Solvated Titanyl(IV) Ion in Solution and Solid State. *J. Solution Chem.* **2017**, *46* (2), 476–487.
- (141) Weng, Z.; Wu, Y.; Wang, M.; Jiang, J.; Yang, K.; Huo, S.; Wang, X. F.; Ma, Q.; Brudvig, G. W.; Batista, V. S.; et al. Active Sites of Copper-Complex Catalytic Materials for Electrochemical Carbon Dioxide Reduction. *Nat. Commun.* **2018**, *9* (1), 1–9.
- (142) Wang, L. P.; Leconte, Y.; Feng, Z.; Wei, C.; Zhao, Y.; Ma, Q.; Xu, W.; Bourrioux, S.; Azais, P.; Srinivasan, M.; et al. Novel Preparation of N-Doped SnO₂ Nanoparticles via Laser-Assisted Pyrolysis: Demonstration of Exceptional Lithium Storage Properties. *Adv. Mater.* **2017**, *29* (6), 1603286.
- (143) Wei, C.; Feng, Z.; Baisariyev, M.; Yu, L.; Zeng, L.; Wu, T.; Zhao, H.; Huang, Y.; Bedzyk, M. J.; Sritharan, T.; et al. Valence Change Ability and Geometrical Occupation of Substitution Cations Determine the Pseudocapacitance of Spinel Ferrite XFe₂O₄ (X = Mn, Co, Ni, Fe). *Chem. Mater.* **2016**, *28* (12), 4129–4133.
- (144) Wei, C.; Feng, Z.; Scherer, G. G.; Barber, J.; Shao-Horn, Y.; Xu, Z. J. Cations in Octahedral Sites: A Descriptor for Oxygen Electrocatalysis on Transition-Metal Spinel. *Adv. Mater.* **2017**, *29* (23), 1–8.
- (145) Feng, Z.; Ma, Q.; Lu, J.; Feng, H.; Elam, J. W.; Stair, P. C.; Bedzyk, M. J. Atomic-Scale Cation Dynamics in a Monolayer VOX/ α -Fe₂O₃ catalyst. *RSC Adv.* **2015**, *5* (126), 103834–103840.
- (146) Pottier, A.; Cassaignon, S.; Chanéac, C.; Villain, F.; Tronc, E.; Jolivet, J.-P. Size Tailoring of TiO₂ Anatase Nanoparticles in Aqueous Medium and Synthesis of Nanocomposites. Characterization by Raman Spectroscopy. *J. Mater. Chem.* **2003**, *13* (4), 877–882.
- (147) Manicone, P. F.; Rossi Iommetti, P.; Raffaelli, L. An Overview of Zirconia Ceramics: Basic Properties and Clinical Applications. *J. Dent.* **2007**, *35* (11), 819–

826.

- (148) Ganguly, C. Advances in Zirconium Technology for Nuclear Reactor Application. In *Proceedings of the symposium Zirconium - 2002*; 2002; pp 1–27.
- (149) Lemaignan, C.; Motta, A. T. *Zirconium Alloys in Nuclear Applications*; Wiley-VCH Verlag GmbH & Co. KGaA: Weinheim, Germany, 2006.
- (150) Lee, D. B. N.; Roberts, M.; Bluchel, C. G.; Odell, R. A. Zirconium: Biomedical and Nephrological Applications. *ASAIO J.* **2010**, *56* (6), 550–556.
- (151) Abd El-Ghany, O. S.; Sherief, A. H. Zirconia Based Ceramics, Some Clinical and Biological Aspects: Review. *Futur. Dent. J.* **2016**, *2* (2), 55–64.
- (152) Oleksak, R. P.; Ruther, R. E.; Luo, F.; Fairley, K. C.; Decker, S. R.; Stickle, W. F.; Johnson, D. W.; Garfunkel, E. L.; Herman, G. S.; Keszler, D. A. Chemical and Structural Investigation of High-Resolution Patterning with HafSOx. **2014**, 2–6.
- (153) Wang, L. Y.; Lee, M. S. A Review on the Aqueous Chemistry of Zr(IV) and Hf(IV) and Their Separation by Solvent Extraction. *J. Ind. Eng. Chem.* **2016**, *39*, 1–9.
- (154) Poriel, L.; Favreréguiillon, A.; Pelletrostaing, S.; Lemaire, M. Zirconium and Hafnium Separation, Part 1. Liquid/Liquid Extraction in Hydrochloric Acid Aqueous Solution with Aliquat 336. *Sep. Sci. Technol.* **2006**, *41* (9), 1927–1940.
- (155) Xu, L.; Xiao, Y.; Van Sandwijk, A.; Xu, Q.; Yang, Y. Production of Nuclear Grade Zirconium: A Review. *J. Nucl. Mater.* **2015**, *466*, 21–28.
- (156) Shannon, R. D. Revised Effective Ionic Radii in Halides and Chalcogenides. *Acta Cryst.* **1976**, No. A32, 751.
- (157) Veliscek-Carolan, J. Separation of Actinides from Spent Nuclear Fuel: A Review. *J. Hazard. Mater.* **2016**, *318*, 266–281.
- (158) Choppin, G. R.; Liljenzin, J.-O.; Rydberg, J.; Ekberg, C. *Radiochemistry and Nuclear Chemistry*.
- (159) Baldwin, A. G.; Bridges, N. J.; Braley, J. C. Distribution of Fission Products into Tributyl Phosphate under Applied Nuclear Fuel Recycling Conditions. *Ind. Eng. Chem. Res.* **2016**, *55* (51), 13114–13119.
- (160) Bagawde, S. V.; Ramakrishna, V. V.; Patil, S. K. Oxalate Complexing of Tetravalent Actinides. *J. Inorg. Nucl. Chem.* **1976**, *38* (9), 1669–1672.
- (161) Orr, R. M.; Sims, H. E.; Taylor, R. J. A Review of Plutonium Oxalate

- Decomposition Reactions and Effects of Decomposition Temperature on the Surface Area of the Plutonium Dioxide Product. *J. Nucl. Mater.* **2015**, *465*, 756–773.
- (162) Kojic-Prodic, B.; Ruzic-Toros, Z. Structure of Tetrapotassium Tetrakis (Oxalato) Zirconate (IV) Pentahydrate. *Acta Crystallogr.* **1978**, *B 34* (1978), 2001–2002.
- (163) Yang, J. Y.; Fu, Y. L.; Ren, J. L.; Ng, S. W. Calcium Dipotassium Tetraoxalatozirconate(IV) Octahydrate. *Acta Crystallogr. Sect. E Struct. Reports Online* **2006**, *62* (10), 2424–2426.
- (164) Gavilan, E.; Audebrand, N.; Jeanneau, E. A New Series of Mixed Oxalates $MM'(C_2O_4)_3(H_2O)_3 \cdot NH_2O$ (M = Cd, Hg, Pb; M' = Zr, Hf) Based on Eight-Fold Coordinated Metals: Synthesis, Crystal Structure from Single-Crystal and Powder Diffraction Data and Thermal Behaviour. *Solid State Sci.* **2007**, *9* (11), 985–999.
- (165) Johnson, F. A.; Larsen, E. M. Compounds Exhibiting Coördination Number Eight. The Potassium Tetraoxalatometallates of Zirconium(IV), Hafnium(IV), Thorium(IV), and Uranium(IV). *Inorg. Chem.* **1962**, *1* (1), 159–165.
- (166) Baggio, R.; Garland, M. T.; Perec, M. A Binuclear Zirconium(IV) Oxalate Complex with a μ -Oxalate Coordination Mode. Crystal Structure of $K_6\{Zr(C_2O_4)_3\}_2(\mu-C_2O_4)$, $4H_2O$. *Inorg. Chem.* **1997**, *36* (14), 3198–3200.
- (167) Baggio, R.; Garland, M. T.; Perec, M. Preparation and X-Ray Crystal Structure of the Polymeric Zirconium(IV) Oxalate Complex $[K_2\{Zr(C_2O_4)_3\}, H_2C_2O_4, H_2O]_n$. *Inorg. Chem.* **1997**, *36* (14), 3198–3200.
- (168) Tranqui, P. D. Structure Cristalline Du Tetrakisoxalatohafniate de Potassium Pentahydrate $[K_4Hf(C_2O_4)_4 \cdot 5H_2O]$. *Acta Crystallogr.* **1977**, *33*, 3126–3133.
- (169) Friend, M. T.; Wall, N. A. Hafnium(IV) Complexation with Oxalate at Variable Temperatures. *Radiochim. Acta* **2017**, *105* (5), 379–388.
- (170) V. Ya. Kuznetsov, L. M. Dikareva, D. L. Rogachev, M. A. P.-K. Structure of the Double Sulfate of Hafnium and Ammonium $(NH_4)_5Hf_6(O_4OH)(SO_4)_{10}(H_2O)_7$. *J. Struct. Chem.* **1985**, *26* (6), 923–929.
- (171) Christensen, H.; Sunder, S. Current State of Knowledge of Water Radiolysis Effects on Spent Nuclear Fuel Corrosion. *J. Nucl. Technol. J. Vol. 131; J. Issue 1; Other Inf. Copyr. 2006 Am. Nucl. Soc. (ANS), United States, All rights Reserv.*

- <http://epubs.ans.org/>; Ctry. input Int. At. Energy Agency (IAEA **2000**, 5450 (May), 102–123.
- (172) Goberna-Ferrón, S.; Park, D. H.; Amador, J. M.; Keszler, D. A.; Nyman, M. Amphoteric Aqueous Hafnium Cluster Chemistry. *Angew. Chemie - Int. Ed.* **2016**, 55 (21), 6221–6224.
- (173) Bassil, B. S.; Mal, S. S.; Dickman, M. H.; Kortz, U.; Oelrich, H.; Walder, L. 6-Peroxo-6-Zirconium Crown and Its Hafnium Analogue Embedded in a Triangular Polyanion: $[M_6(O_2)_6(OH)_6(\gamma-SiW_{10}O_{36})_3]^{18-}$ (M = Zr, Hf). *J. Am. Chem. Soc.* **2008**, 130 (21), 6696–6697.
- (174) Siegbahn, P. E. M. Binding in Second-Row Transition Metal Dioxides, Trioxides, Tetraoxides, Peroxides, and Superoxides. *J. Phys. Chem.* **1993**, 97 (36), 9096–9102.
- (175) Chernyshov, B.N.; Didenko, N.A.; Bukvetskij, B.V.; Gerasimenko, A.V.; Kavun, V.Ya.; Sergienko, S. S. (AN. Synthesis and Structure of Polynuclear Peroxyfluorozirconates $K_6Zr_3F_{12}(O_2)_3 \cdot 2H_2O \cdot 2H_2O$. *Zhurnal Neorg. Khimii* **1989**, 34 (11), 2786–2794.
- (176) Jere, G. V.; Gupta, G. D. Studies on Peroxo Sulphato Zirconium(IV) Complex. *J. Inorg. Nucl. Chem.* **1970**, 32, 537–542.
- (177) R. Schwarz, H. G. Über Die Peroxyde Des Titans, Zirkons, Hafniums Und Thoriums. *Zeitschrift für Anorg. und Allg. Chemie* **1928**, 176 (1), 209–232.
- (178) Chernyshov, B.N.; Didenko, N.A.; Bakeeva, N.G.; Bukvetskij, B.V.; Gerasimenko, A. V. Synthesis and Structure of Dimeric Peroxofluorohafnates $K_4Hf_2F_{10}O_2 \cdot 2H_2O$. *Zhurnal Neorg. Khimii* **1991**, 36 (5), 1112–1116.
- (179) Dengel, A. C.; Griffith, W. P. Studies on Transition Metal Peroxo Complexes-IX. Carboxylato Peroxo Complexes of Niobium(V), Tantalum(V), Zirconium(IV) and Hafnium(IV). *Polyhedron* **1989**, 8 (11), 1371–1377.
- (180) Glen, G. L.; Silverton, J. V.; Hoard, J. L. Stereochemistry of Discrete Eight-Coördination. III. Tetrasodium Tetrakisoxalatozirconate(IV) Trihydrate. *Inorg. Chem.* **1963**, 2 (2), 250–255.
- (181) Chen, Y.; Zhang, X.; Ma, K.; Chen, Z.; Wang, X.; Knapp, J.; Alayoglu, S.; Wang, F.; Xia, Q.; Li, Z.; et al. Zirconium-Based Metal – Organic Framework with 9 - Connected Nodes for Ammonia Capture. *ACS Appl. Nano Mater.* **2019**, 1–20.

- (182) Rude, L. H.; Corno, M.; Ugliengo, P.; Baricco, M.; Lee, Y. S.; Cho, Y. W.; Besenbacher, F.; Overgaard, J.; Jensen, T. R. Synthesis and Structural Investigation of $Zr(BH_4)_4$. *J. Phys. Chem. C* **2012**, *116* (38), 20239–20245.
- (183) Wang, G. C.; Sung, H. H. Y.; Williams, I. D.; Leung, W. H. Tetravalent Titanium, Zirconium, and Cerium Oxo and Peroxo Complexes Containing an Imidodiphosphinate Ligand. *Inorg. Chem.* **2012**, *51* (6), 3640–3647.
- (184) Mal, S. S.; Nsouli, N. H.; Carraro, M.; Sartorel, A.; Scorrano, G.; Oelrich, H.; Walder, L.; Bonchio, M.; Kortz, U. Peroxo-Zr/Hf-Containing Undecatungstosilicates and -Germanates. *Inorg. Chem.* **2010**, *49* (1), 7–9.
- (185) Falber, A.; Todaro, L.; Goldberg, I.; Favilla, M. V.; Drain, C. M. Routes to New Hafnium(IV) Tetraaryl Porphyrins and Crystal Structures of Unusual Phosphate-, Sulfate-, and Peroxide-Bridged Dimers. *Inorg. Chem.* **2008**, *47* (2), 454–467.
- (186) Gambarotta, S.; Chiang, M. Y. Synthesis of a Diamagnetic Fulvalene Zirconium(III) Derivative. The Crystal Structure of $(\eta^5\text{-C}_{10}\text{H}_8)(\eta^5\text{-C}_5\text{H}_5)\text{Zr}(\mu\text{-Cl})_2$. *Organometallics* **1987**, *6* (4), 897–899.
- (187) Albert Cotton, F.; Diebold, M. P.; Kibala, P. A. Synthesis and Structural Characterization of Three Compounds with Zr(III)-Zr(III) Bonds: $Zr_2Cl_6(Dppe)_2$, $Zr_2Cl_6(PMe_2Ph)_4$, and $Zr_2Cl_6(PEt_3)_4$. *Inorg. Chem.* **1988**, *27* (5), 799–804.
- (188) Jin, W. T.; Yang, F.; Deng, L.; Chen, M. L.; Chen, J. F.; Chen, H. Bin; Zhou, Z. H. Wheel-Like Icosanuclear Peroxotitanate - A Stable Water-Soluble Catalyst for Oxygen Transfer Reactions. *Inorg. Chem.* **2018**, *57* (22), 14116–14122.
- (189) Frederick, R. T.; Amador, J. M.; Goberna-Ferrón, S.; Nyman, M.; Keszler, D. A.; Herman, G. S. Mechanistic Study of $HfSO_x$ Extreme Ultraviolet Inorganic Resists. *J. Phys. Chem. C* **2018**, *122* (28), 16100–16112.
- (190) Vlaisavljevich, B.; Gagliardi, L.; Burns, P. C. Understanding the Structure and Formation of Uranyl Peroxide Nanoclusters by Quantum Chemical Calculations. *J. Am. Chem. Soc.* **2010**, *132* (41), 14503–14508.
- (191) Sorenson, J. M.; Hura, G.; Glaeser, R. M.; Head-Gordon, T. What Can X-Ray Scattering Tell Us about the Radial Distribution Functions of Water? *J. Chem. Phys.* **2000**, *113* (20), 9149–9161.

- (192) SAINT Plus Version 8.34a, Bruker Analytical X-Rays Systems, Madison, WI. *SAINT Plus Version 8.34a, Bruker Anal. X-rays Syst. Madison, WI* **2013**.
- (193) Sheldrick, G. M. SADABS, Bruker-Siemens Area Detector Absorption. *SADABS, Bruker-Siemens area detector absorption and other correction, Version 2008/1*. 2006.
- (194) Sheldrick, G. M. SHELXT - Integrated Space-Group and Crystal-Structure Determination. *Acta Crystallogr. Sect. A Found. Crystallogr.* **2015**, *71* (1), 3–8.
- (195) Sheldrick, G. M. A Short History of SHELX. *Acta Crystallogr. Sect. A Found. Crystallogr.* **2008**, *64* (1), 112–122.
- (196) Dolomanov, O. V.; Bourhis, L. J.; Gildea, R. J.; Howard, J. A. K.; Puschmann, H. OLEX2: A Complete Structure Solution, Refinement and Analysis Program. *J. Appl. Crystallogr.* **2009**, *42* (2), 339–341.
- (197) Wang, H.-W.; Wesolowski, D. J.; Proffen, T. E.; Vlcek, L.; Wang, W.; Allard, L. F.; Kolesnikov, A. I.; Feyngenson, M.; Anovitz, L. M.; Paul, R. L. Structure and Stability of SnO₂ Nanocrystals and Surface-Bound Water Species. *J. Am. Chem. Soc.* **2013**, *135* (18), 6885–6895.
- (198) Sheldrick, G. SADABS v. 2.01, Bruker/Siemens Area Detector Absorption Correction Program. **1998**.
- (199) Sheldrick, G. M. Crystal Structure Refinement with SHELXL. *Acta Crystallogr. Sect. C Struct. Chem.* **2015**, *71* (Md), 3–8.

8. Appendix A

Probing the local structure of crystalline $\text{NaBiO}_3 \cdot \text{XH}_2\text{O}$ and its acidified derivatives

8.1 Experimental

8.2 Materials and reagents

$\text{NaBiO}_3 \cdot \text{XH}_2\text{O}$ (Fischer), $\text{Ce}(\text{NO}_3)_3 \cdot 6\text{H}_2\text{O}$ (Sigma Aldrich, 99%), $(\text{NH}_4)_2\text{Ce}(\text{NO}_3)_6$ (Alfa Aesar, 98+%) and concentrated HNO_3 (Macron Fine Chemicals) solution were used as received. Deionized water (18.2 M Ω , Millipore) was used to prepare all solutions.

8.3 Treatment of $\text{NaBiO}_3 \cdot \text{XH}_2\text{O}$ with HNO_3

For structural characterizations, the $\text{NaBiO}_3 \cdot \text{XH}_2\text{O}$ starting material was heat-treated at 210°C for three hours in the air as described elsewhere.⁴⁰

Acidified $\text{NaBiO}_3 \cdot \text{XH}_2\text{O}$ samples were prepared via suspending 1.00 g $\text{NaBiO}_3 \cdot \text{XH}_2\text{O}$ in eight, 10 mL volumes of HNO_3 dilutions in water at different concentrations. The $\text{NaBiO}_3:\text{HNO}_3$ molar ratio and the pH of these suspensions, along with the concentration and the pH of the initial HNO_3 solutions, are shown in **Table 2.1**. The suspensions were stirred for two hours at room temperature and a solid phase was isolated from these mixtures by centrifugations, washed three times with water and finally dried under vacuum. The color of these dry samples varied from light orange to dark brown as a function of the $\text{NaBiO}_3:\text{HNO}_3$ ratio (**Figure A 1**).



Figure A 1 Images of the $\text{NaBiO}_3 \cdot 3\text{H}_2\text{O}$ and the acidified samples. $\text{NaBiO}_3:\text{HNO}_3$ ratio is increased from left to the right. Reaction conditions are collected in **Table 2.1**.

8.4 Cerium oxidation tests

We compared the ability of pristine and acid-treated NaBiO_3 to oxidize Ce^{3+} by suspending the same mass of these solids in 8 mM solutions of $\text{Ce}(\text{NO}_3)_3$ in 1M HNO_3 . The $\text{NaBiO}_3:\text{Ce}(\text{NO}_3)_3$ in these mixtures was 2:1. The oxidation reactions were halted at different time intervals by passing aliquots through 0.45 μm nylon mesh filters, using plastic disposable syringes, into quartz cuvettes of 1 cm path length. UV-Vis spectra of these filtrates were recorded and the intensity of the absorption band at 380 nm was used to quantify the concentration of Ce^{4+} via a calibration previously obtained with $(\text{NH}_4)_2\text{Ce}(\text{NO}_3)_6$. Calibration curve was generated with Ce^{4+} concentration ranging from 1 mM to 9 mM, in relevant solution conditions (**Figure A 2**).

8.5 Powder X-ray diffraction (PXRD)

Powder X-ray diffraction (PXRD) was performed on a Rigaku Miniflex diffractometer (Cu- $\text{K}\alpha$ irradiation, $\lambda=1.54 \text{ \AA}$). The chosen 2θ range was 5-60 degree with the scan speed of 1.5 degree/minute.

8.6 X-ray total scattering measurements for pair distribution function analysis (PDF)

To perform pair distribution function (PDF) analysis we used Rigaku Smartlab X-ray diffractometer with Mo- $\text{K}\alpha$ irradiation ($\lambda=0.71 \text{ \AA}$) in the 2θ range of 3-158.6° with Bragg-Brentano geometry. The theoretical Q -range is up to a Q_{max} of 17.49 \AA^{-1} . A 0.5 degree/minute data collection time was used to ensure high quality scattering data.

PDFgetX3 was to process scattering data into the corresponding PDF.¹⁸ Simulations were created in PDFgui.¹⁹

8.7 Thermogravimetric analysis (TGA)

Thermogravimetric analysis (TGA) was performed on TA Instruments SDT Q600. Little amount (20 mg) was placed in alumina crucible for thermogravimetric measurement up to 900 C under air flow using.

8.8 Scanning Electron Microscopy (SEM) and Energy-Dispersive X-ray Spectroscopy (EDX)

Energy dispersive X-ray spectroscopy (EDX) measurements were performed on Quanta 600 scanning electron microscopy (SEM) to extract composition information of the samples.

8.9 Elemental analysis

Elemental analysis to obtain compositional information was performed by Galbraith Laboratories (Knoxville, TN).

8.10 X-ray Photoelectron Spectroscopy (XPS)

X-ray photoelectron spectroscopy (XPS) was performed utilizing PHI 5600 system with monochromatic Al K α X-ray source ($h\nu=1486.6$ eV) to determine the ratio of different oxidation states of bismuth in acidified samples as well as in the commercial sample

8.11 UV-Vis spectroscopy

UV-visible (UV-Vis) spectra were recorded with Thermoscientific Evolution 220 UV-Visible Spectrophotometer. Quartz cuvette with 10 mm path length was used as a sample holder. The spectra were recorded between $\lambda=230-600$ nm, and the Ce⁴⁺ peak was monitored at 380 nm for quantification and to avoid overlap with other species.

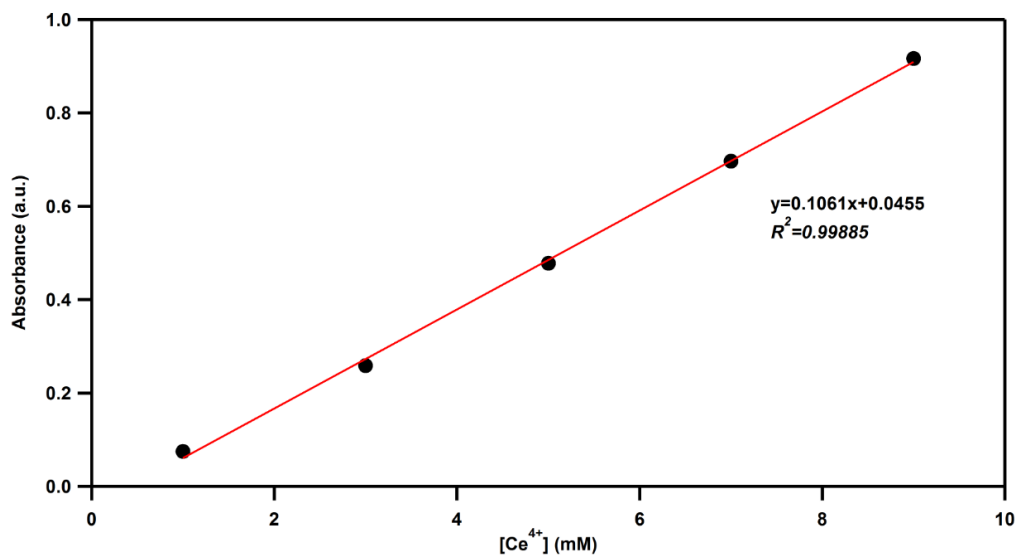


Figure A 2 Calibration curve to determine Ce^{4+} concentration in the Ce^{3+} oxidation tests. Absorbance values were recorded at 380 nm.

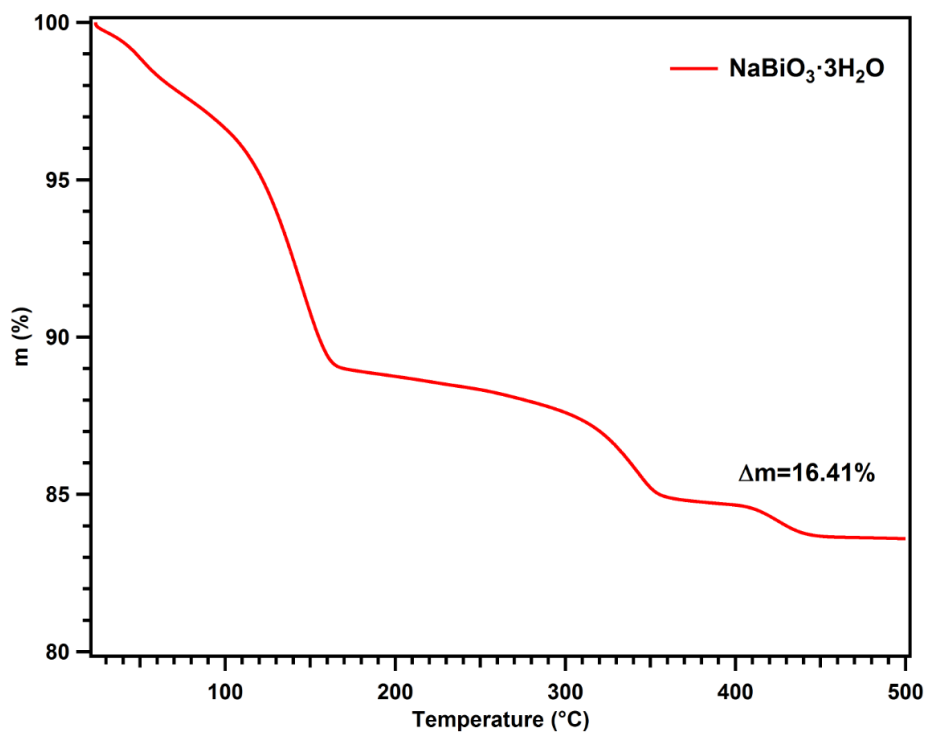


Figure A 3 TGA of hydrous sodium bismuthate starting material. Mass loss indicates the total water content of $\text{NaBiO}_3 \cdot 3\text{H}_2\text{O}$.

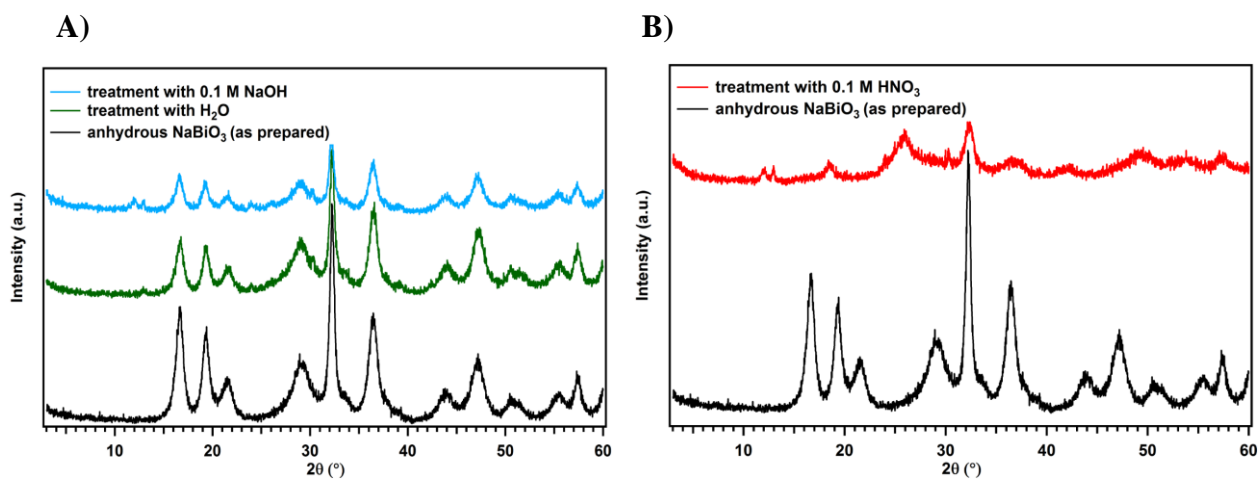


Figure A 4 Powder X-ray diffraction pattern of the anhydrous NaBiO₃ (black) and following its suspension in neutral and basic conditions (A) or in acidic conditions (B).

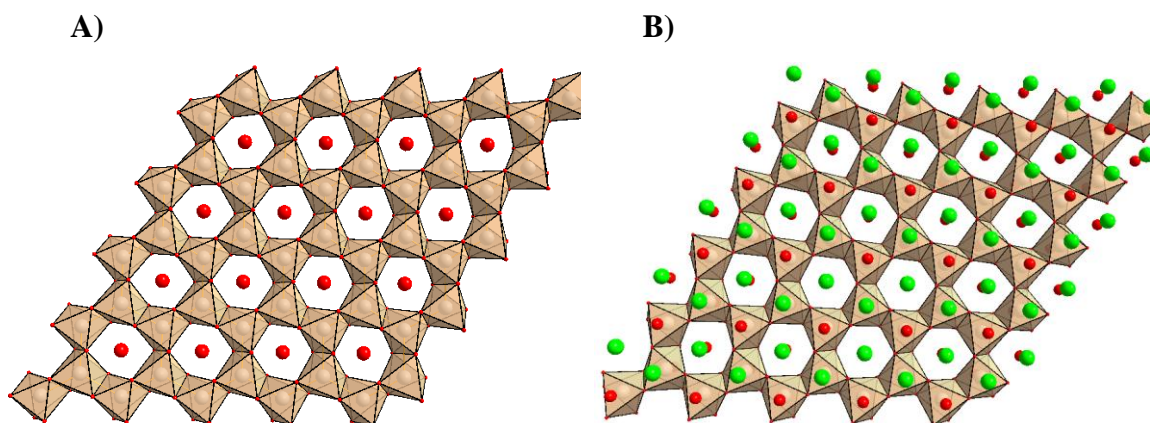


Figure A 5 Models derived from NaBiO₃ structure: H₂O is in the voids of {Bi-O} sheet (A) and {Bi-O} and {Na-O} sheets are together with H₂O molecules (B). (Bi-O brown octahedra, Na-green, O-red spheres)

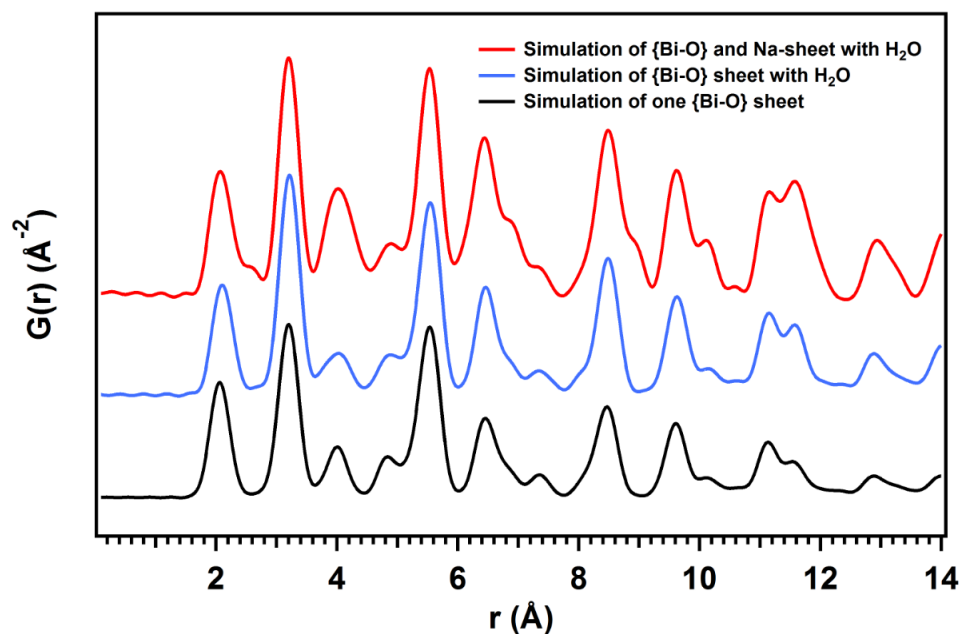


Figure A 6 Comparison of the simulated PDF curves of one {Bi-O} sheet (black) and this single sheet with the presence of H₂O (blue) and with Na⁺ (red).

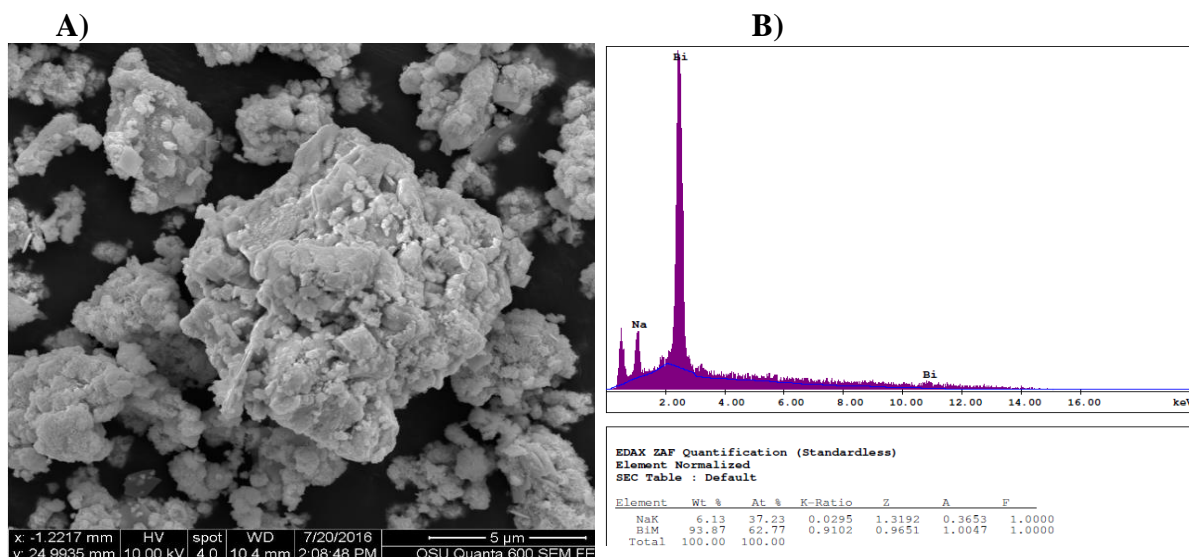


Figure A 7 (A) Scanning electron microscope (SEM) image of NaBiO₃·3H₂O and (B) EDX spectrum. EDX analysis shows 0.6:1 ratio to Na:Bi diverges greatly from the theoretical 1:1 ratio.

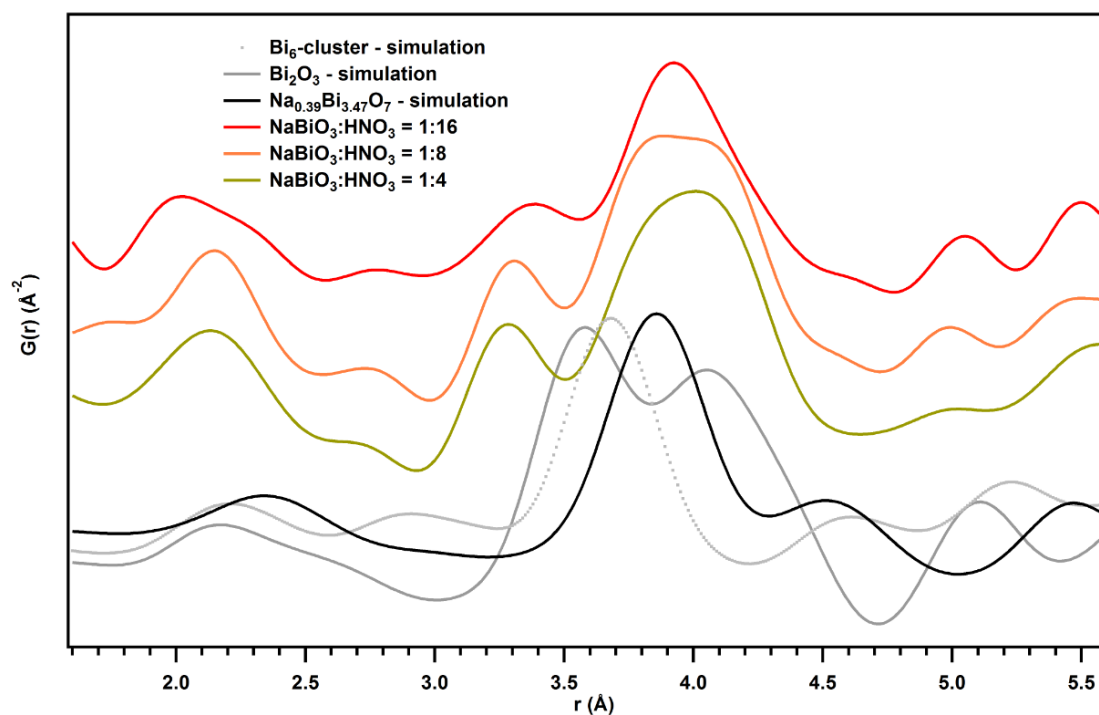


Figure A 8 Comparison of the PDF of selected acid-treated samples with the simulations of α - Bi_2O_3 (ICSD-15072) and $\{\text{Bi}_6\}$ -cluster (ICSD-300008). The common Bi-Bi correlations in these known phases possess a Bi-Bi correlation are not observable in the acidified products.

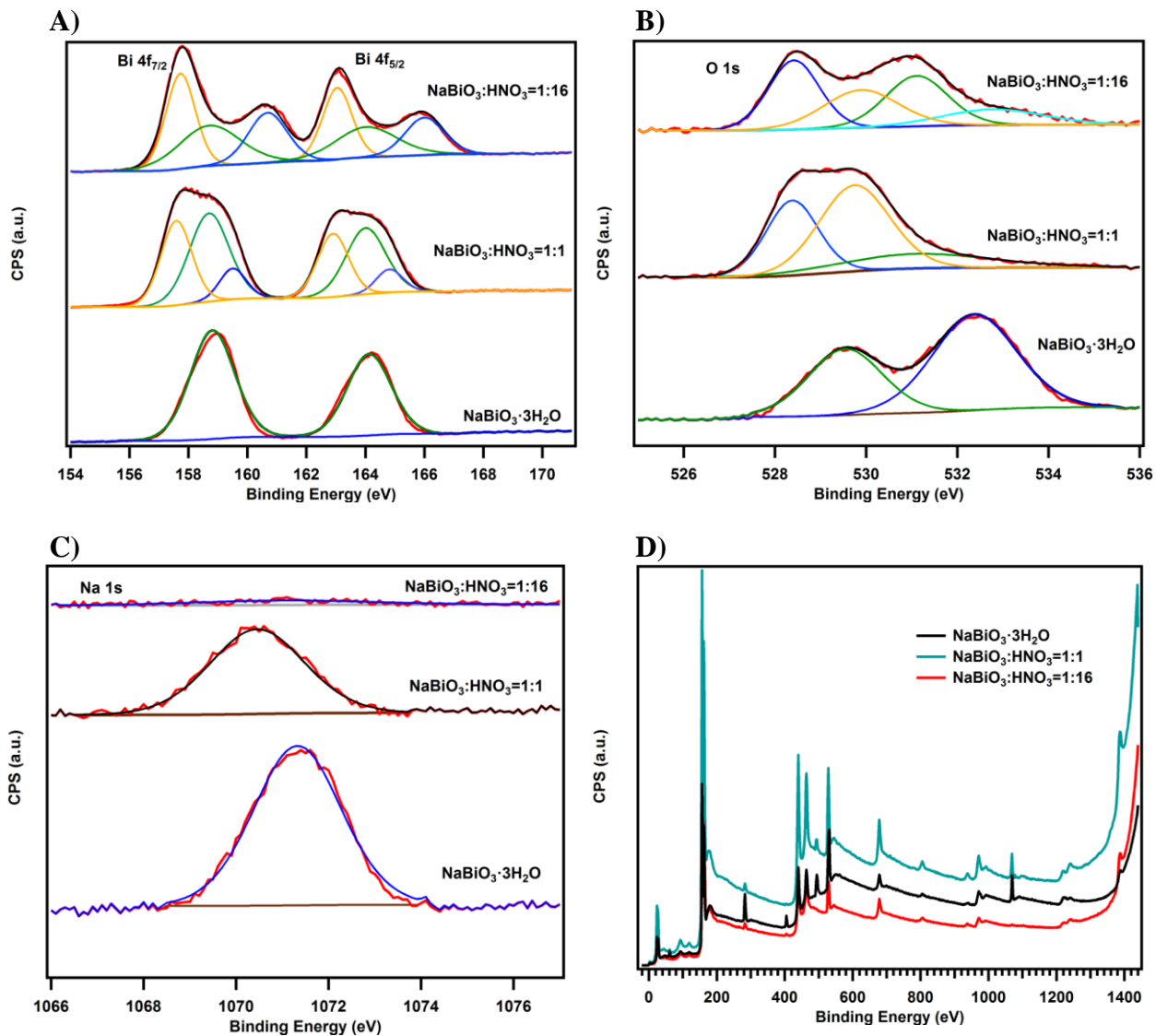


Figure A 9 XPS data of $\text{NaBiO}_3 \cdot 3\text{H}_2\text{O}$ and two acid-treated samples (A)-Bi, (B)-O, (C)-Na and (D) surveys).

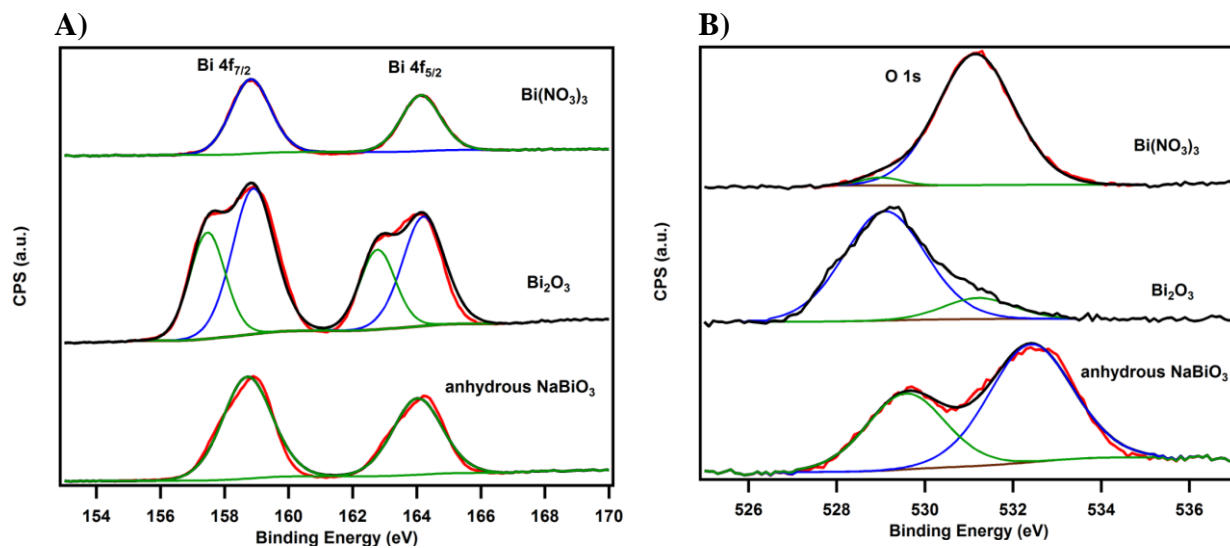


Figure A 10 XPS spectra of **A)** Bi and **B)** O for anhydrous NaBiO₃, Bi₂O₃ and Bi(NO₃)₃.

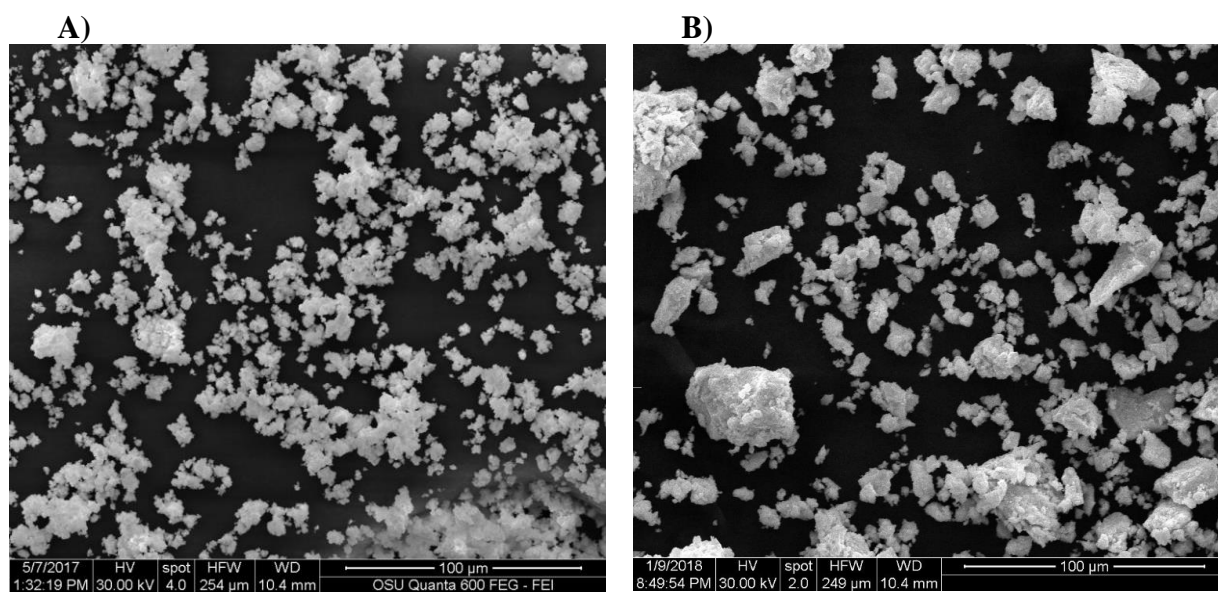


Figure A 11 Scanning electron microscope (SEM) images of acid-treated samples of **(A)**- NaBiO₃:HNO₃=1:1 ratio and **(B)**-NaBiO₃:HNO₃=1:16 ratio.

Table A 1 Comparison of unit cell parameters of the two different NaBiO₃ phases.

Formula	NaBiO ₃	NaBiO ₃ ·2H ₂ O
PDF Card No.	00-030-1160	00-030-1161
ICSD code	91776	-
Crystal system	Trigonal	Hexagonal
Space group	R-3 (148)	P3 (143)
Cell parameter – a, b	5.562	5.605
Cell parameter – c	16.054	7.425
Cell parameter – α , β	90	90
Cell parameter - γ	120	120

Table A 2 Selected atomic distances in anhydrous NaBiO₃ (ICSD: 91776)

Bi-O distances (Å)	Na-O distances (Å)	Bi-Na distances (Å)	Bi-Bi distances (Å)	Na-Na distances (Å)
2.09	2.40	3.17	3.23	3.29
2.14	2.47	3.87	5.03	4.62
2.92	3.63	4.05	5.57	
4.14	4.09	4.31	6.22	
4.38	4.33		6.44	
4.77	4.58			
4.78				
4.95				

Table A 3 Calculated parameters of the refinement for anhydrous NaBiO₃.

$R\bar{3}$	$R_{wp} = 20.5\%$		reduced $\chi^2 = 0.061$		
Atom	X	Y	Z	Occ	U_{iso}
Na	0	0	0.137	1	0.0294
Bi	0	0	0.342	1	0.0168
O	0.295	0.953	0.257	1	0.0380
$a = 5.57216 \text{ \AA}$			$c = 16.0863 \text{ \AA}$		

Table A 4 The refined anisotropic parameters extracted from the refinement of anhydrous NaBiO₃.

Element	U_{iso}	U_{11}	U_{22}	U_{33}	U_{12}	U_{13}	U_{23}
Na	0.0294	0.0231	0.0231	0.0422	0.0115	0	0
Bi	0.0168	0.0092	0.0092	0.0322	0.0046	0	0
O	0.0380	0.0380	0.0380	0.0380	0.0190	0	0

Table A 5 Atom percent ratios obtained by elemental analysis of the pristine NaBiO₃·3H₂O and one selected acidified sample.

Atom	NaBiO ₃ ·3H ₂ O	NaBiO ₃ :HNO ₃ =1:1
Bi	59.9	71.1
Na	7.41	1.68
O	21.64	13.84
H	1.13	0.5
<i>Total*</i>	<i>90.08</i>	<i>87.12</i>
Na:Bi ratio	1.12	0.215
O:Bi ratio	4.72	2.54

* *Total value is below 100% due to error and uncertainty in the technique.*

Table A 6 Summary of XPS data on NaBiO₃·3H₂O and the acid-treated samples.

Sample	Element	Elemental ratio Bi-base	Components	Peak position (eV)	Distribution (%)
NaBiO₃·3H₂O	Bi	1.00	Bi(1)	158.81	100.00
	O	4.13	O(1)	529.54	61.94
			O(2)	532.38	38.06
Na	0.68	Na(1)	1071.33	100.00	
NaBiO₃:HNO₃=1:1	Bi	1.00	Bi(1)	157.59	37.75
			Bi(2)	158.70	50.33
			Bi(3)	159.50	11.92
	O	2.23	O(1)	528.38	33.63
			O(2)	529.75	14.60
			O(3)	531.07	51.77
Na	0.22	Na(1)	1070.45	100.00	
NaBiO₃:HNO₃=1:16	Bi	1.00	Bi(1)	157.73	38.76
			Bi(2)	158.72	29.07
			Bi(3)	160.69	34.34
	O	1.97	O(1)	531.11	28.29
			O(2)	528.42	31.75
			O(3)	532.78	14.41
			O(4)	529.90	25.54
Na	0.05	Na(1)	1071.01	100.00	

Table A 7 Summary of XPS results for anhydrous NaBiO₃, Bi₂O₃ and Bi(NO₃)₃ measurements.

Material	Element	Elemental ratio Bi-base	Components	Peak position (eV)	Distribution (%)
Anhydrous NaBiO₃	Bi	1.00	Bi(1)	158.71	100.00
	O	3.88	O(1)	529.57	37.63
			O(2)	532.40	62.37
Na	0.60	Na(1)	1071.25	100.00	
Bi₂O₃	Bi	1.00	Bi(1)	157.47	37.90
			Bi(2)	158.90	62.10
	O	1.41	O(1)	529.09	85.91
			O(2)	531.21	14.09
Bi(NO₃)₃	Bi	1.00	Bi(1)	158.82	100.00
	O	9.52	O(1)	529.01	3.20
			O(2)	531.15	96.80
	N	5.31	N(1)	398.56	63.89
N(2)			405.64	36.11	

9. Appendix B

The role of titanium-oxo clusters in sulfate process for TiO₂ production

9.1 Characterization methods

9.2 Small-angle X-ray scattering (SAXS)

Small-angle X-ray scattering data were collected on Anton Paar SAXSess instrument using Cu-K α radiation ($\lambda=1.54056$ Å), line collimation, 2D image plates and the range of momentum transfer (q) of 0.018-2.5 Å⁻¹. All solutions, including background solutions, were contained in sealed borosilicate tubes of 1.5 mm in diameter and 0.01 mm wall thickness (HR6-124, Hampton Research) placed at a distance of 26.1 cm from the image plates. Data collection time of 30 minutes was utilized.

We used SAXSQUANT software for data collection and treatment including normalization, primary beam removal, background subtraction, desmearing and smoothing. Analyzes, fits were carried out utilizing IRENA macros with IgorPro 6.3 (Wavemetrics) software¹⁴. To simulate scattering data from the crystal structure we used SolX software^{15,16}.

9.3 Extended X-ray absorption fine structure (EXAFS)

EXAFS measurements were done at 9BM and 20BM of Advanced Photon Source of Argonne National Laboratory. The solution is filled in a custom-designed holder that has

a small window covered by Kapton film. The X-ray can penetrate the Kapton film without too much attenuation. The fluorescence mode is used to collect Ti K-edge signal.

To perform EXAFS, 0.2 mL solution filtered through a syringe is filled in a custom-designed holder that has a $20 \times 5 \text{ mm}^2$ Kapton window. All data were collected in a fluorescence mode. A Vortex ME4 detector was used to collect the Ti K fluorescence signal while a Si(111) monochromator scanned the incident X-ray photon energy through the Ti K absorption edge. The monochromator was detuned to 65% of the maximum intensity at the Ti K edge to minimize the presence of higher harmonics. At least four scans for each sample were carried out to ensure data statistics for XAS. The X-ray beam was calibrated using a Ti metal foil. Data reduction, data analysis, and EXAFS fitting were performed with the Athena, Artemis, and IFEFFIT software packages. Standard procedures were used to extract the EXAFS data from the measured absorption spectra. The pre-edge background was linearly fitted and subtracted. The post-edge background was determined using a spline-interpolation procedure and then subtracted. Normalization was performed by dividing the data by the height of the absorption edge at 50 eV. For quantitative analysis, phase shifts and back-scattering amplitudes were generated by the FEFF calculations based on crystal structures of TiO_2 and $\{\text{Ti}_{18}\}$, and were then calibrated through performing the FEFFIT of the EXAFS data of the reference samples, mainly to obtain the amplitude reduction factor (S_0^2) values. With S_0^2 known, the EXAFS data of the materials were fitted with such generated phase shifts and amplitudes.

9.4 Pair distribution function analysis (PDF) of X-ray total scattering measurements

To perform pair distribution function (PDF) analysis we used Rigaku Smartlab X-ray diffractometer with Mo- $K\alpha$ irradiation ($\lambda=0.71 \text{ \AA}$) in the 2θ range of $3\text{-}118.0^\circ$ with transmission geometry. The theoretical q -range is up to a q_{max} of 15.4 \AA^{-1} . A 0.2 degree/minute data collection time was used to ensure high quality scattering data. Samples were loaded in Kapton capillary with 1.46 mm inner diameter for irradiation. PDFgetX3 was used to process scattering data into the corresponding PDF¹⁸. Simulations were created in PDFgui¹⁹.

9.5 Transmission Electron Microscopy (TEM)

Images were acquired using a high angle annual dark field detector on an FEI Titan TEM operated at 200 keV in STEM mode. Specimens were supported on holey carbon grid. The specimens were prepared by micro-pipetting a droplet of solution on a TEM grid and allowing it to dry completely in air.

9.6 Energy-Dispersive X-ray Spectroscopy (EDX)

Energy dispersive X-ray spectroscopy (EDX) measurements were performed on Quanta 600 scanning electron microscopy (SEM) to extract composition information of the precipitated solid sample.

9.7 Crystallography

Single crystal X-ray diffraction data on the obtained crystals were collected on a Bruker DUO-APEX2 CCD area-detector diffractometer at 173 K using Cu-K α (1.54178 Å) radiation. Data reduction was accomplished using SAINT V8.34a¹⁹². The substantial redundancy in data allowed a semiempirical absorption correction¹⁹³ to be applied, based on multiple measurements of equivalent reflections. The structures were solved by the intrinsic phasing method from the SHELXT program¹⁹⁴, developed by successive difference Fourier syntheses, and refined by full-matrix least squares on all F² data using SHELX¹⁹⁵ via OLEX2¹⁹⁶ interface. The crystal data is given in **Table B 2**. CCDC files number: 1898206 contains the supplementary crystallographic data for this paper. These data can be obtained, free of charge, from The Cambridge Crystallographic Data Centre via www.ccdc.cam.ac.uk/structures

9.8 Details about structural refinement and sulfate-Cl disorder for crystallized {Ti₁₈}

We had significant difficulties obtaining the precise crystal structure of the investigated compound. Several data collections with different crystals were made. All crystals tested for single-crystal X-ray diffraction are twinned, consisting of two plates joined together with opposite orientations. Standard integrations of the data as for two component twin in all cases were failed; such integrations did not improve the quality of the model outside the main {Ti₁₈}-cluster core. Therefore, a twin law (-1 0 0; 0 -1 0; 0 0 1) found based on Cell_now was applied during the refinement process (BASF 0.09 and flack 0.11).

Furthermore, all crystals were weakly diffracting due to a strong disorder for counter-ions and solvent molecules outside the main Ti_{18} -cluster. Even using a strong Incoatec Cu $I\mu\text{S}$ source it was possible to collect data only up to 2θ max = 100 degrees (**Figure B 7**). This is mainly due to the presence of highly disordered solvent molecules. However, with these limitations, the data provided an appropriate number of measured reflections per refined parameters, 19697/2207 and allowed to prove we crystallized the $\{\text{Ti}_{18}\}$ cluster.

However, the $\{\text{Ti}_{18}\}$ -cluster in the structure is suitably determined. As presented prior, three layers of $\text{Ti}(\text{Ti})_5$ form the Ti_{18} cluster and we were able to localize eight fully occupied sulfate positions. Seven of these are located on the outside layers, each bridging two Ti^{4+} . The eighth fully occupied sulfate is terminally bound to a Ti on one of the outside layers. There is an additional sulfate that is half-occupied, also terminally bound on the outside layer. One of the oxos of this sulfate is disordered with a Cl^- , $\sim 3.0 \text{ \AA}$ from a Ti-bound water (**Figure B 9**). The second disordered sulfate is actually three sites; two are terminally bound to the outside layer on adjacent Ti's (illustrated in **Figure B 8**). The third sulfate is free from the cluster, but also mutually shares an oxo position with one of the other disordered sulfates. To determine the occupancies, these three sulfur sites were first freely refined, which gave values close to $1/3^{\text{rd}}$ for each. Therefore we fixed each of these at 0.333 occupancy, for a total of one sulfate. The sum total of sulfates based on this model is 9.5 per $\{\text{Ti}_{18}\}$. The aforementioned half-occupied, cluster-bound sulfate likewise has one oxo ligand disordered with chloride. This mixed oxo-Cl site freely refined close to $1/2\text{S}-1/2\text{O}$, in agreement with occupancy of the sulfur. Finally, we located 4 fully occupied Cl in the electron density map, and one $1/2$ -occupied Cl for a total of 5.5 Cl. The chlorides are mostly frequently located $\sim 3 \text{ \AA}$ from terminal water ligands of the cluster, likely serving a role in stabilizing the cluster for crystal growth via non-covalent interactions. Six TBA molecules were fully located in the electron density map but also highly disordered, especially for the terminal groups. Crystallographic details about structure refinement for the obtained structure is collected in **Table B 2**.

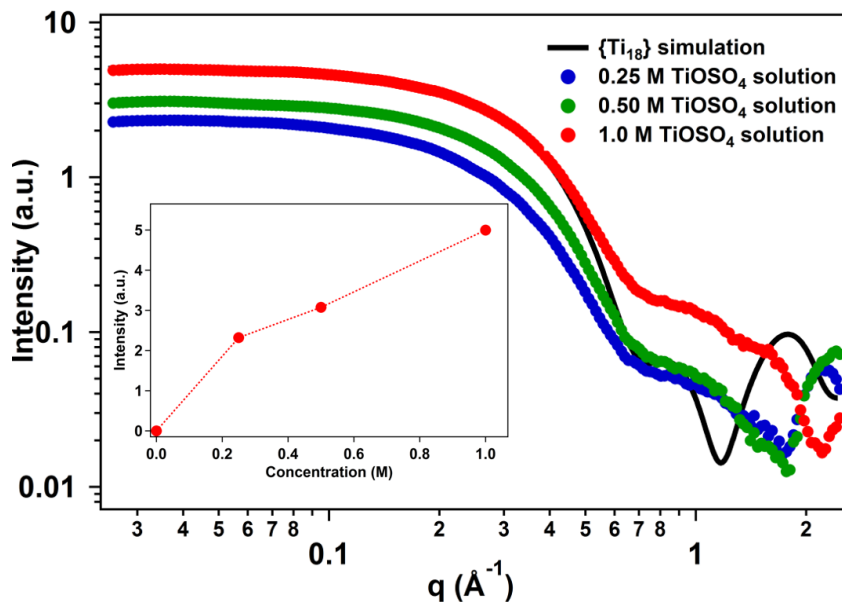


Figure B 1 SAXS curves of dissolved TiOSO_4 in water (blue: 0.25M, green: 0.5M and red: 1.0M concentration). Inset shows the relation between the concentration at the observed intensity at $q=0.3 \text{ \AA}^{-1}$.

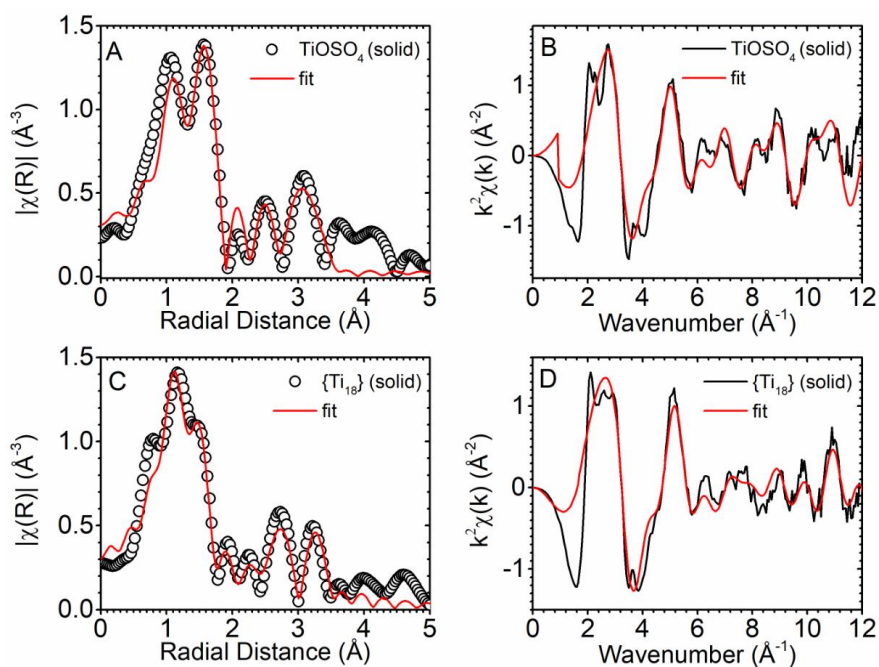


Figure B 2 Ti K-edge EXAFS Fourier Transformation R-space modeling based fitting of (A) TiOSO_4 powder and (C) $\{\text{Ti}_{18}\}$ powder; K-space of (B) TiOSO_4 powder and (D) $\{\text{Ti}_{18}\}$ powder

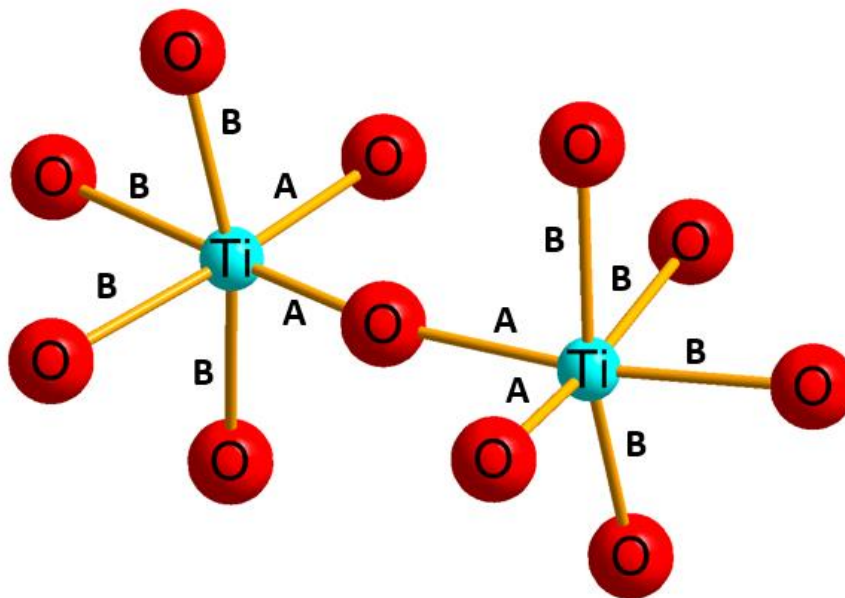


Figure B 3 The observed Ti-O distances in Ti-O polyhedra in the $\text{TiOSO}_4 \cdot \text{H}_2\text{O}$ unit cell (ICSD: 72973). Sulfate groups are eliminated for clarification. Letters represents the observed Ti K-edge EXAFS correlations assigned in **Table B 1**.

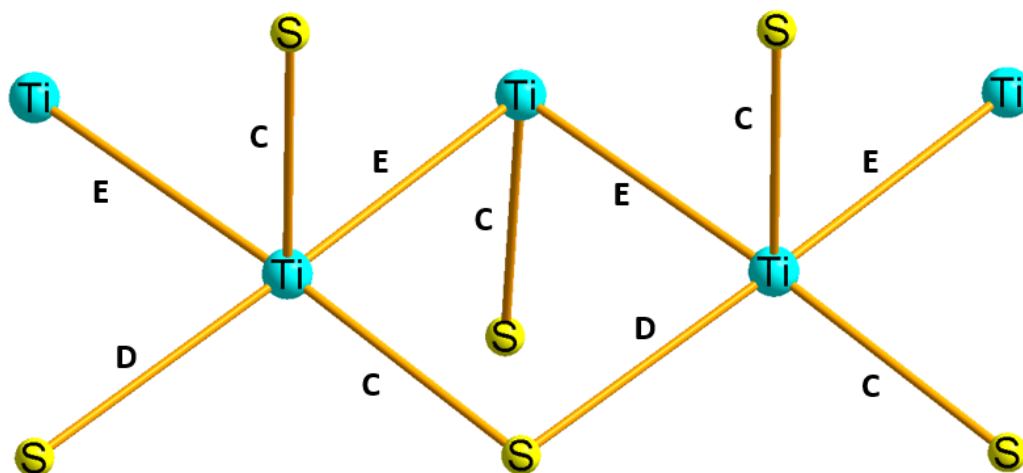


Figure B 4 The observed Ti-Ti and Ti-S correlations in $\text{TiOSO}_4 \cdot \text{H}_2\text{O}$ crystal structure (ICSD: 72973) Oxygens and hydrogens are eliminated for clarification. Letters represents the observed Ti K-edge EXAFS correlations assigned in **Table B 1**.

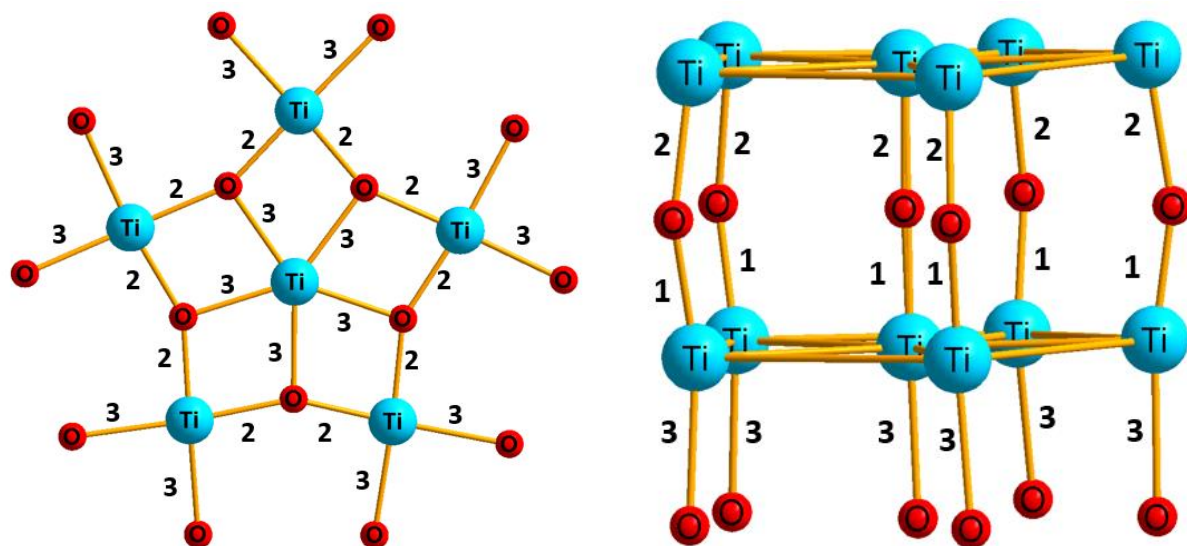


Figure B 5 The observed equatorial Ti-O correlations in a pentagonal $\text{Ti}(\text{Ti})_5$ unit (left) and the horizontal Ti-O correlations between two $\text{Ti}(\text{Ti})_5$ layers in $\{\text{Ti}_{18}\}$ -cluster (right). Sulfur, oxygen and hydrogen atoms are eliminated for clarification. Numbers represents the observed Ti K-edge EXAFS correlations assigned in **Table B 1**.

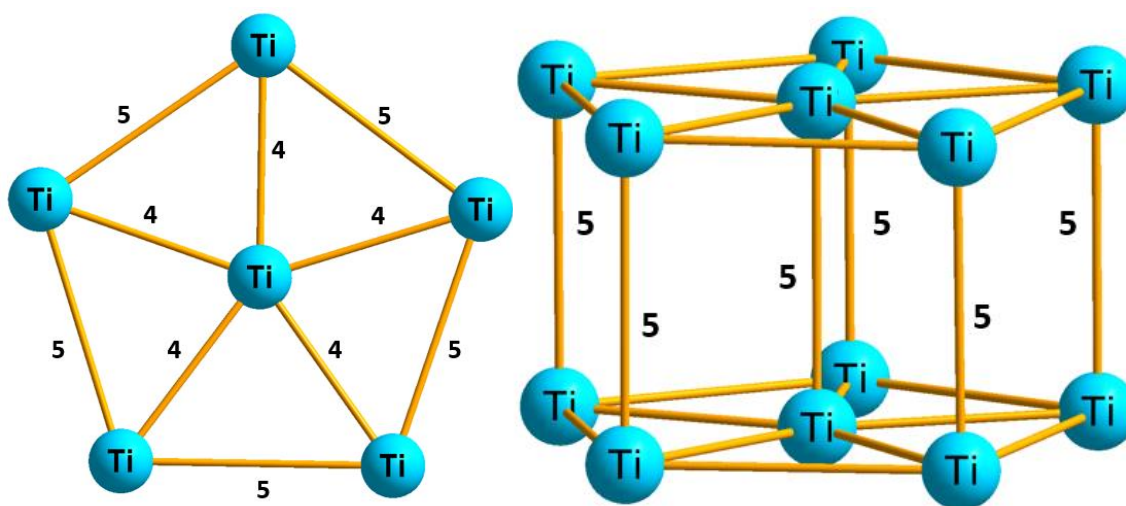


Figure B 6 The observed Ti-Ti correlations in one pentagonal $\text{Ti}(\text{Ti})_5$ unit (left) and between two layers of $\text{Ti}(\text{Ti})_5$ unit in the $\{\text{Ti}_{18}\}$ -cluster (right). Sulfur, oxygen and hydrogen atoms are eliminated for clarification. Numbers represents the observed Ti K-edge EXAFS correlations assigned in **Table B 1**.

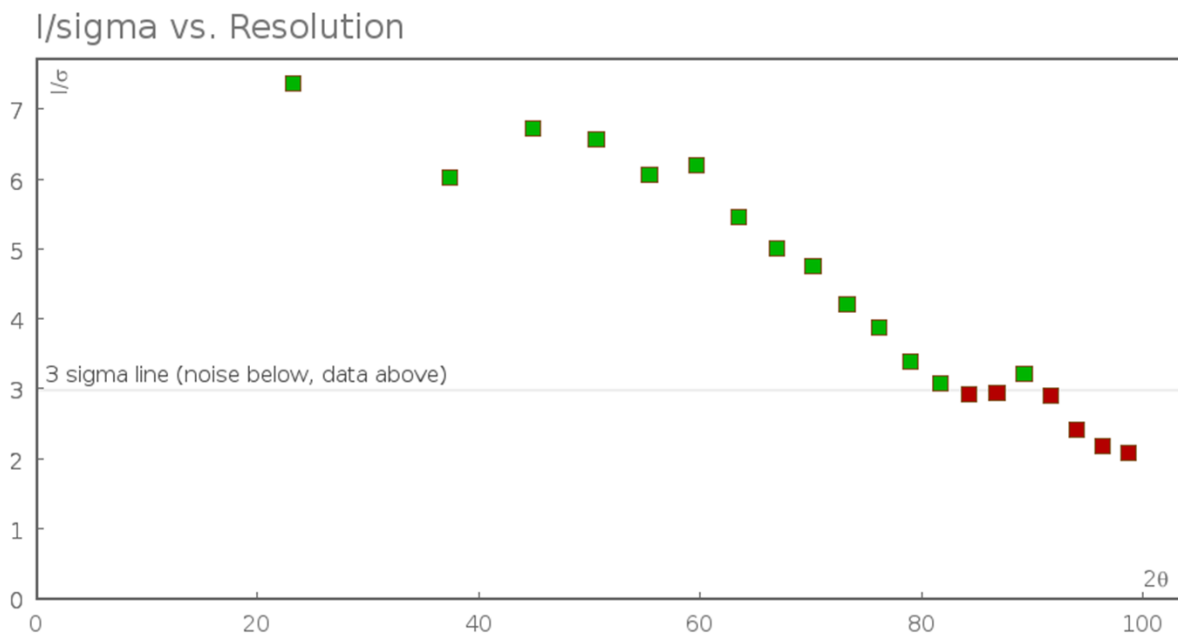


Figure B 7 Representation of the average intensity according to the 2θ angle.

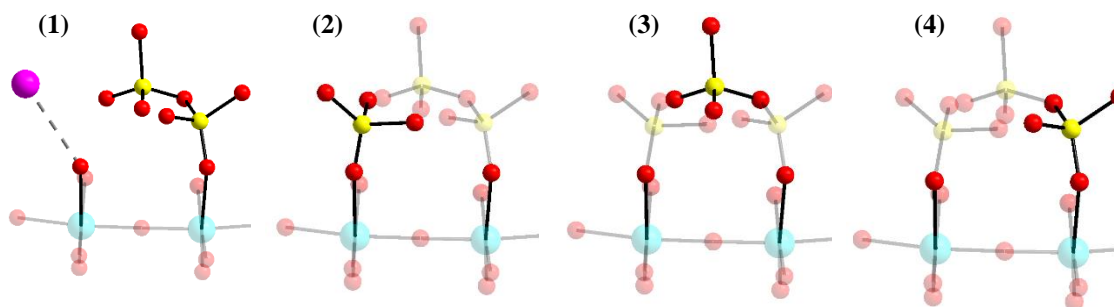


Figure B 8 Illustration of disorder model between three sulfates and a Cl^- anion on one face of the $\{\text{Ti}_{18}\}$ cluster. The two Ti-centers of the cluster to which the disordered sulfates bind/associate are shown partially transparent (Ti is turquoise, O is red, S is yellow, Cl is pink). (1) half-occupied Cl^- , $\sim 3 \text{ \AA}$ from the Ti-bound water ligand, present only when sulfate 3 or 4 is present. (2) sulfate-1; $1/3^{\text{rd}}$ occupied; (3) sulfate-2; $1/3^{\text{rd}}$ occupied; (4) sulfate-3; $1/3^{\text{rd}}$ occupied. The sulfur atoms freely refined around $1/3^{\text{rd}}$ occupancy, so we fixed the occupancy to $1/3^{\text{rd}}$; and likewise fixed the associated oxos appropriately. When a sulfate is not bound to the Ti, there is a water molecule (H's not show, nor located in the electron density map). Therefore Ti is always octahedrally-coordinating to six oxygen atoms.

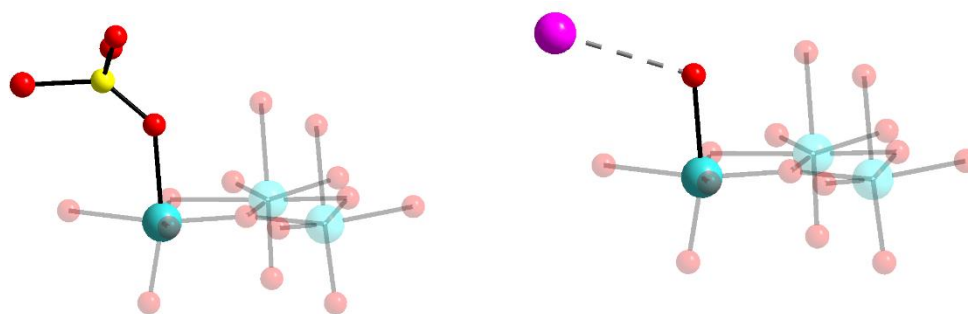


Figure B 9 Illustration of sulfate-chloride disorder model on the opposite face of the cluster that is described in **Figure B 8**. There are two settings (each 50% occupied) in this model. The first is with sulfate terminally bound to a Ti in the capping layer of Ti_{18} . The second is with a water molecule bound to the Ti; the Cl-atom is 3 Å from the oxygen of this water molecule. Color scheme is the same as described for **Figure B 8**.

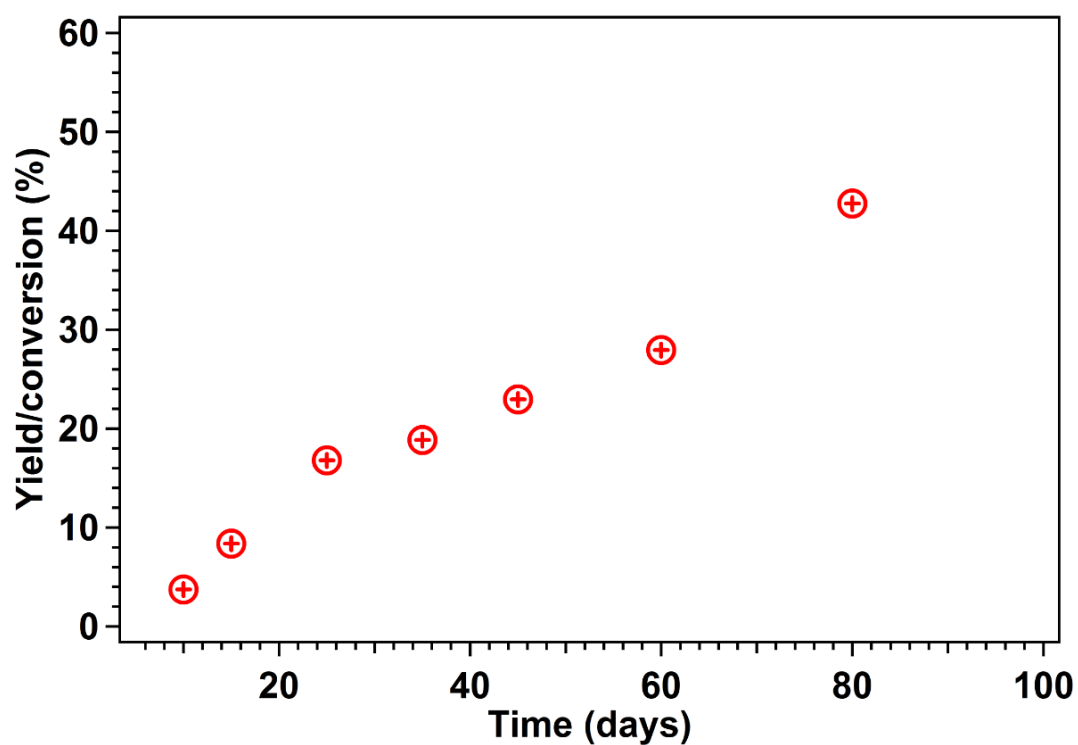


Figure B 10 Calculated yield of anatase formation from 0.25M $TiOSO_4$ solution at ambient conditions.

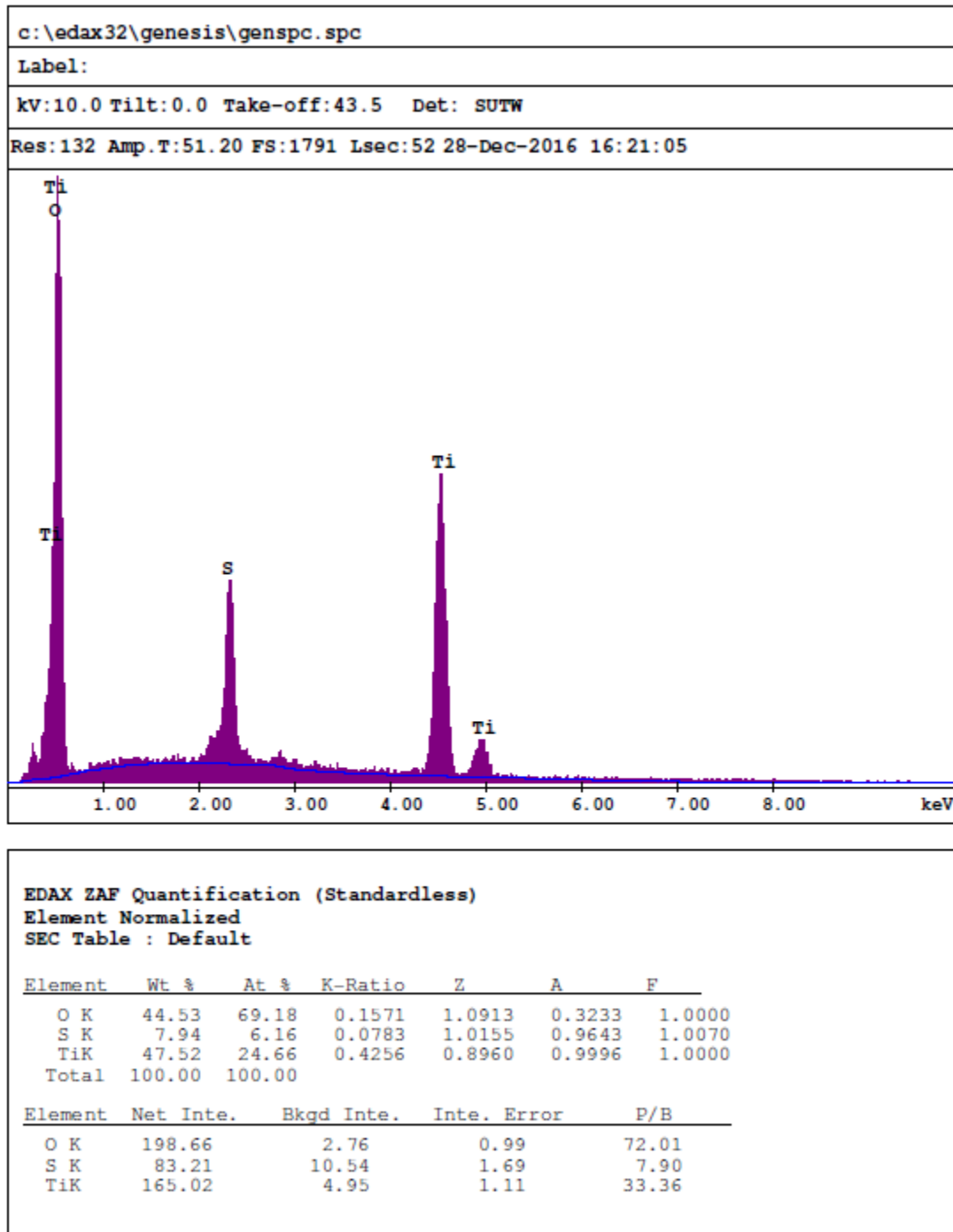


Figure B 11 EDX spectrum of the obtained precipitated solid from 0.25 M TiOSO_4 solution. The observed S:Ti ratio is 1:4.

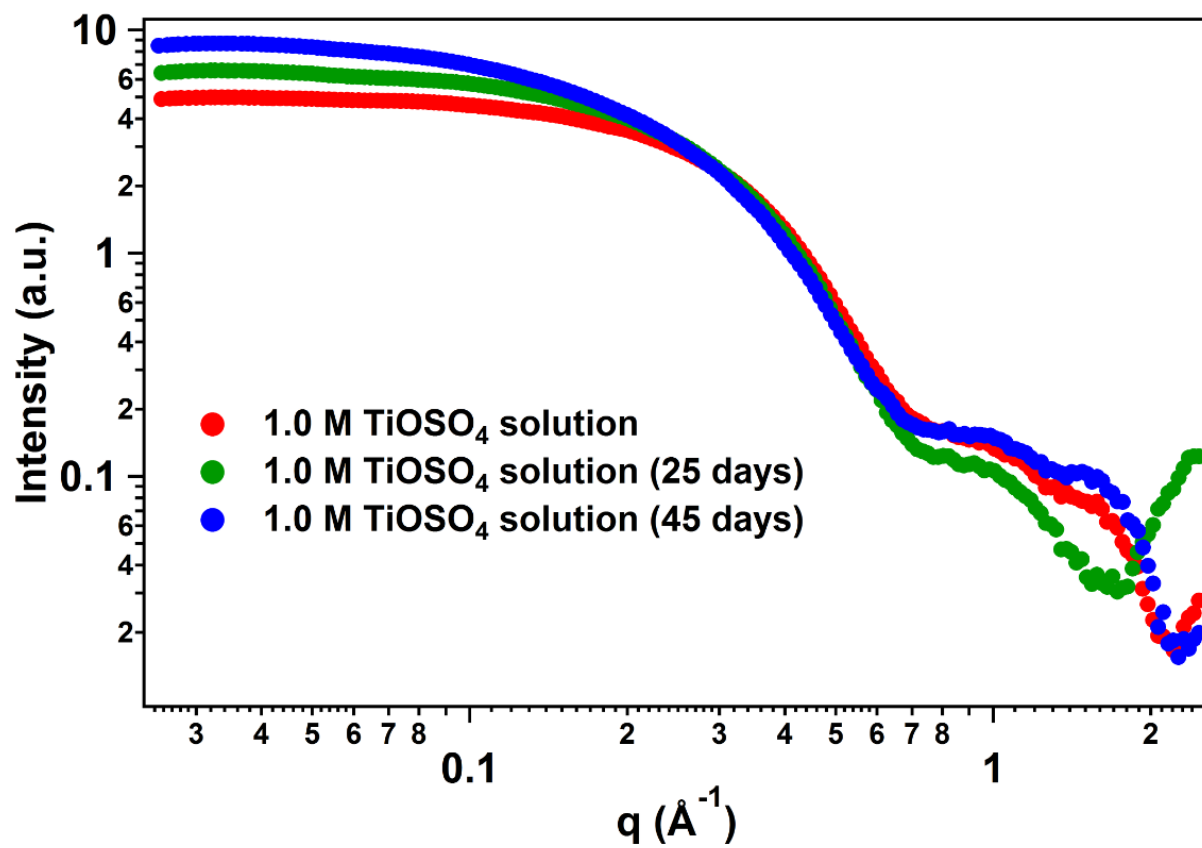


Figure B 12 SAXS curves of aged samples of 1.0M TiOSO_4 solutions.

Table B 1 EXAFS fitting parameters for TiOSO_4 and $\{\text{Ti}_{18}\}$ in both solid phase and aqueous solution phase (CN: the coordination number; R: bonding distance; E_0 : energy shift; σ^2 : mean-square disorder)

Scattering Path	CN	R	E_0	σ^2	Notation
TiOSO₄ solution					
Ti-O	0.94±0.20	1.77±0.20	7.05±3.02	0.0007±0.0013	
Ti-O	1.88±0.40	1.94±0.03	7.05±3.02	0.0113±0.0782	
Ti-O	0.94±0.20	1.98±0.03	7.05±3.02	0.0039±0.0613	
Ti-S / Ti-Ti	1.88±0.40	3.23±0.04	7.05±3.02	0.0013±0.0046	
Ti-O-S	1.88±0.40	3.51±0.05	7.05±3.02	0.0077±0.0457	
Ti-Ti	1.88±0.40	3.58±0.05	7.05±3.02	0.0094±0.0396	
Ti-O-Ti	3.75±0.80	3.59±0.05	7.05±3.02	0.0054±0.0116	
Ti-O-Ti	1.88±0.40	3.60±0.5	7.05±3.02	0.0080±0.0223	
{Ti₁₈} solution					
Ti-O	0.61±0.17	1.78±0.13	8.71±2.48	0.0008±0.0012	
Ti-O	0.61±0.17	1.88±3.40	8.71±2.48	0.0022±0.2446	
Ti-O	0.61±0.17	1.90±3.20	8.71±2.48	0.0008±0.0012	
Ti-O	1.22±0.34	2.06±0.12	8.71±2.48	0.0035±0.0243	
Ti-O	0.61±0.17	2.48±0.10	8.71±2.48	0.0055±0.0155	
Ti-S / Ti-Ti	1.22±0.34	3.26±0.03	8.71±2.48	0.0019±0.0045	
Ti-O-Ti	1.22±0.34	3.62±0.04	8.71±2.48	0.0007±0.0011	
Ti-Ti	1.22±0.34	3.65±0.04	8.71±2.48	0.0200±0.0012	
TiOSO₄ powder					
Ti-O	2.00	1.71±0.03	3.13±2.53	0.0007±0.0011	A
Ti-O	4.00	1.93±0.02	3.13±2.53	0.0014±0.0021	B
Ti-S	4.00	3.22±0.04	3.13±2.53	0.0111±0.0076	C
Ti-O-S	4.00	3.50±0.04	3.13±2.53	0.0081±0.0174	D
Ti-Ti	4.00	3.56±0.04	3.13±2.53	0.0007±0.0012	
Ti-O-Ti	8.00	3.58±0.04	3.13±2.53	0.0052±0.0037	E
Ti-O-Ti	4.00	3.59±0.04	3.13±2.53	0.0018±0.0023	
{Ti₁₈} powder					
Ti-O	1.00	1.66±0.03	-0.67±3.05	0.0006±0.0011	1
Ti-O	1.00	1.83±0.03	-0.67±3.05	0.0024±0.0070	2
Ti-O	1.00	1.86±0.03	-0.67±3.05	0.0045±0.0092	2
Ti-O	2.00	1.96±0.04	-0.67±3.05	0.0200±0.0012	3
Ti-O	1.00	1.98±0.05	-0.67±3.05	0.0200±0.0008	3
Ti-S / Ti-Ti	2.00	3.25±0.03	10.5±2.1	0.0007±0.0011	4
Ti-O-Ti	2.00	3.62±0.03	10.5±2.1	0.0019±0.0036	5

¹The coordination number (CN) for the $\{\text{Ti}_{18}\}$ and TiOSO_4 solid samples is set to the ideal coordination number in the crystalline lattice, and the CN in the solution samples are normalized to this value.

Table B 2 Crystal data and structure refinement for the obtained {Ti₁₈}-cluster.

Moiety formula	[Ti ₁₈ O ₂₇ (H ₂ O) ₂₅ (SO ₄) _{9.5}](Cl) _{5.5} (TBA) ₆ · 13.5H ₂ O
Empirical formula	C ₁₉₀ H ₄₁₂ Cl ₁₀ N ₁₂ O _{207.66} S ₁₉ Ti ₃₆
Formula weight	8875.89
Temperature/K	173.15
Crystal system	monoclinic
Space group	P2 ₁
a/Å	18.2006(7)
b/Å	17.8315(7)
c/Å	30.6879(14)
α/°	90
β/°	91.136(2)
γ/°	90
Volume/Å ³	9957.6(7)
Z	1
ρ _{calc} /g/cm ³	1.479
μ/mm ⁻¹	8.152
F(000)	4163.0
Crystal size/mm ³	0.08 × 0.04 × 0.02
Radiation	CuKα (λ = 1.54178)
2θ range for data collection/°	4.856 to 99.808
Index ranges	-17 ≤ h ≤ 18, -17 ≤ k ≤ 17, -30 ≤ l ≤ 30
Reflections collected	50933
Independent reflections	19697 [R _{int} = 0.0749, R _{sigma} = 0.1049]
Data/restraints/parameters	19697/3/1989
Goodness-of-fit on F ²	1.021
Final R indexes [I ≥ 2σ (I)]	R ₁ = 0.0858, wR ₂ = 0.2191
Final R indexes [all data]	R ₁ = 0.1099, wR ₂ = 0.2400
Largest diff. peak/hole / e Å ⁻³	1.06/-0.55
Flack parameter	0.111(6)

Table B 3 Calculated parameters of the refinement for TiO₂ anatase nanoparticle.

I 41/a m d	R _{wp} = 45.25%*	reduced χ ² = 0.0192
Atom	Occ	U _{iso}
Ti	1	0.01330
O	1	0.02475
a = b = 3.774 Å	c = 9.546 Å	d (diameter) = 19.56 Å

*: the relatively great number is due to the nanoparticle refinement, see ref ¹⁹⁷.

Table B 4 Extracted quantitative data[†] from aged 0.25 M and 1.0 M TiOSO₄ solutions. Size is represented in Å in terms of R_g, while the percentage represents the relative population.

	0.25 M TiOSO ₄ [‡]	1.0 M TiOSO ₄ [§]
Freshly prepared sample		
<i>1st population</i>	5.5 Å – 100 %	5.3 Å – 100 %
<i>2nd population</i>	N.A.	N.A.
Half-way to precipitation		
<i>1st population</i>	5.8 Å – 93.9 %	5.7 Å – 98.8 %
<i>2nd population</i>	10.6 Å – 6.1 %	10.0 Å – 1.2 %
At precipitation		
<i>1st population</i>	5.4 Å – 92.7 %	5.5 Å – 93.7 %
<i>2nd population</i>	10.8 Å – 7.3 %	10.0 Å – 6.3 %

[†] Analyses to determine size and relative populations were carried out utilizing IRENA macros with IgorPro 6.3 (Wavemetrics) software.¹⁴

[‡] Precipitates after 6 days of aging

[§] Precipitates after 45 days of aging

10. Appendix C

Counter cation controlled structural diversity of Zr/Hf oxalates and Zr-peroxo oxalates

10.1 Experimental

10.2 Materials and syntheses

10.3 Reagents and solution preparation

ZrOCl₂·8H₂O (99.9%) and HfOCl₂·8H₂O (98+% metal basis excluding Zr) were purchased from Alfa Aesar. Oxalic acid dihydrate, (COOH)₂·2H₂O, was purchased from Avantor Performance Materials. H₂O₂ (30% solution) was purchased from Merck. To adjust the pH we used 4M CsOH (Alfa Aesar, 99.9%), 50 m/m% RbOH (Alfa Aesar, 99.6+%), 4M KOH (Macron Fine Chemicals), 4M NaOH (Macron Fine Chemicals), 4M LiOH (Sigma-Aldrich, 98%) or tetramethylammonium hydroxide (TMAOH, 25% solution) (Tokyo Chemicals Industry Co, LTD) solutions. We also used CsCl (Fisher BioReagents, 99.999%), RbCl (Acros Organics, 99.8+%), KCl (Macron Fine Chemicals), NaCl (Macron Fine Chemicals) or LiCl (EMD Chemicals). Deionized water (18.2 MΩ, Millipore) was used to prepare all solutions.

10.4 Compound (1): $\{(\text{NC}_4\text{H}_{12})_4[\text{Hf}_2(\text{OH})_2(\text{C}_2\text{O}_4)_5]\}_n \cdot 12\text{H}_2\text{O}$

We created a mixture of $[\text{Hf}]:[\text{H}_2\text{O}_2]:[\text{H}_2\text{C}_2\text{O}_4]=1:3:1.5$ with the metal concentration of 55mM. We mixed 2.24 mL DI water, 480 μL , 0.5M oxalate and 160 μL , 1M Hf solution. White precipitate formed. Next, we add 50 μL , 30% H_2O_2 solution. We adjusted pH to 4.88 with 25% TMAOH solution, while vigorously stirring. The precipitate dissolved resulting clear solution. The vial containing this solution was covered with parafilm with small holes for slow evaporation. After two weeks only a very few, tiny crystals formed with the gel-like product.

CCDC file number: 1965505.

10.5 Compound (2): $\text{Na}_6[\text{Hf}_2(\text{OH})_2(\text{C}_2\text{O}_4)_6] \cdot 17\text{H}_2\text{O}$

We created a mixture of $[\text{Hf}]:[\text{H}_2\text{O}_2]:[\text{H}_2\text{C}_2\text{O}_4]=1:3:1.5$ with the metal concentration of 55mM. We mixed 1.60 mL DI water, 640 μL , 0.5M NaCl, 480 μL , 0.5M oxalate and 160 μL , 1M Hf solution. White precipitate formed. Next, we add 50 μL , 30% H_2O_2 solution. We adjusted pH to 4.83 with 4M NaOH solution, while vigorously stirring. The precipitate dissolved resulting clear solution. We placed it in an open vial which was then placed in a bigger vial containing acetone for solvent diffusion in a refrigerator at 4°C. White crystalline solid product formed after 5 days. Yield: 23.3%.

CCDC file number: 1965512.

10.6 Compound (3): $\text{Li}_2\text{K}_4[\text{Hf}_2(\text{OH})_2(\text{C}_2\text{O}_4)_6] \cdot 8\text{H}_2\text{O}$

We created a mixture of $[\text{Hf}]:[\text{H}_2\text{O}_2]:[\text{H}_2\text{C}_2\text{O}_4]=1:3:1.5$ with the metal concentration of 55mM. First, we mixed 1.6mL DI water, 500 μL , 0.5M KCl solution, 140 μL , 0.5M LiCl solution, 480 μL , 0.5M oxalate and 160 μL , 1 M Hf solution. White precipitate formed. Next, we added 50 μL , 30% H_2O_2 solution. We adjusted pH to 4.7-4.8 with 4M KOH solution, while vigorously stirring. Dissolution was incomplete so it was filtered and placed in an open vial which was then placed in a bigger vial containing acetone for solvent diffusion in a refrigerator at 4°C. White crystalline solid product formed after one day. Yield: 14.3%.

CCDC file number: 1965509.

10.7 Compound (4): $\text{K}_4\text{Hf}(\text{C}_2\text{O}_4)_4 \cdot 5.1\text{H}_2\text{O}$

The main preparation and crystallization strategy is identical to (3). Compound (4) was prepared under the same reaction conditions, but from a different batch. Yield (calculated to the K-Hf oxalate product): 30.8%.

CCDC file number: 1965510.

10.8 Compound (5): $\text{Rb}_4[\text{Hf}(\text{C}_2\text{O}_4)_4] \cdot n\text{H}_2\text{O}$

The main preparation and crystallization strategy is identical as of (2). Compound (5) was prepared with RbCl instead of NaCl, and the pH was adjusted to 4.8 with 50 m/m% RbOH solution, while vigorously stirring. Dissolution was incomplete (very thin suspension) so it was filtered for crystallization. Crystals formed in 2-3 days by the previously-described acetone diffusion method. Yield: 26.3%.

CCDC file number: 1965495.

10.9 Compound (6): $\text{Cs}_4[\text{Hf}(\text{C}_2\text{O}_4)_4] \cdot 5\text{H}_2\text{O}$

The main preparation and crystallization strategy is identical to (2). Compound (6) was prepared with CsCl instead of NaCl, and the pH was adjusted to 4.88 with 4M CsOH solution, a clear solution formed while vigorously stirring. Crystals formed in 1-2 days by the previously-described acetone diffusion method. Yield: 35.4%.

CCDC file number: 1965511.

10.10 Compound (7): $(\text{NC}_4\text{H}_{12})_6[\text{Zr}_6(\text{O}_2)_6(\text{OH})_6(\text{C}_2\text{O}_4)_6] \cdot 7.58\text{H}_2\text{O}$ ($\{\text{Zr}_6\}$)

We created a mixture of $[\text{Zr}]:[\text{H}_2\text{O}_2]:[\text{H}_2\text{C}_2\text{O}_4]=1:3:1.5$ with the metal concentration of 55mM. First, we mixed 2.24 mL DI water, 480 μL , 0.5M oxalate and 160 μL , 1M Zr solution. White precipitate formed. Next, we added 50 μL , 30% H_2O_2 solution. We set pH around 4.79 with 25 m/m% TMAOH solution, while vigorously stirring. The precipitate dissolved resulting clear solution. The vial containing this solution with parafilm on it with small holes was let to evaporate slowly. After two weeks only a very few, tiny crystals formed with the gel-like product.

CCDC file number: 1965507.

10.11 Compound (8): $\text{Li}_{12}[\text{Zr}_8(\text{O}_2)_{12}(\text{OH})_4(\text{C}_2\text{O}_4)_8] \cdot 30\text{H}_2\text{O}$ ($\{\text{Zr}_8\}$)

We created a mixture of $[\text{Zr}]:[\text{H}_2\text{O}_2]:[\text{H}_2\text{C}_2\text{O}_4]=1:3:1.5$ with the metal concentration of 55mM. First, we mixed 1.6mL DI water, 500 μL , 0.5M LiCl solution, 480 μL , 0.5M oxalate

and 160 μ L, 1M Zr solution. White precipitate formed which dissolved after adding 50 μ L, 30% H₂O₂ solution. Next, we set pH to 4.91 with 4M LiOH solution, while vigorously stirring. We filtered it and placed in an open vial which was then placed in a bigger vial containing acetone for solvent diffusion in a refrigerator at 4 $^{\circ}$ C. White solid product formed after 6 days with a very low yield. Yield: 27.3%.

CCDC file number: 1965518.

10.12 Compound (9): Na₄Zr(C₂O₄)₄·1.5H₂O

The main preparation and crystallization strategy is identical to (8). Compound (9) was prepared with NaCl instead of LiCl, and the pH was adjusted to 4.83 with 4M NaOH solution, while vigorously stirring resulted in a clear solution. Crystals formed in 4 days by the previously-described acetone diffusion method. Yield: 34.4%.

CCDC file number: 1965513.

10.13 Compound (10): K₁₈[Zr₁₂(O₂)₁₈(OH)₆(C₂O₄)₁₂]·30H₂O ({Zr₁₂})

The main preparation and crystallization strategy is identical as of (8). Compound (10) was prepared with KCl instead of LiCl, and the pH was adjusted to 4.8 with 4M KOH solution, while vigorously stirring resulted in a clear solution. Crystals formed in 1 day by the previously-described acetone diffusion method. Yield: ~68%.

CCDC file number: 1965496.

10.14 Compound (11): Rb₂₄[Zr₁₆(O₂)₂₄(OH)₈(C₂O₄)₁₆]·65H₂O ({Zr₁₆})

The main preparation and crystallization strategy is identical as of (8). Compound (11) was prepared with RbCl instead of LiCl, and the pH was adjusted to 4.82 with 50 m/m% RbOH solution, while vigorously stirring resulted in a clear solution. Crystals formed in one week by solvent evaporation method.

CCDC file number: 1965519.

10.15 Compound (12): Rb₄[Zr(C₂O₄)₄]·5.25H₂O

The main preparation and crystallization strategy is identical as of (11). Crystals formed in 5 days by the previously-described acetone diffusion method. Yield: 35.4% (if formation of (11) is not taken account).

CCDC file number: 1965494.

10.16 Compound (13): Cs₄[Zr(C₂O₄)₄]·5H₂O

The main preparation and crystallization strategy is identical as of **(8)**. Compound **(13)** was prepared with CsCl instead of NaCl, and the pH was adjusted to 4.88 with 4M CsOH solution, while vigorously stirring resulted a clear solution. Crystals formed in 1 day by the previously-described acetone diffusion method. Yield: 34.4%.

CCDC file number: 1965516.

10.17 Characterization methods

10.18 Single crystal X-ray diffraction

Diffraction intensities for all compounds were collected at 173 K using CuK α radiation, $\lambda = 1.54178 \text{ \AA}$ on a Bruker Apex2 (**compound 1, 3, 4, 5, 7, 8, 10, and 12**) and a Rigaku SynergyS (**compound 2, 6, 9, 11 and 13**) diffractometers. Space groups were determined based on systematic absences and intensity statistics (2). Absorption corrections were applied by SADABS¹⁹⁸. Structures were solved by direct methods and Fourier techniques and refined on F^2 using full matrix least-squares procedures. All non-H atoms were refined with anisotropic thermal parameters except those in (7) disordered over two positions which were refined with isotropic thermal parameters. H atoms in –OH bridges and water molecules are not found in the structures and not taken into consideration. In some structures counter-ion atoms located outside the main framework are disordered over two or three positions. The solvent water molecules bonded to these counter-ion atoms are disordered as well. In the case when it disordered over three positions its occupation factors were found based on additional refinements and in the final refinements they were fixed at values corresponding the charge balance of the compounds. The (μ -OH)(O₂) bridges in the 6-member framework in (7) are disordered over two positions. It was found that three of NMe₄ counter-ions in (7) are distributed over twelve possible positions and disordered as well. These disordered groups were refined with restrictions; the standard bond lengths were used in the refinements as the targets for corresponding bonds. Two structures (4 and 8) were refined with using RIGU options in SHELXL. The Flack parameter for the non-centrosymmetrical structures is: 0.004(10), 0.042(16), 0.008(15), 0.07(3) and 0.017(13), respectively for 4, 12, 13, 11 and 6. The structure of (9) was refined as a racemic twin consisting of two domains: the Flack is 0.251(18). All calculations were performed by the Bruker SHELXL-2014 package¹⁹⁹. The crystallographic data for each compound are in **Table C 1-C 4**. These data can be obtained, free of charge, from The Cambridge Crystallographic Data Centre via www.ccdc.cam.ac.uk/structures

10.19 Powder X-ray diffraction (PXRD)

Powder X-ray diffraction (PXRD) was performed on a Rigaku Miniflex diffractometer (Cu-K α irradiation, $\lambda=1.54 \text{ \AA}$). The chosen 2θ range was 5-60 degree with the scan speed of 1.5 degree/minute.

10.20 Scanning Electron Microscopy (SEM) and Energy-Dispersive X-ray Spectroscopy (EDX)

Energy dispersive X-ray spectroscopy (EDX) measurements were performed on Quanta 600F (FEI) scanning electron microscopy (SEM) to obtain approximate composition information of the samples.

10.21 Fourier-Transformed Infrared Spectroscopy (FT-IR)

The infrared spectra were recorded in attenuated mode (ATR) using a Nicolet™ iS™ 10 spectrometer (Thermo Scientific).

10.22 Small-Angle X-ray Scattering (SAXS)

Small-angle X-ray scattering data were collected on Anton Paar SAXSess instrument using Cu-K α radiation ($\lambda=1.54056 \text{ \AA}$), line collimation, 2D image plates and the range of momentum transfer (q) of 0.018-2.5 \AA^{-1} . All solutions, including background solutions, were contained in sealed borosilicate tubes of 1.5 mm in diameter and 0.01 mm wall thickness (HR6-124, Hampton Research) placed at a distance of 26.1 cm from the image plates. Data collection time of 30 minutes was utilized.

We used SAXSQWANT software for data collection and treatment including normalization, primary beam removal, background subtraction, desmearing and smoothing. Analyzes, fits were carried out utilizing IRENA macros with IgorPro 6.3 (Wavemetrics) software¹⁴. To simulate scattering data from the crystal structure we used SolX software.^{15,16}

10.23 Pair Distribution Function analysis (PDF) of X-ray total scattering measurements

To perform pair distribution function (PDF) analysis of X-ray total scattering of solution samples we used Rigaku Smartlab X-ray diffractometer with Mo-K α irradiation

($\lambda=0.71073 \text{ \AA}$) in the 2θ range of $3.0\text{-}118.6^\circ$ with transmission geometry. Solution samples were loaded in Kapton capillary with 1.46 mm inner diameter for irradiation. The theoretical q -range is up to a q_{max} of 15.4 \AA^{-1} . A 0.2 degree/minute data collection time and D/teX Ultra-HE high-speed, one-dimensional X-ray detector were used to ensure high quality scattering data. PDFgetX3 was to process scattering data into the corresponding PDF¹⁸. Simulations were created in PDFgui¹⁹.

10.24 Electrospray Ionization Mass Spectroscopy (ESI-MS)

ESI-MS was carried out using an Agilent 6230 ESI-MS system comprised of a Time-of-Flight (TOF) mass spectrometer coupled to an electrospray ionizer. The solutions were nebulized with the aid of heated N_2 (325°C) flowing at 8 L/minute and a pressure of 241 kPa. The voltages of the capillary, skimmer and RT octopole were set at 3500, 65 and 750 V respectively, while the voltage of the fragmentor was set at 100 V. We collected data at both negative and positive mode.

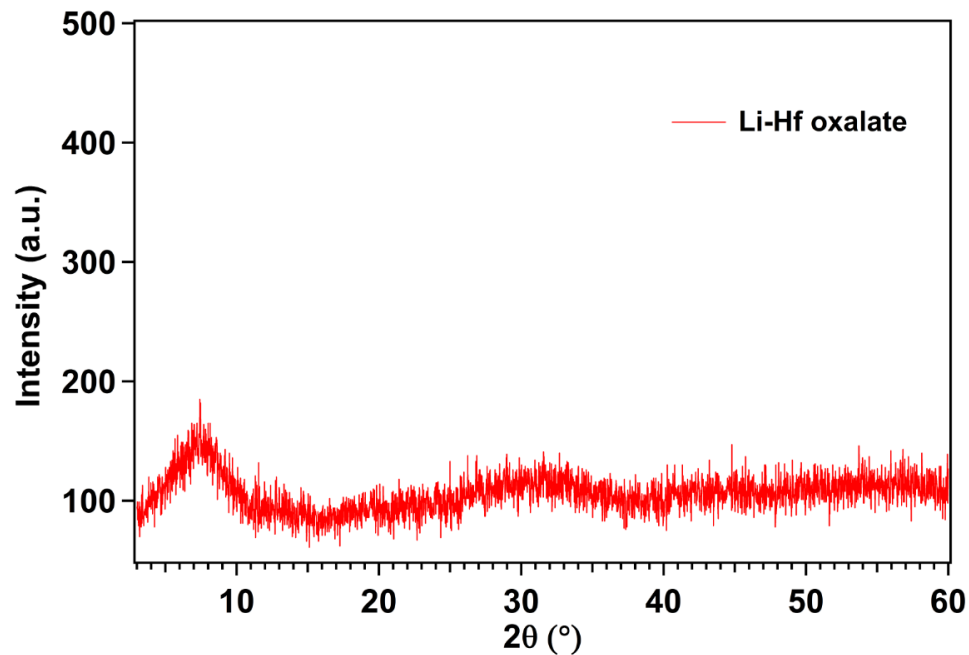


Figure C 1 Experimental PXRD of the obtained Li-Hf oxalate product. It does not indicate crystallinity.

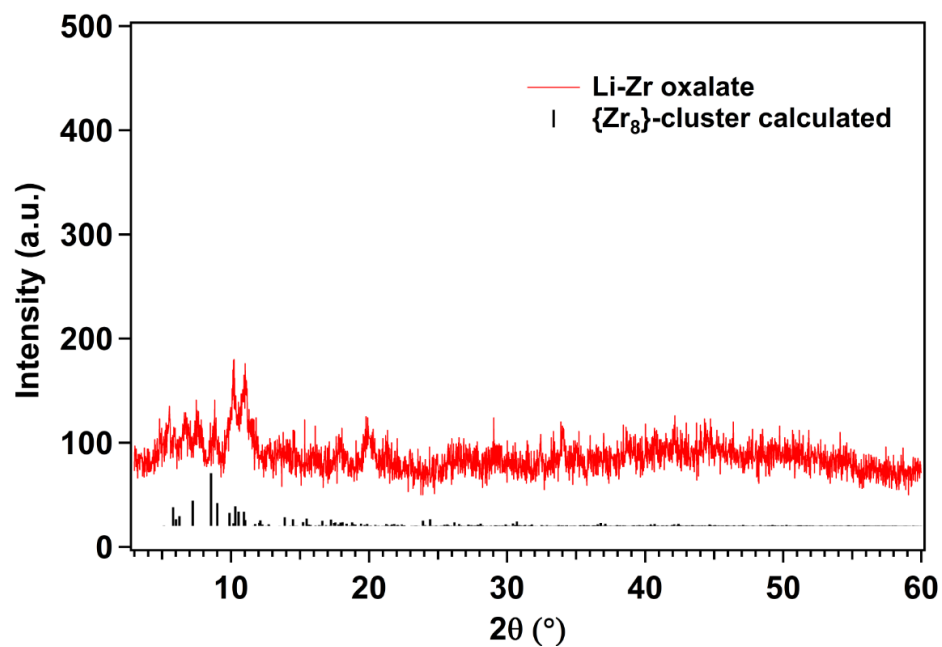


Figure C 2 Experimental PXRD of the obtained Li-Zr oxalate product along with calculated peak position of relevant reference structures. Product shows very poor crystallinity.

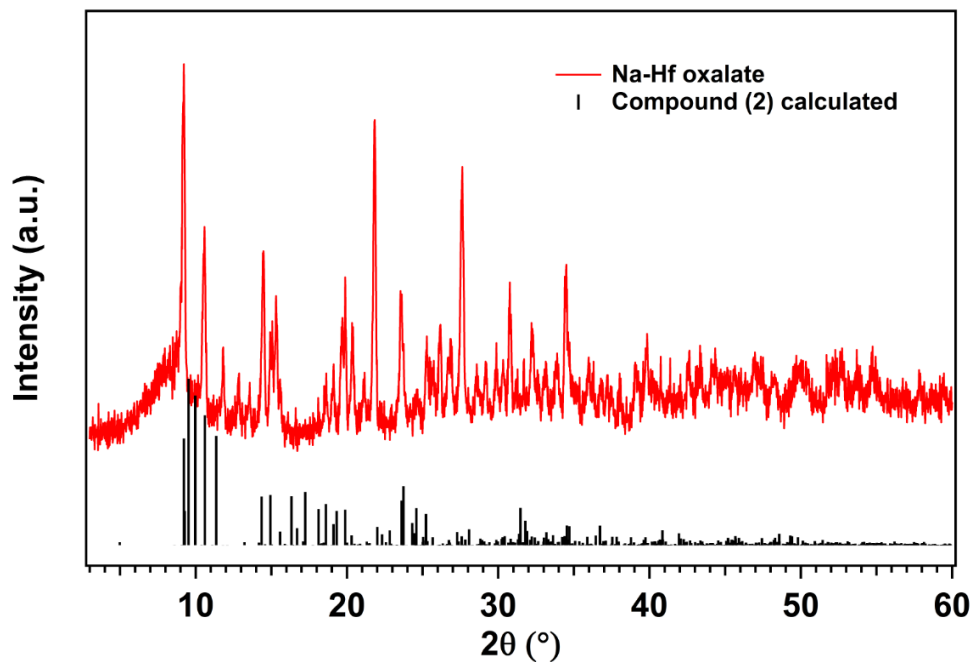


Figure C 3 Experimental PXRD of the obtained Na-Hf oxalate product.

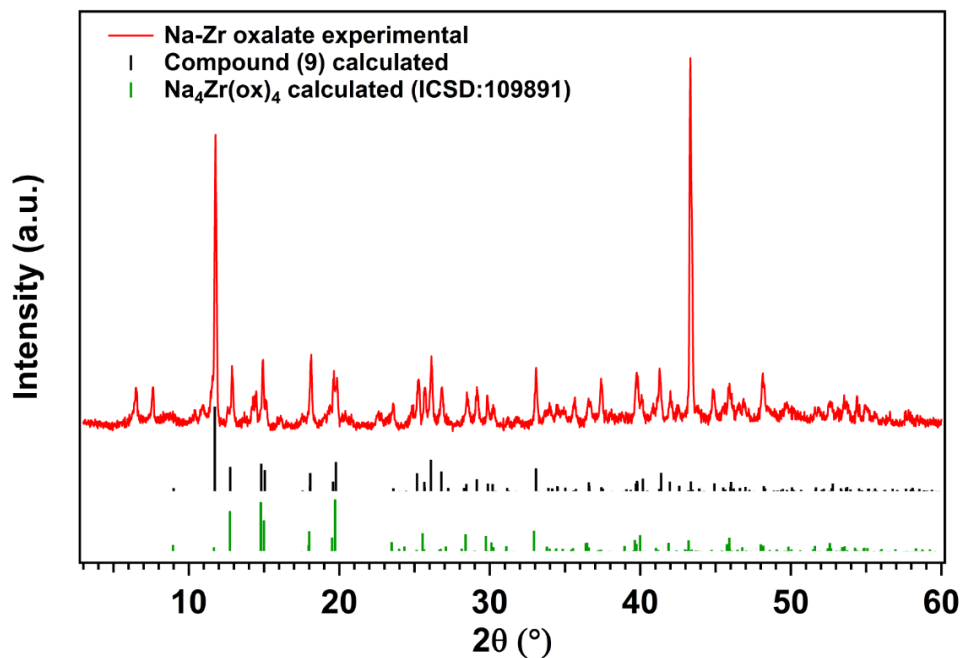


Figure C 4 Experimental PXRD of the obtained Na-Zr oxalate product along with calculated peak position of relevant reference structure. Despite the crystallinity of the product it does not match known relevant phases. (Number in parenthesis indicate the ICSD code of the known phase.)

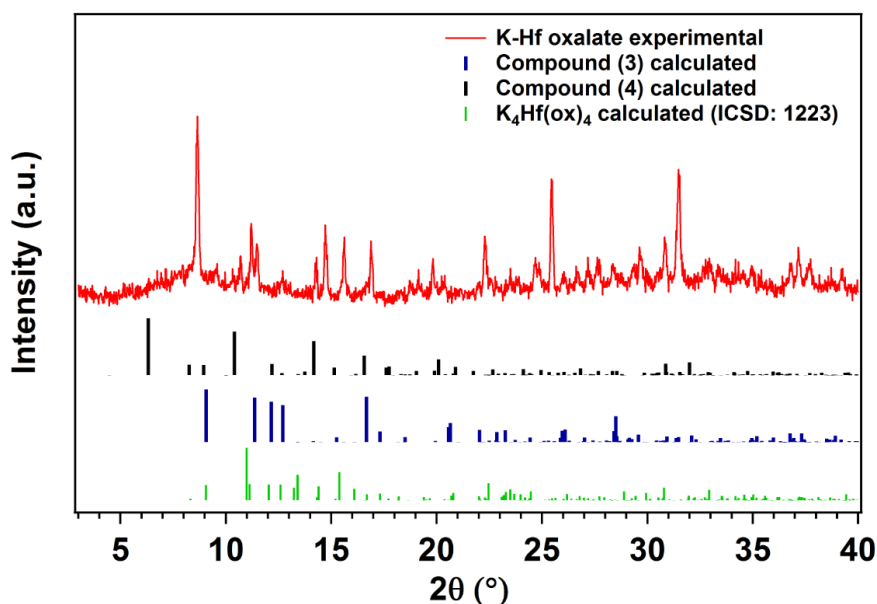


Figure C 5 Experimental PXRD of the obtained K-Hf oxalates along with calculated peak positions of relevant structures. Despite the crystallinity of the product it does not match known relevant phases. (Number in parenthesis indicates the ICSD code of the known phase.)

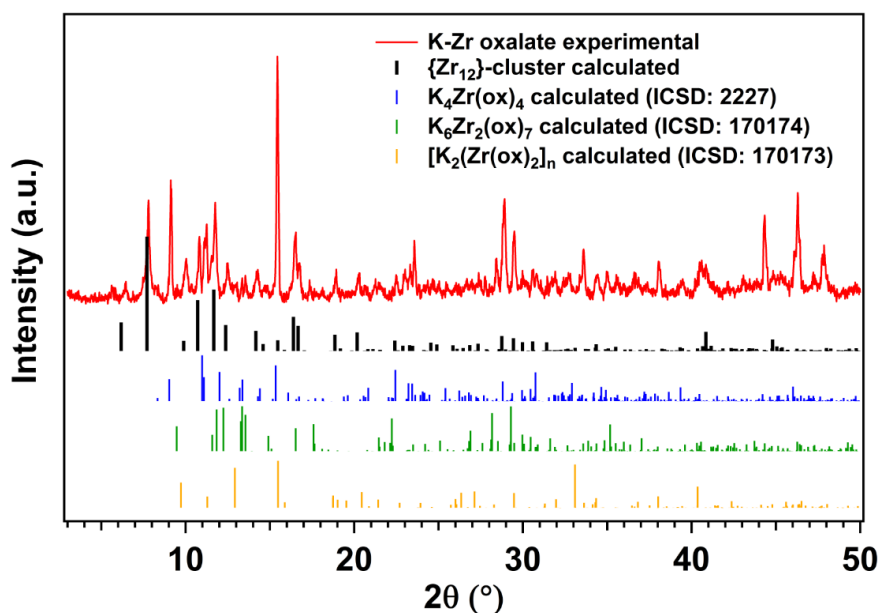


Figure C 6 Experimental PXRD of the obtained K-Zr oxalate product along with calculated peak positions of relevant reference structures. (Numbers in parenthesis indicate the ICSD code of the known phases.)

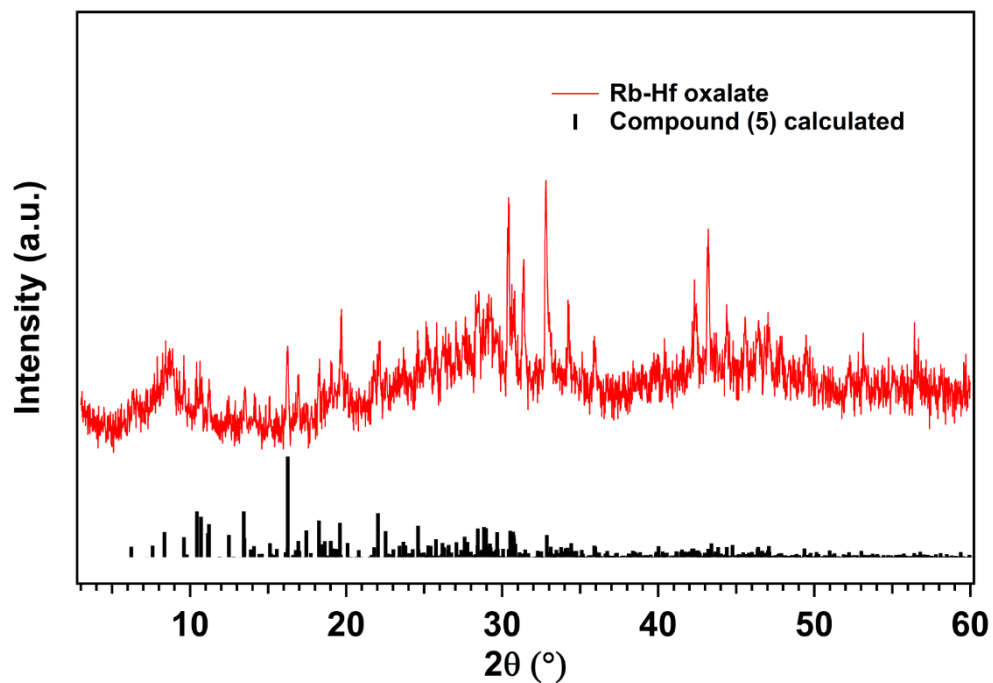


Figure C 7 Experimental PXR D of the obtained Rb-Hf oxalate product. Product shows poor crystallinity.

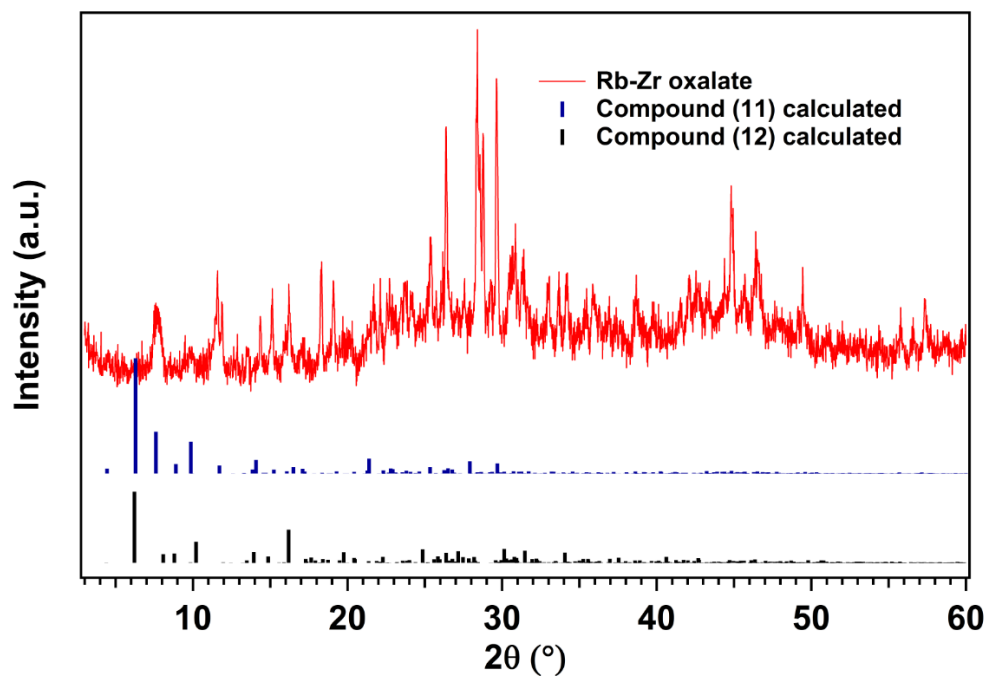


Figure C 8 Experimental PXR D of the obtained Rb-Zr oxalate product. Product shows poor crystallinity.

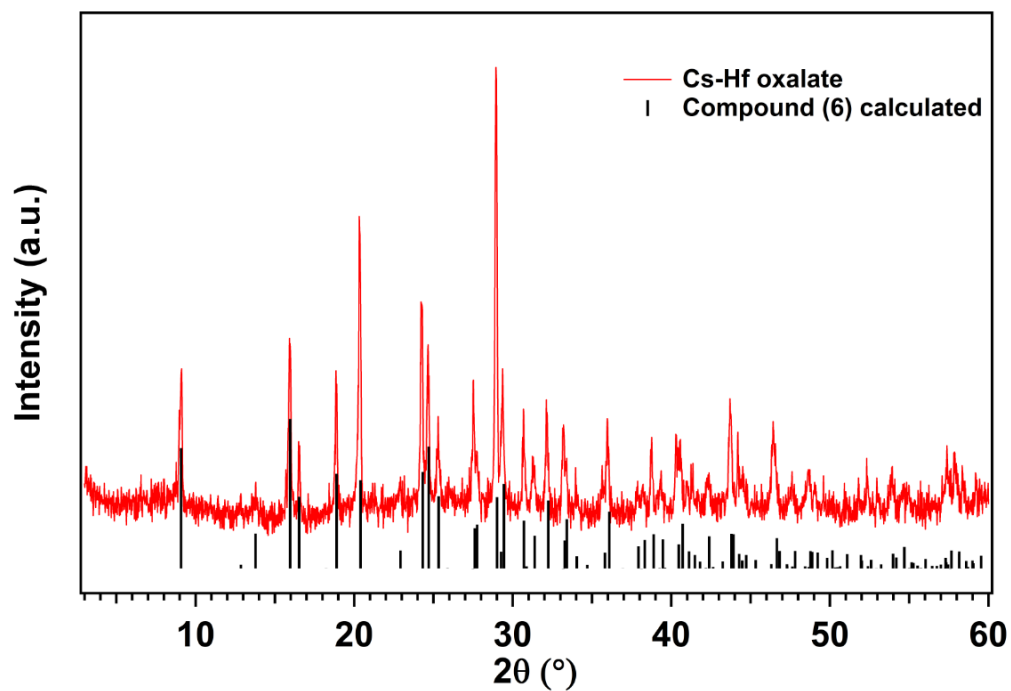


Figure C 9 Experimental PXRD of the obtained Cs-Hf oxalate product.

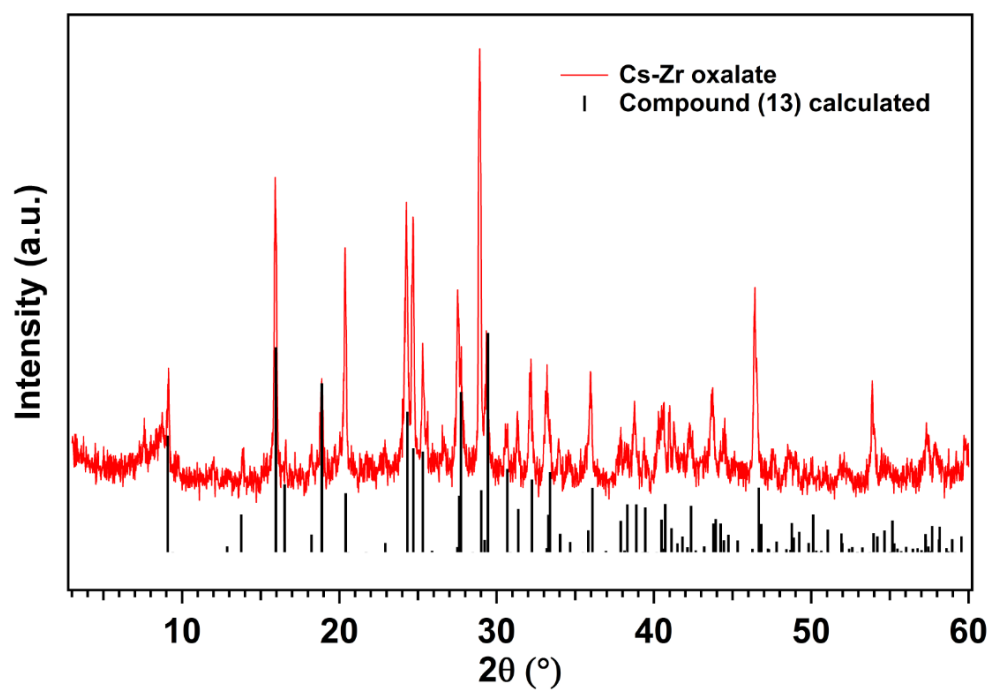


Figure C 10 Experimental PXRD of the obtained Cs-Zr oxalate product.

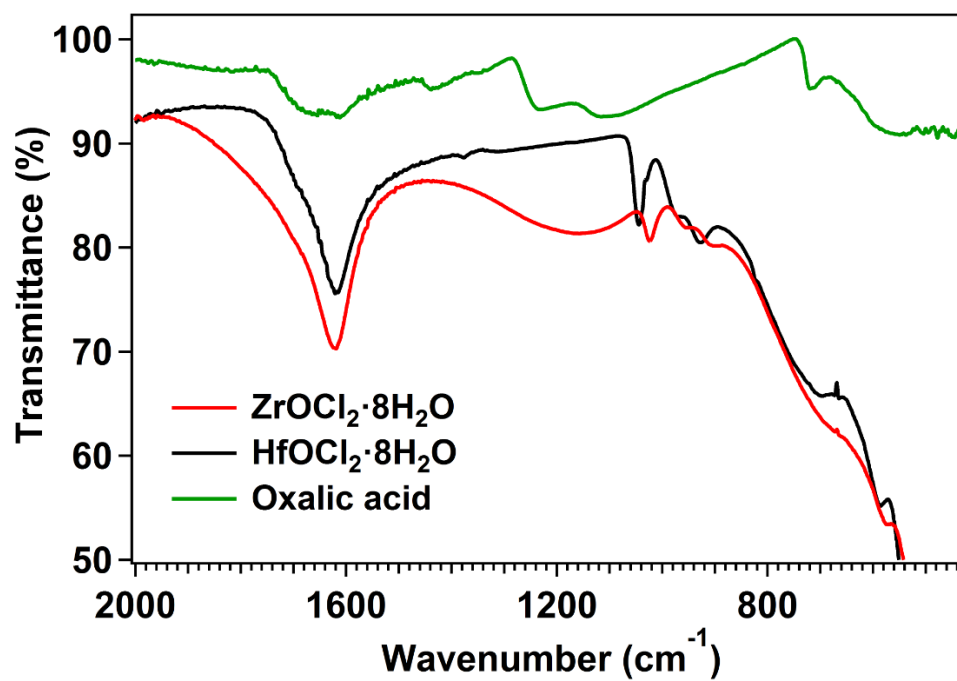


Figure C 11 FT-IR spectra of the starting materials used.

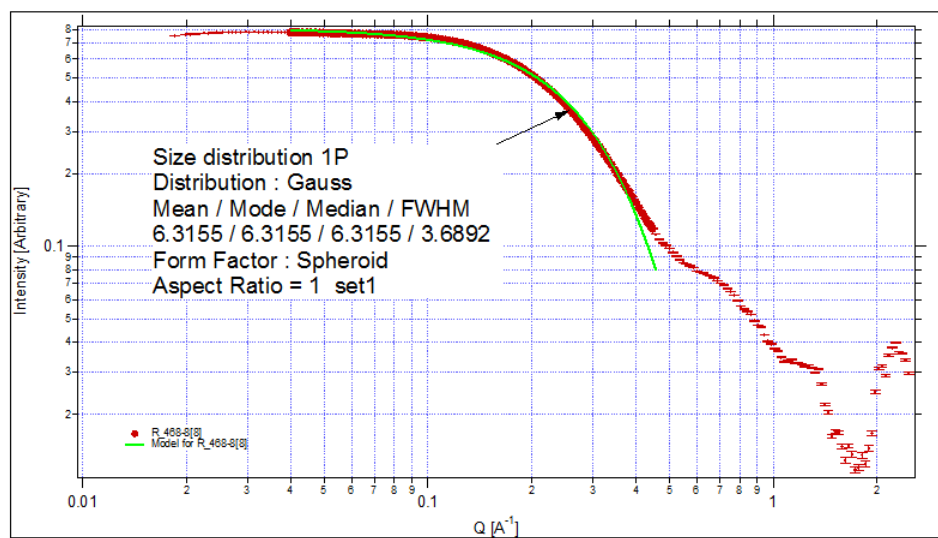
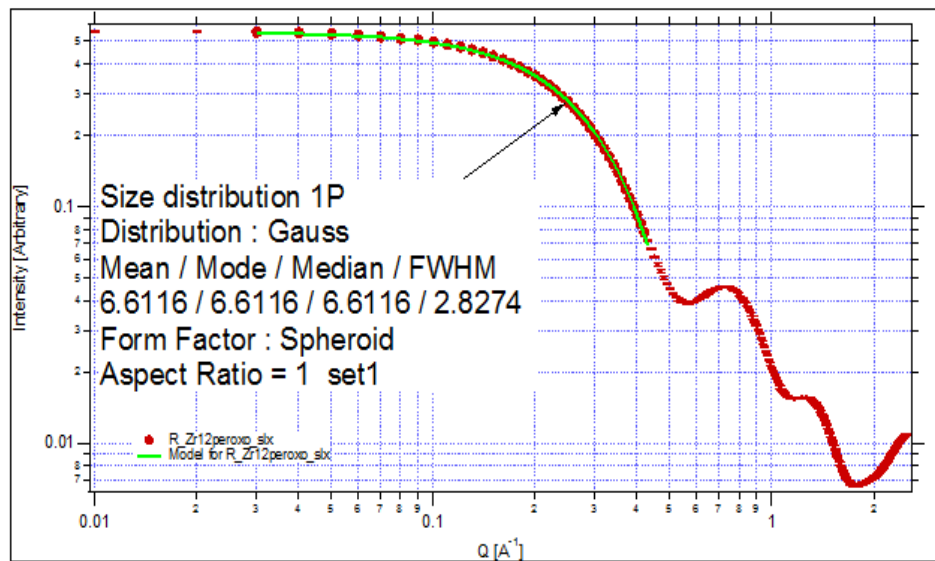


Figure C 12 Top: Simulation of $\{\text{Zr}_{12}\}$ -cluster shows radius of 6.6 \AA . The simulated curve was obtained from the single-crystal structure. Bottom: we observed 6.3 \AA radius modelling the experimental curve.

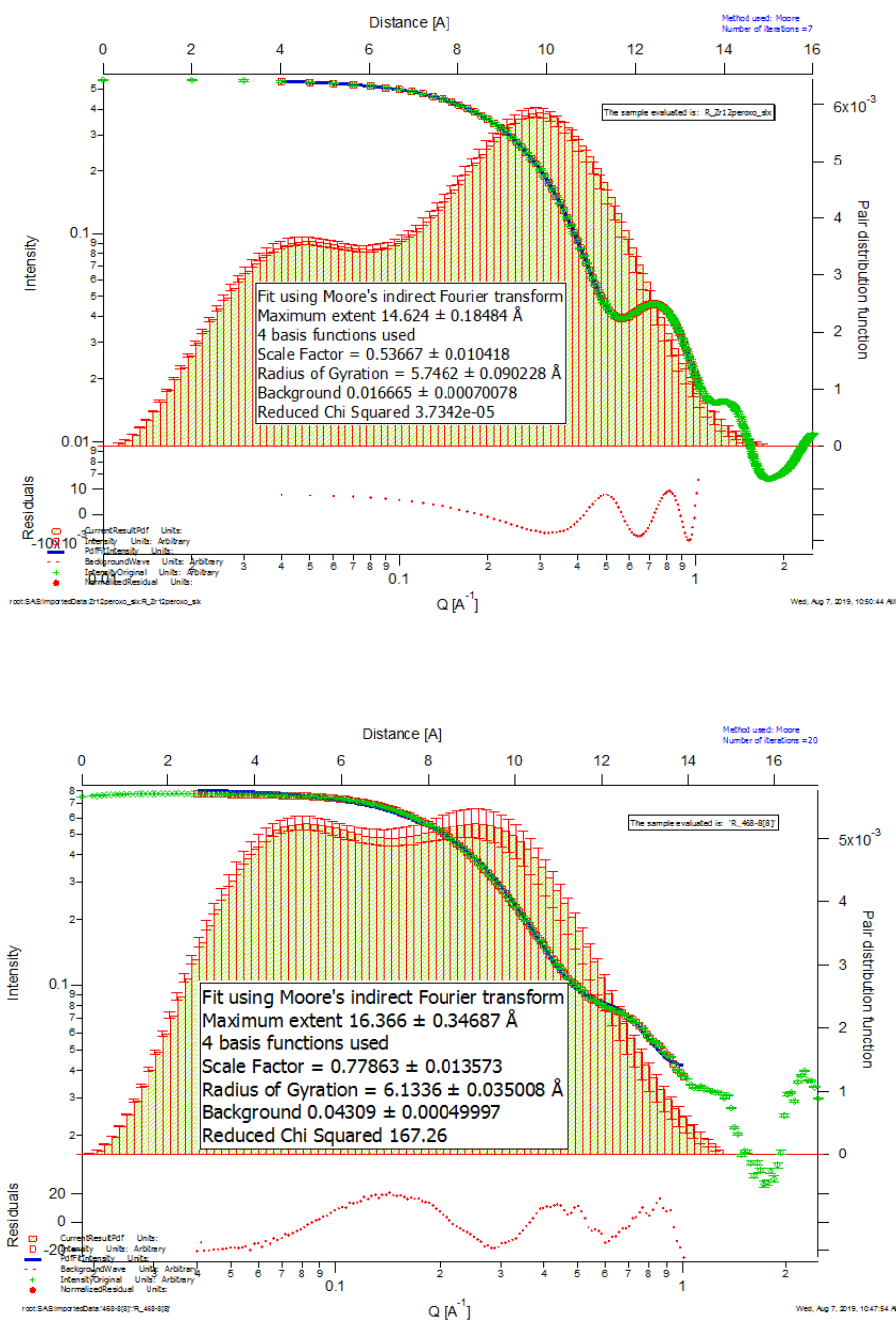


Figure C 13 Pair distance distribution function (PDDF) analysis of the calculated and experimental SAXS profile of $\{Zr_{12}\}$ -cluster. The larger extent and more intense correlation below 6 \AA on the experimental curve indicating association with K^+ counter cations.

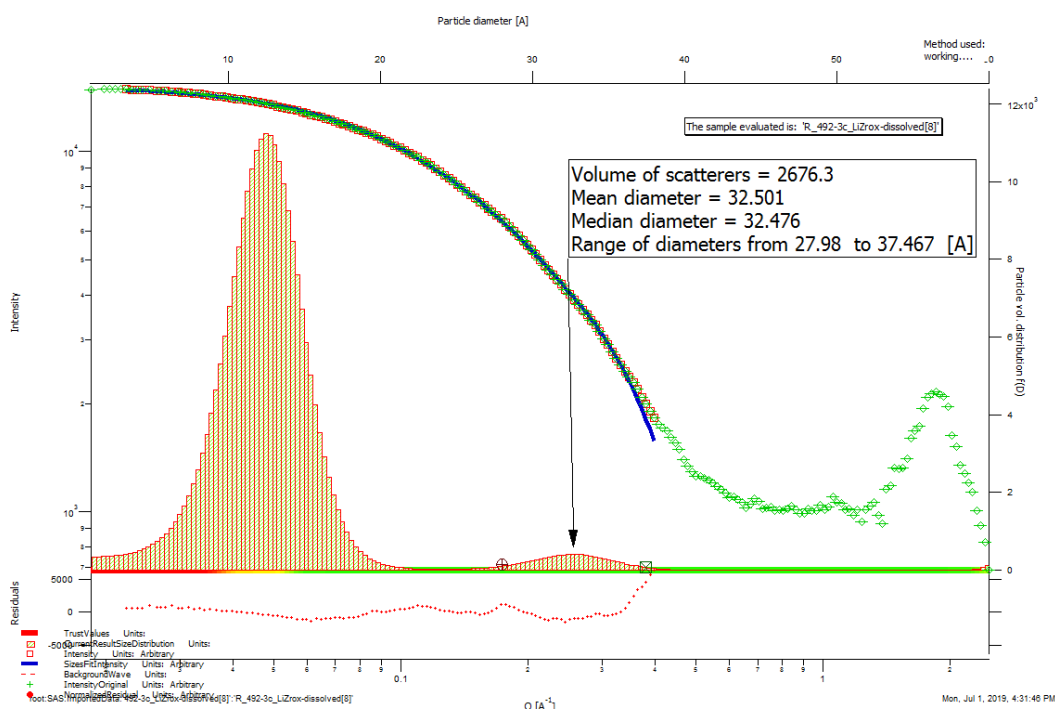
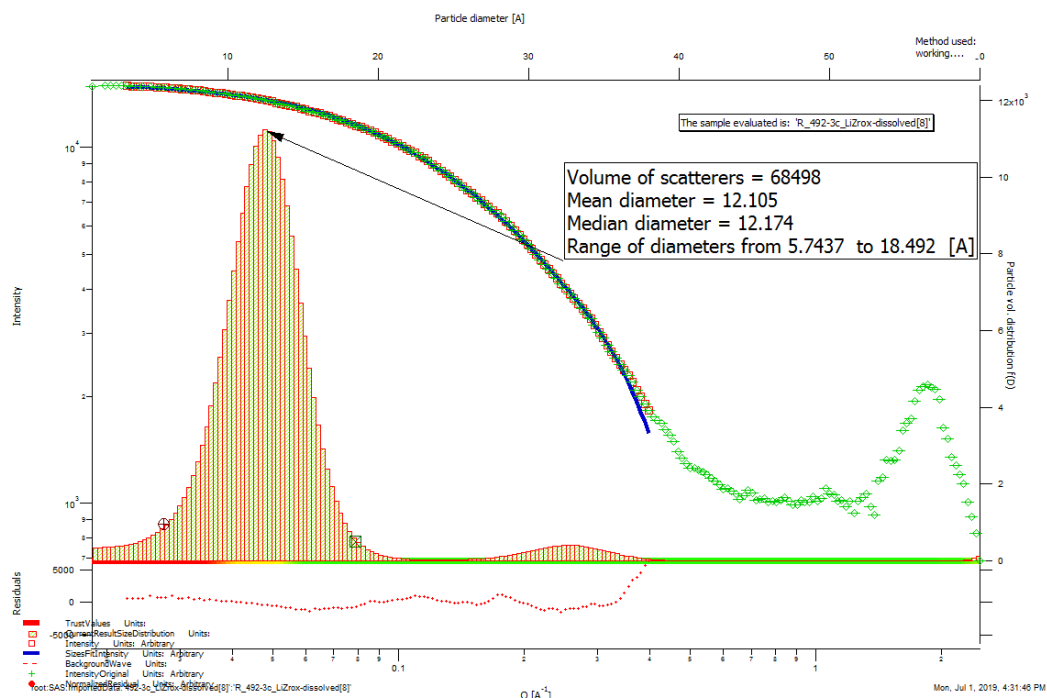


Figure C 14 Size distribution analysis on the dissolved Li-Zr-peroxo-oxalate product, from which $\{Zr_8\}$ crystals are obtained. Analysis indicates two populations present in the solution.

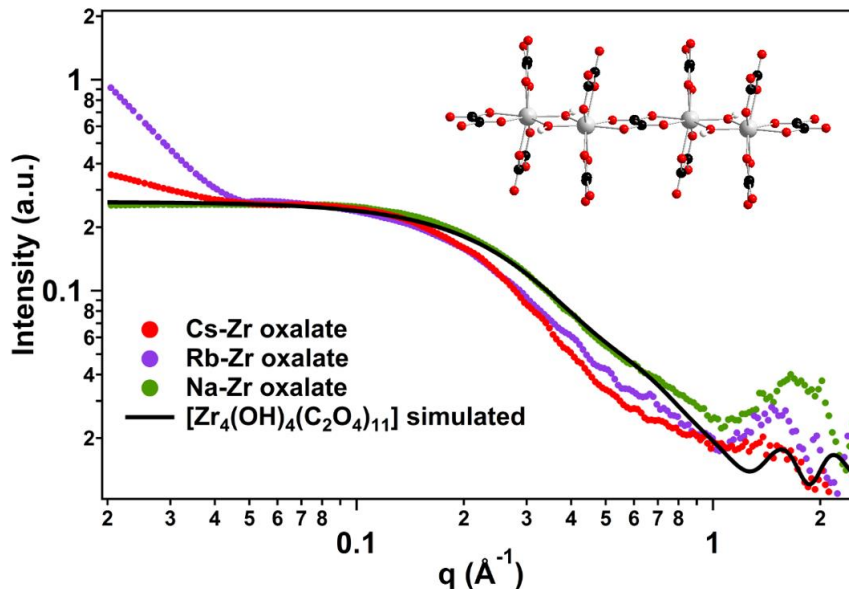


Figure C 15 SAXS curves (scaled) of the dissolved Zr oxalate products. All solutions show scattering indicating formation of a bigger specie, where the inset represents the $[\text{Zr}_4(\text{OH})_4(\text{C}_2\text{O}_4)_{11}]$ fragment used for simulation.

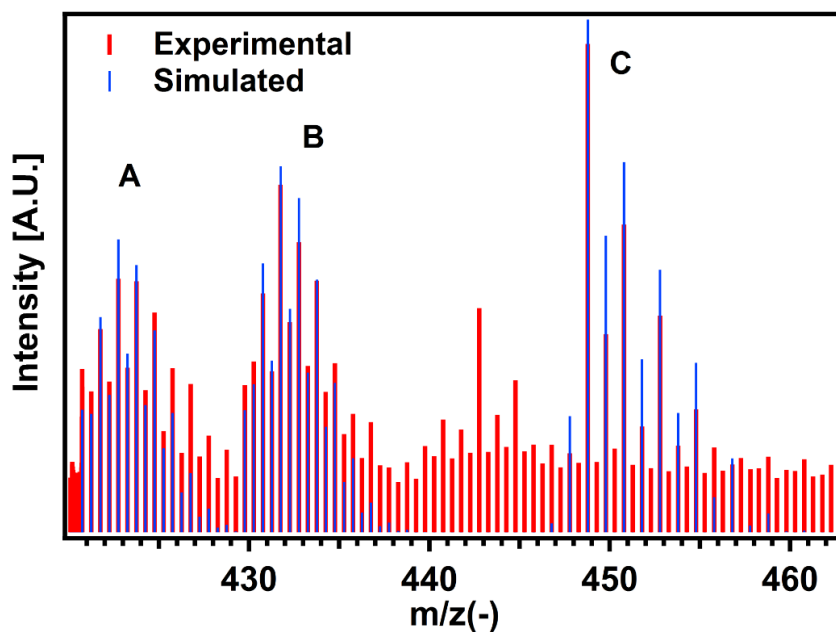


Figure C 16 Experimental and simulated mass spectrum between 420-460 m/z (in negative mode) of the solution obtained from dissolved crystals of $\{\text{Zr}_{12}\}$ -cluster. $A = \{\text{Zr}_4(\text{O}_2)_3(\text{C}_2\text{O}_4)_4(\text{OH})_2\}^{2-}$, $B = \{\text{Zr}_4(\text{O}_2)_3(\text{C}_2\text{O}_4)_4(\text{OH})_2(\text{H}_2\text{O})\}^{2-}$ and $C = \{\text{Li}_3\text{Zr}_2(\text{O}_2)_5(\text{C}_2\text{O}_4)\}^{1-}$ respectively

Table C 1 Crystallographic data of multinuclear Hf compounds of (1), (2) and (3).

Compound	(1)	(2)	(3)
CCDC file number	1965506	1965512	1965509
Empirical formula	C ₂₆ H ₆₂ Hf ₂ N ₄ O ₂₈	C ₁₂ H ₃₆ Hf ₂ Na ₆ O ₄₃	C ₁₂ H ₁₈ Hf ₂ K ₄ Li ₂ O ₃₄
Formula weight	1235.77	1363.33	1233.52
Temperature (K)	173(2)	173(2)	173(2)
Crystal system	Monoclinic	Triclinic	Monoclinic
Space group	<i>P</i> ₂ ₁ / <i>c</i> (14)	<i>P</i> -1 (2)	<i>P</i> ₂ ₁ / <i>n</i> (14)
a (Å)	10.2204(4)	10.9177(3)	7.9432(3)
b (Å)	8.8152(4)	11.3559(3)	15.5600(7)
c (Å)	24.8372(9)	18.2884(6)	12.7663(5)
α (°)	90.00	93.939(2)	90.00
β (°)	90.00	100.874(3)	101.277(3)
γ (°)	90.00	113.565(3)	90.00
Volume (Å ³)	22366.22(16)	2014.67(11)	1547.40(11)
Z	2	2	2
ρ _{calc} (g/cm ³)	1.835	2.247	2.647
μ(Cu) (mm ⁻¹)	9.264	11.219	18.229
F(000)	1228	1324	1176
Crystal size (mm ³)	0.06 x 0.01 x 0.01	0.09 x 0.08 x 0.06	0.06 x 0.04 x 0.03
Radiation	Cu-Kα (λ=1.54178 Å)	Cu-Kα (λ=1.54178 Å)	Cu-Kα (λ=1.54178 Å)
2θ _{max} (°)	133.29	152.04	133.43
Reflections collected	14031	23388	10323
Independent reflections	3930 [R _{int} =0.0622]	8085 [R _{int} =0.0770]	2689 [R _{int} =0.0693]
Number of parameters	279	568	244
GOF and final R indexes for I>2σ(I)	R ₁ =0.0470 wR ₂ =0.1199 GOF=1.058	R ₁ =0.0714 wR ₂ =0.1951 GOF=1.063	R ₁ =0.0405 wR ₂ =0.1025 GOF=1.029
GOF and final R indexes for all data	R ₁ =0.0614 wR ₂ =0.1283 GOF=1.058	R ₁ =0.0786 wR ₂ =0.2007 GOF=1.063	R ₁ =0.0517 wR ₂ =0.1081 GOF=1.029
Largest diff. peak/hole (eÅ ⁻³)	+1.157/-0.671	+2.845/-4.021	+1.001/-2.092
Flack parameter	N/A	N/A	N/A

Table C 2 Crystallographic data of mononuclear Hf compounds of (4), (5) and (6).

Compound	(4)	(5)	(6)
CCDC file number	1965510	1965495	1965511
Empirical formula	C ₈ H _{10.20} HfK ₄ O _{21.10}	C ₈ H ₁₀ HfO ₂₁ Rb ₄	C ₈ H ₁₀ Cs ₄ O ₂₁ Hf
Formula weight	778.85	962.53	1152.29
Temperature (K)	173(2)	173(2)	173(2)
Crystal system	Tetragonal	Monoclinic	Tetragonal
Space group	<i>I</i> 4 ₁ (80)	<i>P</i> 2 ₁ / <i>n</i> (14)	<i>I</i> -4c2 (120)
a (Å)	27.9432(6)	15.2403(12)	13.7545(3)
b (Å)	27.9432(6)	11.7083(9)	13.7545(3)
c (Å)	11.5805(3)	25.1278(18)	12.8436(6)
α (°)	90.00	90.00	90.00
β (°)	90.00	102.616(4)	90.00
γ (°)	90.00	90.00	90.00
Volume (Å ³)	9042.3(5)	4375.5(6)	2429.83(16)
Z	16	8	4
ρ _{calc} (g/cm ³)	2.288	2.922	3.150
μ(Cu) (mm ⁻¹)	16.056	20.534	54.837
F(000)	6000	3568	2072
Crystal size (mm ³)	0.09 x 0.04 x 0.03	0.07 x 0.05 x 0.04	0.11 x 0.04 x 0.03
Radiation	Cu-Kα (λ=1.54178 Å)	Cu-Kα (λ=1.54178 Å)	Cu-Kα (λ=1.54178 Å)
2θ _{max} (°)	133.11	134.04	151.49
Reflections collected	27150	24911	13063
Independent reflections	7376 [R _{int} =0.0443]	7560 [R _{int} =0.0705]	1265 [R _{int} =0.1589]
Number of parameters	669	613	79
GOF and final R indexes for I>2σ(I)	R ₁ =0.0369 wR ₂ =0.0984 GOF=1.051	R ₁ =0.0608 wR ₂ =0.1756 GOF=1.069	R ₁ =0.0587 wR ₂ =0.1596 GOF=1.038
GOF and final R indexes for all data	R ₁ =0.0394 wR ₂ =0.1003 GOF=1.009	R ₁ =0.0753 wR ₂ =0.1982 GOF=1.036	R ₁ =0.0593 wR ₂ =0.1602 GOF=1.038
Largest diff. peak/hole (eÅ ⁻³)	+1.488/-0.688	+2.894/-3.447	+1.760/-1.695
Flack parameter	0.004(10)	N/A	0.017(13)

Table C 3 Crystallographic data of 8-fold Zr compounds of (7), (9), (12) and (13).

Compound	(7)	(9)	(12)	(13)
CCDC file number	1965507	1965513	1965494	1965516
Empirical formula	$C_{48}H_{93.16}N_9O_{49.58}Zr_6$	$C_8H_3Na_4O_{19}Zr$	$C_8H_{10.5}Rb_4O_{21.25}Zr$	$C_8H_{10}Cs_4O_{21}Zr$
Formula weight	2137.07	586.28	879.76	1065.02
Temperature (K)	173(2)	173(2)	173(2)	173(2)
Crystal system	Trigonal	Orthorhombic	Tetragonal	Tetragonal
Space group	<i>P</i> -3 (147)	<i>C</i> 222 ₁ (20)	<i>I</i> 4 ₁ (80)	<i>I</i> -4 (82)
a (Å)	18.8458(6)	7.4137(6)	28.4000(14)	13.7506(4)
b (Å)	18.8458(6)	19.6334(10)	28.4000(14)	13.7506(4)
c (Å)	8.7602(3)	11.7603(8)	11.8556(7)	12.8577(10)
α (°)	90.00	90.00	90.00	90.00
β (°)	90.00	90.00	90.00	90.00
γ (°)	120.00	90.00	90.00	90.00
Volume (Å ³)	2694.47(19)	1711.8(2)	9562.3(11)	2431.1(2)
Z	1	4	16	4
ρ _{calc} (g/cm ³)	1.317	2.275	2.444	2.910
μ(Cu) (mm ⁻¹)	5.300	7.327	14.505	50.579
F(000)	1081	1148	6664	1944
Crystal size (mm ³)	0.09 x 0.06 x 0.04	0.11 x 0.07 x 0.04	0.18 x 0.03 x 0.03	0.11 x 0.04 x 0.03
Radiation	Cu-Kα (λ=1.54178 Å)	Cu-Kα (λ=1.54178 Å)	Cu-Kα (λ=1.54178 Å)	Cu-Kα (λ=1.54178 Å)
2θ _{max} (°)	133.41	151.85	133.15	157.60
Reflections collected	14932	8234	18413	13714
Independent reflections	3122 [R _{int} =0.0846]	1744 [R _{int} =0.0585]	8127 [R _{int} =0.0591]	2508 [R _{int} =0.1508]
Number of parameters	197	147	646	156
GOF and final R indexes for I>2σ(I)	R ₁ =0.0778 wR ₂ =0.2153 GOF=1.026	R ₁ =0.0476 wR ₂ =0.1272 GOF=1.084	R ₁ =0.0547 wR ₂ =0.1445 GOF=1.052	R ₁ =0.0895 wR ₂ =0.2126 GOF=1.088
GOF and final R indexes for all data	R ₁ =0.0931 wR ₂ =0.2294 GOF=1.025	R ₁ =0.0494 wR ₂ =0.1306 GOF=1.084	R ₁ =0.0640 wR ₂ =0.1508 GOF=1.052	R ₁ =0.0944 wR ₂ =0.2196 GOF=1.088
Largest diff. peak/hole (eÅ ⁻³)	+1.599/-0.980	+0.980/-1.155	+1.623/-1.231	+1.642/-1.316
Flack parameter	N/A	0.251(18)	0.042(16)	0.008(15)

Table C 4 Crystallographic data of 9-fold Zr compounds of **(8)**, **(10)** and **(11)**.

Compound	(8)	(10)	(11)
CCDC file number	1965518	1965496	1965519
Empirical formula	C ₁₆ H ₆₄ Li ₁₂ O ₉₀ Zr ₈	C ₂₄ H ₆₆ K ₁₈ O ₁₂₀ Zr ₁₂	C ₃₂ H ₂₀ Rb ₂₄ O ₁₈₅ Zr ₁₆
Formula weight	2509.71	4073.20	6875.28
Temperature (K)	173(2)	173(2)	173(2)
Crystal system	Monoclinic	Trigonal	Tetragonal
Space group	<i>C</i> 2/m (12)	<i>R</i> -3 (148)	<i>I</i> 4mm (107)
a (Å)	32.5031(12)	28.5897(11)	28.0950(6)
b (Å)	16.7558(7)	28.5897(11)	28.0950(6)
c (Å)	18.3219(7)	12.9130(8)	12.7699(4)
α (°)	90.00	90.00	90.00
β (°)	110.560(2)	90.00	90.00
γ (°)	90.00	120.00	90.00
Volume (Å ³)	9342.8(6)	9140.6(9)	10079.7(5)
Z	4	3	2
ρ _{calc} (g/cm ³)	1.784	2.220	2.265
μ(Cu) (mm ⁻¹)	8.191	14.818	14.666
F(000)	4088	5976	6440
Crystal size (mm ³)	0.12 x 0.09 x 0.08	0.11 x 0.09 x 0.04	0.18 x 0.03 x 0.03
Radiation	Cu-Kα (λ=1.54178 Å)	Cu-Kα (λ=1.54178 Å)	Cu-Kα (λ=1.54178 Å)
2θ _{max} (°)	133.67	133.38	151.93
Reflections collected	31949	1872	20903
Independent reflections	8601 [R _{int} =0.0850]	1517 [R _{int} =0.0324]	4463 [R _{int} =0.1096]
Number of parameters	565	262	328
GOF and final R indexes for I>2σ(I)	R ₁ =0.0941 wR ₂ =0.2700 GOF=1.149	R ₁ =0.0620 wR ₂ =0.1647 GOF=1.097	R ₁ =0.0770 wR ₂ =0.2014 GOF=1.060
GOF and final R indexes for all data	R ₁ =0.1313 wR ₂ =0.3083 GOF=1.098	R ₁ =0.0716 wR ₂ =0.1738 GOF=1.097	R ₁ =0.0976 wR ₂ =0.2215 GOF=1.060
Largest diff. peak/hole (eÅ ⁻³)	+2.140/-0.968	+1.458/-0.915	+2.188/-1.867
Flack parameter	N/A	N/A	0.07(3)

Table C 5 Atomic ratios in Hf oxalate samples by EDX-SEM.

Sample	Alkali atom%	Hf atom%	Alkali:Hf	Average composition
Cs-Hf oxalate	59.09	31.73	1.862 : 1	Hf : Cs = 1 : 2.4
	58.52	30.87	1.896 : 1	
	67.95	27.47	2.473 : 1	
	75.94	21.66	3.506 : 1	
Rb-Hf oxalate	67.59	25.75	2.625 : 1	Hf : Rb = 1 : 2.6
	63.46	28.53	2.224 : 1	
	68.74	24.23	2.837 : 1	
	71.53	25.71	2.782 : 1	
K-Hf oxalate	56.96	17.27	3.298:1	Hf : K = 1 : 3.7
	53.38	13.01	4.103:1	
Li-K-Hf oxalate	60.68	30.32	2.001:1	Hf : K = 1 : 2.3
	69.39	24.26	2.859:1	
	63.00	29.04	2.169:1	
Na-Hf oxalate	38.7	54.45	0.711 : 1	Hf : Na = 1 : 0.6
	21.45	73.68	0.291 : 1	
	34.89	53.81	0.648 : 1	
	35.36	58.47	0.605 : 1	

Table C 6 Atomic ratios in of Zr-peroxo oxalate samples by EDX-SEM.

Sample	Alkali atom%	Zr atom%	Alkali:Zr	Average composition
Cs-Zr oxalate	55.38	38.43	1.441 : 1	Zr : Cs = 1 : 2.0
	64.56	32.55	1.983 : 1	
	54.85	38.72	1.417 : 1	
	74.63	23.21	3.215 : 1	
Rb-Zr oxalate	61.72	31.30	1.971 : 1	Zr : Rb = 1 : 2.2
	66.21	28.35	2.335 : 1	
	67.51	26.96	2.504 : 1	
	59.90	31.28	1.915 : 1	
K-Zr oxalate	58.48	36.84	1.587:1	Zr : K = 1 : 1.7
	61.41	33.41	1.838:1	
Na-Zr oxalate	41.14	45.48	0.905 : 1	Zr : Na = 1 : 1.1
	32.44	48.45	0.670 : 1	
	58.15	38.28	1.519 : 1	
	52.64	44.8	1.175 : 1	